Hypervelocity Impact Induced Disturbances on Composite Sandwich Panel Spacecraft Structures

A thesis submitted in fulfilment of the requirements for the degree of Doctor of Philosophy

Shannon Ryan
B.Eng (Aero) (Hon I)

School of Aerospace, Mechanical and Manufacturing Engineering
Science, Engineering and Technology Portfolio
RMIT University
July 2007

Declaration

I certify that except where due acknowledgement has been made, the work is that of the author alone; the work has not been submitted previously, in whole or in part, to qualify for any other academic award; the content of the thesis is the result of work which has been carried out since the official commencement date of the approved research program; and, any editorial work, paid or unpaid, carried out by a third party is acknowledged.

Shannon Ryan

30 July 2007

Abstract

The next generation of European scientific satellites will carry extremely sensitive measurement devices that require platform stability orders of magnitude higher than current missions. It is considered that the meteoroid and space debris (M/SD) environment poses a risk to the success of these missions as disturbances induced by the impact of these particles at hypervelocity may degrade the platform stability below operational requirements.

A comprehensive literature review presented in the PhD thesis found that current M/SD risk assessment considers the probability of structural penetration and catastrophic failure; however these requirements are assessed (in general) for manned space missions only. For scientific satellite missions, the degradation of measurement accuracy represents mission failure in an equally critical yet less dramatic way than spacecraft catastrophic failure. To ensure feasibility of the next generation scientific missions such as ESA's Global Astrometric Interferometer for Astrophysics (GAIA) satellite, M/SD risk analysis addressing both penetration-based failure criteria and impact-induced degradation of the platform stability must be performed.

GAIA will operate in a Lissajous orbit about the Earth-Sun L2 Lagrangian point. In such interplanetary orbits, the dominant debris threat is provided by the natural meteoroid environment. The velocity of meteoroids relevant to the GAIA mission can range from 11 to 72 km/s, with a mean value of 20 km/s. Experimental acceleration facilities are the backbone of hypervelocity impact research. However, the operational capabilities of these facilities are unable to cover the complete range of possible in-orbit impact conditions. For example, two-stage light-gas guns, the most commonly used hypervelocity acceleration facility, are only capable of consistently achieving impact velocities of ~9 km/s. Therefore, numerical methods are required for support of the experimental test program.

Composite sandwich panels with Carbon Fibre Reinforced Plastic facesheets and aluminium honeycomb cores (CFRP/AL HC SPs) are amongst the most commonly used structures in satellites today. Furthermore, due to their high stiffness, low weight, and low thermal expansion, these structures will be the predominant platform applied in future stability-critical satellites. However, in a review of experimental hypervelocity impact research dating back to the Apollo era it became

apparent that the performance of these structures under hypervelocity impact is not well understood. Furthermore, the analysis of impact-induced disturbances on these structure types is complicated by the dependence of excitation modes on penetration resistance of the structure: i.e. different structural excitation modes are expected if the impacting particle is defeated by the sandwich panel front facesheet rather than, for example, completely perforating the sandwich panel structure.

To quantify the vibration environment in satellites, structural analysis codes (such as NASTRAN) are commonly used. However, for the analysis of hypervelocity impact, numerical hydrocodes are superior to structural codes as they allow the coupling of complex material models with a fluid-structure program. Recent advances in the modelling of composite materials within hydrocodes allow orthotropic constitutive behaviour, non-linear equation of state, orthotropic non-linear hardening, and individual material plane interactive failure criteria to be described.

In this PhD thesis, disturbances induced by the impact of M/SD particles at hypervelocity on the GAIA satellite have been investigated. An extensive experimental impact test program has been performed on six different CFRP/Al HC sandwich panel structures, from which an empirical expression that defines the conditions of structural perforation (referred to as a ballistic limit equation, BLE) has been derived. Used in conjunction with an existing BLE capable of predicting penetration limits of monolithic CFRP plates, the protective capability of a GAIA-representative CFRP/Al HC SP has been defined. A numerical model of the CFRP/Al HC SP has been constructed in the commercial hydrocode AUTODYN, and a series of impact simulations have been performed during which the local impact-induced disturbance has been measured. Using the BLE predictions, simulations have been performed for impact causing: cratering in the front facesheet; perforation of the front facesheet but not the rear facesheet, and; perforation of the complete sandwich panel. A number of impact experiments have been performed during which the impact-induced disturbances were recorded using a massless device (laser interferometer). These measurements have been used to validate the numerical model via comparison of the disturbance signals.

In the absence of experimentally-characterised material data, a procedure has been defined which allows the derivation of a complete composite material data set for implementation in AUTODYN. This derivation procedure applies a number of classic composite mechanics theories (e.g.

micromechanics, classical laminate theory) along with shock wave relationships to characterise structural laminates from basic constituent data. The derivation procedure has been validated through comparison with an existing experimentally-characterised data set for a space-representative CFRP laminate.

From the disturbance measurements made in the numerical simulations, a function has been defined which describes the local elastic excitation of a CFRP/Al HC SP under hypervelocity impact. The disturbance characterisation is made such that it is applicable as an excitation force to be applied over a finite area within the satellite FE model, allowing propagation of impact-induced disturbances to critical stability regions (i.e. measurement devices). The disturbance induced upon measurement devices by M/SD impacts at both near- and far-body locations can then be made, allowing the threat to mission objectives to be assessed.

Acknowledgements

This project was completed within the Spacecraft Safety Technology Group, Impact Physics Department, of the Fraunhofer Institute for High-Speed Dynamics, Ernst-Mach-Institute (EMI) in Freiburg, Germany. I would like to express my gratitude to Professor Klaus Thoma, director of EMI, for giving me the opportunity to work under his expert leadership within such a professional and inspirational team of scientists, engineers and technicians.

My stay at EMI was enriched by the guidance, support and friendship of my colleagues, first and foremost Dr Frank K Schäfer. A better scientific mentor, colleague, boss, and friend will be truly difficult to find. I am also indebted to Dr Werner Riedel, Dr Markus Wicklein, Dr Stefan Hiermaier, and Robin Putzar for their expert assistance and fruitful discussions which helped make my stay at EMI such a rewarding experience.

Research for this project was performed as part of three ESA-ESTEC studies completed in part within the spacecraft safety technology group: Composite Materials Impact Damage Analysis (ESA Contract 16721/02/NL/CK), Spacecraft Disturbances from Hypervelocity Impact (ESA Contract 18583/04/NL/CH), and Carbon Fibre Material Models for Hypervelocity Impact Numerical Simulations (ESA Contract 18763/04/NL/SFe). All three projects were managed by Michel Lambert of ESA-ESTEC, who I would like to thank for both his approachable, friendly manner and his efficient technical management skills.

Professor Adrian Mouritz of RMIT University assumed the role of university supervisor during my research project. Although the geographical separation and time-zone difference were extreme, he provided guidance and expertise throughout the duration of the project, for which I offer my appreciation.

Last but not least my thanks go out to Adrian Orifici of RMIT University for his truly tireless work-ethic which cannot fail to inspire the upmost of those around him, myself in particular.

This work would not have been possible without financial support provided through the Australian Postgraduate Award Program of the Australian Department of Education, Science and Training.

Contents

Nomenclature

Abbreviations and Acronyms

ADAMMO	Advanced Damage Model for Numerical Simulation Codes
AE	Acoustic Emission
Al	Aluminium
AMMHIS	Advanced Material Model for Hypervelocity Impact Simulations
AXAF	Advanced X-Ray Astrophysics Facility
BLE	Ballistic Limit Equation
BLGG	Baby Light Gas Gun
CFRP	Carbon Fibre Reinforced Plastic
CLT	Classical Laminate Theory
DCB	Double Cantilever Beam test
DSA	Deployable Sunshield Assembly
DSP	Impact result – Detached Spallation
EMI	Ernst- Mach- Institute (FhG)
ENF	End Notched Flexure test
ENV	ENVISAT (Environmental Satellite)
EOS	Equation Of State
ESA	European Space Agency
ETW BLE	ESA Triple Wall Ballistic Limit Equation
FE	Finite Element
FF	Fibre Failure
FS	Facesheet
GAIA	Global Astrometric Interferometer for Astrophysics
GEO	Geostationary Earth Orbit
GOCE	Gravity Field and Steady-State Ocean Circulation Explorer
H/P	Hershel/Planck structure panel
HC	Honeycomb
HSFC	High-Speed Framing Camera
HVI	Hypervelocity Impact
IADC	Inter-Agency Space Debris Coordination Committee
IFF	Inter-Fibre Failure
ISS	International Space Station
JAXA	Japan Aerospace Exploration Agency
LAG	Lagrangian discretisation
LEO	Low Earth Orbit
LGG	Light Gas Gun
LV	Laser Vibrometer
M/SD	Meteoroid/Space Debris
MLI	Multi Layer Insulation

NASA	National Aeronautics and Space Administration
NP	Impact result – No Detached Spallation
P	Impact result – Perforated
PLM	Payload Module
PNCF	Probability of No Catastrophic Failure
PNP	Probability of No Penetration
PNSP	Probability of No Subcomponent Failure
RAD1	Radarsat-2 +/-Z platform
RAD2	Radarsat-2 shear panel
RAD3	Radarsat-2 cone panel
SAX	BEPPO-SAX structure panel
SLGG	Space Light Gas Gun
SP	Sandwich Panel
SRS	Shock Response Spectra
SVM	Service Module
u.d.	Unidirectional
WP	Witness Plate
WWFE	World Wide Failure Exercise

Symbols

$\overline{\sigma}$	Effective stress
$\overline{\varepsilon}$	Effective strain
σ	Normal stress
τ	Shear stress
ε	Strain
ρ	Density
Γ	Grüneisen gamma
α	Impact angle
[C]	Stiffness matrix
[S]	Compliance matrix
[T]	Transformation matrix
a	Plasticity parameter
A_1	Bulk modulus (in compression)
A_1'	Average (or effective) bulk modulus
A_2	Quadratic bulk modulus (in compression)
A_3	Cubic bulk modulus (in compression)
B_0 and B_1	Polynomial equation of state parameters
c_L	Longitudinal wave soundspeed
c_p	p-wave soundspeed
d_c	Critical projectile diameter
D_{delam}	Diameter of internal delamination in impacted composite

$d_{h,ave}$	Clear hole diameter (average)
d_p	Projectile diameter
d_{SP}	Spall diameter
E	Young's modulus
e	Internal energy
G	Shear modulus
G_f	Fracture energy
KE	Kinetic energy
ν	Poisson's ratio
p	Pressure
P	Momentum
S	Slope of the U_s-u_p relationship
S_{xy}	In-plane shear strength
T_1	Bulk modulus (in tension)
T_2	Quadratic bulk modulus (in tension)
u_p	Particle velocity
U_s	Shock velocity
V	Impact Velocity
V_f	Fibre volume content
X_c	Compression strength in the fibre direction
X_t	Tensile strength in the fibre direction
Y_c	Compression strength transverse to the fibre direction
Y_t	Tensile strength transverse to the fibre direction

Subscripts and superscripts

0	Initial condition
1,2,3	Orthotropic material principle directions (global coordinates)
c	Composite (ply) property
f	Fibre property
k	Laminate ply index
lam	Laminate
m	Matrix property
p	Plastic
r	Reference condition
x,y,z	Orthotropic material principle directions (body coordinates)

1 Introduction

Between the launch of Sputnik-I in 1957 and January of 2002, there were a total of 4,191 successful launches by the international space community, deploying over 17,000 man-made objects into orbit about the Earth. These launches had (as of January 2002) created a man-made debris environment orbiting the Earth consisting of everything from derelict spacecraft and launch vehicle upper stages to paint flakes and solid rocket motor effluents. The expected on-orbit mass of this man-made pollution is in excess of 5500 tons (Klinkrad, 2006), made up of approximately 20,000 objects larger than 10cm, 600,000 objects between 1 and 10cm, and tens of millions of particles smaller than 1cm (Oswald et al., 2006).

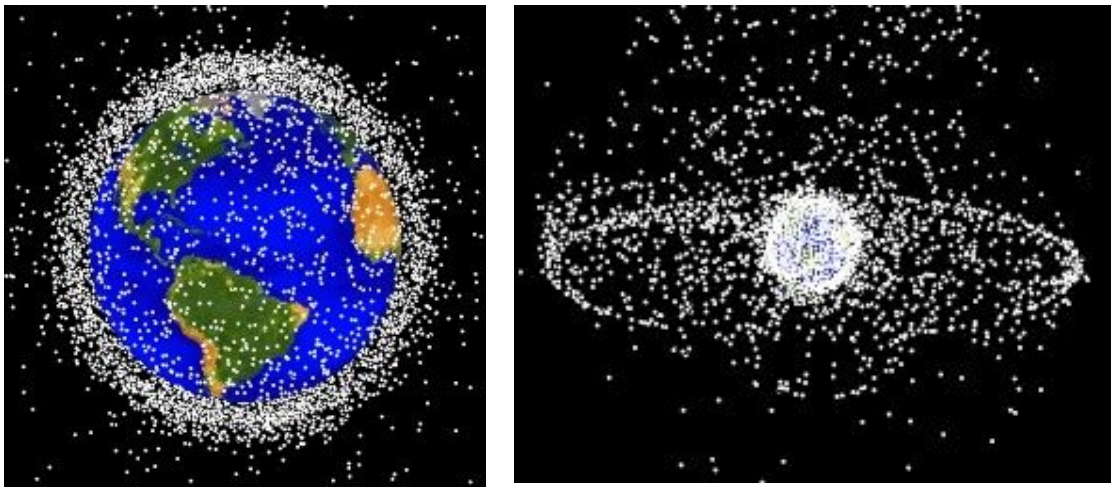

Figure 1-1 The 1997 USSPACECOM space debris catalogue population in low Earth orbit (left) and up to geostationary altitude (right).

The distribution of orbital debris is concentrated around the altitudes of major scientific, commercial, and defence interest (shown in Figure 1-1) with 45% of trackable debris mass found in Low Earth Orbit (LEO: 200-2000 km above the Earth's surface) and 28.8% in Geostationary Earth Orbit (GEO – around 35,786 km altitude) (Klinkrad, 2006). As the debris population increases, collisions between objects become more common. Indeed Liou and Johnson (2006) found that as of 2006, the "critical density" of the debris population in some altitude regimes of LEO has already been exceeded, i.e. even if no new launches were conducted the number of debris objects will continue to uncontrollably increase as a result of collisions between debris bodies producing more fragments than those removed by atmospheric drag (see Figure 1-2).

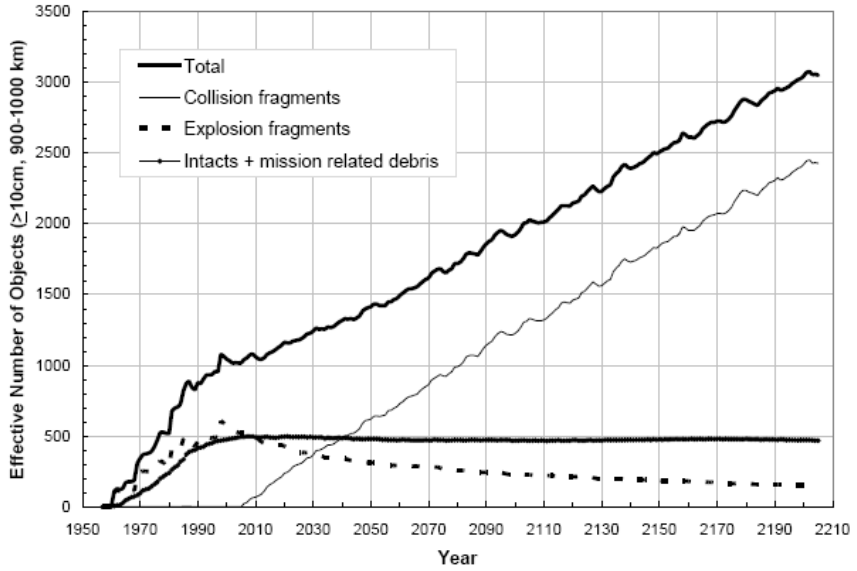

Figure 1-2 The population growth of objects (10cm and larger) orbiting with altitudes between 900 and 1000 km (Liou and Johnson, 2006).

Significant efforts are being undertaken by many national space agencies, including the adoption of voluntary space debris mitigation guidelines by the Scientific and Technical Subcommittee (STSC) of the United Nations' Committee on the Peaceful Uses of Outer Space (COPUOS) in February 2007. The mitigation guidelines call for an effort to (from Liou (Ed.), 2007):

- Reduce debris released during normal spacecraft operations;
- Minimise the potential for break-ups during operational phases;
- Limit the probability of accidental collisions in orbit;
- Avoid intentional destruction and other harmful activities;
- Minimise the potential for post-mission break-up resulting from stored energy; limit the long-term presence of spacecraft and launch vehicle orbital stages in the low-Earth orbit (LEO region after the end of their mission, and;
- Limit the long-term interference of spacecraft and launch vehicle orbital stages with the geosynchronous Earth orbit (GEO) region after the end of their mission.

However, these guidelines are voluntary and are not applied by all space-faring nations. Indeed, on January 11th 2007, a successful Chinese anti-satellite (ASAT) system test destroyed the out-of-service meteorological satellite Fengyun-1C. This event represents the single worst contamination of low Earth orbit in the last half-century (Liou (Ed.),

2007). While the number of objects larger than 5cm is expected to exceed 2000, the number of objects 1cm or more is estimated to be as large as 35,000, indicating an increase of more than 15% over the known debris environment at the beginning of 2007, as shown in Figure 1-3.

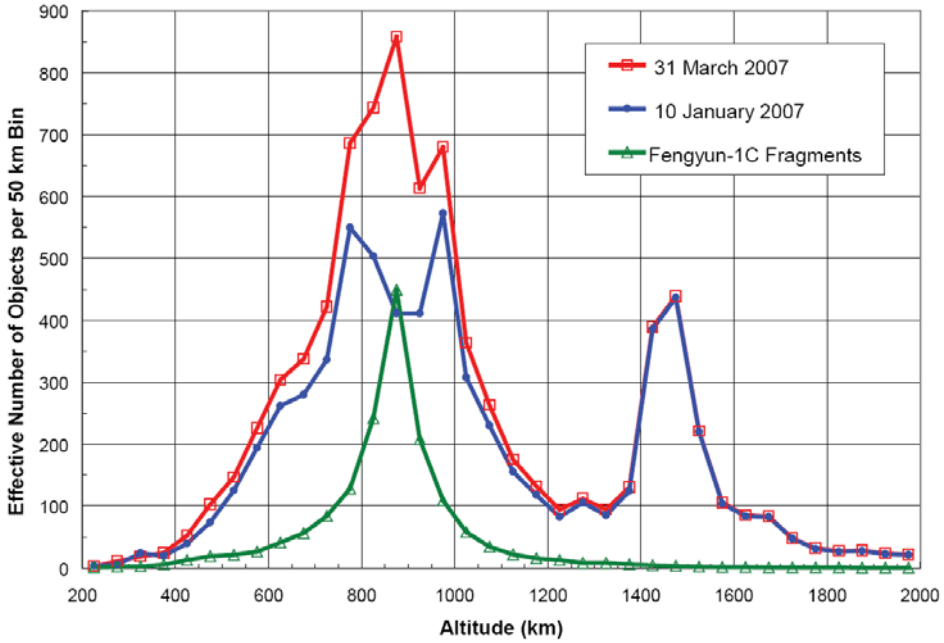

Figure 1-3 Distributions of the US Space Surveillance Network (US SSN) debris catalogue in low Earth orbit on January 10th and March 31st 2007 (Liou (Ed.), 2007).

Due to atmospheric drag and other perturbing forces (e.g. solar activity) orbital objects lose energy, leading to a progressive decrease in orbital altitude. For objects with a circular orbit at altitudes of 200-400 km, this loss of energy causes atmospheric re-entry within months (Anon, 1995). As the altitude increases, the atmospheric density, and with it the decay rate of orbiting bodies, decreases. Objects in geosynchronous orbit have lifetimes in excess of a million years.

Although technically viable, the active removal of space debris remains economically prohibitive. As such, current efforts by national space agencies and international committees such as the Inter-Agency Space Debris Coordination Committee (IADC) focus on the mitigation of future debris generation and the protection of current space missions.

During their operational life-time spacecraft are subject to impact of micrometeoroid and space debris (M/SD) particles. The effects of space

debris impact can be classified into primary and secondary effects. Primary effects refer to the mechanical damage produced by the projectile during the impact event, i.e. penetration of and cratering to the spacecraft outer wall. Although rare, destructive collisions between two bodies in space do occur. In 1993, the first servicing mission to the Hubble Space Telescope found a hole ca. 2 cm in diameter in a high-gain antenna, completely penetrating the dish (although not causing any loss in functionality) (Klinkrad, 2006). In 1996, France's Cerise military reconnaissance satellite collided with an Arianne 4 booster fragment, severing the stabilisation boom.

Secondary effects refer to processes which are caused by a transformation of the impacting projectile's kinetic energy to mechanical and thermal processes, for example:

- Generation of acoustic and shock waves;
- Ejection of material inside the spacecraft hull;
- Ionization phenomena, generation of magnetic fields and optical radiation, etc.

Although it remains extremely difficult to categorise the cause of mission failure or operational anomalies, there exist a large database of events in which secondary effects caused by the impact of space debris are considered the likely candidate. For example the European Space Agency's Olympus Satellite experienced total failure on August 11th, 1993 during a recorded meteoroid storm. It is speculated that a debris particle induced an arc discharge which led to the satellite's failure.

The shielding capability and configuration of a spacecraft play a large role in determining the probability of risk caused by M/SD impact. In manned spacecraft, the outer-walls are generally a double-plate configuration known as a Whipple shield. The outer and inner walls of the shield are designed to meet stringent requirements concerning module unzipping or rupture, as well as atomic oxygen protection, radiation shielding, thermal control, outgassing and repairability (Christiansen, 1987). There exists, therefore, very little flexibility in the selection of Whipple shield materials. Various aluminium alloys represent the globally-accepted standard. The space between the walls of the Whipple shield, however, represents an area of relative flexibility. This area commonly contains what is generally referred to as an M/SD blanket, or Whipple shield stuffing. Some stuffed

Whipple shield concepts of various space agencies are shown in Figure 1-4.

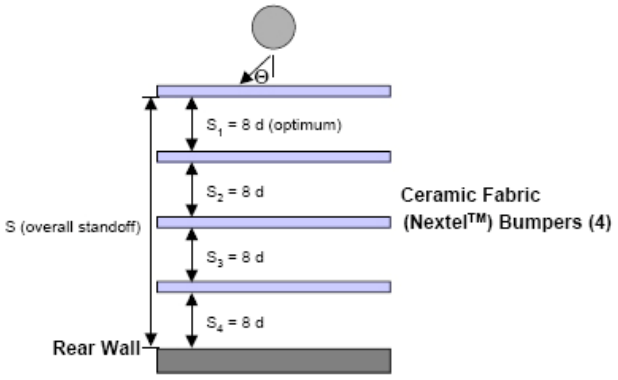

Image © NASA

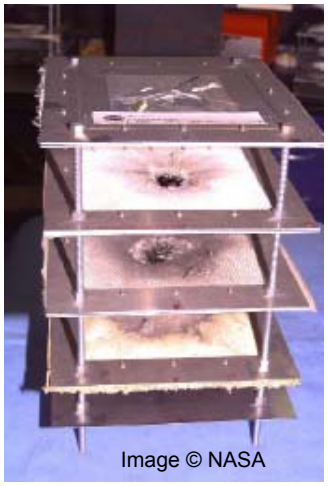

Image © NASA

Image © JAXA

Image © JAXA

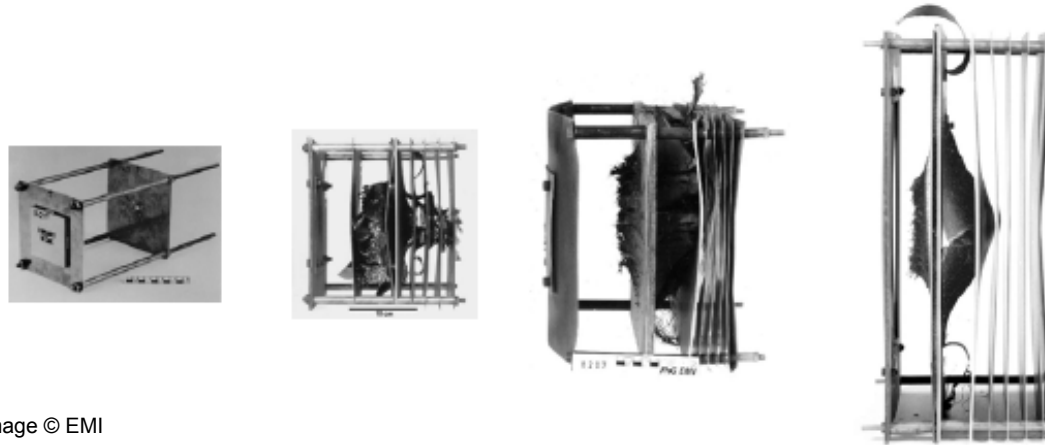

Image © EMI

Figure 1-4 Manned spacecraft shielding configurations. Upper: NASA multishock shield concept; Middle: JAXA stuffed Whipple shield for the JEM module; Lower: Evolution of ESA's Columbus Module debris shield design.

Generally, M/SD blankets consist of flexible, high strength materials such as Aramid (e.g. Kevlar) and ceramic (e.g. Nextel) fibres. These high strength flexible fabrics increase the protective capability of the structural wall by absorbing fragment cloud energy and thus reducing its lethality.

The configuration of manned spacecraft varies according to the mission profile. For example, a reusable launch vehicle such as the US Space Shuttle is designed based on aerodynamic requirements during re-entry. Orbital spacecraft, such as modules of the International Space Station, are configured to maximise available space in launch vehicles.

Unmanned spacecraft are, relatively, more uniform in their configuration, generally involving a service module which carries mission support systems such as electronics, fuel pipes etc, and a payload module. Typical satellite service modules are square or octagonal boxes with a central cone/cylinder and shear panels. The cone cylinder and shear panels are generally constructed from a sandwich panel with CFRP facesheets and an Aluminium honeycomb core (CFRP/Al HC SP). Similarly, the upper and lower platforms are also CFRP/Al HC SPs. The lateral panels of the service module are, due to thermal reasons, generally sandwich panels with Aluminium facesheets and Aluminium honeycomb cores. These panels are also generally wrapped with Multi Layer Insulation blankets (MLI).

Some satellite payload modules have a similar architecture to the service modules, with additional external items (e.g. antennas) attached. In this case the lateral panels may be made with CFRP/Al HC SP (e.g. ENVISAT). Other payloads include telescopes, which require a specific design quite often constructed predominantly of CFRP (for stability and pointing requirements). Truss-type structures are often used for supporting antennas, solar arrays etc, typically made of CFRP.

The use of non-metallic honeycomb cores is limited to applications where radio-frequency transparency is required.

Examples of satellite configurations are given in Figure 1-5-Figure 1-7 for the GAIA, GOCE and Planck (service module only) missions.

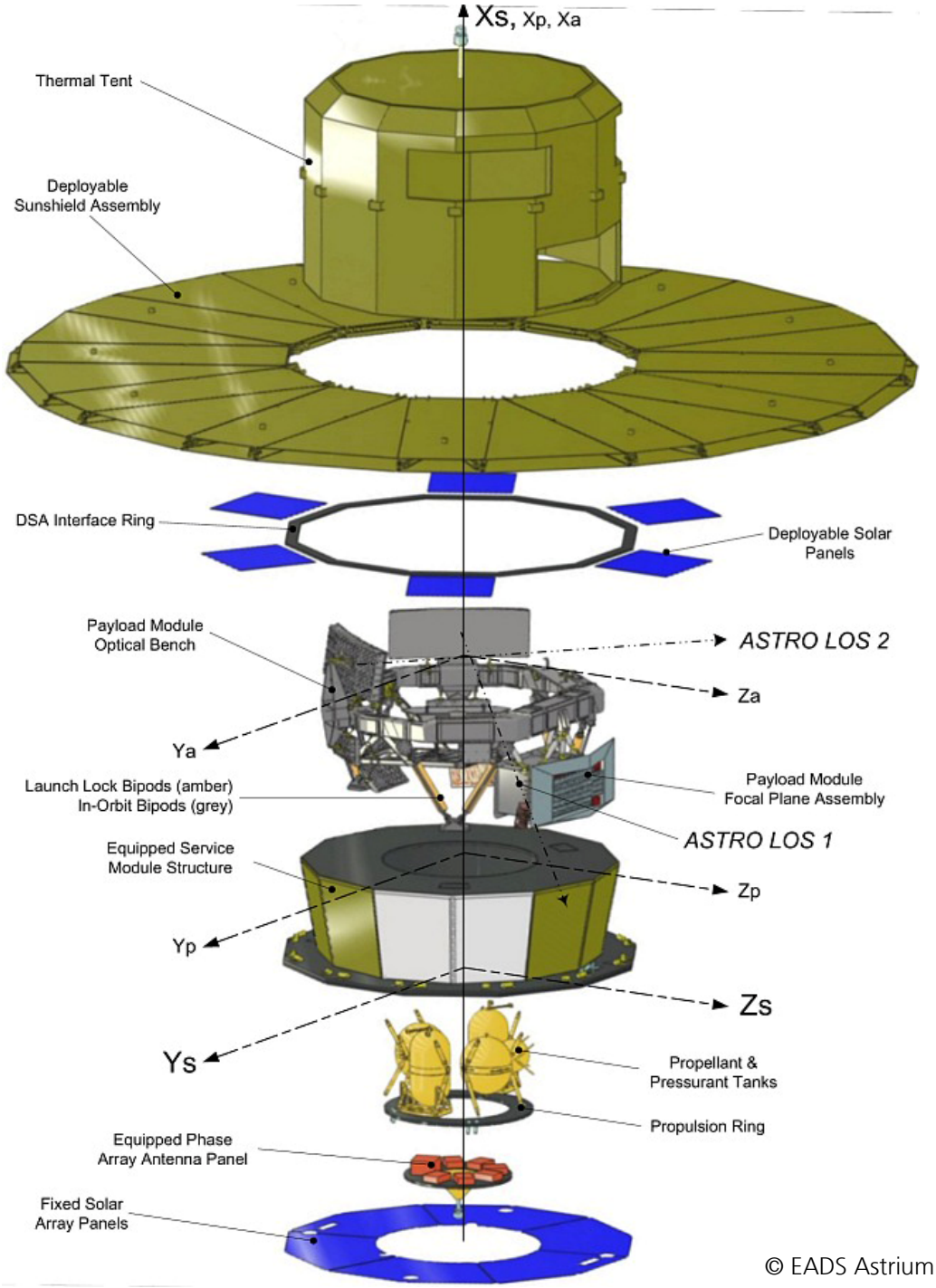

Figure 1-5 Exploded view of the GAIA satellite structure.

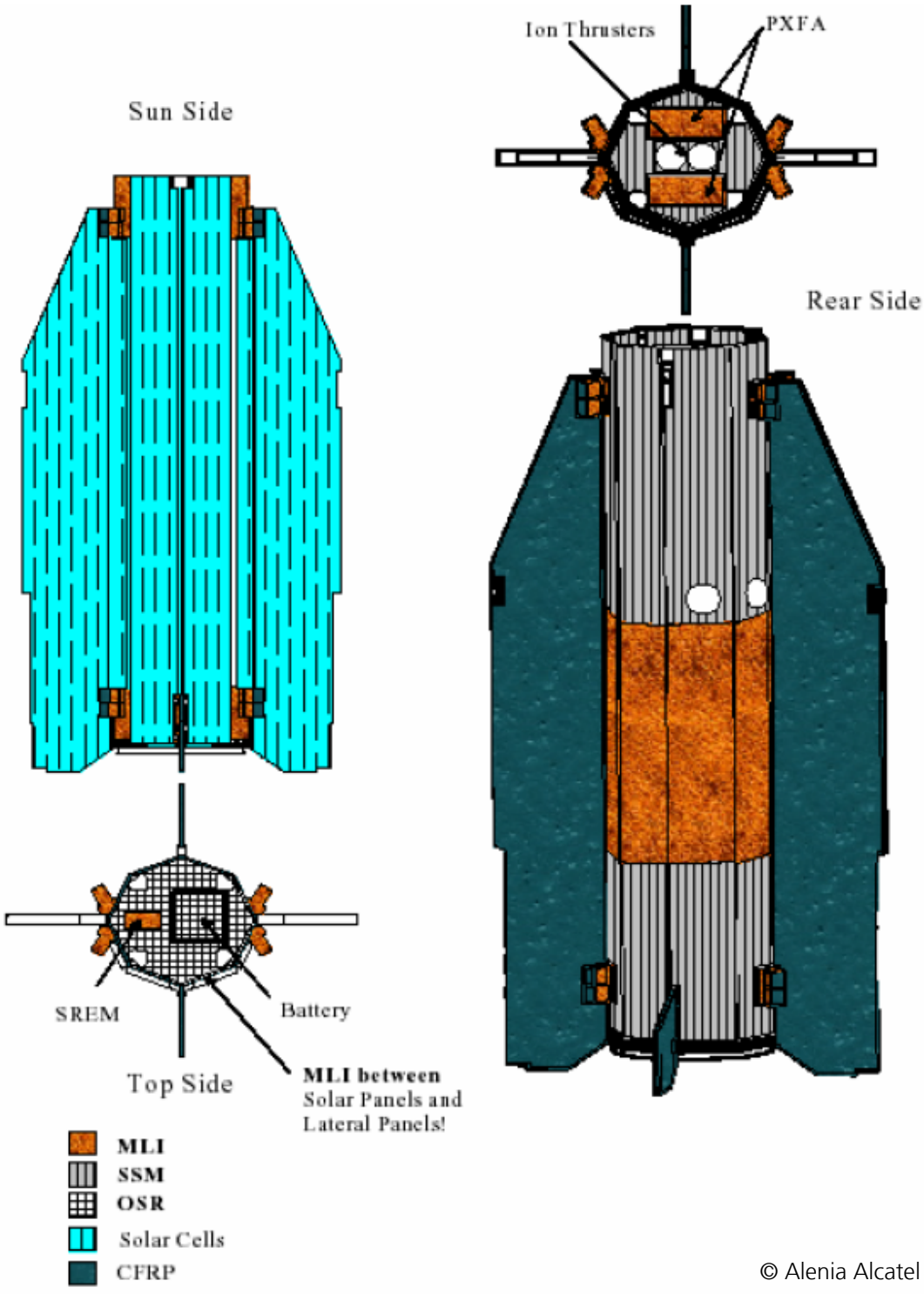

Figure 1-6 GOCE overall design concept for platform thermal control.

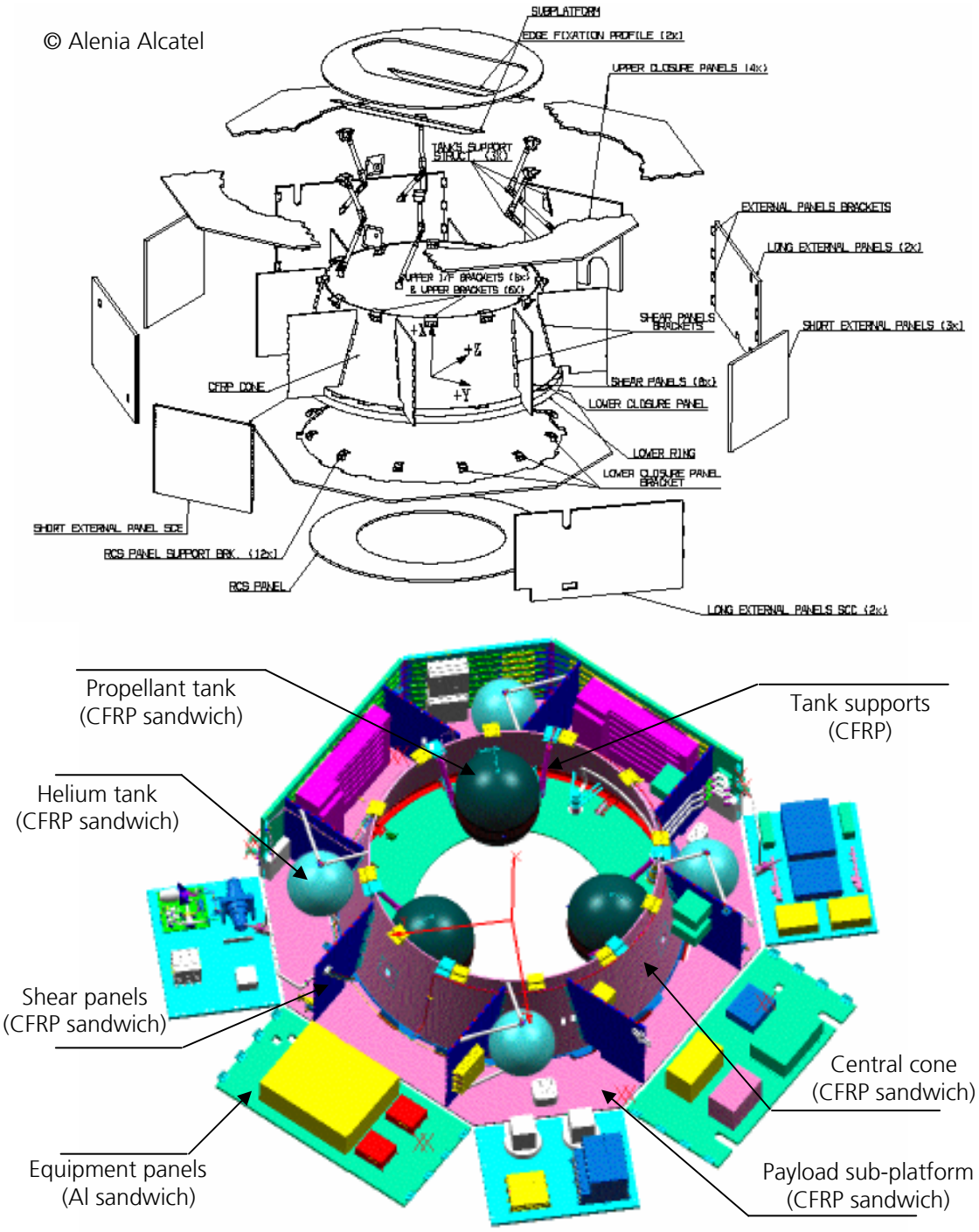

Figure 1-7 Exploded view and configuration of Planck service module structure.

Future ESA science missions incorporate ultra-sensitive measurement equipment (e.g. GOCE, GAIA) and thus require extremely high platform stability, orders of magnitude higher than that of previous missions. In order to meet such stringent performance requirements (e.g. required acceleration stability of GOCE is one millionth of Earth gravity) these

spacecraft will utilize CFRP/Al HC SPs as the primary structure. Given the high stability requirements and the rigidity of the structural platforms of these future missions, the perturbations induced by the impact of small micrometeoroid or space debris particles may be a source of risk to the achievement of mission scientific goals.

This thesis aims to provide a means of quantifying the perturbations induced by the impact of micrometeoroid/space debris particles on satellites with CFRP/Al HC sandwich panel walls. Quantification can be performed using finite element satellite models, for which impact perturbations can be propagated throughout the satellite body to the sensitive measurement locations. This will allow debris risk assessment to consider the threat of spacecraft disturbances induced by hypervelocity impact with respect to the mission performance limits.

In Chapter 2 of this thesis a literature review is presented which describes the current state-of-the-art in micrometeoroid and space debris risk assessment. This review addresses assessment methods and tools, concentrating on the numerical simulation of hypervelocity impact (HVI).

For considering the effects of HVI on sandwich panel structures, and for planning the experimental and numerical simulation campaigns which make up the research quotient of this work, it is important to know the perforation limits of the sandwich panel structure. In Chapter 3 a ballistic limit equation is derived from experimental impact test data and validated against other damage equations and impact test data.

In Chapter 4 a numerical model is constructed for simulation of hypervelocity impact on a space-representative CFRP/Al HC SP structure. The construction of the numerical set-up is described, and validation of the disturbance measurements is made through comparison with experimentally-measured signals.

Chapter 5 considers the simplification and characterisation of the numerically-measured impact-induced disturbance signals to provide an expression for the excitation suitable for implementation in structural analysis codes for quantification of the perturbation magnitude at vibration-sensitive locations in satellites.

Finally, the results of this thesis are summarised and conclusions presented in Chapter 6.

2 Literature Review

2.1 Space Debris / Meteoroid Risk Assessment

Since the beginning of the Apollo program, design requirements have been established to ensure spacecraft are protected from critically damaging meteoroid impacts. However, the International Space Station (ISS) is the first space program to include meteoroid/space debris (M/SD) shielding as an integral part of the design requirements (Avans et al. 1990). The ISS represents a unique challenge for protection against M/SD given its extremely large exposed surface area and orbital lifetime. To address the threat of M/SD impact on the ISS, a management strategy was developed which classified debris into three size categories: small debris (less than 1cm in diameter); mid-size debris (between 1 and 10 cm), and large debris (greater than 10cm) (Carlone, 1992). For small debris particles, passive shielding design is capable of mitigating the threat. For large debris particles, re-orbiting manoeuvres are performed to move the ISS out of the debris flight path. Mid-size debris particles represent the greatest hazard to the station or crew as they are too large to be shielded against, and too small to enable tracking by ground based-sensors (Anon, 1997).

M/SD requirements for the ISS have the following objectives (Christiansen et al., 2006):

- Protect the crew from meteoroid/debris impact
- Protect ISS critical hardware from meteoroid/debris impact
- Minimise damage to all station elements from meteoroid/debris impacts.

These goals are achieved through the definition of specific requirements for M/SD shielding of the ISS. These specific requirements are expressed in terms of the Probability of No Penetration (PNP), the Probability of No Catastrophic Failure (PNCF), and the Probability of No Subcomponent Penetration (PNSP). The PNP is a measure of the penetration resistance of the spacecraft structure to impacts predicted during its operational lifetime. The complete ISS is required to exceed a PNP of 0.76, i.e. the probability of a single penetration of the complete ISS structure must be less than 24% over a 10 year period. The PNCF is an assessment of the potential risk of vehicle and/or crew member loss. This measure includes

an assessment of the effects of a penetration on the vehicle and its crew. Module/spacecraft depressurisation rates, equipment response, and crew response (per procedure as applicable) are included in this assessment. The ISS is required to meet/exceed a PNCF of 0.95, i.e. the probability of vehicle/crew loss must be lower than 5% a for 10 year mission duration. The PNSP allows for the separate definition of penetration into "critical items" and "functional items" (Nieder, 1990). Functional items are those whose failure results only in the loss of functionality and do not immediately affect the crew's safety, e.g. avionics cabling.

These global design requirements were refined by NASA for each critical element of the ISS. Critical elements were identified as: US Habitation Module, the US Laboratory Module, the Node structure, the Pressurised Logistics Module, the Unpressurised Logistics Module, and any critical pressure bottles external to these modules. These critical elements were designed for a PNP of 0.9955 (99.55%) (Avans et al., 1990).

For unmanned spacecraft, the absence of crew (and the subsequent risk to crew life) has resulted in little attention being given to the risk posed by M/SD impact. An exception to this is the Canadian-led RADARSAT remote sensing satellite. A preliminary survivability analysis performed by the RADARSAT Program Technical Office found that the spacecraft would be subject to sufficient orbital debris impacts to warrant concern (Terrillon et al., 1991). To address this issue, an extensive impact test campaign was performed, and five major changes were made to the RADARSAT bus design to improve the survival chances of critical spacecraft components. These changes included: additional shielding via the thickening of existing walls and the inclusion of specific shielding materials (e.g. Nextel™), rerouting of external propulsion lines, and the closure of gaps between the bus and payload modules. Another exception is the Advanced X-Ray Astrophysics Facility (AXAF) (later known as the Chandra X-Ray observatory). AXAF was launched by NASA in 1999 as part of the Great Observatory program. The AXAF mission was required to have a probability of no failure of any critical item due to M/SD impact of at least 0.92 for the five year mission duration (Frost & Rodriguez, 1997).

Putzar et al. (2006) have investigated the vulnerability of key satellite components to M/SD impacts. From extensive impact testing on fuel and heat pipes, pressure vessels, electronic boxes, harnesses and batteries, they found that the inherent protection capability of spacecraft equipment significantly decreases the threat of M/SD induced system failure. As such it is understood that for unmanned spacecraft,

penetration of the primary structure will not necessarily result in its failure. Indeed in order to achieve failure a subsystem or component essential to vehicle operation and/or mission objectives must be hit and destroyed by an impacting particle. This kind of damage is influenced by a number of parameters, such as: accommodation of equipment and components inside the spacecraft; equipment integration density; redundancy on an equipment/component level; residual kinetic energy of debris fragments following perforation of the primary structure, and; intrinsic equipment protection capability. Hence, for unmanned spacecraft, the probability of structural penetration and the probability of impact-induced spacecraft failure are clearly not the same. Therefore, blind application of penetration-based safety requirements for unmanned spacecraft will lead to unnecessarily massive shielding configurations.

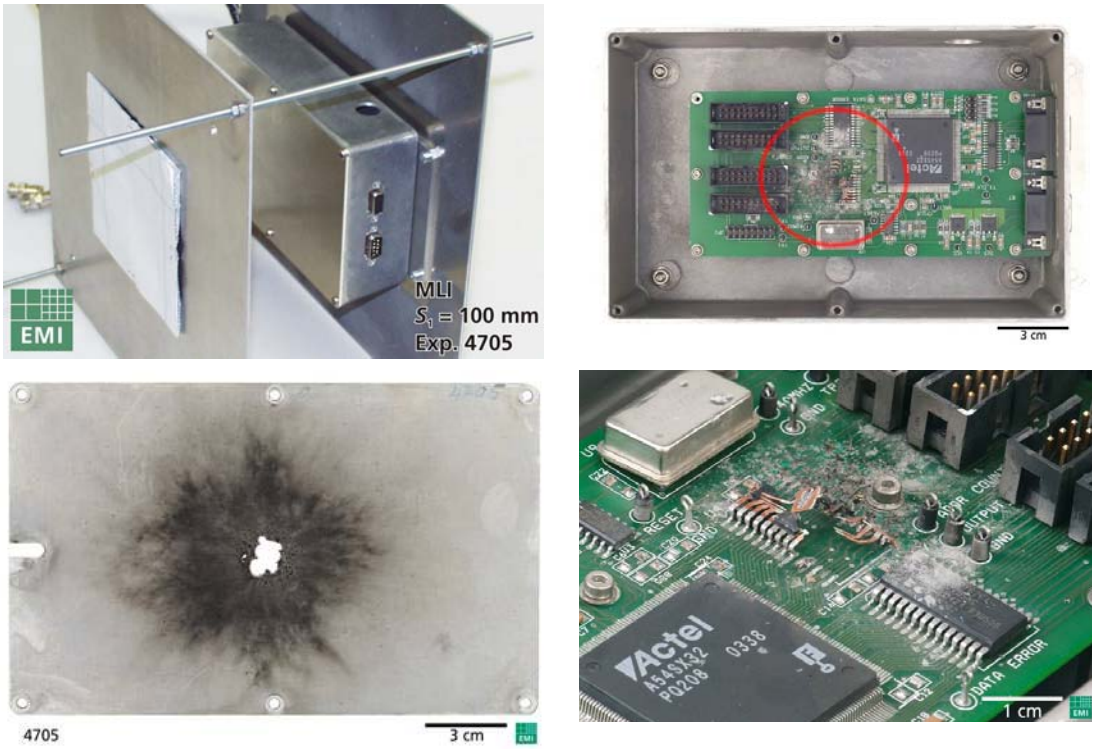

Figure 2-1 Damage to an electronics box located behind an MLI structure wall (EMI Exp. 4705) caused by normal impact of a 2.8 mm Al-sphere at 6.5 km/s. Upper left: target setup, Upper right: Internal damage in the e-box, Lower left: Damage to the e-box lid, Lower right: destruction of electronic components.

The work of Putzar et al. (2006) addressed system failure for components located behind monolithic aluminium structures, aluminium honeycomb sandwich panels and multi layer insulation (MLI). Schäfer et al. (2005) reviewed the increasingly common application of aluminium sandwich

panels with carbon fibre composite facesheets in satellite primary structures. In a complementary study to that of Putzar et al. (2006), Schäfer et al. considered the vulnerability of satellite components located behind these composite sandwich panels to impact of M/SD particles. In addition to the mechanical damage caused by the impact of solid fragments, the authors found that the large amount of conductive CFRP fibres ejected into the satellite interior induced electrical shorts on simplified electronic boxes and battery cells. Additional tests on cable harnesses found both temporary and permanent perturbations induced by the impact of ejected fragment clouds following perforation of the primary composite sandwich panel structure. The test set-ups and high-speed photographs from the experiments are shown in Figure 2-2 showing the dispersion of conductive CFRP fibres in the representative satellite interior.

The future generation of ESA scientific satellites will carry equipment capable of measuring, amongst others, the location of objects as far away as the galactic centre (GAIA mission, Perryman et al. (2001)), and the gravitational surface of the Earth (GEOID) (GOCE mission, Haagmans et al. (2003)) at levels of accuracy significantly higher than those previously achievable. As a result, the stability requirements of the satellite platforms exceed by orders of magnitude those of previous missions.

Experimental research has found that the shock environment induced by M/SD impact at hypervelocity could be close to that generated by pyroshock devices (e.g. separation charges) (Pavarin et al., 2002). Pyrotechnic shock, or pyroshock, is the transient structural response induced by ignition of pyrotechnic devices. Due to their high acceleration amplitudes and high-frequency content, pyroshocks can cause spacecraft hardware to fail (Hughes & McNelis, 2002). Many instances of flight hardware failure have been attributed to pyroshock, some resulting in catastrophic mission loss (Moening, 1985). As such, spacecraft are routinely subject to numerous ground shock tests to ensure scientific equipment and avionics components can withstand pyrotechnic shock-induced disturbances. Indeed, NASA requires pyroshock verification of spacecraft platforms for all space missions (NASA Pyroshock Test Criteria – Anon, 1999). However, no assessment of M/SD impact-induced disturbances and their effect on equipment is currently made.

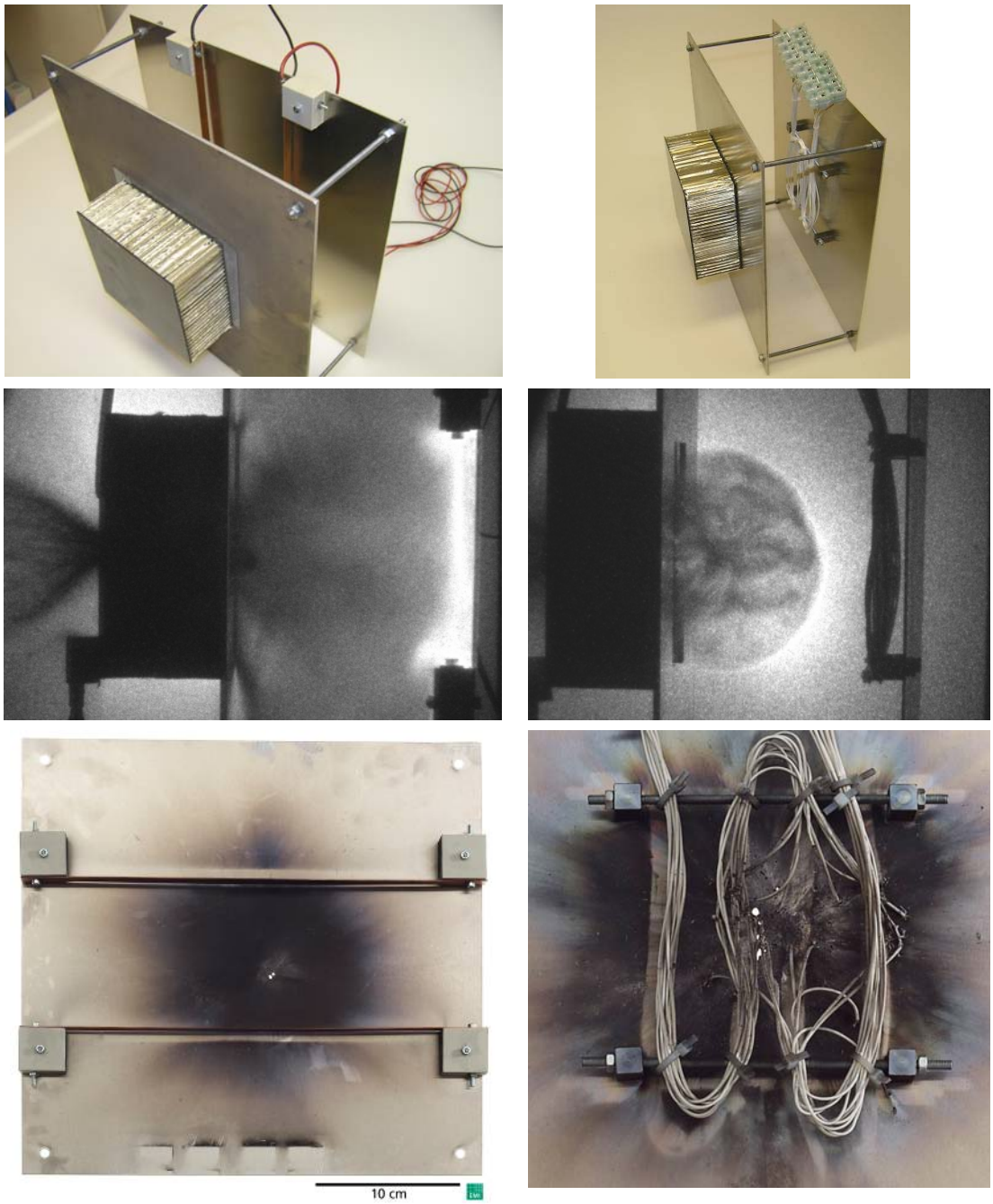

Figure 2-2 Simplified electrodes and cable harness setups investigated by Schäfer et al. (2005). Left: simplified electrode set up; Right: Cable harness.

Prosser (1996) and Prosser et al. (1999) examined the propagation of acoustic waves in complex composite structures using waveform based Acoustic Emission (AE) techniques. AE is the release of elastic waves in materials under external stimuli (e.g. mechanical loading) and was historically used for fatigue crack growth tracking in metallic bodies (e.g. Finlayson et al. (2001), Gorman (1991)). Prosser found that in thin

composite plates, acoustic waves propagate as Lamb waves, the lowest order symmetric and antisymmetric modes representing the plate extensional and flexural modes respectively. Under out-of-plane excitation (pencil lead fracture), the extensional mode (or waveform) was measured with a higher propagation velocity than the flexural mode (as shown in Figure 2-3). Prosser investigated attenuation of acoustic waves during propagation and demonstrated that geometric spreading is the dominant source of attenuation near to the disturbance origin while conversion of sound energy into heat dominates far field attenuation.

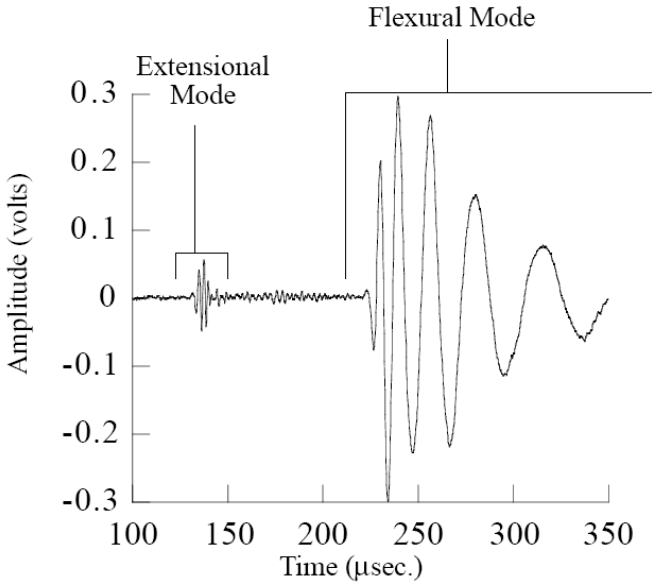

Figure 2-3 Extensional and flexural plate modes identified in an 8 ply quasi-isotropic composite plate subject to excitation (Prosser, 1996).

Pavarin et al. (2005, 2006) investigated the vibration environment induced by hypervelocity impact on a spacecraft structure to identify the propagation of transient waveforms through panel joints typically used onboard satellites. The goal of the work was to allow the risk of M/SD impact on the GOCE spacecraft to be quantified in terms of disturbances to measurement devices and the subsequent degradation of scientific measurements. The GOCE spacecraft has two stability requirements relative to micro-vibrations: in the time domain – expressed in terms of maximum acceleration amplitude, and in the frequency domain – as spectral density of the vibration disturbance. If the time-domain requirement is violated, the output of the scientific channel can be saturated, while if the frequency-domain requirement if exceeded, the quality of the scientific measurements can be degraded such that mission objectives are not achieved.

2.2 Hypervelocity Impact Simulation

2.2.1 Hypervelocity Impact Testing

For M/SD risk analysis to be performed, the spacecraft structural response to HVI must first be understood. Generally, characterisation of structural performance is made through experimental impact test programs. There exist a number of different methods for accelerating particles to hypervelocities; however they can be grouped into two broad categories: gun accelerators and explosive accelerators. Gun accelerators are classified by guidance of the projectile during the acceleration process and include two-stage light gas guns, electromagnetic rail guns, etc. In explosive accelerators the projectile is essentially unguided. Types of explosive accelerators include shaped charge, plasma drag, etc. Cable (1970) and Schneider and Schäfer (2001) provide a good overview of the working principles and achievable acceleration conditions of the different acceleration facility types. The most versatile (and therefore most commonly used) acceleration facility for hypervelocity acceleration is the two-stage light-gas gun.

Hypervelocity impact testing of space hardware began as part of the Apollo mission, for which knowledge of the penetration resistance and failure mode of each component exposed to the meteoroid environment was required (Cour-Palais, 1985). Penetration tests were performed at the NASA Manned Spacecraft Center (now Johnson Space Center) using two-stage light-gas guns to determine the critical threshold for the Service Module honeycomb structure, the Command Module heat shield, the Command Module outer windows, and the Extra-vehicular (EVA) suit. The impact test data was used to derive empirical relationships defining the critical projectile conditions for penetration (or pressure leak for the EVA suit). The meteoroid environment relevant for the Apollo mission was understood to travel at velocities ranging from 11 to 72 km/s (Maiden et al., 1965), however meteoroid density, flux, composition, etc was relatively unknown (Maiden, 1964). In an Engineering Criteria Bulletin published by NASA (Anon., 1963), a standard density of 0.5 g/cm³ was defined for all meteoroid sizes.

The magnitude of impact testing performed during the Apollo program provided a large database of both test data and basic knowledge related to hypervelocity impacts – particularly on dual-sheet metallic targets. Following an increase in the use of honeycomb sandwich panels, Jex et al.

(1970) performed a series of impact tests to better understand the channelling of debris in a honeycomb and the extent to which channelling would affect the protective capability of a dual-wall structure. A series of impact tests were performed by Jex et al. within a velocity range of 3.5 to 8.23 km/s, and the performance of the honeycomb sandwich panel was compared to that of an identical double-sheet structure without the honeycomb core. The authors found that the presence of the honeycomb core acted to channel the debris, resulting in a point concentration of small debris particles which caused bulging and tearing of the target rear wall. Contrary to expectations, Jex et al. (1970) found that the presence of the honeycomb core actually improved the protective capability of the structure for normal (perpendicular) impact as a result of secondary collisions of primary debris fragments on the honeycomb cell walls. The additional fragmentation and energy loss associated with these secondary collisions overcompensated for the adverse effect of channelling within the velocity range considered.

In 1991, recognising the increasing danger of a manmade debris environment, Christiansen extended the impact test data base for dual-wall aluminium structures (or Whipple shields) to consider shielding performance against projectiles up to 1.3 cm in diameter (Apollo impact testing was only performed for threats up to 0.16 cm in diameter).

As the use of composite materials in space applications was rapidly increasing, Yew and Kendrick (1987) performed a preliminary study investigating the damage in graphite/epoxy composite panels caused by hypervelocity impact. Although low velocity impact damage in composite materials had received considerable attention at that stage (e.g. Williams et al. (1979), Chai et al. (1983)), the only investigation of high-strength composite performance under hypervelocity impact was made by the US military and was not made available to the general public (Cour-Palais, 1987). Yew and Kendrick performed tests using nylon and aluminium cylindrical projectiles impacting at velocities between 3 and 7.5 km/s. Quasi-isotropic composite laminates (AS4/3501-6) were subject to impact ranging from 2.34 mm to 17mm thick. Although not giving a damage analysis for each individual test, Yew and Kendrick describe the ejecta following perforation of the test plate as consisting almost totally of material from the composite plate. The debris deposits were categorised as either very small powdery particles (diameter ~0.02 mm) or long flakes (1 – 50 mm long). Minimum aluminium deposits were located on the witness plate using a mass spectrum analysis. The authors suggest the projectile was liquidised upon impact in the velocity range tested.

Schonberg (1990) continued research into composite material performance under hypervelocity impact in order to assess their potential application in long-duration space structures. Schonberg performed hypervelocity impact tests on three dual-wall structure configurations: an all-aluminium system in which the front wall (bumper) was made of 6061-T6 aluminium alloy and the rear wall 2219-T87 aluminium; a composite configuration using IM6/3501-6 graphite/epoxy for the bumper material and 2219-T87 aluminium for the rear wall, and; a composite configuration using Kevlar 49 for the bumper material and 2219-T87 aluminium for the rear wall. The thicknesses of the front wall plates were selected such that all three configurations had approximately the same areal density. Schonberg found that at low impact velocities, the rear wall of the Kevlar configuration showed a single hole or crater while the damage in the aluminium configuration rear wall was more widely dispersed and contained numerous small holes or craters. At higher impact velocities the rear wall of the Kevlar configuration was penetrated, while the aluminium system's was not. The rear wall of the graphite/epoxy configuration was also perforated; however the penetrations consisted of several small holes or craters rather than the single large hole seen in the Kevlar test. Schonberg (1990) concluded that in comparison to aluminium, Kevlar is less effective in dispersing debris generated by initial impact of the projectile on the front plate. This can be caused by a mismatch in shock impedance between the Kevlar plate and aluminium projectile, which results in a non-optimum interaction of the impact-induced shock waves and thus prevents complete fragmentation of the projectile. The graphite/epoxy configurations showed significantly larger rear wall damage than the aluminium system, thus providing no advantage over equivalent aluminium panels for hypervelocity shielding.

Recognising that the use of composites for bumper plates in dual-wall structures offered no significant advantages over equal weight aluminium plates, Schonberg and Walker (1991) continued the investigation of composite material performance under hypervelocity impact by testing double-bumper shield configurations (shown in Figure 2-4) which incorporated intermediate composite layers of Spectra, Spectra/epoxy, Kevlar 49, and Kevlar 49/epoxy. They found that under high-energy impact on double-bumper shields, the use of Spectra/epoxy and Kevlar cloth in the intermediate layer provided higher levels of protection than similar weight aluminium systems. The superiority of composite materials as an intermediate bumper was considered to be primarily due to: a lower melting temperature of the composite materials than aluminium, and; absorption of fragment cloud energy via fibre/matrix fracture and sub-

surface delamination of the composite material. The combined effect of these phenomena was to decrease the density, number of particles, and energy of the secondary fragment cloud.

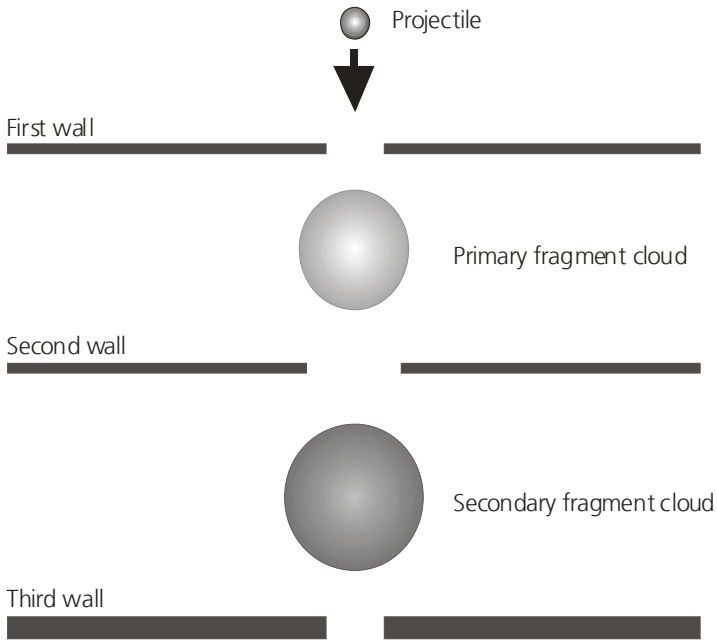

Figure 2-4 Normal impact of a double-bumper shield configuration. Schonberg and Walker (1991) performed impact tests on these type of configurations using composite materials for the intermediate layers.

Having proven that composite materials were more effective as a secondary wall than a bumper plate, Schonberg and Walker went on to investigate hypervelocity impact of dual wall structures using aluminium bumper plates and graphite/epoxy composites for the rear wall (Schonberg & Walker, 1994). They found that for impact velocities above 5.5 km/s, use of graphite/epoxy as the inner wall provided superior ballistic performance over equal weight aluminium systems. Furthermore, severe cracking and petalling observed in aluminium rear walls was not present in the composite structure. However, for lower impact velocities it was revealed that perforation holes in the graphite/epoxy panels were approximately 4-5 times larger than those in the corresponding aluminium inner walls.

Tennyson and Manuelpillai (1994) considered the performance of graphite/epoxy and graphite/PEEK composite laminates under impact of micrometer-sized particles accelerated in Auburn University's electro-magnetic particle accelerator. Using projectiles smaller than 100 μm, Tennyson and Manuelpillai were able to more accurately reproduce the

effects of micrometeoroid impact on composite spacecraft systems than previous researchers (e.g. Yew and Kendrick (1987)) who were constrained within the operational limits of two-stage light gas guns. Tennyson and Manuelpillai derived a linear relationship between entry crater size and front surface damage. In the case of perforation, minimal and/or low energy secondary ejecta was observed, from which the authors concluded that both graphite/epoxy and graphite/PEEK composites are well suited for shielding applications in space.

Lambert (1997) presented an overview of European Space Agency hypervelocity impact test research. The performance of thermal insulation materials (MLI and flexible external insulation (FEI)), glass, carbon-carbon, as well as composite sandwich panels and metallic pressure vessels is discussed. In this wide-ranging publication, Lambert noted that for single plates MLI provides a much more effective shielding performance than equivalent-weight aluminium structures. He found that for plate structures, CFRP fabrics were more effective than aluminium; however this was not substantiated for unidirectional CFRP lay-ups. Although better than monolithic plates, the shielding performance of sandwich panels is not as good as equivalent dual-wall structures. This finding is in direct conflict with those reported by Jex et al. (1970).

The use of high strength composite materials in unmanned spacecraft continued to increase, however its application was primarily in facesheets of aluminium honeycomb sandwich panels (CFRP/Al HC SPs). Subsequently, Taylor et al. (1997) performed 15 preliminary hypervelocity impact tests on a representative external spacecraft primary wall structure which consisted of 1.62 mm thick CFRP facesheets and a 45mm thick Al-honeycomb core. The authors noted that a direct comparison between CFRP/Al HC sandwich panels and dual-wall aluminium shields was not appropriate given the lack of experimental data available.

Around the same time, Frost and Rodrieguez (1997) published the results of an extensive test campaign performed on six different composite sandwich panel configurations on use aboard NASA's Advanced X-Ray Astrophysics Facility (AXAF). In addition, future impact tests were planned for impact on the multi-layer insulation blanket, cable bundles located behind the MLI, and cable bundles located behind the composite sandwich panel.

Until 1999, all hypervelocity impact tests on CFRP/Al HC sandwich panels had been performed at normal incidence. As the effects of debris

channelling were expected to be more severe at oblique impact angles based on the results of metallic sandwich panel structure (Jex et al., 1970), an investigation of the composite sandwich panel performance under oblique hypervelocity impact was made by Taylor et al. (1999). It was found that an increase in impact incidence from 0° to 15° allows the composite sandwich panel to defeat a projectile with double the kinetic energy. In general, an increase of impact angle was found to be proportional to the protection capability of the structure. For normal impact, Taylor et al. (1999) were able to compare experimental results with dual-wall metallic structures by introducing a scaling factor of 0.5 to the composite rear facesheet thickness. This suggests the presence of the honeycomb core acts to significantly decrease the shielding performance of the panel.

2.2.2 Numerical Simulation of Hypervelocity Impact

Two-stage light gas guns are capable of accelerating particles to 9 km/s. This is in the order of the average encounter velocity of space debris in low-Earth orbit. For assessing the performance of structures impacted by debris particles in low-Earth orbit with above average velocities, as well as meteoroid particles, additional means are required. In early studies (e.g. Maiden et al., 1965) momentum scaling was used to assess shielding performance at higher velocities. However, the accuracy of this approach remains questionable. As such, numerical techniques have received increasing attention in the hypervelocity impact community for the extrapolation of impact test data to higher impact velocities.

Prior to 1957, severe difficulties in modelling problems with large distortions in two or more dimensions plagued numerical techniques. The development of a methodology called the particle-in-cell (PIC) technique by Evans and Harlow (1957) led to the development of a mixed Euler-Lagrange which was capable of overcoming these problems. Based on a hydrodynamic expression of the continuum equations (i.e. ignoring material strength), the PIC technique, although originally derived for fluid flow problems, was quickly adopted for hydrodynamic impact (Johnson & Anderson, 1987). Frazier et al. (1965) made the first comparison between experimental data and computer results, considering a series of hypervelocity impact tests performed on semi-infinite wax targets at the US Ballistics Research Laboratory. It was justified that the use of purely hydrodynamic theories for hypervelocity impact was reasonable as the impact pressures generated upon impact were considerably higher than the material yield strengths (Anderson, 1987). However, as the impact

disturbance propagates into a semi-infinite target, the hydrodynamic pressure will reduce, eventually becoming comparable with material yield stresses. Thus, at late times the hydrodynamic approximation no longer provides a valid solution for the simulation hypervelocity impact.

Wilkins (1964) investigated the discrepancies between experimental data and hydrocode predictions of the initiation and expansion of detonation products in high explosives. Realising the importance of strength effects at late times in the expansion process, Wilkins developed the procedures for incorporating material strength into hydrocode calculations. Swegle (1978) performed an important series of numerical simulations investigating the hypervelocity impact of a nylon sphere on a steel plate, in which he compared the predictions of recently improved Lagrangian- and Eulerian codes. Both codes, although using fundamentally different mathematical and numerical descriptions, produced results in excellent agreement with experiments.

The continuing development of hydrocode techniques led to the distribution of commercial packages outside research institutions. One of the most widely used hydrocodes today is the commercial package AUTODYN. AUTODYN-2D and 3D are a two and three dimensional codes respectively which use classical continuum mechanics to describe the dynamics of a continuous media (Anon., 2005). Based on explicit finite difference, finite volume and finite element techniques, AUTODYN allows the spatial discretisation of a media to be made with either the Lagrange or Euler formulations of the conservation laws. The Eulerian description uses a spatially-fixed grid across which material is free to flow. The Lagrangian description uses a discretisation which moves and distorts with the physical material. Previous studies using AUTODYN (e.g. Pezzica (1996), White (2001)) have demonstrated the code's applicability to hypervelocity impact problems.

AUTODYN additionally enables application of a grid-less Lagrangian technique called Smooth Particle Hydrodynamics (SPH). The advantages of SPH over traditional Lagrangian techniques is that under high-distortion, SPH is not subject to grid tangling, a well documented problem with Lagrangian grid-based techniques. However, SPH is subject to problems of its own, including: numerical instability, global energy loss or divergence, incorrect plastic strain estimation, maximum pressure overestimation and unphysical row-to-row pressure oscillations between adjacent smooth particles (Faraud et al., 1999). Nonetheless, the potential of SPH over conventional grid based Lagrange- and Euler techniques has

been demonstrated (e.g. Hayhurst & Clegg (1997)). The authors performed a number of hypervelocity impact simulations on thin Al-plates and dual-wall structures using the SPH technique in AUTODYN. Their results showed a very good level of agreement with experimental measurements at a computational cost much lower than an Eulerian-based model.

2.2.3 Material Modelling of Composite Materials

Hydrocodes utilise the differential equations governing unsteady dynamic motion expressing the local conservation laws of mass, momentum and energy. To solve these laws, a relationship which relates material stress to deformation and internal energy (or temperature) is required. This relationship is referred to as a material model and generally includes an equation of state, which relates the material density (or specific volume) and internal energy (or temperature) to hydrostatic pressure, and a constitutive relation which describes the material shear stresses.

The work of Hiermaier et al. (1999) provided a significant improvement in the modelling of composite materials in hydrocodes. The "Advanced Material Model for Hypervelocity Impact Simulations" (AMMHIS) allowed the definition of orthotropic elastic constitutive relations, non-linear shock effects and energy dependence of the thermodynamic material pressure coupled to orthotropic constitutive relations, directional tensile and compressive material failure criteria, orthotropic post-failure constitutive relations. This model was shown to significantly improve the simulation of uniaxial strain flyer plate experiments on both the ceramic fibre (Nextel) and Kevlar/ epoxy composites. Simulations of hypervelocity impact on a representative manned spacecraft wall (Al Whipple shield incorporating Nextel and Kevlar/epoxy intermediate stuffing) highlighted the capability of the new model in reproducing many of the experimentally-observed damage phenomena (e.g. fragmentation, delamination etc).

Limitations in the AMMHIS model such as linear elasticity and instantaneous directional failure were identified by Riedel et al. (2003) (alternatively published as Riedel et al. (2006) and Clegg et al. (2006)), who followed up on the AMMHIS study with their "Advanced Damage Model for Numerical Simulation Codes" (ADAMMO). The ADAMMO model incorporated non-linear orthotropic hardening, as well as failure initiation and energy based softening criteria to control the rate of damage growth. Additionally, this model was developed for application with both flexible, energy-absorbing shielding materials such as Kevlar,

and high-strength, high-stiffness composites such as CFRP. The new model was able to provide significant improvements over the previous state-of-the-art model (AMMHIS) in the simulation of characterisation experiments, thus confirming the treatment of shockwave propagation and non-linear material behaviour was well made. Improvements to the definition of material characteristics did not provide a significant increase in accuracy for simulation of hypervelocity impact on the stuffed Whipple shield configuration, specifically for the real Al-wall deformation, however improvements on fine details (such as delamination of the composite panels) were made.

Importantly, the applicability of the non-linear orthotropic ADAMMO material model to CFRP composites was demonstrated through the simulation of hypervelocity impact on a CFRP/Al honeycomb sandwich panel structure. Although material data was only roughly approximated, the simulated damage in the composite sandwich panel showed reasonable agreement to experimental measurements.

2.2.3.1 Basic Orthotropic Stiffness and Shock Response

A shock wave can be defined as a discontinuity in pressure, P, temperature (or internal energy, E) and density, ρ. Therefore, in the analysis of shock wave propagation within a continuum, and the effect of such a shock wave on the continuum properties, equations are developed by considering regions immediately ahead (reference condition indicated by the subscript 0) and behind the infinitely thin shock. The conservation laws across a shock front were originally defined by Rankine and Hugoniot for fluids, and are defined as:

Conservation of mass:

$$\rho_0 U_s = \rho\left(U_s - u_p\right) \tag{1}$$

Conservation of momentum:

$$\left(p - p_0\right) = \rho_0 U_s u_p \tag{2}$$

Conservation of energy:

$$E - E_0 = \frac{1}{2}\left(p + p_0\right)\left(V_0 - V\right) \tag{3}$$

where: $V = 1/\rho$

U_s – shock velocity.

U_p – particle velocity.

To solve the conservation equations the equation of state (EOS) is required, which is commonly expressed for isotropic solid continua in the Mie-Grüneisen form:

$$p = p_r(v) + \frac{\Gamma(v)}{v}\left[E - E_r(v)\right] \tag{4}$$

where Γ is the Grüneisen gamma: $\Gamma(v) = v\left(\frac{\partial p}{\partial E}\right)_v$

The functions $p_r(v)$ and $e_r(v)$ refer to the internal pressure and energy of the compressed material in terms of volume, and are generally known functions on some reference curve, e.g.:

- The shock Hugoniot,
- A standard adiabat,
- The 0 Kelvin isotherm,
- The isobar p = 0,
- The curve e = 0,
- The saturation curve.
- Some composite curve of one or more of the above curves to cover the complete volume range of interest.

Thus the internal energy and pressure can be calculated at any point by using the reference curve and the Grüneisen gamma. For example, with the Hugoniot as reference:

$$p - p_H = \Gamma\rho\left(E - E_H\right) \tag{5}$$

The Mie-Grüneisen is a hydrodynamic EOS that describes the thermodynamic response of a material under shock loading (i.e. the material behaves like a gas or fluid, having no strength). During hypervelocity impact, pressures are generated that can exceed the strengths of impacting materials by orders of magnitude (Lambert et al., 1991), thus the materials are effectively behaving hydrodynamically. However, there exist two regimes – far field and late time – where strength effects may be important. As the impact-induced stresses decrease with distance from the impact location, there may be regions in the target where local stress levels are of the order of material strength or lower. Furthermore, as the projectile is slowed within the target the impact-induced stresses will also decrease. If the target is sufficiently thick, the stresses may decrease to the level of magnitude (or lower) of

the material strength. Description of the strength effects under shock loading is referred to as constitutive modelling.

Historically the thermodynamic (equation of state) response of a material and its ability to carry shear loads (strength) were dealt with separately by partitioning the strain into volumetric and deviatoric components. However, for anisotropic materials this approach is unsuitable, as (Anderson et al., 1994):

- Strain is not uniform in all three (principal) directions under hydrostatic pressure, and;
- Deviatoric strain will produce volumetric dilation since the coefficients in the stress/strain relation are not all equal.

A new formulation of the equation of state for composite materials that provides a coupled deviatoric and volumetric response was derived by Anderson et al. (1994) and takes the form:

$$P = P_H - \Gamma\rho(e - e_H) - \frac{1}{3}[C_{11} + C_{21} + C_{31}]\varepsilon_{11}^d - \frac{1}{3}[C_{12} + C_{22} + C_{32}]\varepsilon_{22}^d - \frac{1}{3}[C_{13} + C_{23} + C_{33}]\varepsilon_{33}^d \quad (6)$$

where ε_{ii}^d - deviatoric strain component.

The polynomial form of the Mie-Grüneisen EOS combines an expansion series defining the hydrostatic (Hugoniot) curve, and an energy term based on the Grüneisen gamma which defines pressure states off the reference curve. Under tensile and compression loading, the polynomial for of the Mie-Grüneisen EOS is expressed as:

Compression:

$$p = A_1\mu + A_2\mu^2 + A_3\mu^3 + (B_0 + B_1\mu)\rho_0 e \quad (7)$$

Tension:

$$p = T_1\mu + T_2\mu^2 + B_0\rho_0 e \quad (8)$$

For an isotropic Hookean material, the first term on the right hand side of Eq. (7) is equivalent to a linear EOS, where A_1 represents the material bulk modulus. For an anisotropic material, to ensure consistency in the elastic regime, the bulk modulus is considered as an "effective" or "average" bulk modulus A_1' and is defined from the orthotropic stiffness matrix:

$$A_1' = \frac{1}{9}[C_{11} + C_{22} + C_{33} + 2(C_{12} + C_{13} + C_{23})] \quad (9)$$

2.2.3.2 Non-Linear Hardening

Chen et al. (1997) derived a three-dimensional (3D) quadratic yield stress function which relaxes the constant pressure assumption of the Tsai-Hill anisotropic yield criterion, allowing a change in volume (and thus pressure) contribution from the deviatoric strain. The yield function also includes a hardening parameter to describe increasing strength with increasing inelastic strain growth. The quadratic yield function is expressed as:

$$f(\sigma_{ij}) = a_{11}\sigma_{11}^2 + a_{22}\sigma_{22}^2 + a_{33}\sigma_{33}^2 + 2a_{12}\sigma_{11}\sigma_{22} + 2a_{23}\sigma_{22}\sigma_{33} + \ldots + 2a_{13}\sigma_{11}\sigma_{33} + 2a_{44}\sigma_{23}^2 + 2a_{55}\sigma_{31}^2 + 2a_{66}\sigma_{12}^2 = k \quad (10)$$

The nine a_{ij} coefficients are referred to as plasticity coefficients, and are used to describe the amount of anisotropy in plasticity, while *k* is a state variable defining the instantaneous value of the limit surface. In the quadratic yield function a so-called *master effective stress-effective strain curve* is defined. The nine plasticity coefficients are then capable of collapsing specific loading conditions onto the master curve, thus the plasticity in any 3D loading case can be simply determined. The master curve can, in general, be defined from any of the three uniaxial tension or shear stress-strain curves, where:

Effective stress:

$$\overline{\sigma} = \sqrt{\frac{3a_{ii}}{2}}\sigma_{ii} \qquad \text{in unidirectional loading (i = 1,2,3)} \qquad (11)$$

$$\overline{\sigma} = \sqrt{3a_{rr}}\sigma_{ij} \qquad \text{in shear loading (i} \neq \text{j, r = 4,5,6)} \qquad (12)$$

Effective plastic strain increment:

$$d\overline{\varepsilon^p} = \sqrt{\frac{2}{3a_{ii}}}d\varepsilon_{ii}^p \qquad \text{in unidirectional loading (i = 1,2,3)} \qquad (13)$$

$$d\overline{\varepsilon^p} = \frac{2d\varepsilon_{ij}^p}{\sqrt{3a_{rr}}} \qquad \text{in shear loading (i} \neq \text{j, r = 4,5,6)} \qquad (14)$$

Generally it is accepted that the master curve should be defined based on the loading condition which shows the greatest amount of plastic strain. As the entire yield surface is defined by a single master surface and the nine plasticity constants, the effective shape of the individual stress-strain curves in the plastic regime is constrained to that of the master curve. By

defining the loading condition with the largest plasticity, it ensures that plasticity is not restricted in any of the loading cases.

The three plasticity coefficients related to uniaxial tension and the three coupling coefficients can be calculated from the so-called plastic Poisson's ratios (PPRs) of the structure:

$$a_{11} = a_{22}\frac{\nu_{21}^p}{\nu_{12}^p} \qquad a_{22} = a_{33}\frac{\nu_{32}^p}{\nu_{23}^p} \qquad a_{33} = a_{11}\frac{\nu_{13}^p}{\nu_{31}^p} \tag{15}$$

$$a_{12} = -a_{22}\nu_{21}^p \qquad a_{23} = -a_{22}\nu_{23}^p \qquad a_{13} = -a_{33}\nu_{31}^p$$

The plastic Poisson ratios (PPRs) are defined as:

$$\nu_{ij}^p = -\frac{d\varepsilon_{jj}^p}{d\varepsilon_{ii}^p} \tag{16}$$

where $$d\varepsilon_{ii}^p = d\varepsilon_{ii} - d\varepsilon_{ii}^{el} \tag{17}$$

The shear plasticity coefficients a_{44}, a_{55}, and a_{66} are selected to collapse the defined master curve onto the three material stress-strain curves

Restrictions on the Selection of Plasticity Parameters

The selection of plasticity parameters is subject to restriction as a result of the calculation algorithm implemented within AUTODYN in the case of inelastic loading. The typical series of calculations carried out by AUTODYN in each time step are shown in Figure 2-5.

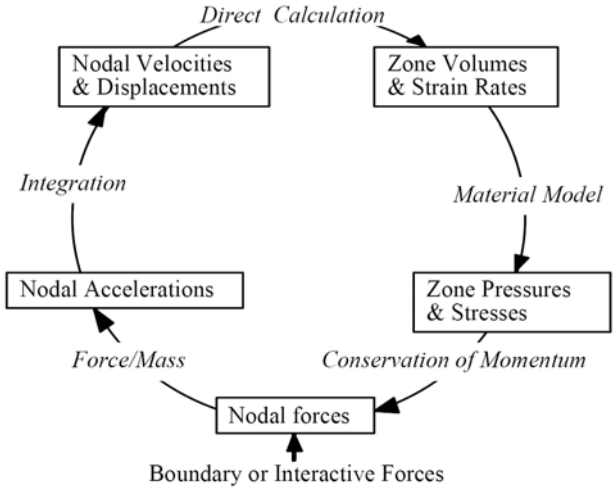

Figure 2-5 AUTODYN computation cycle for Lagrangian solver (Anon., 2005).

Following the determination of strain rates and the volume change, the material stresses are calculated. These stresses are checked against the quadratic limit criteria of Eq. (10). Initially, all stresses are updated using an elastic relationship. If these stresses remain within the yield surface then the material is assumed to have either loaded or unloaded elastically. If, however, the resultant updated stress state lies outside of the yield surface (identified as point B in Figure 2-6), an algorithm is required to return the stresses to the yield surface (point C in Figure 2-6). In AUTODYN, a backward-Euler return algorithm is implemented.

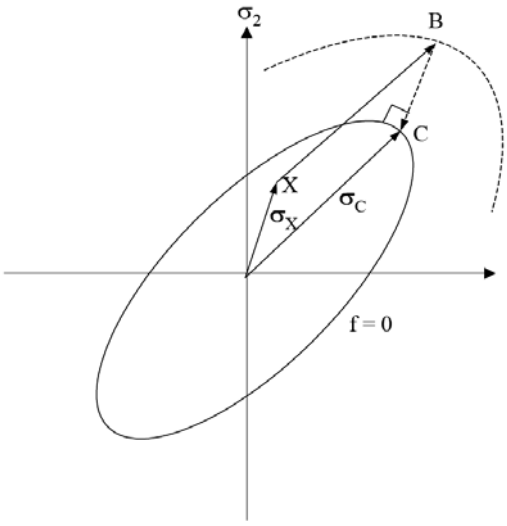

Figure 2-6 In-elastic updated stress state and the subsequent return to the yield surface performed by a backward-Euler return algorithm in AUTODYN (Anon., 2005).

To ensure that the return algorithm is stable it is required that the yield surface defined by Eq. (10) is elliptical. Two matrices of the plasticity parameters are defined:

$$e = \begin{bmatrix} a_{11} & a_{12} & a_{13} \\ a_{12} & a_{22} & a_{23} \\ a_{13} & a_{23} & a_{33} \end{bmatrix} \tag{18}$$

$$E = \begin{bmatrix} a_{11} & a_{12} & a_{13} & 0 \\ a_{12} & a_{22} & a_{23} & 0 \\ a_{13} & a_{23} & a_{33} & 0 \\ 0 & 0 & 0 & -k \end{bmatrix} \tag{19}$$

Stability of the return algorithm is assured when the following conditions are met:

- $|E| < 0$;
- Rank [e] = 3;
- Rank [E] = 4; and
- Non-zero roots of [e] all have the same sign.

2.2.3.3 Failure

Failure initiation is defined by criteria based on modified forms of the well-known Hashin criteria which include out-of-plane shear stresses for fibre failure and matrix cracking (Hou et al., 2000):

$$e_{iif}^2 = \left(\frac{\sigma_{ii}}{\sigma_{ii,\,fail}}\right)^2 + \left(\frac{\sigma_{ij}}{\sigma_{ij,\,fail}}\right)^2 + \left(\frac{\sigma_{ki}}{\sigma_{ki,\,fail}}\right)^2 \geq 1 \qquad (20)$$

NOTE: Initiation criteria only applied in tension

If one of the failure criteria are exceeded ($e_{iif}^2 > 1$), the orthotropic damage model (softening) is activated.

2.2.3.4 Non-Linear Softening

If a state of stress is calculated to lie outside the surface defined by Eq. (20) an inelastic strain increment is accumulated as crack strain, ε_{cr}. The maximum stress that can be sustained by the material is reduced as a function of crack strain (damage). Crack strain grows until reaching an ultimate value, ε^u, upon which ultimate failure occurs. Post-failure softening (i.e. damage) is assumed linear, and the area under the softening portion of the stress-strain curve is therefore related to the fracture energy, G_f, as:

$$G_f = \int_{\varepsilon^{cr}=0}^{\varepsilon^{cr}=\varepsilon^u} \sigma \cdot L \; d\varepsilon^{cr} \qquad (21)$$

where L – characteristic cell dimension in the direction of failure.

This is illustrated in Figure 2-7.

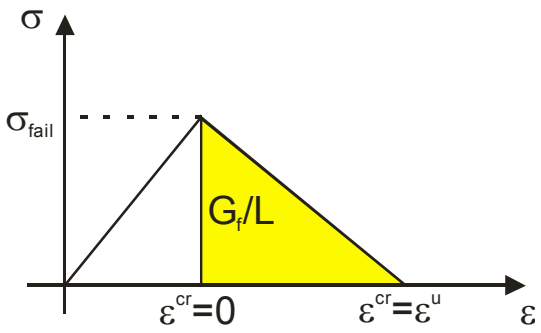

Figure 2-7 Graphical representation of crack softening.

The maximum sustainable stress is calculated at any instant as a function of damage, as:

$$\sigma_{\max} = \sigma_{fail}(1 - Dam) \tag{22}$$

where $Dam = \dfrac{h \cdot \varepsilon_{cr}}{\sigma_{fail}}$

and h is the gradient of the linear softening slope (see Figure 2-7)

$$h = \frac{L\sigma_{fail}^2}{2G_f}$$

Damage is implemented as a tensor, with a component associated with each orthotropic failure plane. Thus, fracture of the composite is considered from a volumetric perspective, as shown in Figure 2-8.

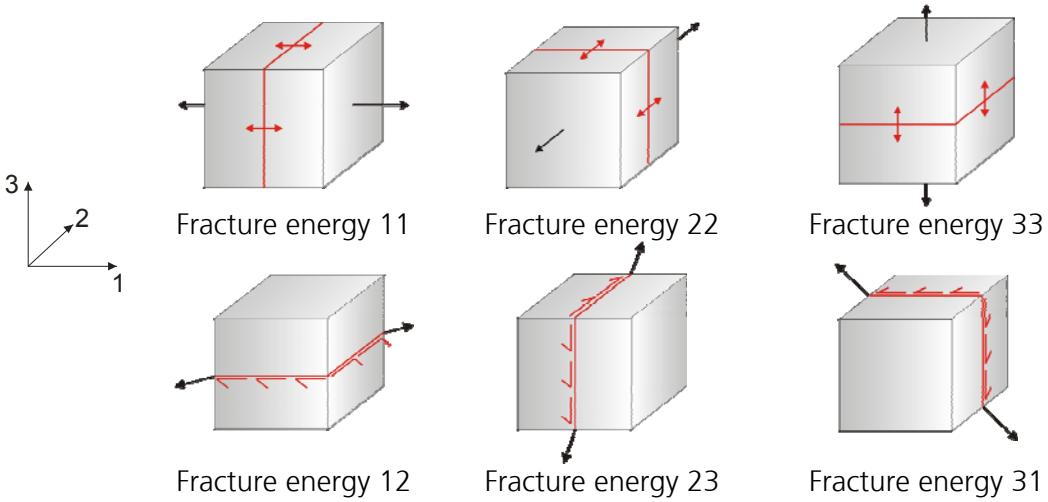

Figure 2-8 Macroscopic laminate fracture planes. Upper left: σ_{11}; middle: σ_{22}; right: σ_{33}; Lower Left: τ_{12}; middle: τ_{23}; right: τ_{31}.

CFRP laminates usually fail in a brittle-type fracture mode, regardless of load direction. A stress-strain profile such as that seen in Figure 2-7 is therefore impossible as the composite cannot carry load beyond the maximum failure stress σ_{fail}. However, in a macromechanic model the post-fracture softening must also incorporate geometric fracture. The results from of a multi-directional CFRP composite subject to in-plane uni-axial tensile stress (at 0°) and through-thickness tensile stress (double cantilever beam) are shown in Figure 2-9. It can be seen that the magnitude of the applied force does not immediately reduce to zero once the maximum failure stress is exceeded. Instead, as the crack propagates along the pre-crack plane (interlaminar) the load-carrying capability of the laminate is reduced, resulting in the step-like shape of the post-failure curve. This geometric effect represents a non-zero fracture energy in the post fracture softening model.

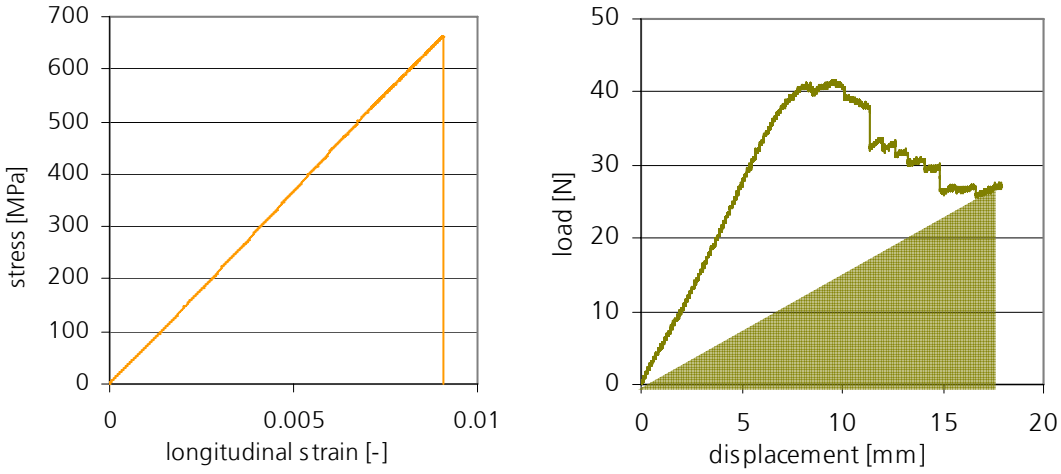

NOTE: triangular area represents elastically stored energy

Figure 2-9 Experimental stress-strain curves of a multi-directional CFRP composite (from Wicklein et al. 2007). Left: uni-axial in-plane tension at 0°. Right: through-thickness tension (DCB).

2.2.3.5 Characterisation of Composite Material Dynamic Properties

In development and validation of the AMMHIS and ADAMMO models, a pragmatic experimental characterisation campaign was performed for derivation of the extensive material parameter list required for these models. This is representative of the conventional approach for application of new materials in any engineering scenario, and is required for validation of new modelling techniques. For standard isotropic materials this approach is certainly beneficial in a general sense, however

for application with anisotropic, fibre-reinforced composites, of which the variation of directional performance can be altered through composition, orientation of the constituents, and fibre packing geometry, the time and expense involved in experimental determination of the overall material behaviour can be prohibitive.

The general difficulties associated with the certification of composite materials have, in coupling with a desire to utilize their capabilities to the full extent, provided motivation for development of a broad range of composite mechanics theories. Beginning with constitutive relationships which can be used to predict material performance in terms of composition and constituent performance, and extending all the way to strength theories for multi-layered, multi-directional composite laminates describing the interaction of stress and strain across the individual composite lamina, the mechanics of composite materials has enjoyed a significant degree of attention in the scientific community.

In the absence of experimentally-characterised data there exists, therefore, the means to theoretically predict the performance of complex composite structures from the composition and properties of the constituent materials. A brief review of elastic and strength theories applicable to this problem is made below.

2.2.3.6 Micromechanics

Micromechanics considers the relationship of the composite material properties to that of its constituents (see Figure 2-10), and is therefore ideal for utilizing constituent data sheets to determine the composite material properties.

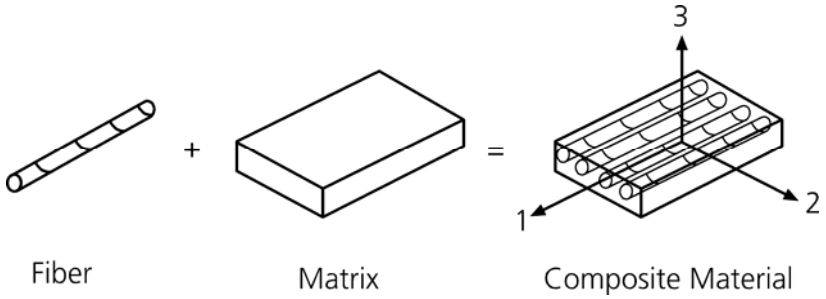

Figure 2-10 Basic elements of micromechanics.

Micromechanical theories can generally be classified into elastic- or strength theories.

2.2.3.6.1 Micromechanics for Elastic Properties

The various elastic micromechanics theories can be broadly grouped into categories based on the assumptions introduced in the respective theories, namely:

- Numerical;
- Mechanics of materials;
- Self-consistent field (or embedding);
- Bounding; and
- Semi-empirical.

The application of micromechanics for predicting the elastic properties of composite lamina is widely accepted, although no single theory receives universal application.

2.2.3.6.2 Micromechanics for Strength Properties

Strength characteristics of composite materials are very sensitive to pre-existing material defects. In the derivation of material stress, integrated averages are usually expressed for the material volume, smoothing the local stress and strain perturbations. However, in mechanical testing of composite materials, failure initiation often occurs in defective regions, thus their effect is very significant. For example, the tensile strength of boron filaments used for composite reinforcement was considered by Weeton et al. (Ed.) (1987). As shown in Figure 2-11, the variability in the strength of the reinforcing fibres was found to be very significant. Large scatter is also found in the strength of carbon fibres in the absence of a polymer matrix.

As a result of the increasing complexity of micromechanics strength theories there exists significantly more approaches; however they are less accurate in general and as such less widely accepted than the elastic theories. A number of micromechanics strength theories require Finite Element Modelling (e.g. unit cell method (Kwon & Berner, 1995), Multicontinuum theory (Mayes & Hansen, 2004)), while others can be used to calculate stress and strain states in the constituents which can be used in conjunction with selected failure theories for strength predictions (e.g. method of cells (Aboudi, 1991), bridging model (Huang, 2004)).

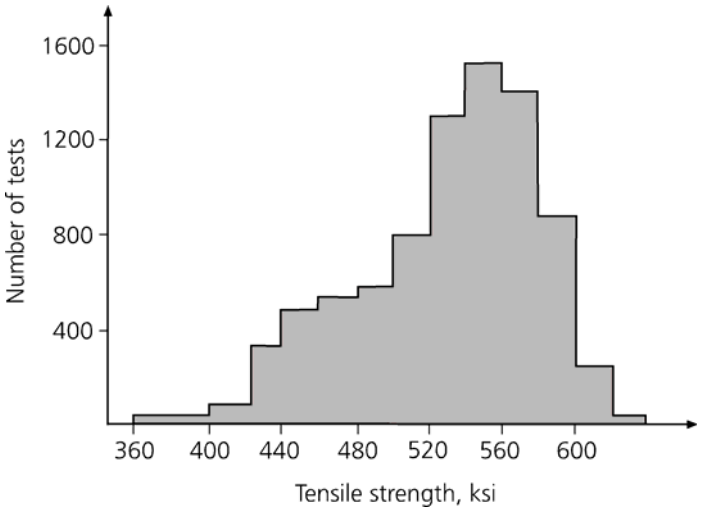

Figure 2-11 Statistical distribution of tensile strength for boron filaments (Weeten et al. 1987). Average strength 518 ksi, coefficient of variation 15%.

2.2.3.7 Laminate Theory

Classical Laminate Theory (CLT) provides the means to determine the elastic behaviour of thin composite plates from the stacking sequence of the structural laminate and the properties of the individual layers, as shown in Figure 2-12.

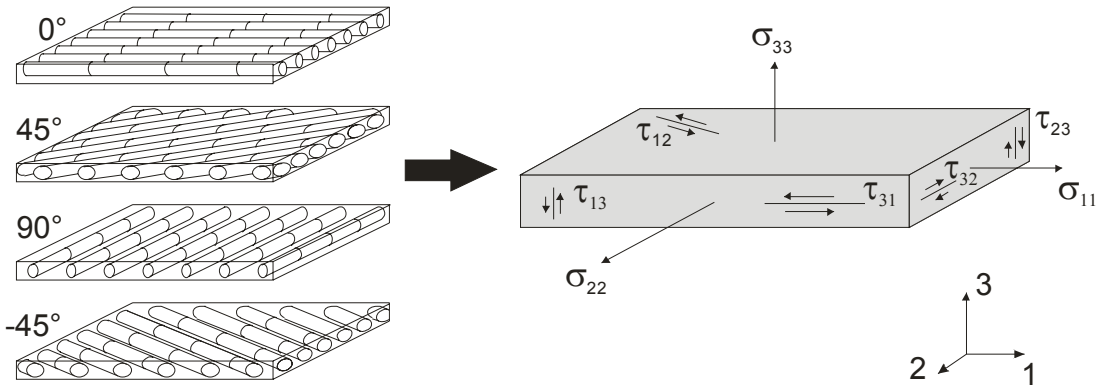

Figure 2-12 Basic principle of Classical Laminate Theory.

This is performed within the framework of the following assumptions:

- Each layer in the composite plate is quasi-homogenous and orthotropic;
- The laminate is thin with lateral dimensions much larger than its thickness;
- The laminate is loaded in a state of plane stress (i.e. $\sigma_z = \tau_{xz} = \tau_{yz} = 0$);
- There is no transverse shear, i.e. lines normal to the laminate middle surface will remain normal following deformation of the laminate.

For the case of a thin, unidirectional composite ply a reduced stiffness matrix can be defined as:

$$\begin{bmatrix} \sigma_1 \\ \sigma_2 \\ \tau_6 \end{bmatrix} = \begin{bmatrix} Q_{11} & Q_{12} & 0 \\ Q_{12} & Q_{22} & 0 \\ 0 & 0 & Q_{66} \end{bmatrix} \begin{bmatrix} \varepsilon_1 \\ \varepsilon_2 \\ \gamma_6 \end{bmatrix} \tag{23}$$

The transformed lamina stiffness matrix $[\overline{Q}_{ij}]_k$, referred to a global coordinate system (x,y) can be determined by multiplying the local stiffness matrix by:

$$\begin{bmatrix} \sigma_x \\ \sigma_y \\ \tau_s \end{bmatrix}_k = \begin{bmatrix} Q_{xx} & Q_{xy} & 2Q_{xs} \\ Q_{yx} & Q_{yy} & 2Q_{ys} \\ Q_{sx} & Q_{sy} & 2Q_{ss} \end{bmatrix} \begin{bmatrix} \varepsilon_x \\ \varepsilon_y \\ \gamma_s \end{bmatrix} \tag{24}$$

where

$$\begin{bmatrix} Q_{xx} & Q_{xy} & 2Q_{xs} \\ Q_{yx} & Q_{yy} & 2Q_{ys} \\ Q_{sx} & Q_{sy} & 2Q_{ss} \end{bmatrix} = \left[T^{-1}\right] \begin{bmatrix} Q_{11} & Q_{12} & 0 \\ Q_{12} & Q_{22} & 0 \\ 0 & 0 & Q_{66} \end{bmatrix} [T] \tag{25}$$

and

$$[T] = \begin{bmatrix} m^2 & n^2 & 2mn \\ n^2 & m^2 & -2mn \\ -mn & mn & m^2 - n^2 \end{bmatrix} \tag{26}$$

where $m = \cos\theta$; $n = \sin\theta$

The laminate stiffness matrix can now be determined:

$$[C]=\begin{bmatrix} A_{11} & A_{12} & A_{16} & B_{11} & B_{12} & B_{16} \\ A_{21} & A_{22} & A_{26} & B_{21} & B_{22} & B_{26} \\ A_{61} & A_{62} & A_{66} & B_{61} & B_{62} & B_{66} \\ B_{11} & B_{12} & B_{16} & D_{11} & D_{12} & D_{16} \\ B_{21} & B_{22} & B_{26} & D_{21} & D_{22} & D_{26} \\ B_{61} & B_{62} & B_{66} & D_{61} & D_{62} & D_{66} \end{bmatrix} \tag{27}$$

where

$$A_{ij} = \sum_{k=1}^{n} Q_{ij}^{k}\left(h_k - h_{k-1}\right)$$

$$B_{ij} = \frac{1}{2}\sum_{k=1}^{n} Q_{ij}^{k}\left(h_k^2 - h_{k-1}^2\right) \tag{28}$$

$$D_{ij} = \frac{1}{3}\sum_{k=1}^{n} Q_{ij}^{k}\left(h_k^3 - h_{k-1}^3\right)$$

and $A_{ij} = A_{ji}$ $B_{ij} = B_{ji}$ $D_{ij} = D_{ji}$

The laminate stiffness matrix consists of three sub-matrices: [A], [B] and [D]. Terms in matrix [A] represent extensional stiffnesses, or in-plane laminate moduli relating in-plane loads to in-plane strains. Terms in matrix [B] define the laminate coupling stiffnesses, or in-plane/flexure coupling moduli relating in-plane loads to curvatures and moments to in-plane strains. If B is non-zero, then in-plane forces produce flexural and twisting deformations, and moments produce extension of the middle surface in addition to twisting. The bending or flexural laminate stiffnesses relating moments to curvatures are defined by the terms in matrix [D].

In the case of a symmetrical laminate, no coupling exists between in-plane loading and out-of-plane deformation (curvatures) and between bending and twisting moments and in-plane deformation, therefore B_{ij} = 0. A laminate is considered symmetric when for each layer on one side of a reference plane (middle surface) there is a corresponding layer at an equal distance from the reference place on the other side with identical thickness, orientation, and properties.

The terms h_k and h_{k-1} in Eq. (28) define the thickness and distance of the individual laminates from the reference plane, as shown in Figure 2-13.

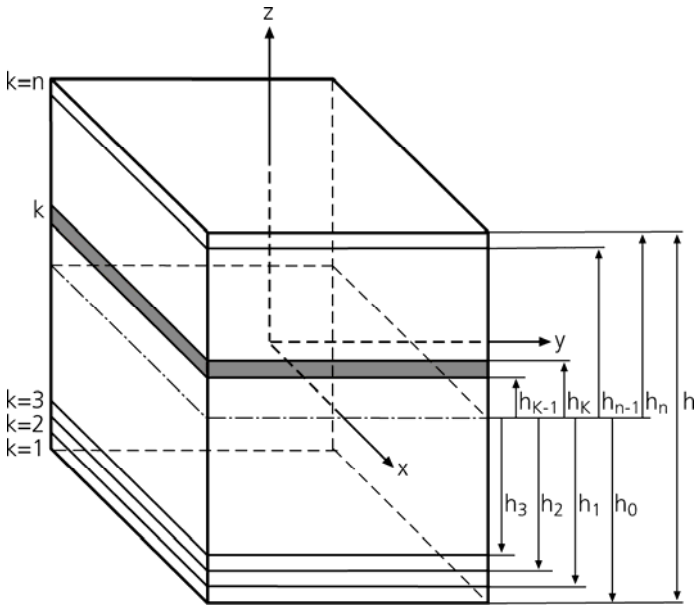

Figure 2-13 Coordinate notation and individual ply positioning measurements for a multidirectional composite laminate.

The laminate compliance matrix is calculated as the increase of the stiffness matrix. The in-plane engineering properties of the multidirectional laminate can then be simply calculated:

$$[S] = [C]^{-1} \tag{29}$$

$$E_{11} = \frac{1}{t_{lam} \cdot S_{11}} \qquad E_{22} = \frac{1}{t_{lam} \cdot S_{22}}$$
$$\nu_{12} = -\frac{S_{21}}{S_{11}} \qquad G_{12} = \frac{1}{t_{lam} \cdot S_{33}} \tag{30}$$

Classical laminate theory assumes a state of plane stress to enable derivation of the in-plane engineering properties without the need for consideration of the though-thickness behaviour of the composite laminate. For derivation of the out-of-plane properties, Hooke's Law for an orthotropic composite can be applied. Hooke's law describes the mechanical performance of an orthotropic composite in terms of the stiffness matrix, [C]. Written in matrix form:

$$\begin{bmatrix}\sigma_1\\ \sigma_2\\ \sigma_3\\ \sigma_4\\ \sigma_5\\ \sigma_6\end{bmatrix}=\begin{bmatrix}C_{11} & C_{12} & C_{13} & 0 & 0 & 0\\ C_{12} & C_{22} & C_{23} & 0 & 0 & 0\\ C_{13} & C_{23} & C_{33} & 0 & 0 & 0\\ 0 & 0 & 0 & C_{44} & 0 & 0\\ 0 & 0 & 0 & 0 & C_{55} & 0\\ 0 & 0 & 0 & 0 & 0 & C_{66}\end{bmatrix}\begin{bmatrix}\varepsilon_1\\ \varepsilon_2\\ \varepsilon_3\\ \varepsilon_4\\ \varepsilon_5\\ \varepsilon_6\end{bmatrix} \quad (31)$$

If the nine engineering constants (E_{11}, E_{22}, E_{33}, G_{23}, G_{13}, G_{12}, ν_{12}, ν_{13}, ν_{23}) are known, then the stiffness constants can be calculated:

$$C_{11}=\frac{1-\nu_{23}\nu_{32}}{E_2E_3\Delta} \quad (32) \qquad C_{22}=\frac{1-\nu_{13}\nu_{31}}{E_1E_3\Delta} \quad (33) \qquad C_{33}=\frac{1-\nu_{12}\nu_{21}}{E_1E_2\Delta} \quad (34)$$

$$C_{12}=\frac{\nu_{21}+\nu_{32}\nu_{13}}{E_1E_3\Delta} \quad (35) \qquad C_{13}=\frac{\nu_{13}+\nu_{12}\nu_{23}}{E_1E_2\Delta} \quad (36) \qquad C_{23}=\frac{\nu_{23}+\nu_{21}\nu_{13}}{E_1E_2\Delta} \quad (37)$$

$$C_{44}=G_{23} \quad (38) \qquad C_{55}=G_{13} \quad (39) \qquad C_{66}=G_{12} \quad (40)$$

where $$\Delta=\frac{1-\nu_{12}\nu_{21}-\nu_{23}\nu_{32}-\nu_{31}\nu_{13}-2\nu_{21}\nu_{32}\nu_{13}}{E_1E_2E_3} \quad (41)$$

When a single laminate layer is oriented at a different angle to the primary coordinate system, the lamina stiffness matrix and engineering properties can be effectively 'transformed' from the ply coordinate system to the global laminate coordinate system using the transformation matrix:

$$A=\begin{bmatrix}\cos\theta & \sin\theta & 0\\ -\sin\theta & \cos\theta & 0\\ 0 & 0 & 1\end{bmatrix} \quad (42)$$

When a state of plane stress is assumed, then this matrix is sufficient to relate the individual ply stress state to the global system. In the case where a 2nd order stress tensor is considered, i.e. the response of the laminate in the through-thickness is required, the transformation matrix is a factor of the stress tensor, and must take into account the through-thickness stress state, i.e.:

For plane stress,

$$[\sigma]=\begin{bmatrix}\sigma_1\\ \sigma_2\\ \sigma_6\end{bmatrix} \quad \text{or in body-coordinate system} \quad [\sigma]=\begin{bmatrix}\sigma_{xx}\\ \sigma_{yy}\\ \sigma_{xy}\end{bmatrix} \tag{43}$$

For 2D stress-tensor,

$$[\sigma]=\begin{bmatrix}\sigma_1\\ \sigma_2\\ \sigma_3\\ \sigma_4\\ \sigma_5\\ \sigma_6\end{bmatrix} \quad \text{or in body-coordinate system} \quad [\sigma]=\begin{bmatrix}\sigma_{xx}\\ \sigma_{yy}\\ \sigma_{zz}\\ \sigma_{yz}\\ \sigma_{xz}\\ \sigma_{xy}\end{bmatrix} \tag{44}$$

Therefore, to transform the lamina stress state to the global coordinate system, the following equation is used:

$$C_{1,2} = T_\sigma C_{x,y} T_\varepsilon^{-1} \tag{45}$$

where $$T_\sigma = \begin{bmatrix} \cos^2\theta & \sin^2\theta & 0 & 0 & 0 & \sin\theta\cos\theta \\ \sin^2\theta & \cos^2\theta & 0 & 0 & 0 & -2\sin\theta\cos\theta \\ 0 & 0 & 1 & 0 & 0 & 0 \\ 0 & 0 & 0 & \cos\theta & -\sin\theta & 0 \\ 0 & 0 & 0 & \sin\theta & \cos\theta & 0 \\ -\sin\theta\cos\theta & \sin\theta\cos\theta & 0 & 0 & 0 & \cos^2\theta-\sin^2\theta \end{bmatrix}$$

and $$T_\sigma = \begin{bmatrix} \cos^2\theta & \sin^2\theta & 0 & 0 & 0 & -\sin\theta\cos\theta \\ \sin^2\theta & \cos^2\theta & 0 & 0 & 0 & \sin\theta\cos\theta \\ 0 & 0 & 1 & 0 & 0 & 0 \\ 0 & 0 & 0 & \cos\theta & \sin\theta & 0 \\ 0 & 0 & 0 & -\sin\theta & \cos\theta & 0 \\ 2\sin\theta\cos\theta & -2\sin\theta\cos\theta & 0 & 0 & 0 & \cos^2\theta-\sin^2\theta \end{bmatrix}$$

Once the stiffness matrix for the laminate is known, the compliance matrix can be determined by taking the inverse of the stiffness matrix, i.e.:

$$[S]=[C]^{-1} \tag{46}$$

The laminate engineering constants can now be calculated from the coefficients of the compliance matrix.

2.2.3.8 Puck's Action Plane Failure Criteria

In general, the analysis of strength properties of composite laminates requires the following:

- Analysis of strains and stresses in each individual ply;
- Specified ply failure criteria;
- Degradation models which are used to re-evaluate the contribution of failed plies to the continuing load performance of the intact laminate.

The World Wide Failure Exercise (WWFE) was a global exercise which assessed the maturity and predictive capability of 19 leading theoretical approaches for predicting the deformation and failure response of polymer composite laminates when subjected to complex states of stress (Hinton et al., 2002). It was found that no single theory could predict to within ±10% of the experimentally-measured strengths in more than 40% of the test cases. Puck's action plane failure theory (Puck & Schürmann (1998, 2002)) was deemed the "winner" of the WWFE based on a systematic comparison; results of which are shown in Figure 2-14. In his derivation, Puck used the well-established Classical Laminate Theory to initially determine the laminate elastic stiffness matrix (and therefore the elastic properties). His so-called "Action Plane Failure Criteria" was used to define failure in the individual plies, and the degradation of the failed plies was controlled by degradation factors based on the ply failure mode. Quantitatively, Puck's action plane failure criteria was capable of predicting to within ±50% of the measured final failure strengths in more than 85% of the cases considered.

The WWFE considered 14 test cases from simple uniaxial tension to highly complex bi-axial tension/shear loading. The non-linear orthotropic yield strength and orthotropic softening failure models within the advanced composite material damage model of Riedel et al. (2003) considers only unidirectional loading cases, using coupling coefficients to relate the various unidirectional stress-strain curves.

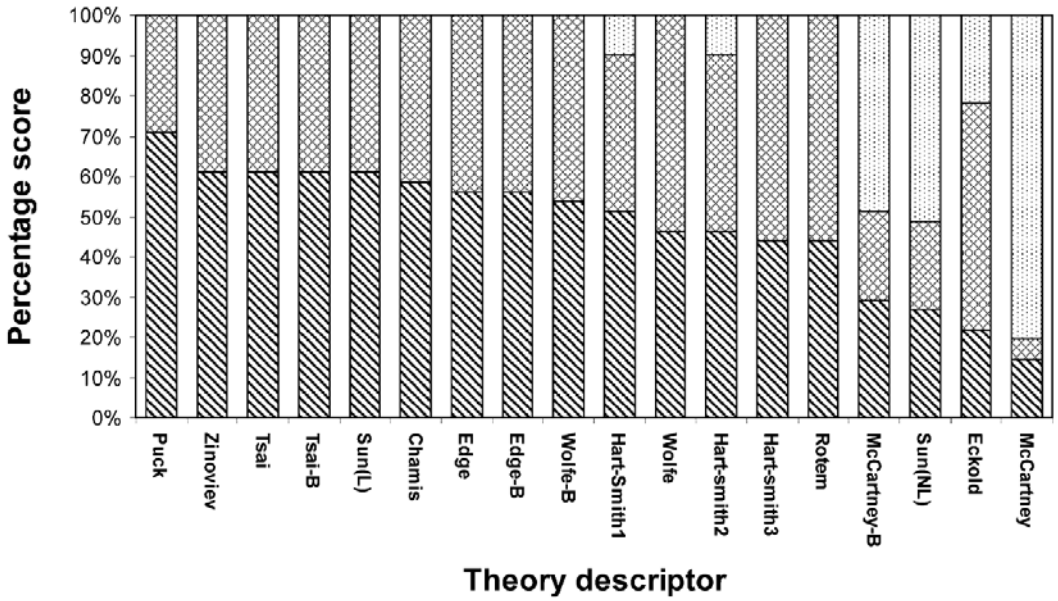

Figure 2-14 Final ranking of the various failure theories in exhibited in the WWFE (Hinton et al., 2002).

For unidirectional loading of multi-directional laminates, the predictions of Puck were "generally in good agreement with the measured ones" (Hinton et al., 2002), and the discrepancies occurred primarily in those test cases where large non-linear deformations were present. For the multi-directional CFRP laminates considered the failure is highly brittle (low strain-to-failure), exhibiting very little plastic deformation prior to catastrophic failure. As such these discrepancies are not expected to have a significant affect.

Puck's failure theory defines two independent fracture criteria to determine lamina strength: fibre failure (FF) and inter-fibre failure (IFF) within the matrix. The fibre failure criterion is based on a modified version of the maximum stress formulation, in which the effect of stress magnification caused by the differing constituent moduli during biaxial loading is taken into account:

$$\begin{aligned} \frac{1}{\varepsilon_{1T}}\left(\varepsilon_1 + \frac{\nu_{f12}}{E_{f11}} m_{\sigma f}\sigma_2\right) &= 1 \text{ for } (\ldots) \geq 1 \\ \frac{1}{\varepsilon_{1C}}\left(\varepsilon_1 + \frac{\nu_{f12}}{E_{f11}} m_{\sigma f}\sigma_2\right) &= -1 \text{ for } (\ldots) < 1 \end{aligned} \tag{47}$$

where $m_{\sigma f}$ – mean magnification factor of the transverse stress (fibre).

The IFF criterion is based on the failure criteria of Mohr, originally developed for isotropic materials exhibiting brittle fracture induced by normal and shear stresses acting on the fracture plane (Figure 2-15).

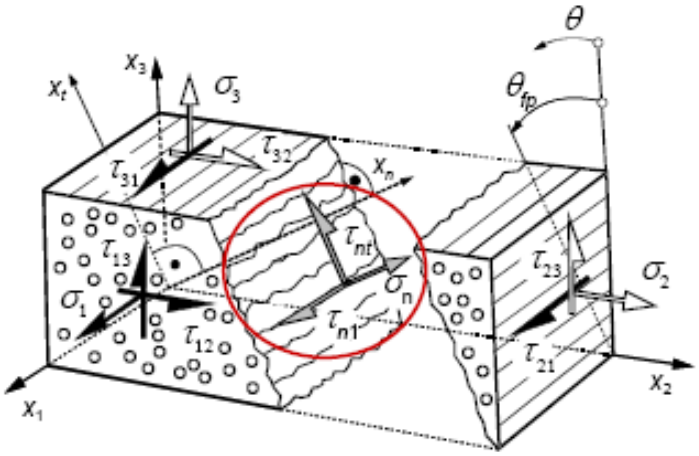

Figure 2-15 Brittle fracture of a unidirectional fibre-reinforced material and definition of the fracture plane stress components (from Kaiser et al., 2004).

Three IFF modes (A, B and C) are identified by Puck and are used to generate a so-called master fracture curve. Mode A corresponds to failure under applied transverse tension or in-plane shear, mode B corresponds to a longitudinal shear failure under high applied shear stress and moderate transverse compression stress, and mode C involves failure occurring on an inclined fracture plane under high applied transverse compression and shear stresses:

Mode A ($\sigma_2 \geq 0$): (48)

$$f_E\,|_{\sigma_{fp}=0^\circ} = \frac{1}{R_{\perp\parallel}}\left[\sqrt{\left(\frac{R_{\perp\parallel}}{R_{\perp}^{(+)}} - p_{\perp\parallel}^{(+)}\right)\sigma_2^2 + \tau_{21}^2} + p_{\perp\parallel}^{(+)}\sigma_2\right] = 1$$

Mode B ($\sigma_2 < 0$): (49)

$$f_E\,|_{\theta_{fp}=0^\circ} = \frac{1}{R_{\perp\parallel}}\left[\sqrt{\tau_{21}^2 + \left(p_{\perp\parallel}^{(-)}\sigma_2\right)^2} + p_{\perp\parallel}^{(-)}\sigma_2\right] = 1$$

Mode C ($\sigma_2 < 0$): (50)

$$f_E\,|_{\theta_{fp}\neq 0^\circ} = \frac{\tau_{21}^2}{4\cdot\left(R_{\perp\parallel} + p_{\perp\parallel}^{(-)}R_{\perp\perp}^{A}\right)^2}\cdot\frac{R_{\perp}^{(-)}}{(-\sigma_2)} + \frac{(-\sigma_2)}{R_{\perp}^{(-)}} = 1$$

where $R_{\perp}^{(+)}$ - u.d. composite transverse tensile strength
$R_{\perp}^{(-)}$ - u.d. composite transverse compression strength
$p_{\perp\parallel}^{(+)}$ and $p_{\perp\parallel}^{(-)}$ - Fracture surface inclination parameter.

The fracture modes and resulting failure envelope (referred to by Puck and Schürmann as the master fracture curve) for the case $\sigma_1 = 0$ are shown in Figure 2-16.

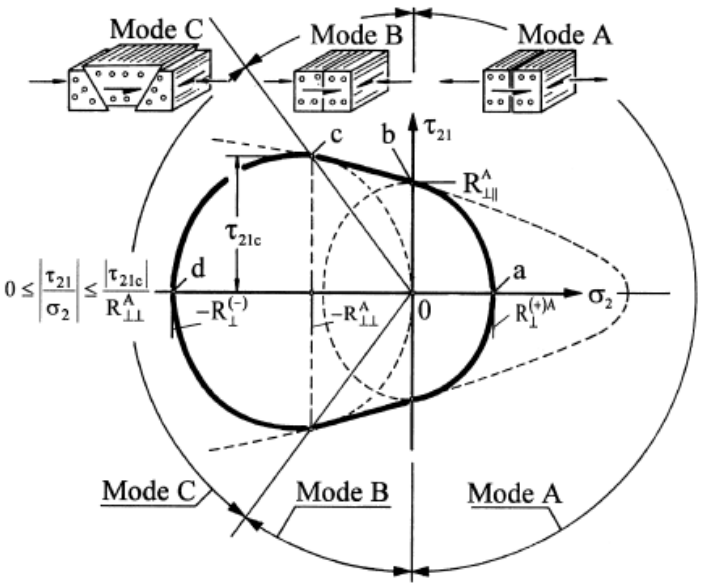

Figure 2-16 Fracture curve showing three IFF failure modes A, B, C (from Puck & Schürmann, 1998).

The shape of Puck's failure envelope (fracture curve), defined by Eq. (48)-(50), requires definition of the inclination parameters ($p^{(+)}_{\perp\parallel}$, $p^{(-)}_{\perp\parallel}$, $p^{(+)}_{\perp\perp}$, $p^{(-)}_{\perp\perp}$). These parameters are visualized as the inclination at $\sigma_n = 0$ of lines running tangential to the master fracture body, as shown in Figure 2-17.

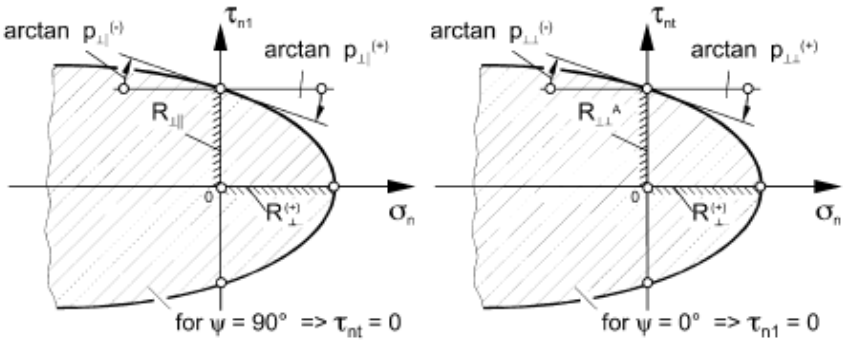

Figure 2-17 Inclination parameters of Puck's master fracture body (from Kaiser et al., 2004).

An example of Puck's master fracture surface is given in Figure 2-18 for a unidirectional material at $\sigma_1 = 0$.

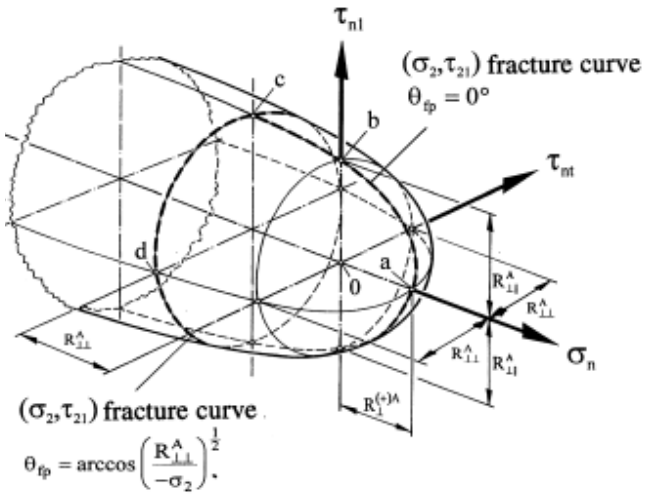

Figure 2-18 Master fracture surface for a u.d. laminate in (σ_n, τ_{nt}, τ_{nl}) stress space (from Puck & Schürmann, 1998).

Under additional applied longitudinal stress, σ_1, progressive failure of single fibres causes a degradation of the IFF strengths $R_{\parallel}^{(+)}, R_{\perp\parallel}, R_{\perp}^{(-)}$. This degradation is taken into account via a weakening factor, f_w, where:

$$f_w = \frac{(ca)^2 + 1}{c \cdot \left(a\sqrt{c^2\left(a^2 - s^2\right)+1} + s\right)} \tag{51}$$

where $c = \left(f_E / f_{E(FF)}\right)$

s –starting point of the weakening effect

a – axis of an assumed elliptical fracture curve $\rightarrow a = \frac{1-s}{\sqrt{1-m^2}}$

and m – assumed minimum value of the degradation factor f_w.

The effects of the weakening factor terms *s* and *m* are shown in Figure 2-19 in terms of the shape of the IFF failure envelope.

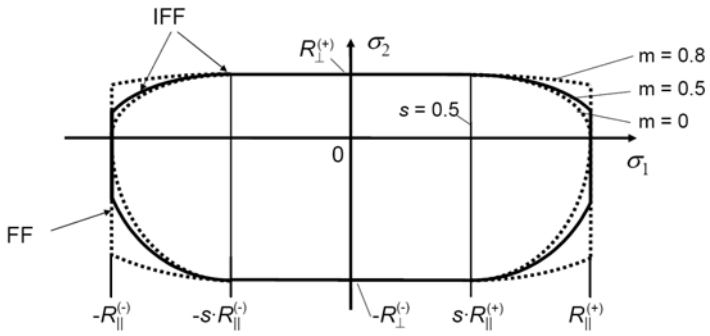

Figure 2-19 Effect of parameters *m* and *s* on the shape of the IFF failure envelope (from Kaiser et al., 2004).

Additional degradation is incorporated into Puck's failure theory for the case of Mode A IFF (Eq. (48)). In this failure case, cracks are assumed to open under a perpendicular tensile load, meaning that at the location of the crack the secant moduli (E_{2s} and G_{21s}) drop to zero. Puck resolves this problem by introducing a degradation factor, η, which effectively smears the effect of the crack by providing a gradual reduction in the secant moduli from the crack location. An empirical formula for the degradation factor is given in Puck and Schürmann (1998):

$$\eta = \frac{1-\eta_r}{1+c\left(f_{E(IFF)}-1\right)^{\xi}} + \eta_r \quad \text{for} \quad f_{E(IFF)} \geq 1 \tag{52}$$

where c, ξ - Empirical factors
η_r – small remaining stiffness ($\eta_r < 1$).

2.3 Summary

For the next generation of European scientific satellites, the impact of small meteoroid and space debris (M/SD) particles threatens to degrade the accuracy of high-sensitivity measurement equipment such that the successful completion of mission objectives is at risk. Current M/SD risk analysis is performed primarily on manned space missions, in which the risk is assessed in terms of the probability of no penetration, probability of no critical failure, and probability of no subcomponent penetration. In other words, they are all penetration-based requirements. In the case of unmanned spacecraft, penetration of the primary structure does not necessarily represent a critical event. It is only when penetration leads to the destruction of mission critical equipment/subsystems that failure is induced. Thus, the adoption of manned spacecraft M/SD risk requirements for unmanned spacecraft is insufficient in that it:

- Fails to address the threat of mission failure resulting from the degradation of scientific equipment measurement accuracy, and;
- Leads to the design of unnecessarily heavy shielding structures which are required to protect the entire spacecraft volume to meet penetration-based risk criteria.

For risk analysis, performance of the spacecraft primary structure when subjected to hypervelocity impact is required. Traditionally, experimental acceleration facilities such as two-stage light gas guns have been used to

perform extensive impact test programs towards this goal. As experimental facilities are only capable of reproducing a limited range of expected in-orbit impact conditions, numerical methods have often been used as a complementary technique in allowing extrapolation to higher impact velocities and a wider range of projectile diameters.

Hydrocodes are ideal for simulation of non-linear highly dynamic impact events, allowing the coupling of sophisticated material models with a fluid-structure program. Recent developments in the modelling of fibre-reinforced composite materials provide a significant improvement over existing capabilities for hypervelocity impact modelling. In the absence of experimentally-characterised material data, theoretical methods are available which allow the derivation of coarse composite structural data from constituent properties for modelling in the commercial hydrocode AUTODYN.

3 A New Ballistic Limit Equation for CFRP/Al HC Sandwich Panels

The excitation induced by impact of a space debris particle travelling at hypervelocity on a sandwich panel structure is dependent on the type of penetration and failure mechanisms caused by the impact event. Four penetration conditions are considered which are expected to induce significantly different types of disturbances in a sandwich panel structure:

1. Non-penetration case: projectile does not penetrate the outer facesheet of the sandwich panel;

2. Penetration case 1: projectile penetrates the sandwich panel structure and is stopped inside the sandwich panel;

3. Penetration case 2: projectile minimally penetrates the sandwich panel;

4. Penetration case 3: projectile penetrates the sandwich panel completely.

The four penetration cases are illustrated in Figure 3-1.

Each of the penetration cases results in a different energy transformation and momentum transfer condition. For the non-penetrating case, all elastic energy imparted to the sandwich panel will be realized in the front facesheet. In penetration case 1, following perforation of the front facesheet, the fragment cloud propagates through the honeycomb core, eventually impacting on the rear facesheet. At the onset of front facesheet perforation, the momentum of the perforated fragments will be low, and as such the excitation will be confined mostly to the front facesheet. As the degree of perforation increases (i.e. as the penetration approaches case 2) the projectile will show an increasing "punch-out" type perforation of the front facesheet as a result of an increasing energy overload. In this case, the response of the front facesheet will reduce, and the majority of the excitation will now occur in the rear facesheet. In this context, minimal perforation refers to the state in which an increase in projectile momentum will correspond to an increase in momentum transfer and therefore excitation of the respective perforated facesheet.

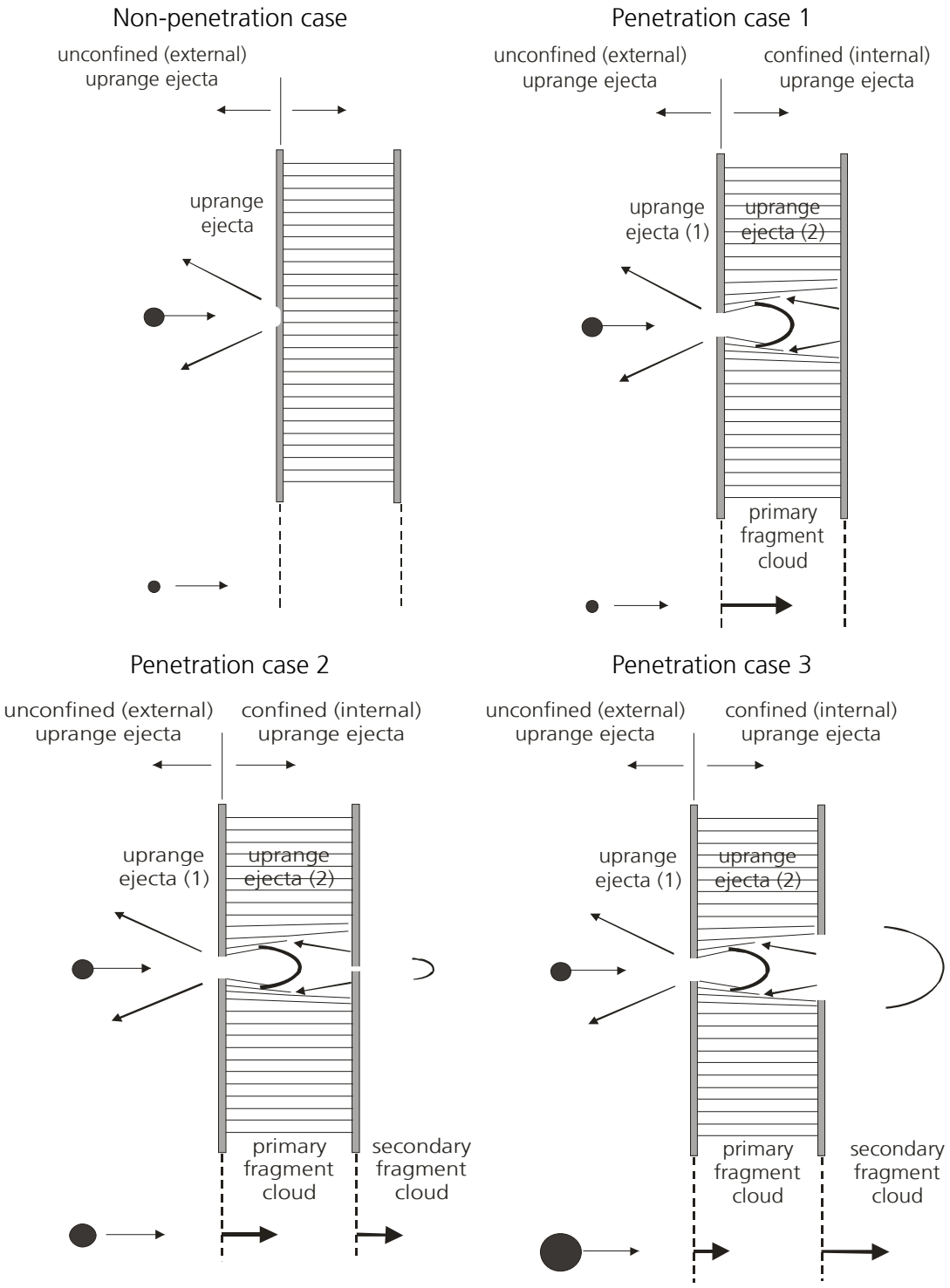

Figure 3-1 Phenomena of the four penetration cases for impact on a HC SP.

As the sandwich panel (i.e. rear facesheet) is perforated, the behaviour described for perforation of the front facesheet will be repeated. At low levels of perforation (i.e. penetration case 2), the majority of projectile

kinetic energy will still be imparted on the rear facesheet. As the size (and thus lethality) of the projectile increases (i.e. approaches penetration case 3), the majority of impactor kinetic energy will be ejected from the sandwich panel within the fragment cloud.

For a thorough analysis of the disturbances induced by impact on a CFRP/Al HC sandwich panel structure it is necessary to consider all four penetration cases. Ballistic Limit Equations (BLEs) are used to define the limits of perforation for a specific structure in terms of impactor mass, velocity and approach angle. Schäfer et al. (2004) have defined and validated a BLE capable of determining the perforation limits of the sandwich panel front CFRP facesheet, however no experimentally-validated means exist for definition of the rear facesheet (i.e. complete sandwich panel).

Ballistic limit equations, owing to the complexity of failure mechanisms and material behaviour at such high strain-rate loading, are generally empirical equations which, although based on laws of impact physics (e.g. momentum loading in the hypervelocity range), are adjusted to fit experimental data. The volume of hypervelocity impact test data on CFRP/Al HC SPs is limited. For this reason, this chapter presents a comprehensive experimental research program of hypervelocity impacts on multiple structural configurations for the derivation and validation of a new BLE for CFRP/Al HC sandwich panels. The derived ballistic limit equation can then be used to predict impact conditions which result in the four penetration cases relevant for the investigation of hypervelocity impact induced disturbances in satellite structures (presented in Figure 3-1), minimising the time and cost otherwise required for initial shielding performance analysis.

3.1 Description of the Experimental Facilities

During the course of the experimental program, two facilities, both of which are two-stage light-gas guns, were used to perform impact tests: the “Space Gun” (SLGG) and “Baby Gun” (BLGG).

3.1.1 Space Light Gas Gun

The Space Gun facility (SLGG) at the Ernst Mach Institute is shown in Figure 3-2. The primary use of this facility is for evaluation of space

qualified hardware under near-realistic hypervelocity impact conditions. It is capable of launching millimeter sized projectiles at velocities up to and exceeding 9 km/s.

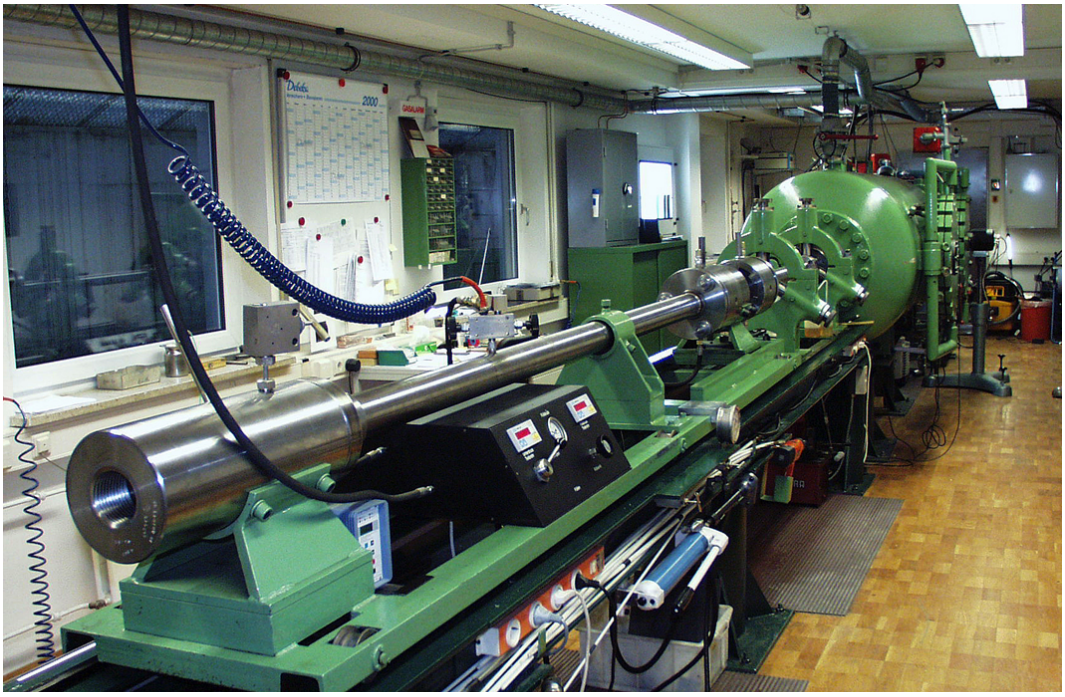

Figure 3-2 EMI's Space Gun Facility.

In order to generate such high velocities, this gun takes advantage of the effects from coupling two independent guns. This concept is illustrated in Figure 3-3. The acceleration process begins in the powder chamber of a conventional gun, where gun powder and an igniter are used to launch a small plastic piston in the first tube (referred to as the pump tube). The pump tube is filled with a light weight gas, usually Helium (He) or Hydrogen (H). As the piston is forced along the pump tube by expanding gas from the powder chamber it is simultaneously compressing the light weight gas in front of it in the pump tube. In the high pressure section, which is the joining point between the two gun barrels, a thin metal diaphragm is strategically placed. This diaphragm prevents the light weight gas in the pump tube from escaping into the launch tube until the gas is compressed to a specific pressure upon which the diaphragm ruptures. The projectile is placed immediately behind the diaphragm, which is launched by the now escaping light weight gas from the pump tube.

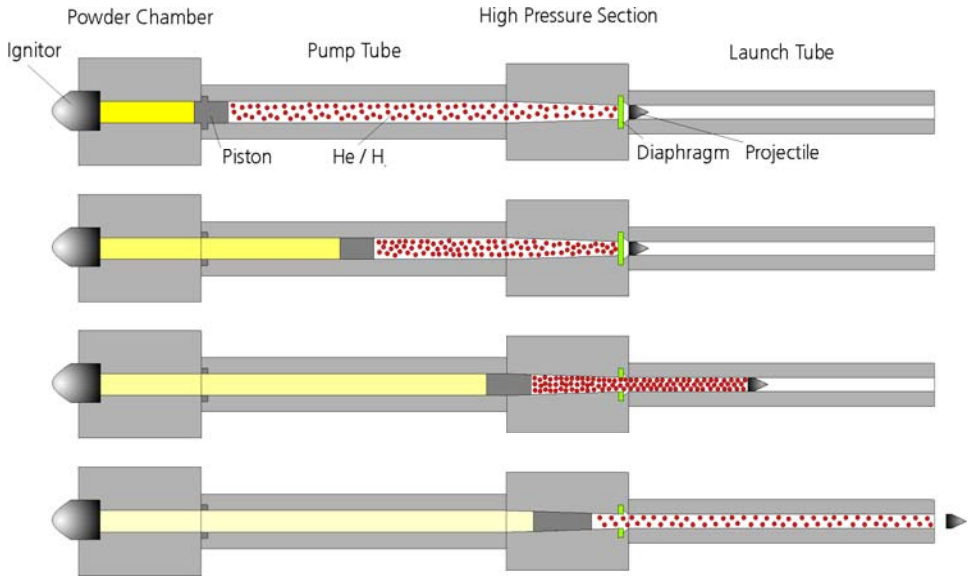

Figure 3-3 Two-stage light-gas gun method of operation.

Due to the characteristics of the projectiles launched by this gun, it is required that a sabot be used to carry the projectile down the launch tube. The sabot is required:

1. to prevent the gas from escaping around the projectile, thus ensuring the maximum force from the expanding gas is used during the launch of the projectile,

2. to absorb the enormous friction heating by melting at the interface between sabot and launch tube, and

3. to enable the acceleration of (almost) arbitrary projectile shapes.

The sabot is scored so that once it exits the launch tube into free flight it splits into several parts and separates from the projectile, allowing the projectile a non-disruptive approach to the target. A common sabot configuration is shown in Figure 3-4.

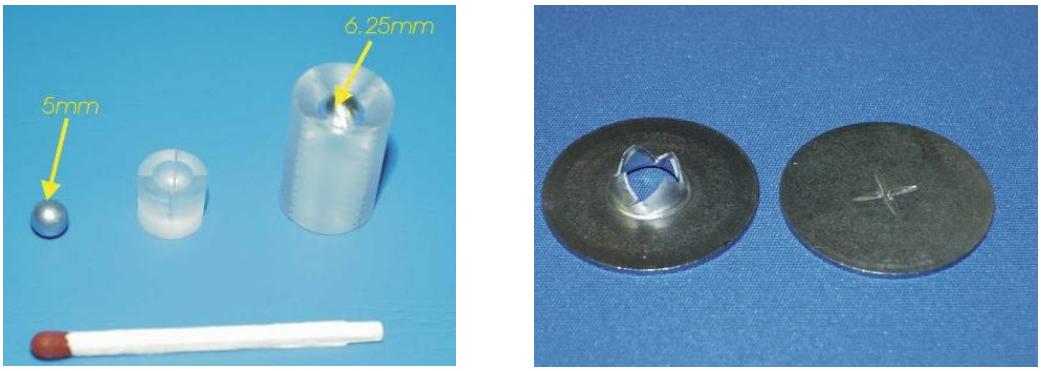

Figure 3-4 Sabot and projectile along with high pressure section membrane.

After the projectile exits the launch tube it enters the blast tank. The blast tank is at reduced pressure (typically 100 mbar or ~1/10 atmosphere at this facility). This is the location where the sabot separates from the projectile by the action of atmospheric drag on the sabot parts. The gas from the pump tube exits the launch tube behind the projectile and expands within the blast tank. As the use of helium as driver gas results in considerable gun barrel erosion and simultaneously prevents reaching the highest velocities, hydrogen is used in most cases as the driver gas. In this case hot and compressed hydrogen gas is released into the blast tank, which then combusts with the residual air. This combustion generates a strong blast wave in the wake of the projectile and sabot that propagates in the direction of the target chamber. To reduce this blast, several containment chambers have been integrated along the length of the gun.

After passing through the blast tank, the projectile enters the velocity measurement section where a laser light barrier system measures its velocity. In this section a high speed photography system is also installed which captures two images of the projectile during flight. This can be used to determine velocity as well as view the projectile's location with regards to the shot axis. Finally, the projectile enters the target chamber. In this section, a second high speed framing camera has been integrated to capture images of the projectile as it impacts on the target. The entire Space Gun facility is illustrated in Figure 3-5. Also depicted are the dimensions of the target chamber with a photo showing the installation of a standard target setup.

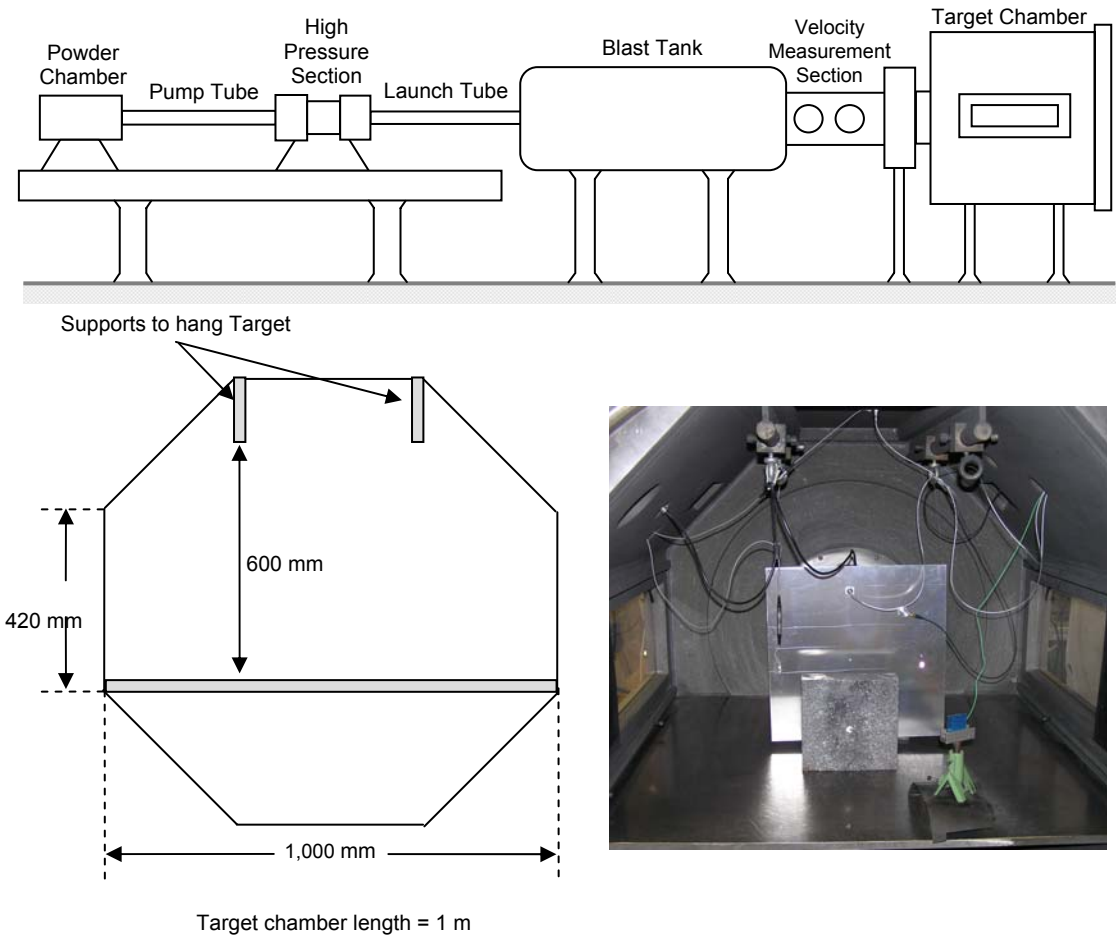

Figure 3-5 Space Gun illustration and target chamber dimensions.

The Space Gun also has the capability to conduct tests in which the target chamber is under high vacuum. This is advantageous for further reducing the effect of the combusting hydrogen blast on the target. To this purpose, the target chamber is sealed at its entrance with a thin membrane (thickness in the order of μm), and the air is evacuated using a two-stage pumping system. The high vacuum condition for the target chamber is on the order of $< 10^{-4}$ mbar.

The velocity regime of the Space Gun spans from ca. 3 to above 9 km/s, using projectiles with a mass between ca. 10^{0} and 10^{-3} grams, corresponding to Al-spheres with diameters between ca. 10 mm and 1.5 mm, respectively. The advantages of this facility include the wide range of projectile sizes capable of being launched, and wide velocity range achievable. The size of the target chamber also allows for large and complex target configurations.

3.1.2 Baby Light Gas Gun

The second facility at EMI used in this study is the Baby Gun (BLGG), which is shown in Figure 3-6. The primary use of this facility is to complement the Space Gun in evaluation of the impact behaviour of space qualified hardware. The operating principle of the BLGG is identical to that of the Space Gun, albeit on a much smaller scale.

Figure 3-6 Baby Gun facility.

An illustration of the Baby Gun is given in Figure 3-7. It can be observed that the blast tank and the velocity measurement sections have been integrated into one section. The size and shape of the target chamber (shown in Figure 3-7) is also worth noting in comparison to the Space Gun.

The blast tank residual pressure is larger for this facility than for the Space Gun, as the sabot separation needs to be completed over a much shorter distance, requiring higher aerodynamic drag. This is achieved by operating the Baby Gun blast tank at around 200 mbar (1/5 atmosphere).

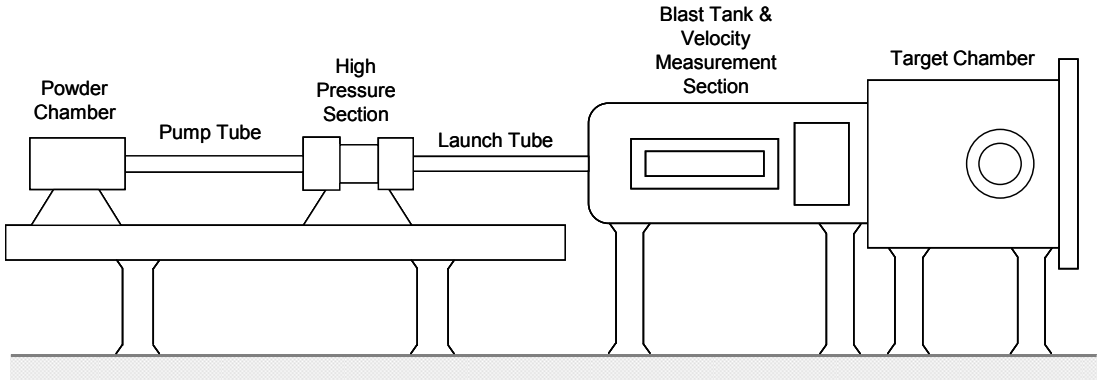

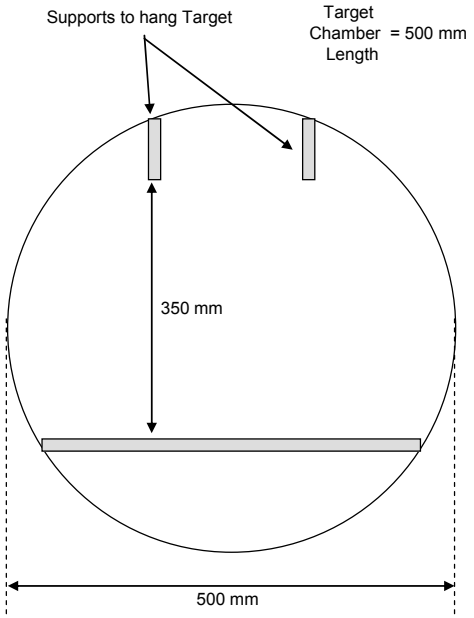

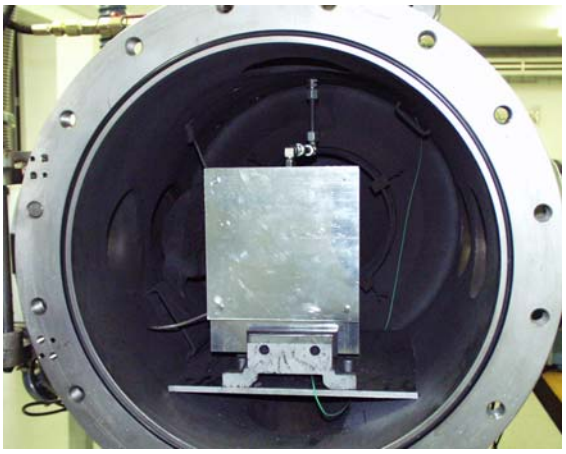

Figure 3-7 Baby Gun illustration and target chamber dimensions.

The BLGG has the capability of accelerating projectiles between 10^{-4} and 10^{-2} grams (corresponding to Al-spheres with diameters between 0.5mm and 3mm) to velocities in the range of 3 to ca. 8 km/s. The BLGG also has the capability of conducting tests in high vacuum (<10^{-4} mbar).

The primary advantage for using the BLGG over the SLGG is its capability to launch smaller projectiles. In comparison to the Space Gun the range of achievable velocities is not as wide, nor is the target chamber as large.

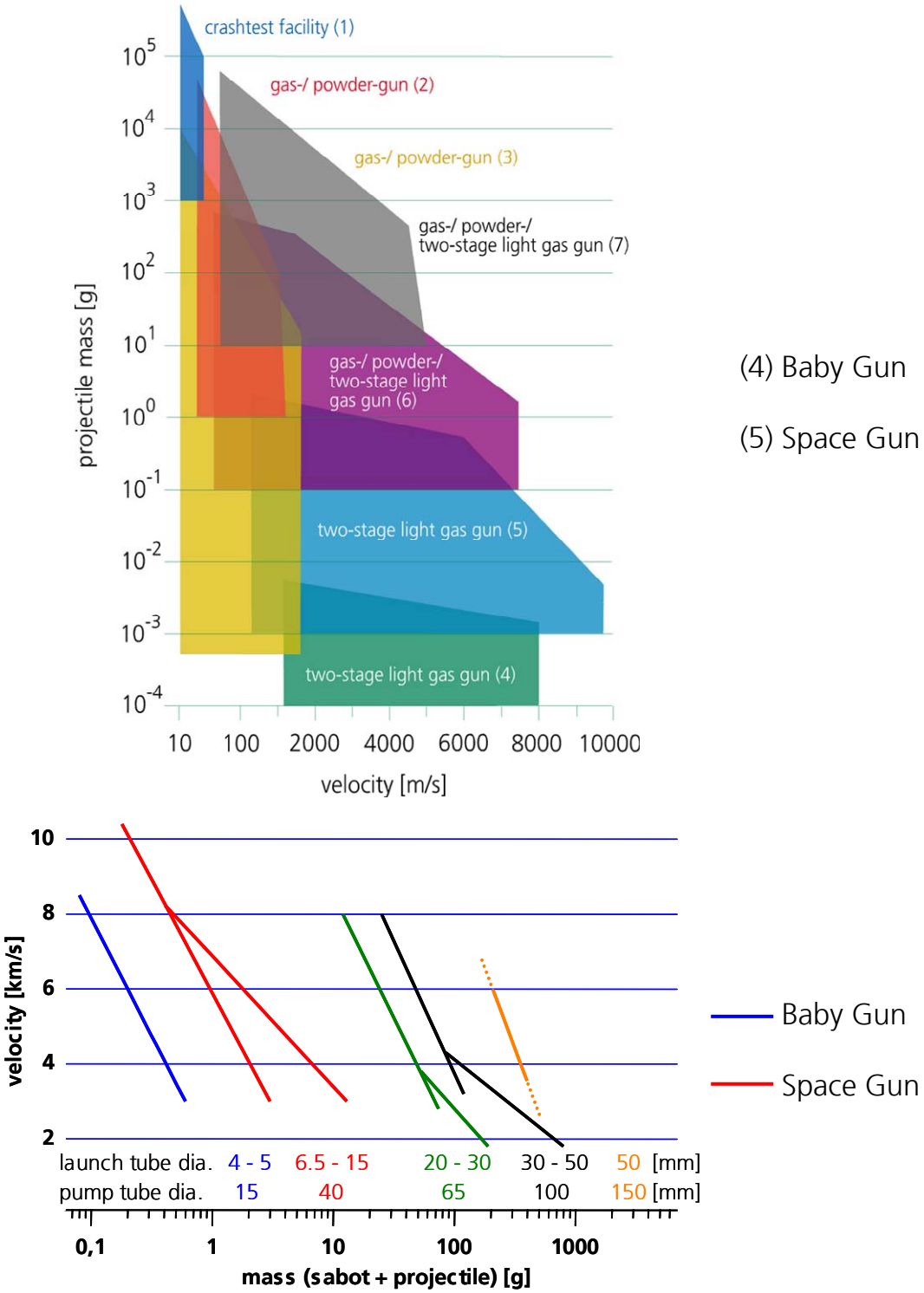

Figure 3-8 EMI facility performance capabilities.

3.1.3 Performance of the Experimental Facilities

The acceleration capabilities of the SLGG and BLGG are shown in Figure 3-8 expressed in terms of projectile mass and achievable velocity range. Also shown in Figure 3-8 are the other acceleration facilities at EMI and their respective achievable performance. These facilities are generally not used in the investigation of space debris impact risk as they are designed for use with much larger projectiles. The versatility of the SLGG is clearly apparent in Figure 3-8, showing the wide range of projectiles capable of acceleration to hypervelocity. The motivation behind application of the SLGG and BLGG in tandem to allow investigation with a broader range of projectile masses for the experimental program can be observed.

3.2 HVI Damage and Ballistic Limit Equations

Upon impact of a projectile and target at hypervelocity, shock compression waves are propagated into both structures. If the target is thin relative to the projectile, the shock wave is reflected from the rear surface as a tensile release wave, overtaking the compression wave within the projectile. As the target thickness increases, the location in which the reflected release wave will overtake the compression wave moves towards the rear surface of the projectile. Eventually, the projectile shock wave will be reflected, leading to later superposition of the target and projectile release waves. The impact of a one-dimensional cylinder on a thin shield at hypervelocity is portrayed schematically in Figure 3-9. Initially, the two shock waves (S_1 and S_2) propagate away from the impact interface, while two rarefaction waves (R_1 and R_2) are transmitted towards the impact axis (axis of symmetry). The formation of these rarefaction waves has resulted in the upwave ejection of projectile and target materials. The target shock wave S_2 is reflected from the rear surface as rarefaction wave R_3.

As the materials are compressed (and released) they are subject to shock heating, providing a subsequent decrease in the materials fracture strength. Additionally, if the impact pressures are high enough, melting and vaporisation of the projectile and its fragments can occur.

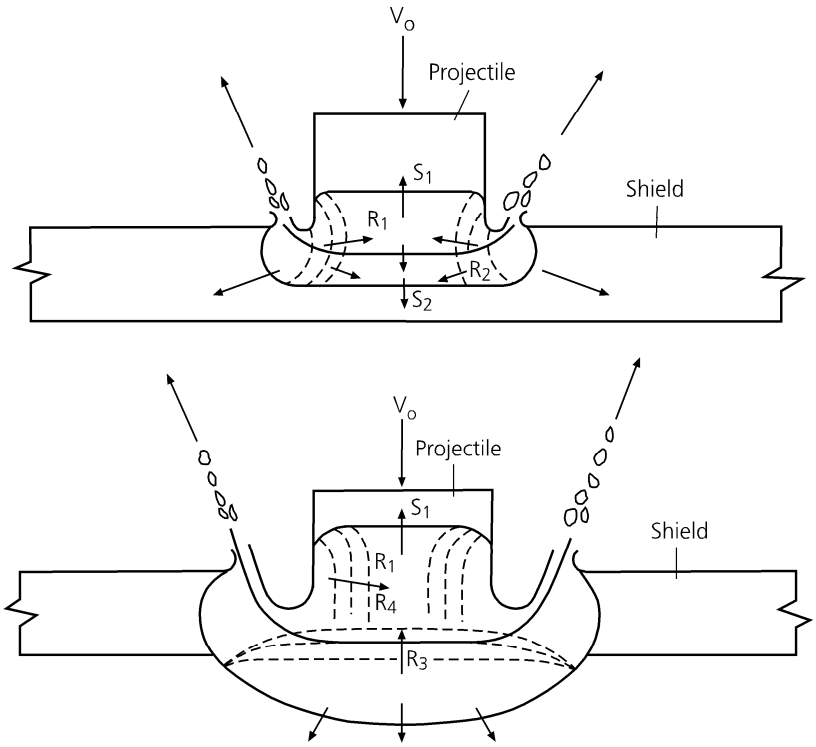

Figure 3-9 One-dimensional simplification of shock and rarefaction waves induced by impact of a projectile and shield at hypervelocity (Gehrig, 1970).

The range of impact velocities relevant for micrometeoroid and space debris research can be classified depending on the physical behaviour of the materials during impact, defined as:

- Ballistic regime;
- Shatter regime;
- Hypervelocity regime.

The ballistic regime concerns the velocity range in which the impact pressures are insufficient to cause fragmentation of the projectile. For penetration of a single plate, the projectile will pass through the shield fully intact with a velocity and direction similar to that of the initial particle.

As the impact velocity increases, so do the pressures generated in the projectile and target materials. The shatter phase represents the velocity range in which the impact-induced shock is of sufficient magnitude to fracture the projectile. In the case of single plate penetration, the shattered projectile material penetrates the shield and creates an expanding cloud of debris. For dual wall structures this regime introduces an increase in shielding capability, as the expanding cloud disperses the

impact energy of the projectile over a larger area of the dual-wall rear sheet. The degree of projectile fragmentation increases with impact velocity, producing a more evenly distributed fragment cloud of smaller individual particles, as shown in Figure 3-10. Characteristics (formation and propagation) of the debris cloud can be investigated using engineering models such as that presented by Schäfer (2006).

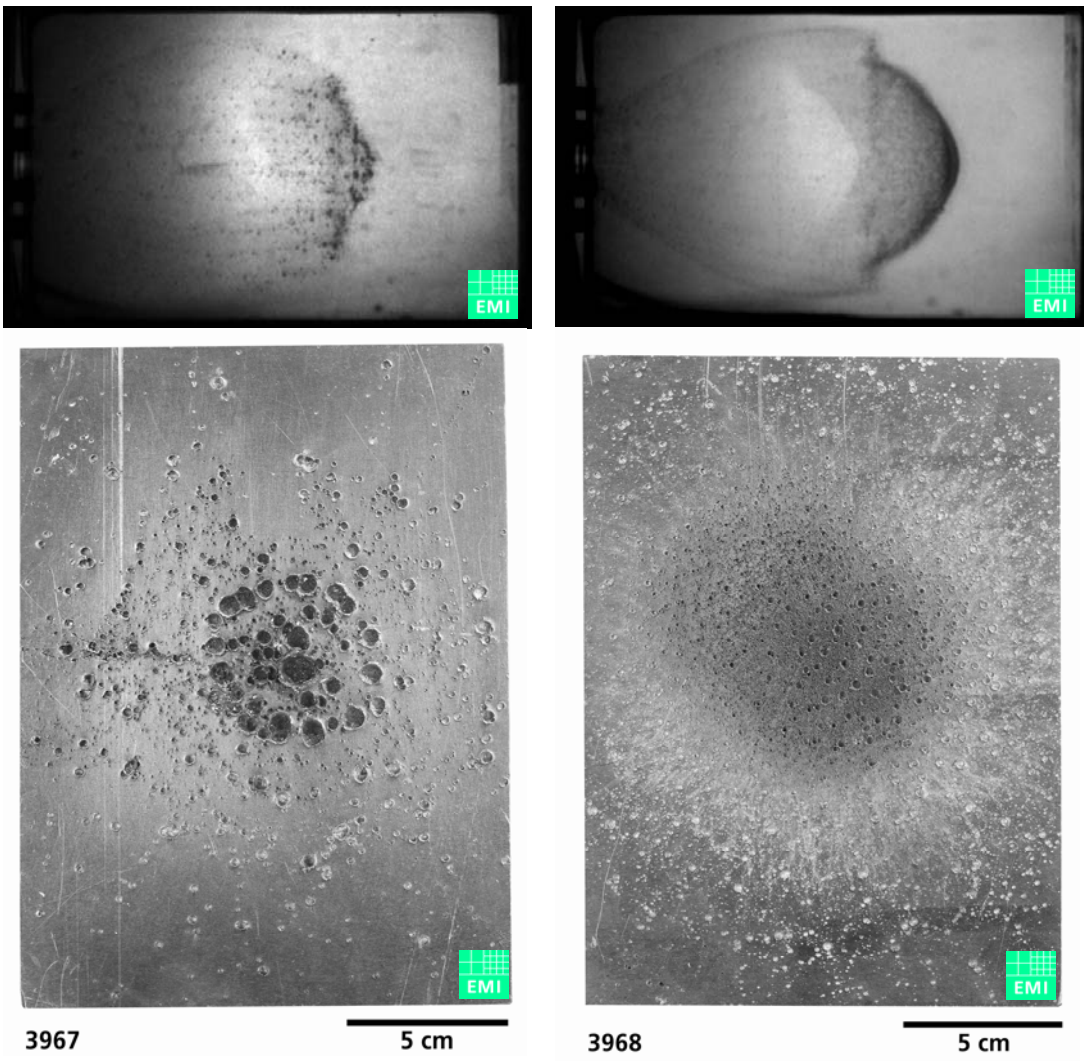

Figure 3-10 Fragment cloud and resulting impact damages in thick aluminium witness plated for two impact tests on thin Al-plates in the shatter regime (left: 4.8 km/s; right: 6.7 km/s).

The hypervelocity regime is defined for impacts in which pressure levels reach such a degree that the projectile and target material melt and vaporise. For a single plate structure, as the projectile penetrates it creates an expanding cloud of molten and vaporised projectile and shield material. Further increases in impact velocity will lead to more extensive

melting and vaporisation of the projectile and shield material, producing a more evenly distributed debris cloud of finer particles. Similar to the shatter regime, for impact on a dual wall structure in the hypervelocity regime the projectile mass and momentum are spread over a larger area of the rear sheet.

The three impact velocity regimes are shown in Figure 3-11 in terms of penetrating projectile diameters for a single and dual wall structure. The advantage of dual-wall structures over monolithic shields, provided by fragmentation and melting of the projectile upon impact with the front (bumper) plate, can be clearly seen in the shatter- and hypervelocity regimes.

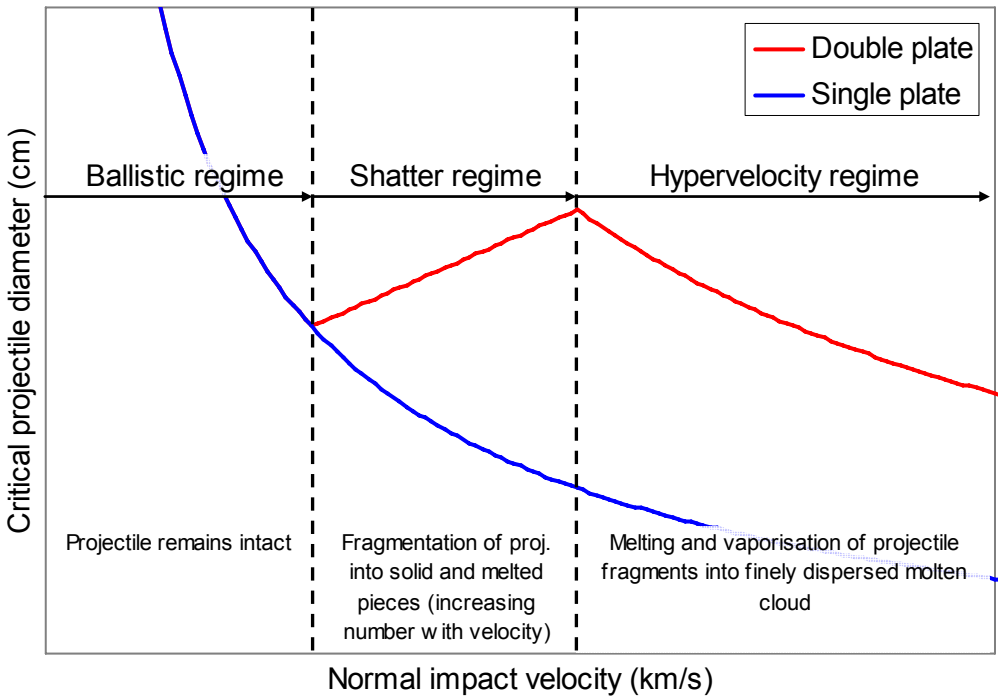

Figure 3-11 The effect of impact velocity on the shielding capability of monolithic and dual-wall shielding configurations.

Cour-Palais (1969) studied the phenomena of projectile fragmentation during hypervelocity impact. He developed sizing equations for dual wall spacecraft structures (coined Whipple shields after their creator Fred Whipple) in order to prevent perforation of and detached spallation from the shield rear surface. Based on analytical considerations, he used experimental data to empirically "anchor" the expressions at the highest obtainable impact velocities.

Cour-Palais found that for impact velocities high enough to permit complete projectile fragmentation and melting, a shield thickness to projectile diameter ratio (t_s/d_p) of 0.2 is optimum to ensure ideal interaction of shock and rarefaction waves. For this condition the fragment cloud is completely molten during impact on the Whipple shield rear wall and therefore the loading condition can be considered as an impulse or blast load. For the optimum t_s/d_p condition the thickness of a Whipple shield rear wall required to prevent spall detachment from the rear surface is proportional to impactor momentum:

$$t_w = \frac{C \cdot m \cdot V}{S^2} \tag{53}$$

where C – empirical factor (41.5 ± 14.0 for Al7075-T6).

The optimum rear wall thickness equation shows an inverse square dependence on spacing, S. Based on experimental evidence, Cour-Palais considered that the exponent of S is a function of the debris state upon impact with the rear wall. For solid debris without any gaseous or molten component n = 0, while for the full melt condition (such as that defined in Eq. (53)), n = 2.

In the case of non-optimum t_s/d_p (both above and below 0.2), the fragment cloud generated through impact on the front wall contains solid fragments of the projectile and shield. Thus sizing of the rear wall is performed based on the kinetic energy of impacting fragments ($t_w \propto KE^{1/3}$). For this condition the rear wall is sized using:

$$t_w = \frac{0.075 \cdot m_p^{1/3} \cdot V}{S^{1/2}} \tag{54}$$

The non-optimum equation shows an inverse square root dependence on spacing. This represents an intermediate condition for the state of the fragment cloud. This equation was derived from experimental data using Al-alloys with a yield stress of ~70 ksi. For other materials, a yield-strength conversion factor $\left(\frac{70}{\sigma_y}\right)^{1/2}$ can be applied. Furthermore, Cour-Palais identified that the constant 0.075 factor can depend on both shield and projectile densities. To ensure conformance with perforation and cratering equations which showed a $1/6^{th}$ density dependence (e.g. Summers, 1959), the non-optimum sizing equation was adjusted to:

$$t_w = \frac{0.05 \cdot (\rho_p \cdot \rho_b)^{1/6} \cdot m_p^{1/3} \cdot V}{S^{1/2}} \cdot \left(\frac{70}{\sigma}\right)^{1/2} \tag{55}$$

As impact velocities obtainable in the laboratory cannot cover the complete range of expected in-orbit, a kinetic energy scaling relationship ($t_w \propto KE^{1/3}$) is included in the Whipple shield equation to allow conservative extrapolation to higher impact velocities.

The Whipple shield equation was derived using HVI data for projectiles up to ~0.16 cm in diameter. Christiansen (1991), in sizing Whipple shields for the International Space Station, extended this experimental database to projectiles up to 1.9 cm in diameter and found a dependence of the 0.075 constant (termed K factor) on projectile diameter. Christiansen (1991) defined the modified Cour-Palais Whipple shield equation as:

$$t_w = \frac{K \cdot (\rho_p \cdot \rho_b)^{1/6} \cdot m_p^{1/3} \cdot V}{S^{1/2}} \cdot \left(\frac{70}{\sigma}\right)^{1/2} \tag{56}$$

where $K = 0.16 \cdot d_p^{1/2}$ cm^2-sec/g$^{2/3}$-km.

At low impact velocities, impact pressures are insufficient to cause fragmentation of the projectile. Spacing of the Whipple shield therefore has effectively no influence and the shield sizing is performed using empirical single plate cratering expressions. From Cour-Palais (1985):

$$P = \frac{5.24 \cdot d_p^{18/19} \cdot \rho_p \cdot V^{2/3}}{H_b^{1/4} \cdot \rho_b^{1/6} \cdot E_b^{1/3}} \tag{57}$$

where P – penetration depth.

Sizing of the rear wall is then performed based on the failure definition:

For no perforation	t_w = 1.8P
For no perforation or detached spall	t_w = 2.2P
For no attached spall	t_w = 2.0P

For Al-on-Al impact, Anderson et al. (1990) found that Eq. (57) is valid for normal impact velocities < 3 km/s (i.e. the onset of projectile fragmentation occurs at 3 km/s). Complete break-up and melting of projectile fragments occurs for velocities > 7 km/s (Eq. (55)/(56)).

The magnitude of shock pressures induced at impact are dependent on the impacting materials' density, bulk sound speeds, and particle velocity-shock velocity relationships. Thus, for impact of Al-projectiles on CFRP it is expected that the transition velocities for the onset of projectile fragmentation and full melt conditions will be different than those for Al-on-Al impact. To determine the transition velocities for Al-on-CFRP impact, a 1D shock-Hugoniot analysis is performed using basic shockwave theory for dissimilar materials (Anderson, 1987). The Hugoniot pressures generated in the projectile and target material can be approximated by solving the Rankine-Hugoniot jump conditions using linear particle velocity-shock velocity relationships for the impacting materials. Machens et al. (2005) defined the U_s-u_p relationship of a multidirectional CFRP from flyer plate impact tests as:

$$U_s(u_p) = 1763 + 1.93 \cdot u_p \tag{58}$$

The U_s-u_p relationship for Aluminium was determined by Schäfer (2001):

$$U_s(u_p) = 5300 + 0.94 \cdot u_p \tag{59}$$

Using these relations, the shock Hugoniot curves for the impact of Al-projectiles on Al- and CFRP targets can be calculated. It is shown in Figure 3-12 that the Hugoniot pressures achieved in Al-CFRP impacts are considerably lower than for Al-Al impacts at the same impact velocity. Assuming that the onset of fragmentation for an Al-projectile during impact on a thin CFRP plate occurs at the same shock pressures as for an Al-projectile impacting a thin Al-bumper, the spall threshold impact velocity for the case of Al-CFRP impacts is calculated as 4.2 km/s. The same assumption is used in determining the transition velocity from the shatter-hypervelocity regime, for which an impact velocity of 8.4 km/s is determined.

3.3 Ballistic Limit Impact Test Program

A ballistic limit equation for CFRP/Al HC SP structures must be general to allow application across a large range of configurations with different properties, including constituent mechanical properties, facesheet layups, facesheet and HC cell wall thicknesses, HC cell size, etc. As such, for the ballistic limit test program, panels were selected for both their relevance to satellite application and to provide a wide range of different configurations.

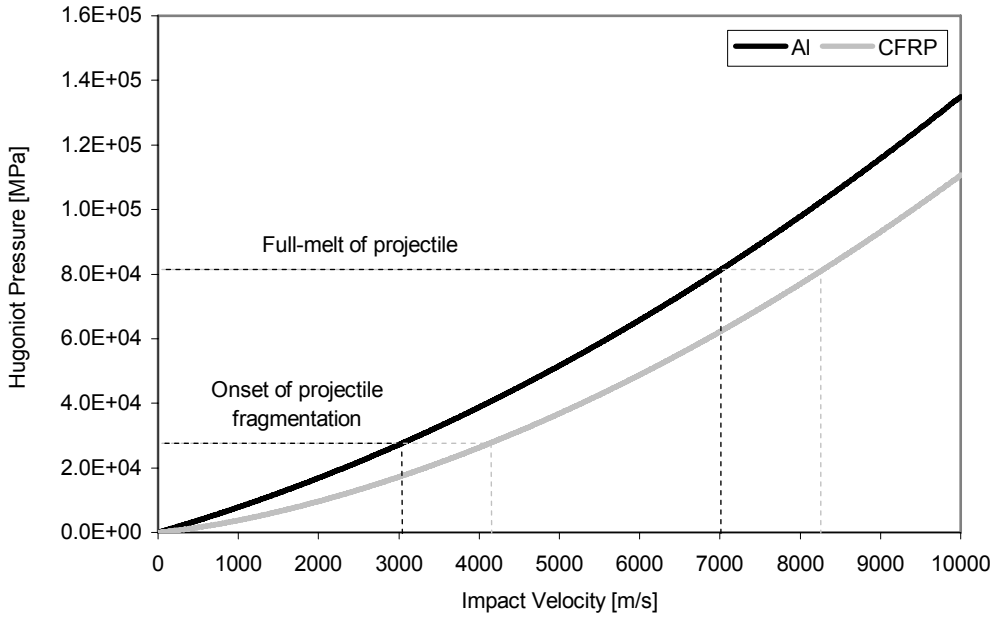

Figure 3-12 Shock Hugoniot curves for Al-projectile impact on Al and CFRP targets. ρ_{Al} = 2.7 g/cm², ρ_{CFRP} = 1.55 g/cm².

Three different CFRP HC SP structures were available from the RADARSAT2 satellite: shear panels, cone panels, and +/-Z platforms. These panels were designated RAD1, RAD2, and RAD3 respectively (shown in Figure 3-13). Additionally, structure panels from the GOCE (GOCE), BEPPO/SAX (SAX), and Herschel-Planck (H/P) satellites were used in the experimental program.

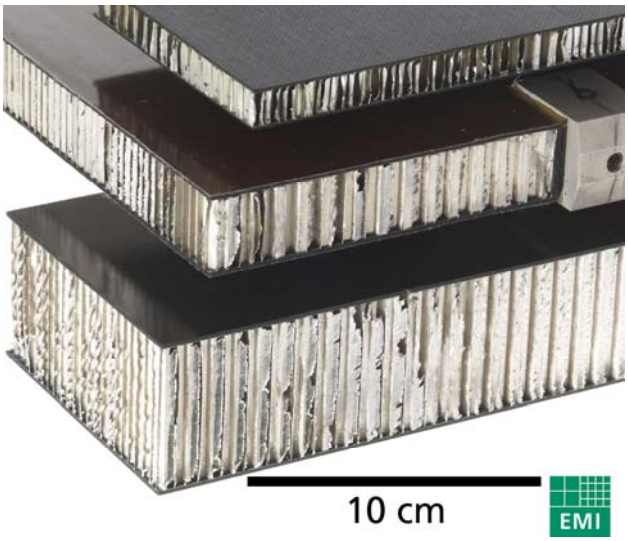

Figure 3-13 RADARSAT2 CFRP/Al HC sandwich panel structures tested in the BL experimental program (from top to bottom: RAD3, RAD2, RAD1).

An overview of the sandwich panel structures is given in Table 3-1 (see Appendix B for a full description).

Table 3-1 Overview of the sandwich panel structures used in the ballistic limit impact test program.

CFRP HC SP	*Facesheet thickness (mm)*	*Honeycomb core thickness (mm)*	*Areal weight (g/cm²)*
RAD1	1.13	50.8	0.7017
RAD2	1.25	25.4	0.5847
RAD3	1.25	12.7	0.4217
GOCE	2.0	11.0	0.7807
SAX	0.75	31.5	0.4405
H/P	0.4	20	0.2300

The six panels tested covered a wide range of sandwich panel configuration types, as shown in Figure 3-14. The GOCE and H/P panels represented realistic extremes for sandwich panel facesheet thicknesses used onboard satellites, while the RAD1 and RAD3 panels provided a wide range of honeycomb core thicknesses. The HC core used in all sandwich panels was of Al5056 with a cell length of 3/16" and a foil thickness of 0.001" (H/P HC foil thickness 0.0007").

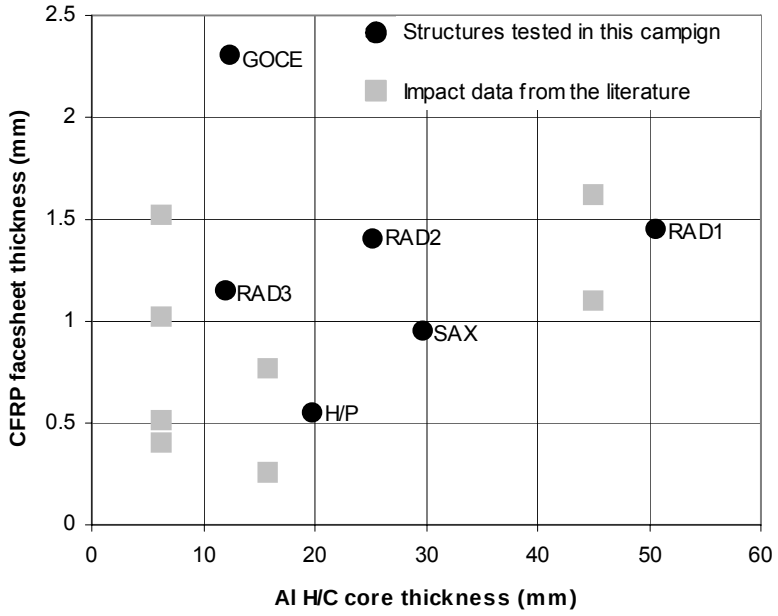

Figure 3-14 Distribution of CFRP facesheet and Al HC core thicknesses of the BL test samples together with structures for which existing impact data is available.

Precise measurement of the actual thicknesses of the sandwich panel structures provided the averaged values listed in Table 3-2. The measurements deviated up to +20% from the nominal values for the facesheet thicknesses. Measured thicknesses were used in the analysis of test results.

Table 3-2 Average measured thicknesses of the test sandwich panels.

CFRP HC SP	*Front face-sheet [mm]*	*Rear face-sheet [mm]*	*Honeycomb core [mm]*
RAD1	1.45	1.45	50.6
RAD2	1.40	1.40	25.3
RAD3	1.15	1.15	12.1
GOCE	2.30	2.30	12.5
SAX	0.95	0.95	29.7
H/P	0.55	0.55	19.9

3.3.1 Target Setup

The CFRP/Al HC sandwich panels were fixed with removable adhesive to an aluminium frame holder which was connected via threaded rods to a 1.5mm thick Al7075 witness plate (WP), as shown in Figure 3-15. The WP is used to capture ejecta fragments following perforation of the sandwich panel. For this experimental program the offset and thickness of the witness plate were selected based on results of a literature survey to best represent the lid of an electronics box.

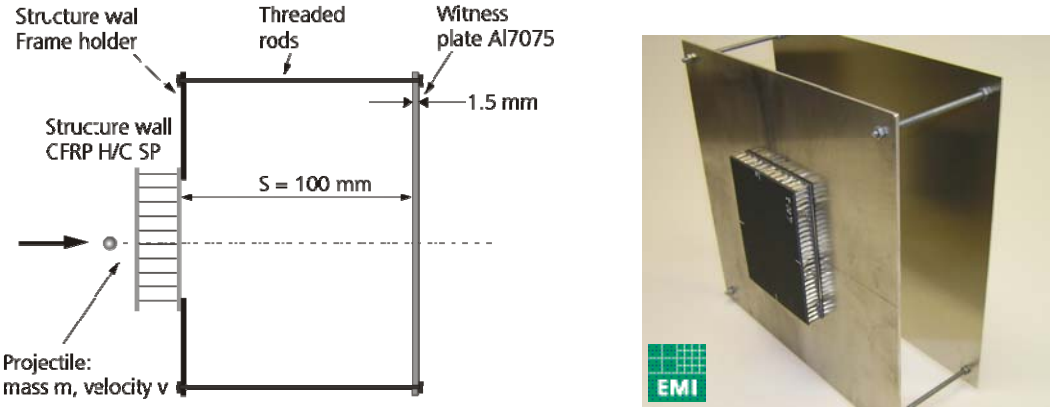

Figure 3-15 Sandwich panel target set-up.

3.3.2 Definition of Failure

The test results were defined as "perforated" (P), "detached spall" (DSP), or "no detached spall" (NSP). A perforated sample showed a clear, measurable hole in the sandwich panel rear facesheet. Detached spall refers to the case in which material was spalled from the rear facesheet of the sandwich panel or rear side of the witness plate yet no clear perforation hole exists. No detached spall represents no visible damage on the target rear side. Examples of the appearance of spalled and perforated panels are shown in Figure 3-16.

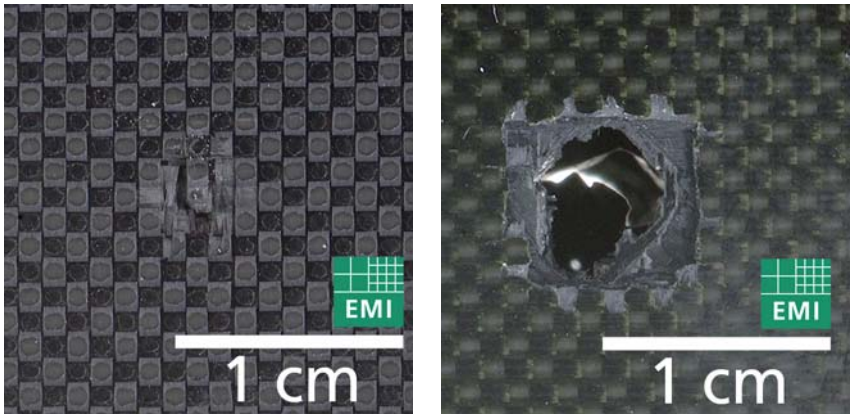

Figure 3-16 Photos showing a "detached spall" (left) and "perforated" result (right).

3.3.3 Test Results

The impact conditions and results of the ballistic limit tests are provided in Table 3-3 (SP + WP impact tests) and Table 3-4 (stand alone SP impact tests). Detailed damage measurements are given in Appendix C.

Table 3-3 Ballistic limit test results of CFRP/Al HC sandwich panels with witness plate.

Panel	*EMI no.*	*v* *(km/s)*	*α* *(°)*	d_p *(mm)*	m_p *(mg)*	E_k *(J)*	*Result* *SP*	*Result* *WP*
RAD1	S-4671	2.6	0	4.0	87.5	296	P	P
	S-4672	3.57	0	4.0	87.1	555	P	P
	S-4673	6.47	0	4.0	86.5	1810	P	P
	S-4616	6.99	0	4.0	87.2	2131	P	P
	S-4682	7.75	0	4.0	86.9	2610	P	NP
	S-4617	6.91	45	4.0	87.5	2089	P	NP
	S-4618	6.85	45	5.0	176	4129	P	NP
	S-4695	6.45	0	4.0	87.7	1824	P	P
	S-4694	6.53	0	4.0	86.8	1851	P	P
RAD3	S-4610	6.73	0	3.0	37.1	840	P	DSP
	S-4611	6.72	0	4.0	87.5	1976	P	P
GOCE	S-4693	4.13	0	4.0	87.3	745	P	NP
	S-4692	6.40	0	4.0	87.4	1790	P	DSP
SAX	S-4621	6.92	0	4.0	87.4	2093	P	P
	S-4622	6.64	45	4.0	86.7	1911	P	NP

3.3.4 Analysis of Impact Test Results

3.3.4.1 General Classification of Damage in CFRP/Al HC SPs

Generally, the damage in CFRP produced by hypervelocity impact is predominantly brittle fibre breakage, matrix breakage and layer delamination. For the sandwich panel front facesheet the impact crater or perforation hole is, for normal impacts, roughly circular, showing fractured fibre strands along the crater edge (shown in Figure 3-17). Typically, in the impact vicinity, the surface layer of the laminate is spalled off or completely delaminated. Severe debonding of the remaining composite plies is observed. Cracks and surface spallations are strongly influenced by the type surface ply type (i.e. u.d. or fabric) and generally extend along the fibre direction of the surface ply.

Table 3-4 Ballistic limit test results of CFRP/Al HC sandwich panels.

Panel	*EMI no.*	*v (km/s)*	*α (°)*	*d_p (mm)*	*m_p (mg)*	*E_k (J)*	*Result*
RAD1	B-107	2.02	0	1.25	2.9	2.9	NSP
	B-106	2.36	0	1.0	1.3	1.8	DSP
	B-164	3.13	0	1.5	5.61	27	P
	B-119	6.24	0	1.0	1.2	20	P
	B-117	6.27	0	1.0	1.2	24	P
	S-4577	5.72	0	1.5	5.4	88	P
	S-4578	5.72	0	1.5	5.4	88	P
	B-108	6.27	0	1.5	5.6	110	P
	B-161	4.27	45	1.0	1.52	14	NSP
	B-167	3.39	45	1.25	2.87	17	NSP
	S-4579	5.87	45	1.5	5.3	91	NSP
	S-4580	6.12	45	2.0	11.8	221	DSP
	S-4583	6.07	60	2.0	12	221	P
	S-4582	6.52	60	2.5	21	446	P
	S-4581	6.23	60	3.0	37.2	722	P
RAD 2	B-149	5.93	0	1.0	1.6	28	NSP
	B-155	6.26	0	1.25	2.88	56	P
	S-4612	6.62	0	2.0	11.9	262	P
	B-150	5.96	45	1.0	1.56	28	NSP
	S-4613	5.48	45	1.5	5.09	97	P
RAD3	B-105	2.82	0	1.0	1.3	2.5	P
	B-139	3.36	0	1.0	1.51	8.5	P
	B-127	5.88	0	0.50	0.4	6.9	NSP
	B-131	5.88	0	0.50	0.4	6.9	NSP
	B-132	6.05	0	0.70	0.45	8.2	NSP
	B-154	5.94	0	0.80	0.31	16	DSP
	B-147	5.87	0	1.0	1.68	29	P
	B-162	3.42	45	1.0	1.51	8.8	NSP
	B-140	3.33	45	1.25	2.92	16	DSP
	B-156	6.45	45	0.80	1.46	30	NSP
	B-133	6.18	45	1.0	1.44	28	DSP
	B-160	6.62	60	1.0	2.05	45	NSP
	B-134	5.77	60	1.55	5.48	91	P
	B-138	2.96	0	0.076	0.55	2.4	NP
GOCE	B-146	5.98	0	1.0	1.57	28	NSP
	B-152	6.26	0	1.5	5.85	115	P
	B-145	5.80	45	1.0	1.52	26	NSP
SAX	B-153	5.94	0	0.80	0.91	16	NSP
	B-148	5.96	0	1.0	1.52	27	P
H/P	B-176	5.93	0	1.0	1.73	30	P

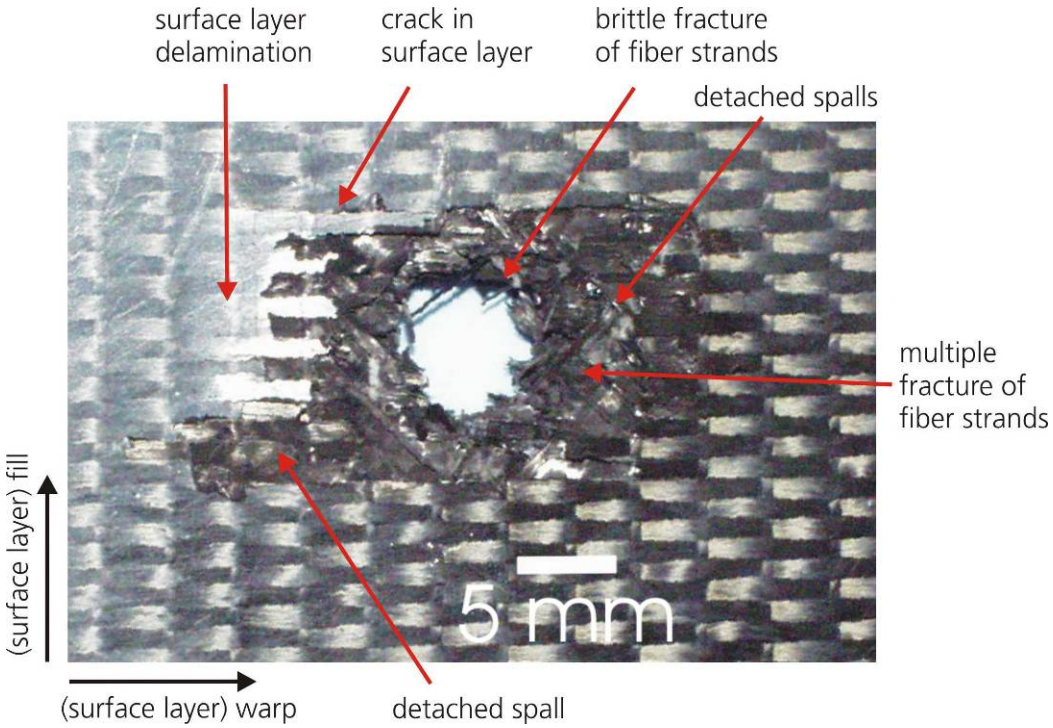

Figure 3-17 Damage to CFRP caused by impact of an Al-sphere at hypervelocity (EMI Exp. no. 4277: 3 mm Al-sphere at 4.55 km/s).

The principal damages observed in the rear facesheet of a composite sandwich panel are generally similar to that seen in the front facesheet. In the event of projectile fragmentation, the impact is spread over a larger area, producing more extensive delamination and cracking. The characteristics of the perforation hole depend on the degree of perforation. Initially, as the structure ballistic limit is exceeded, the shape and location of the perforation hole are strongly influenced by the impact location of the projectile relative to the honeycomb core. For projectiles smaller than the honeycomb core cells this influence is particularly strong. At low velocities the impact location can significantly affect the protective capability of the sandwich panel, while at high velocities (> projectile fragmentation velocity) the dispersion of ejecta following perforation of the complete sandwich panel is affected. In Figure 3-18 the dispersion of fragment ejecta following perforation of a CFRP/Al HC SP is compared for three different projectile impact locations (relative to the honeycomb core cells). At the impact velocity investigated (6.3 km/s), the impact location is shown to play a significant role.

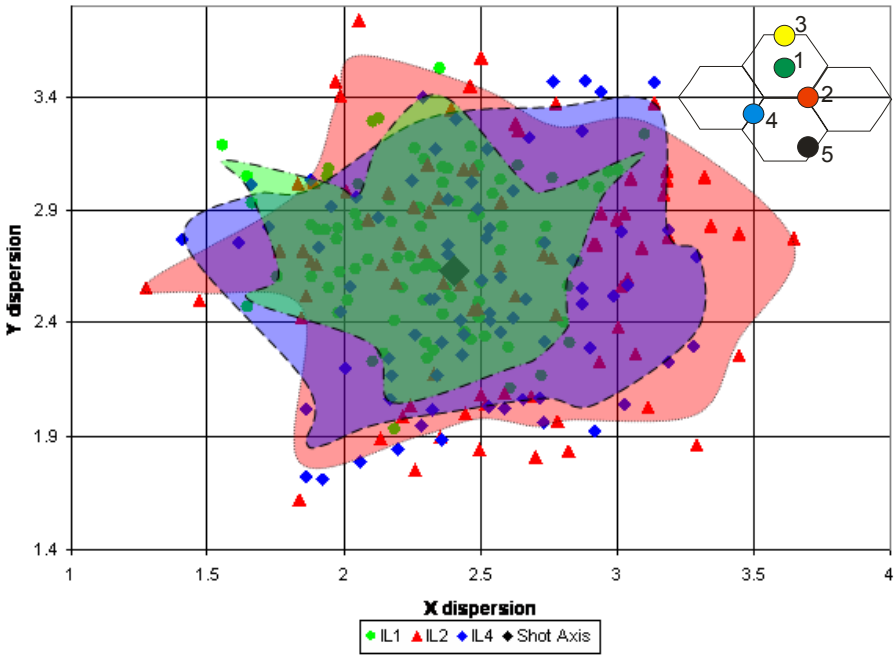

Figure 3-18 Ejecta dispersion 100 mm behind the rear facesheet of a CFRP/Al HC SP following impact of a 1.1 mm Al-sphere at 6.3 km/s.

Three different honeycomb cell damage modes can be defined: deformation and crushing, perforation, and complete disintegration. For normal impact, the damaged honeycomb volume is typically tubular or conical in shape depending on impact velocity and projectile lethality. Complete disintegration of the honeycomb cells takes place along the shot axis. As damage extends outwards, the honeycomb cells are perforated and deformed.

3.3.4.2 Impact Test Damage Discussion

To assess the effect of impact conditions and structure configuration a comparison of the impact damages can be made. In Figure 3-19 the damage caused to the RAD1 sandwich panel by normal impact of a 1.0 mm Al-sphere is shown for three impact velocities.

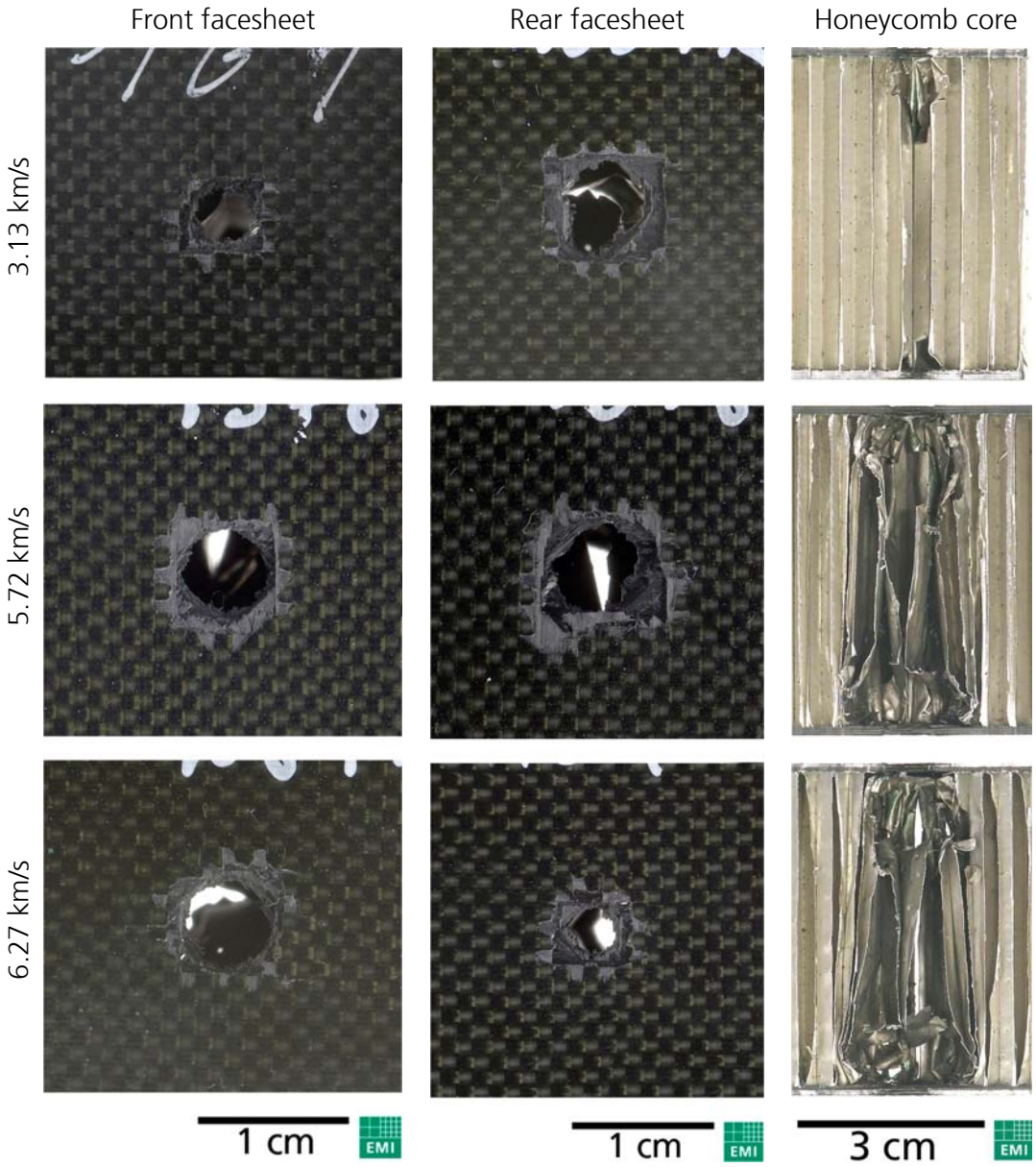

Figure 3-19 The effect of increasing impact velocity on damage caused by impact of a 1.0 mm Al-sphere impacting normally on the RAD1 sandwich panel (EMI exp. no. (top to bottom): 164, 4578, 108).

In Figure 3-19 it can be seen that the impact velocity has little effect on the front facesheet damage. At the lowest velocity the clear perforation hole is smaller than for the higher impact velocities. Surface spallation and shape of the perforation hole are similar for the three samples. On the rear facesheet there is also minimal variation of the observable damage. All three cases show a clear, circular perforation hole. At the highest velocity (6.27 km/s) the hole diameter is smaller than the lower velocity

tests. In all three impact tests a roughly square spallation zone is observable around the rear facesheet perforation hole. The most notable difference between the three impact samples can be seen in the sectioned honeycomb cores. At low velocities the impact damage is minimal, suggesting little or no fragment expansion following perforation of the front facesheet. As the impact velocity increases, the honeycomb core damage becomes more significant. The honeycomb core damage cone is roughly tubular with a slight increase in cross section towards the rear facesheet. Disintegration and crushing of the honeycomb core cells can be clearly observed.

In Figure 3-20 the effect of impact velocity on damage to the RAD1 sandwich panel was further investigated, in this instance considering impact of a much more destructive 4.0 mm Al-sphere at normal incidence. In the front facesheet it can again be seen that the clear perforation hole at the lowest velocity is smaller than the other impact tests. There appears to be little sensitivity of the clear hole for impact velocities above 6.47 km/s. The three higher impact velocities tested show little to no surface spallation around the clear perforation hole. This is in contrast to the rectangular spallation seen in the 3.57 km/s impact experiment. Damage to the rear facesheet is shown to vary significantly. At the lowest impact velocity the perforation hole is of an unusual shape and is seen to partially line up with the front facesheet hole. For increasing impact velocities (6.47, 6.99 and 7.75 km/s) the shape of the perforation hole remains highly irregular, however the perforation is more aligned with the front facesheet hole. Along the edges of the irregular rear facesheet perforation holes, small circular indentations are observed. This could suggest impact of individual projectile fragments. At the highest two impact velocities significant rear facesheet surface spallation is observed. For damage to the honeycomb core, it is apparent that an increase in impact velocity results in a larger expansion of honeycomb core damage. In all impact experiments the honeycomb core damage zone is roughly tubular in shape, and clear disintegration and crushing of the honeycomb cells can be observed. At higher impact velocities (> 6.47 km/s) partial detachment of the honeycomb core from the front facesheet is shown.

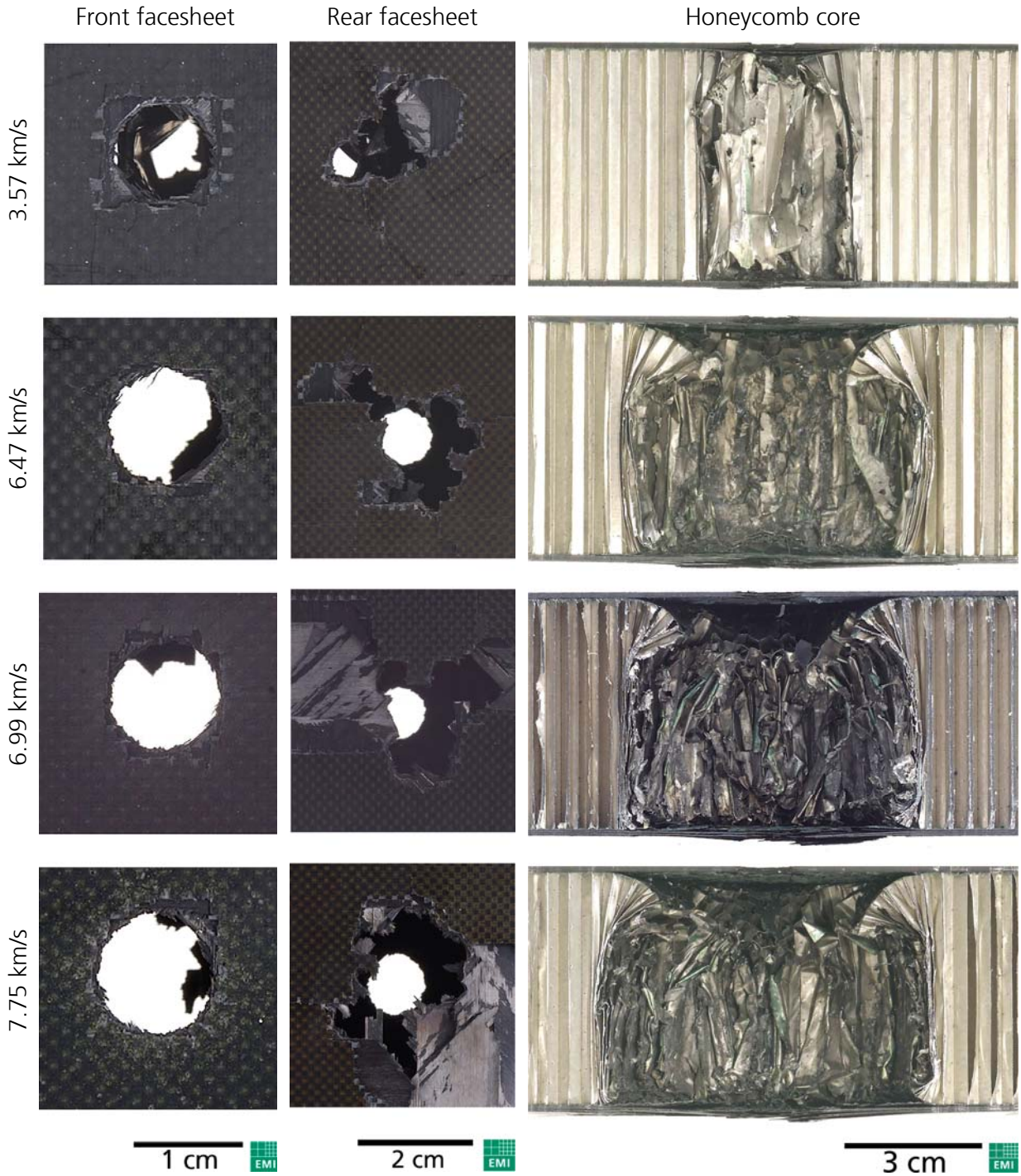

Figure 3-20 The effect of increasing impact velocity on damage caused by impact of a 4.0 mm Al-sphere impacting normally on the RAD1 sandwich panel (EMI exp. no. (top to bottom): 4672, 4673, 4616, 4682).

In Figure 3-21 the effect of projectile diameter on impact-induced damage is shown for the RAD3 sandwich panel. All projectiles impacted at normal incidence with a velocity of 6.30 ± 0.43 km/s. In the front facesheet, a clear relationship between projectile diameter and perforation hole diameter can be observed. It can be noted from the rear facesheet damages that the SP critical projectile diameter is between 0.7 and 0.8 mm at these impact conditions. As the projectile diameter increases, so does the rear facesheet damage. Initially the onset of perforation is achieved, followed by an increasing clear perforation hole diameter. In all cases of perforation, the rear facesheet hole is in line directly with the front facesheet perforation hole. Damage to the witness plate is caused by fragment ejection from the sandwich panel rear facesheet. Thus, damage to the witness plate only occurs for projectiles larger than 1.0 mm in diameter. Initially, a small amount of black dust is seen on the witness plate. These dust deposits are charred carbon fibres. As the projectile diameter increases, so does the amount of ejecta from the sandwich panel and as such, so does the amount of carbon fibre deposits on the witness plate. In impact of a 4.0 mm Al-sphere the witness plate is perforated in a number of places. These perforation holes are expected to be caused by the impact of individual projectile fragments.

In Figure 3-22 the effect of impact angle on damage to the RAD1 sandwich panel is shown. In the front facesheet the clear perforation hole is seen to distend with increasing impact angle. In the rear facesheet the diameter of the perforation hole decreases with increasing impact angle, however direct comparison is difficult as the 60° impact test was performed with a smaller projectile (3.0 mm compared to 4.0 mm for the 0° and 45° tests). The shape of the honeycomb core damage cone is shown to be dependent on the impact angle: for oblique impact, the normal damage tube extends in the direction of the projectile velocity vector. It is shown clearly in the 60° impact test that following perforation of the front facesheet, the fragment cloud propagates both normal to the facesheet surface and along the initial projectile velocity vector.

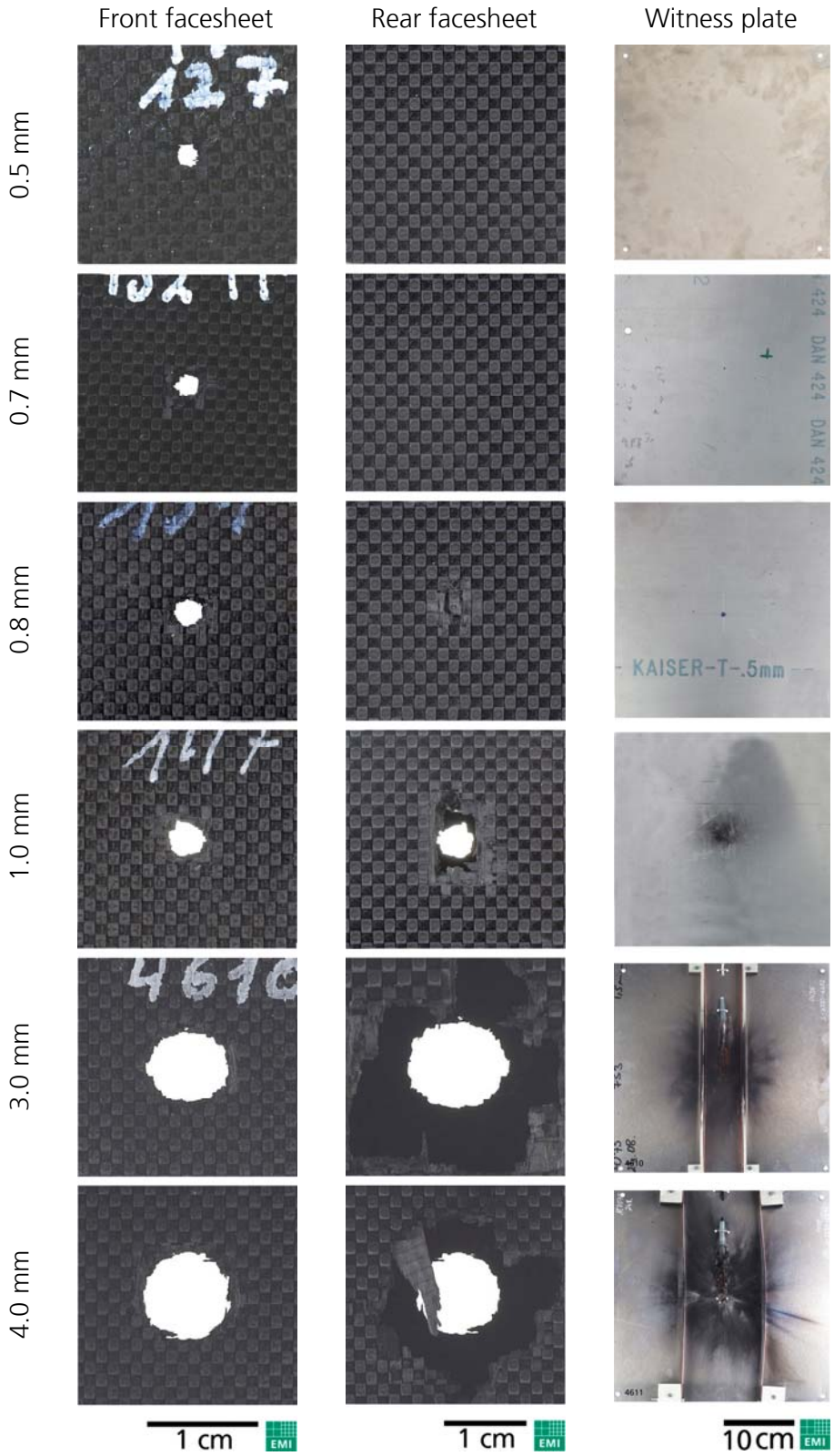

Figure 3-21 The effect of increasing projectile diameter on hypervelocity impact-induced damage in the RAD3 sandwich panel (EMI exp. no. (top to bottom): 127, 132, 154, 147, 4610, 4611) (impact velocity ~6 km/s).

Figure 3-22 The effect of impact angle on damage caused by impact of an Al-sphere at ~6.5 km/s on the RAD1 sandwich panel.
NOTE: 4 mm Al-sphere used in EMI exp. 4616 and 4617, 3 mm Al-sphere used in 4581

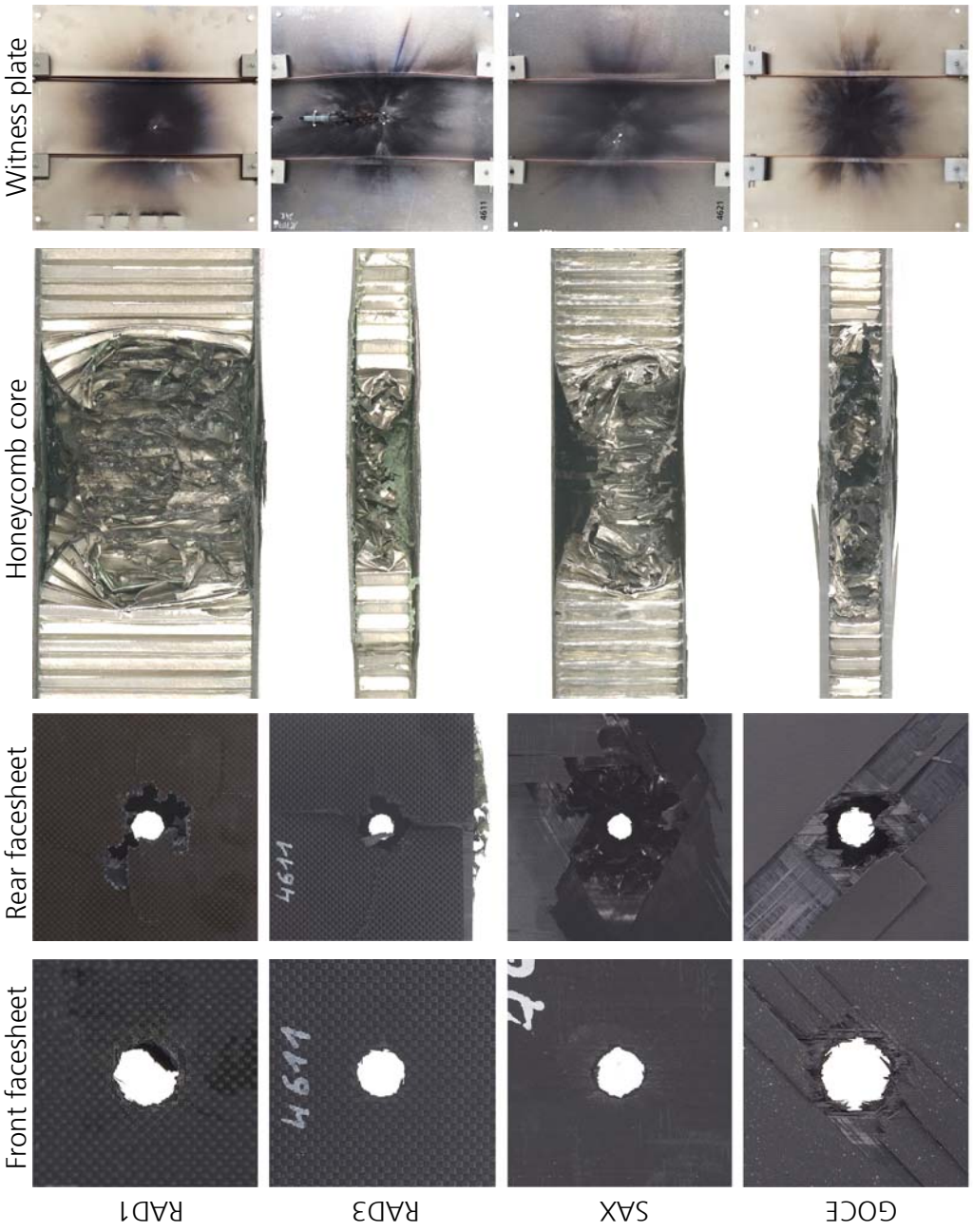

Figure 3-23 Comparison of damages caused by normal impact of a 4 mm Al-sphere at ~6.66 km/s on different CFRP/Al HC SPs.

The effect of configuration on damage caused by impact of a 4 mm Al-sphere at 6.66 ± 0.26 km/s is shown for the RAD1, RAD3, GOCE and SAX sandwich panels in Figure 3-23. At this impact velocity the material properties have little effect. All four SP's considered are clearly perforated. The GOCE panel shows a large amount of surface spallation on both the front and rear facesheets. The SAX panel shows the most significant rear facesheet damage, while the RAD1 panel shows the least. The lateral extension of HC core damage is similar, and appears to be independent of honeycomb core thickness. Carbon fibre deposits of the witness plates are also similar for the different panels considered, however the RAD1 WP shows a single small perforation hole, while the RAD3 and SAX panel show multiple perforation holes. The GOCE WP is not perforated.

A series of high speed framing camera (HSFC) images are shown in Figure 3-24 for impact of a 4 mm Al-sphere on the RAD1, RAD3, GOCE and SAX panels. Image trigger times are listed in Table 3-5.

Table 3-5 High speed shadowgraph trigger times.

Structure	*Test no.*	*Image delay time (after impact) (μs)*				
RAD1	4673	10	20	30	50	200
RAD3	4611	5	10	20	50	120
GOCE	4692	0	10	30	80	200
SAX	4621	5	10	20	40	320

The images are not all taken with the same delay after impact as a result of changes to the facility set-up and triggering of the HSFC; however they can be used to give a good indication of the penetration and fragment ejection process, and the role that structure type plays. Severe disintegration of the sandwich panel rear facesheet can be observed, along with perforation of the witness plate well above the shot axis in the SAX image series. This suggests that damage within the sandwich panel is severe, and fragment cloud ejecta is not symmetrically dispersed.

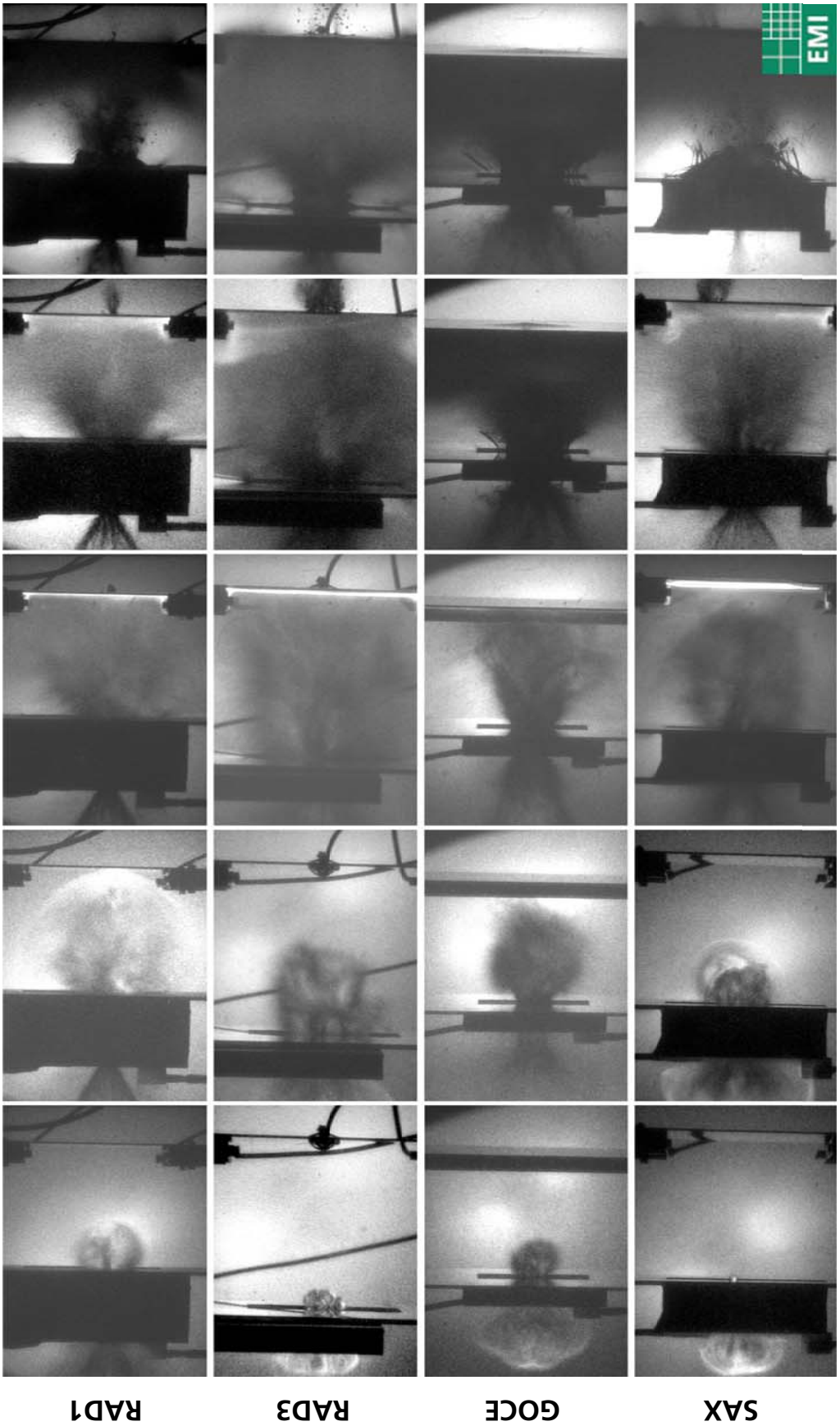

Figure 3-24 The effect of structure type on penetration and fragment expansion caused by impact of a 4 mm Al-sphere at hypervelocity (High Speed Framing Camera images from EMI exp. no. (top to bottom): 4673, 4611, 4692, 4621).

3.3.5 Ballistic Protection Capability

The impact tests on stand-alone CFRP HC SP provided ballistic limit information at selected velocities and impact angles for the RAD1, RAD2, RAD3, GOCE, and SAX sandwich panels. In Table 3-6 the critical projectile diameter for these structures has been summarised in terms of impact angle and velocity regime.

Table 3-6 Critical diameter ranges for CFRP HC SP.

Structure	α *(°)*	*Velocity Regime (LV / HV)*	d_c *limits*
RAD1	0	LV	ca. 1.0[+]
		HV	< 1.0
	45	HV	1.50 – 2.0
	60	HV	< 2.0
RAD2	0	HV	1.0 – 1.25
	45	HV	1.0 – 1.5
RAD3	0	HV	0.70 – 0.80
		LV	0.71 – 1.0
	45	LV	1.0 – 1.25
		HV	0.80 – 1.0*
	60	HV	1.0 – 1.55
GOCE	0	HV	1.0 – 1.5
	45	HV	> 1.0
SAX	0	HV	0.80 – 1.0

NOTES:
Velocity regime: LV (v < 3 km/s), HV (v > 3km/s)
Critical diameter defined for projectile which results in ANY contamination to the satellite interior (i.e. detached spallation and beyond).
[+] One test (1.25 mm projectile at 1.40 km/s) caused no spallation, however another test (1.0 mm projectile at 1.65 km/s) caused detached spall.
* A no-spall result was also obtained for 1.0 mm projectile diameter impact. However this test was performed at a reduced kinetic energy.

In order to allow a quantitative comparison between the protection performances offered by the different CFRP HC SPs tested, the "normalized ballistic protection capability" (NBPC) is defined as:

$$NBPC = \frac{d_c}{AW} \tag{60}$$

This factor is the ratio of critical projectile diameter divided by the areal weight of the sample, and hence is an engineering global measure of the protection offered per areal weight of the CFRP HC SP. In Figure 3-25 the

NBPC of five structure panels are shown for normal impact at velocities exceeding 3 km/s. The H/P panel is not included in Figure 3-25 as the ballistic limits of the panel were not determined in the experimental program. The NBPC is presented as a range of values for each configuration given that the amount of impact tests performed during the test campaign does not allow exact determination of the failure criterion thresholds. It can be seen that of the five configurations considered, the NBPC of four structures is relatively constant. The RAD1 structure has a clearly lower normalised protective capability. The primary difference of the RAD1 structure to the other four panels is the thick honeycomb core (50.8 mm).

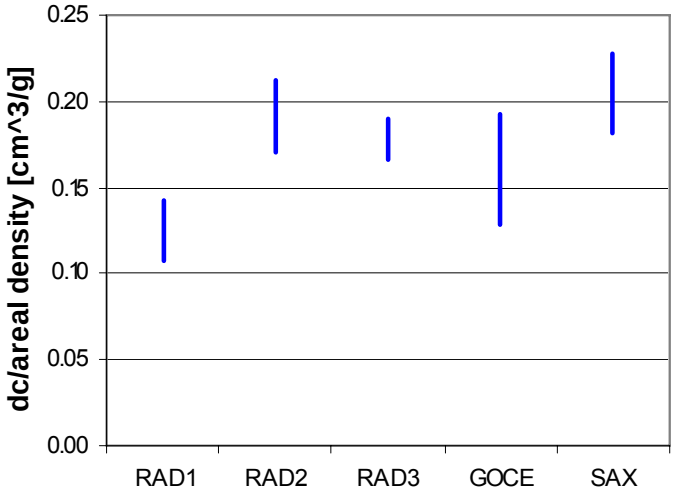

Figure 3-25 Normalized Ballistic Protection Capability (NBPC) of the tested CFRP HC SP (impact angle: 0°, range of impact velocities: 3 ... 7 km/s).

3.4 The New Ballistic Limit Equation

Ballistic limit equations are used to predict the critical projectile diameter (d_c) which, at a given impact velocity and angle, will perforate the structure under consideration. The new BLE, derived herein, can be applied to calculate the critical projectile diameter for both standalone CFRP/Al HC sandwich panels (d_c^{SP}) and CFRP/Al HC SP structures with a thin Al plate placed behind it at a standoff (d_c^{SP+WP}). The principle set-up is shown in Figure 3-26.

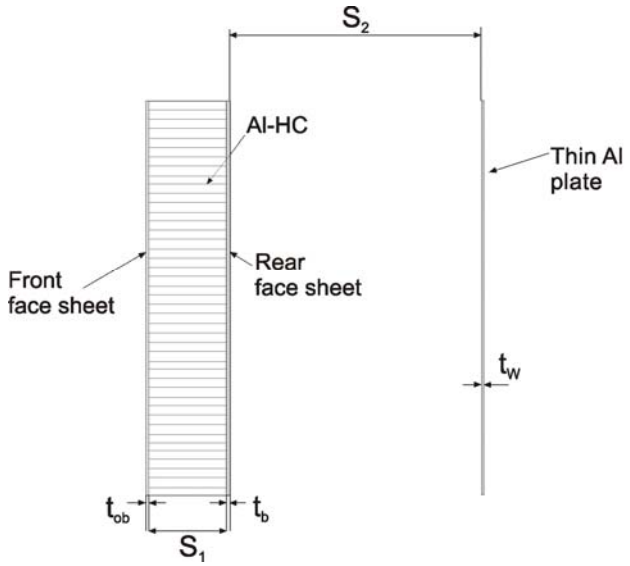

Figure 3-26 Principle set-up for application of the new BLE.

The new equation is based on the ESA Triple Wall equation (ETW) from Drolshagen and Borde (1992). The ETW equation does not define a limit angle at which increasing impact obliquity does not further affect the critical projectile diameter, unlike the Christiansen/Cour-Palais equation (Christiansen, 1993) which assumes that at angles above 65° the primary source of rear wall damage are fragments of the front facesheet. The limit angle of 65° will be adopted for the new equation. Different forms of the equation are applied for the ballistic regime ($v_n \leq 4.2$ km/s) and hypervelocity regime ($v_n \geq 8.4$ km/s). A linear interpolation is used in the mid-range velocities.

The new BLE is given as:

Ballistic regime ($v_n \leq 4.2$ km/s):

$$d_c(v) = \left[\frac{\left(t_w^{1/2} + t_b\right)}{K_{3S}} \cdot \left(\frac{\sigma_y}{40} \right)^{1/2} + t_{ob} \over 0.6 \cdot (\cos\theta)^{4/3} \cdot \rho_p^{1/2} \cdot v^{2/3} \right]^{18/19} \tag{61}$$

Transition/shatter regime ($4.2 < v_n < 8.4$ km/s):

$$d_c(v) = d_c(v_1) + \frac{d_c(v_2) - d_c(v_1)}{v_2 - v_1} \cdot (v - v_1) \tag{62}$$

$$v_1 = \frac{4.2\ km/s}{\cos\theta} \qquad v_2 = \frac{8.4\ km/s}{\cos\theta}$$

Hypervelocity regime ($v_n \geq 8.4$ km/s):

$$d_c(v) = \frac{1.155 \cdot \left(S_1^{1/3} \cdot (t_b + t_w)^{2/3} + S_2^{1/3} \cdot t_w^{2/3}\right) \cdot \left(\frac{\sigma_y}{70}\right)^{1/3}}{K_{3D}^{2/3} \cdot \rho_p^{1/3} \cdot \rho_b^{1/9} \cdot v^{2/3} \cdot \cos\theta^{4/3}} \tag{63}$$

An overview of the constants and parameters for use with the equation is given in Table 3-7.

Table 3-7 Ballistic limit equation parameter list for application with CFRP/Al HC SPs.

Par.	*Description*	*Suggested value*
ρ	Density of reference Al-alloy (Al 2024 T81)	2.78 g/cm^3
σ	Yield strength of reference alloy (Al 2024 T81)	59.5 ksi (410.3 MPa)
t_{ob}	Front facesheet thickness	$t_{ob,CFRP} \cdot \frac{\rho_{CFRP}}{2.78} + \frac{\rho_{AD,MLI}}{2.78}$
t_b	Rear facesheet thickness	$t_{b,CFRP} \cdot \frac{\rho_{CFRP}}{2.78}$
S_1	Spacing between facesheets	t_{HC}
K3S	Ballistic fit factor	1.1
K3D	Hypervelocity fit factor	0.4

Several assumptions were made in derivation of the new equation. These are listed below.

1: The space-facing (front) facesheet of the sandwich panel, having a thickness of t_{ob} (index ob = "outer bumper"), is replaced by an aluminium plate having the same areal weight as the CFRP face-sheet. The same procedure is repeated for the inner face-sheet, having a thickness of t_b (index b = "bumper").

2: The effects on fragmentation and expansion of the projectile fragment cloud caused by the presence of the sandwich panel honeycomb core, having a thickness S_1, were ignored. The presence of the honeycomb core acts to restrict expansion of the debris cloud following penetration of the front facesheet by concentrating or channelling the debris within a finite number of cells. The effect of channelling on the protective capability of debris shielding remains inconclusive. For instance, Jex et al. (1970) found that in velocity regimes inducing solid fragmentation of the projectile, the honeycomb core increases the ballistic protective capability compared to a standard Whipple shield structure. This is achieved through secondary impacts of fragments on honeycomb cell walls which leads to further

fragmentation, overshadowing the detrimental effect of fragment channelling. Alternatively, Taylor (1999) introduced a ballistic limit equation for metallic sandwich panels which considered the channelling effect by decreasing the effective thickness of a Whipple shield rear wall by a factor of two (across all impact angles and velocities).

The honeycomb cores of the structures tested in this study all have, with the exception of the H/P closure panel, the same configuration (3/16" cell size, 0.001" foil thickness, Al5056 alloy). As such, the experimental data is insufficient to enable the effects of the honeycomb core properties, beyond core depth, to be characterized. Thus, the effect of the honeycomb core on the protection capability is taken into account by fit coefficients and the exponential in the impact angle term ($\cos\theta$).

3: The ballistic effect of multi-layer insulation (MLI) placed on top of the space-facing facesheet of the sandwich panel can be accounted for by increasing the effective aluminium facesheet thickness by an amount equal to the surface weight of the MLI. It should be noted that there were no impact tests performed on configurations with MLI in this study, hence the validity of this treatment method must still be proven through future testing.

4: The aluminium plate located behind the CFRP HC SP structure wall at a standoff of S_2 has a thickness of t_w (index w = "backwall"). In the ballistic velocity regime, S_2 does not need to be considered because it is assumed that the projectile does not fragment upon impact with the CFRP HC SP. This assumption is in line with that applied by Christiansen (1993) for the BLE of metallic Whipple Shields.

5: Given that the equation is applied to calculate the ballistic limit of two different structure types (CFRP HC SP and CFRP HC SP + WP), an important requirement for the equation is that of convergence. When either the thickness or standoff of the witness plate approaches zero, the predicted ballistic limit converges to the stand-alone CFRP HC SP result, i.e.:

$$d_c^{(SP+WP)}\left(v, t_{ob}, t_b, t_w, S_1, S_2\right) \xrightarrow{t_w \to 0} d_c^{(SP)}\left(v, t_{ob}, t_b, S_1\right)$$
and (64)
$$d_c^{(SP+WP)}\left(v, t_{ob}, t_b, t_w, S_1, S_2\right) \xrightarrow{S_2 \to 0} d_c^{(SP)}\left(v, t_{ob}, t_b + t_w, S_1\right)$$

A demonstration of the equation convergence can be made through manipulation of Eqs (61)-(63) for the case of no back wall, i.e. : (1) $t_w = 0$, and; $S_2 = 0$:

Ballistic regime ($v_n \leq 4.2$ km/s):

$$d_c(v) = \left[\frac{\frac{t_b}{K_{3S}} \cdot \left(\frac{\sigma_y}{40} \right)^{1/2} + t_{ob}}{0.6 \cdot (\cos\theta)^{4/3} \cdot \rho_p^{1/2} \cdot v^{2/3}} \right]^{18/19} \tag{65}$$

Transition/shatter regime ($4.2 < v_n < 8.4$ km/s):

$$d_c(v) = d_c(v_1) + \frac{d_c(v_2) - d_c(v_1)}{v_2 - v_1} \cdot (v - v_1) \tag{66}$$

$$v_1 = \frac{4.2\ km/s}{\cos\theta} \qquad v_2 = \frac{8.4\ km/s}{\cos\theta}$$

Hypervelocity regime ($v_n \geq 8.4$ km/s):

$$d_c(v) = \frac{1.155 \cdot \left(S_1^{1/3} \cdot t_b^{\ 2/3} \right) \cdot \left(\frac{\sigma_y}{70} \right)^{1/3}}{K_{3D}^{2/3} \cdot \rho_p^{1/3} \cdot \rho_b^{1/9} \cdot v^{2/3} \cdot \cos\theta^{4/3}} \tag{67}$$

6: Fitting of the equation to the experimental results is performed by modification of the following terms:

Fit parameter	*Description*
K3S	ESA TW fit factor (Ballistic regime)
K3D	ESA TW fit factor (Hypervelocity regime)
n	cosine term exponent (ballistic and hypervelocity regimes)

In addition to these parameters, additional terms are available for modification to fit the curve to any future experimental data. These terms are:

- Exponent and coefficient of the t_w term in the equation describing the BL in the ballistic regime;
- Exponent and coefficient of the t_w term in the equation describing the BL in the hypervelocity regime;
- Exponent and coefficient of the S_2 term in the equation describing the BL in the hypervelocity regime.

Due to a lack of variation of the witness plate thickness and witness plate standoff in the experiments, the coefficients and exponents used in the ESA Triple Wall equations were adopted here (with one exception: the exponent of the t_w-term in the BLE equation for the low velocity regime). Obviously, these coefficients can be adjusted pending the availability of corresponding impact test data.

7: The transition velocities are derived for projectile impact on a thin CFRP sheet. Thus, at velocities above the onset of projectile fragmentation the ballistic limit curve of the sandwich panel structure shows an increase in protective capability. When considering penetration of the thin Al-plate located behind the CFRP/Al HC SP, the projectile is shocked twice (sandwich panel front and rear facesheets) and therefore the fragmentation performance is expected to improve, i.e. higher fragmentation and melting at lower impact velocities (similar to the multi-shock shielding concept) (Cour-Palais & Crews, 1990).

In Figure 3-27 damage to Aluminium witness plates located behind the RAD1 panel are shown for impact of 4.0mm Al-spheres in the ballistic- and shatter velocity regimes. For an impact velocity of 3.57 km/s the witness plate shows multiple individual perforation holes and craters most likely caused by the impact of projectile fragments. A similar damage profile was also noted on the witness plate used in Exp. 4671 (v = 2.6 km/s). This clearly demonstrates the benefits of multi-shock shielding concepts.

For impact at 7.75 km/s craters most likely caused by the impact of intact projectile fragments can be seen on the witness plate shown in Figure 3-27. Although the shatter-hypervelocity transition velocity represents the point at which impact pressures are sufficient to induce complete melting of the projectile, the presence of some solid fragments is common. Therefore it is difficult to determine if multiple shocking of the projectile during impact on the sandwich panel front- and rear facesheet reduces the impact velocity required to obtain the full melt condition.

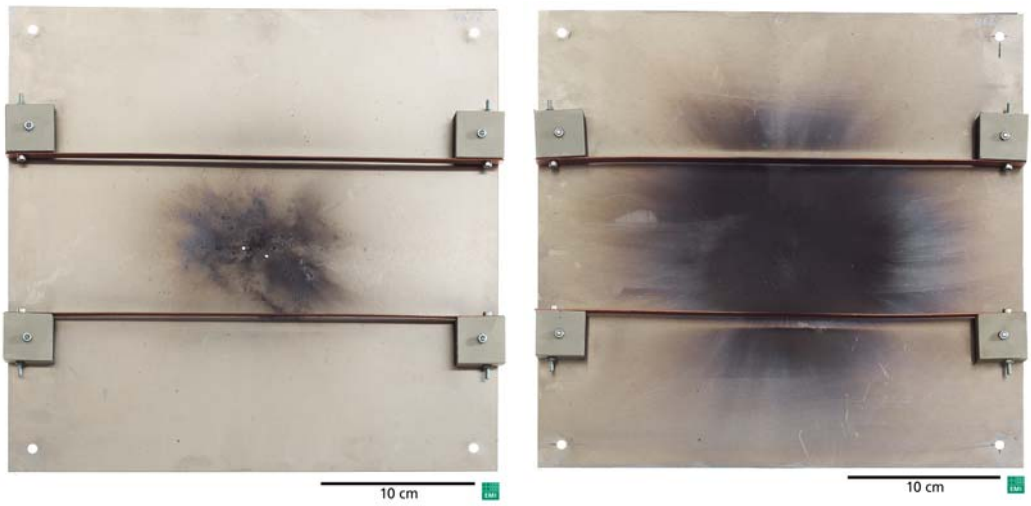

Figure 3-27 Witness plate damage. a) EMI No. S-4672, normal impact (0°) of a 4.0mm projectile at 3.57 km/s; b) EMI No. S-4682, normal impact (0°) of a 4.0mm projectile at 7.75 km/s.

The derivation of an analytical solution to determine the increase in internal pressure at each shock interface was not possible. Additionally, as all impact tests performed to assess the ballistic limit of the thin Al-plate show impact of solid projectile fragments, the transition limits cannot be bounded. As such, the transition velocities determined for the CFRP SP are used for prediction of the thin Al-plate located behind the SP.

8: Prediction of structural ballistic limit in the hypervelocity regime is based on the concept of velocity scaling. That is, the ballistic limit of a given structure scales with constant impactor kinetic energy (i.e. $t_b/t_w \propto KE^{1/3}$). This is consistent with the NASA practice for conservatively extrapolating beyond hypervelocity impact test conditions (Frost, 1970). This method presumes that the debris cloud will contain solid particles in a significant fraction of real in-orbit impacts at velocities above the complete melt condition (i.e. 8.4 km/s for Al-on-CFRP). Thus this equation provides conservative predictions for impact conditions above 8.4 km/s and is applicable for all in-orbit impact conditions.

All other assumptions and coefficients were adopted from the ESA Triple Wall equation.

3.4.1 Application of the new BLE for CFRP/Al HC Satellite Structures

The accuracy of the new equation can be assessed by evaluating its predictive performance across the entire range of composite structures and impact conditions investigated in the experimental program. The test results are plotted in Figure 3-28 in terms of the projectile diameter (d_p) to predicted critical diameter (d_c) ratio. Results above unity represent predicted failure and results below one represent a "no detached spall" prediction. It is shown that for 44 out of the 55 experiments, which covered 10 different structures, 3 impact angles, and an impact velocity range of 2.02 – 7.75 km/s, the equation correctly predicted the result. This represents a success rate of 80%.

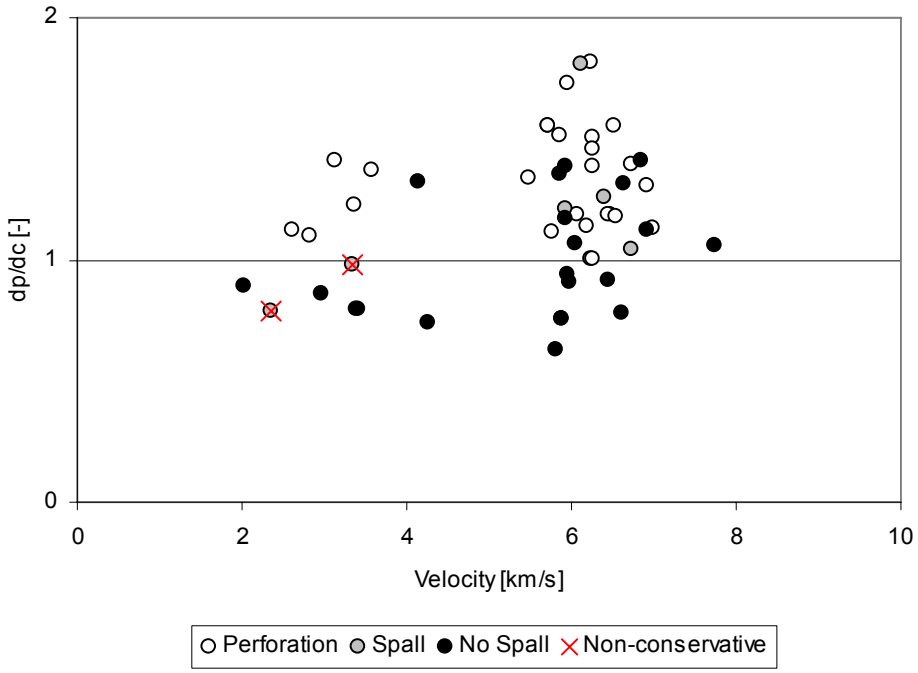

Figure 3-28 Comparison of predicted and actual experimental results.

The calculated Ballistic Limit Curves (BLCs) are plotted in Figure 3-29 for a selection of composite structures tested during the experimental campaign, which includes both standalone sandwich panels and those with witness plates. The impact experiment results are also shown in the figures. In all BLCs the three impact velocity regimes are clearly identifiable. The GOCE SP shows the least improvement in protective capability as a result of projectile fragmentation in the shatter regime due to a thin honeycomb core (11 mm). As expected, the curves generally show very good agreement with experimental data. In the RAD1 SP+WP

at 0° a slightly conservative result is predicted when the no detached spall result is located above the BLC. The RAD1 SP shows a non-conservative prediction at low velocity where a detached spallation result was obtained at conditions for which the new BLE predicted no detached spall. The effect of impact obliquity is realised in the curves by an offset of the impact regime transition velocities (e.g. RAD3 SP, 45°). The magnitude of the offset is determined by the cosine of the impact angle.

An overview of the predictive accuracy of the new BLE, organised by structure, is given in Table 3-8. The prediction accuracy is classified as:

- Good – experimental result is correctly predicted;
- Slightly conservative – No detached spall test result, perforation predicted. Ratio of experiment projectile diameter to predicted critical diameter ≤ 1.2 (i.e. prediction is ≤ 20% conservative);
- Very conservative – No detached spall test result, perforation predicted. Ratio of experiment projectile diameter to predicted critical diameter > 1.2 (i.e. prediction is > 20% conservative);
- Non-conservative – No detached spall predicted, detached spall in test.

Of the 55 experiments, 40 (73%) showed a "good" prediction, 5 experiments (9%) were predicted slightly conservatively, 8 experiments (15%) were predicted very conservatively, and 2 experiments (4%) were non-conservatively predicted. Although the new equation uses experimental data to adjust analytical expressions, it is not possible to adjust the empirical factors such that all experimental results are predicted correctly. The empirical factors are adjusted to ensure the equation provides the most accurate predictions for the widest range of CFRP/Al HC sandwich panels and thin Al-plates located behind those sandwich panels. The empirical factors K3S = 1.1, K3D = 0.4, and n = 4/3 were found to give the best result for all structures considered.

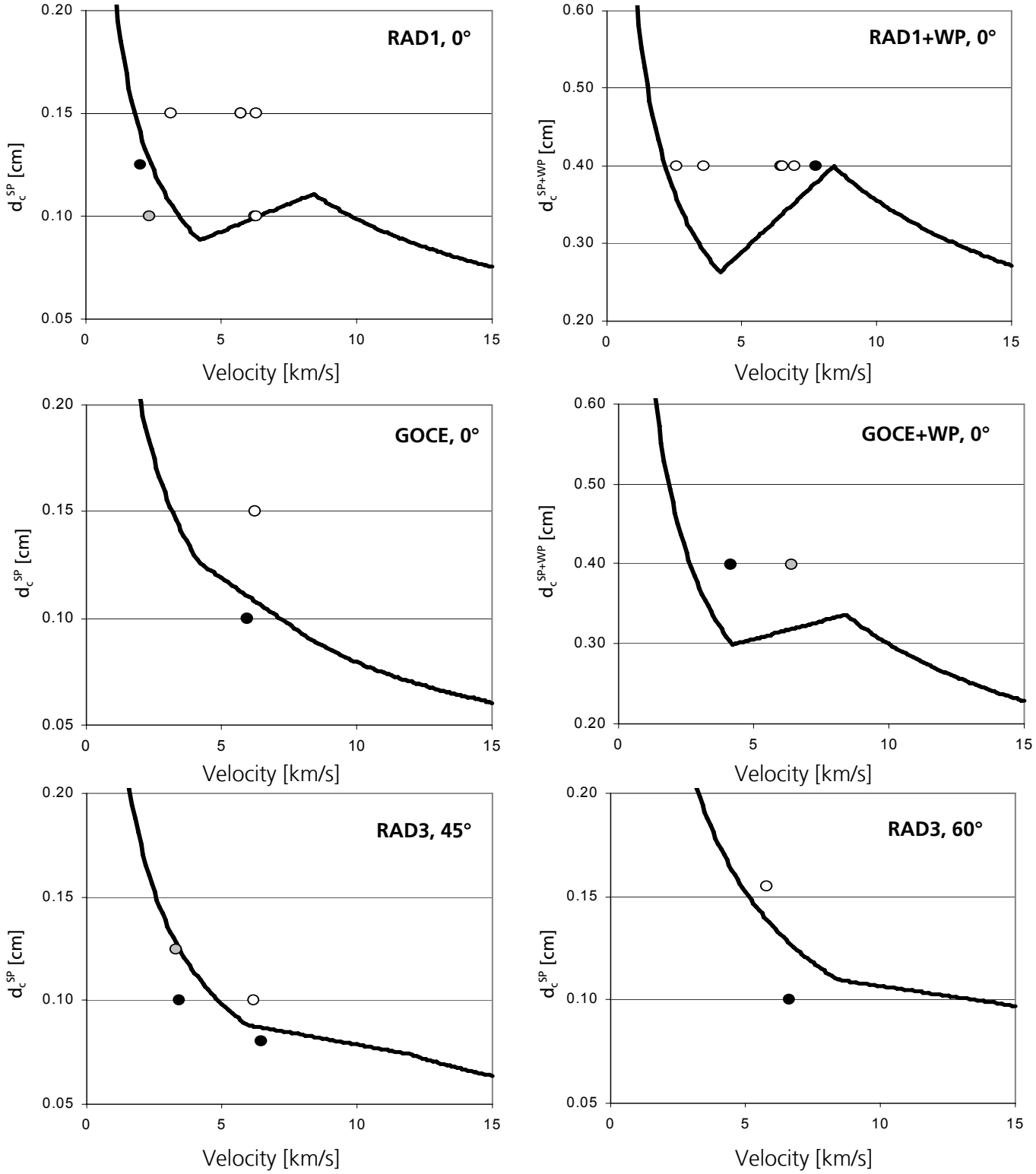

Figure 3-29 Predicted Ballistic Limit Curves and experimental results.

Table 3-8 Assessment of the BLE predictions for each structure versus exp. results.

Structure	*Angle (°)*	*Assessment of results*	*Comments*
RAD1	0	-	One (from 8) NC prediction
	45	+	One (from 5) VC prediction
	60	?	Results only for >BL
RAD1+WP	0	++	
	45	0	Results only for <BL
RAD2	0	+	One (from 3) SC prediction
	45	++	
RAD3	0	++	One (from 8) SC prediction
	45	-	One (from 4) NC prediction
	60	++	
RAD3+WP	0	?	Results only for >BL
GOCE	0	++	
	45	?	Results only for <BL
GOCE+WP	0	+	One (from 2) VC prediction
SAX	0	0	One (from 2) VC prediction
SAX+WP	0	?	Results only for >BL
	45	0	One result, VC prediction
H/P	0	?	Results only for >BL

Legend:

++	Good prediction	+	Slightly conservative prediction
0	Very conservative prediction	-	Non-conservative prediction
?	Inconclusive – Experimental results do not allow assessment of equation accuracy		

3.4.2 Application of the new BLE to Additional CFRP/Al HC Structures

Prior to this test program, the amount of hypervelocity impact test data available in the literature for composite sandwich panels was limited. Impact data related to witness plate, or other types of secondary damages induced by HVI on composite structure walls was almost non-existent. A comprehensive literature survey has been used to compile extra impact test data which is used in this section to further assess the predictive accuracy of the new BLE. A short description of the structures tested by Lambert et al. (2001), Taylor et al. (1999) and Frost and Rodriguez (1997) is given in Table 3-9 (additional information in Appendix B).

Table 3-9 Additional structures used for further assessment of the new BLE accuracy.

Mission	*Ref.*	*CFRP Facesheets*			*Honeycomb*	
		t (mm)	*Density (g/cm³)*	*stacking*	*Configuration*	*t (mm)*
Envisat	Lambert	1.1	1.579	(3x(0/±60))	3/16-.0015-5056P	45
Unknown	Taylor	1.62	1.825	$(0/90)_S$	5.2 ¼-.0025-3003	45
AXAF (A)*	Frost	0.254	1.66+	unknown	unknown	15.875
AXAF (B1)*	Frost	0.762	1.66+	unknown	unknown	15.875
AXAF (B2)*	Frost	0.762	1.66+	unknown	unknown	15.875
AXAF I*	Frost	0.508	1.66+	unknown	unknown	6.35
AXAF (D)*	Frost	1.016	1.66+	unknown	unknown	6.35
AXAF (E)*	Frost	1.524	1.66+	unknown	unknown	6.35
AXAF (F)*	Frost	0.406	1.66+	unknown	unknown	6.35

+ Calculated from density of constituents assuming fibre volume content of 60%
* MLI blanket attached to outer side of front facesheet

The predictive accuracy of the new BLE, organised by structure, is given in Table 3-10. For 28 out of a total 37 experiments, covering 10 different structures, 5 impact angles, and an impact velocity range of 4.80 – 7.26 km/s, the equation is able to correctly predict the result. This represents a success rate of 75.7%. Additionally, 3 experiments (8%) were predicted slightly conservatively, and 6 experiments (16%) were predicted very conservatively. No predictions were non-conservative.

Table 3-10 Assessment of the BLE predictions versus exp results for literature data sets.

Structure	*Angle (°)*	*Assessment of results*	*Comments*
ENV	0	+	One (from 3) VC prediction
ENV+MLI	0	0	One (from 2) VC prediction
Taylor	0	++	
	15	+	One (from 2) SC prediction
	45	+	One (from 3) SC prediction
	60	?	No results >BL
	75	?	No results >BL
AXAF-A	0	0	One (from 3) VC prediction
AXAF-B1	0	?	No results <BL
AXAF-B2	0	0	One (from 2) VC prediction
AXAF-C	0	0	One (from 3) VC prediction
AXAF-D	0	0	One (from 4) VC prediction
AXAF-E	0	+	One (from 4) SC prediction
AXAF-F	0	0	One (from 2) VC prediction

3.4.3 Comparison with Current BLEs for CFRP/Al HC SPs

Schäfer et al. (2004) identified four different approaches for predicting the ballistic limit of CFRP/Al HC sandwich panel structures, all of which are based on the Christiansen / modified Cour-Palais Whipple shield equation (Christiansen, 1993). In this section the new BLE is compared to these other approaches, and the predictive accuracy is assessed to determine whether the new approach gives more reliable predictions of penetration limits.

The modified Whipple shield equation is reproduced from Christiansen (1993) here. It should be noted that the nomenclature has been altered from the original publication.

Ballistic regime ($v_n \leq 3$ km/s):

$$d_c = \left[\frac{t_b \cdot \left(\sigma/40\right)^{0.5} + t_{ob}}{0.6 \cdot \left(\cos\theta\right)^{5/3} \cdot \rho_p^{0.5} \cdot v^{2/3}} \right]^{18/19} \tag{68}$$

Transition/shatter regime ($3 < v_n < 7$ km/s):

$$d_c = \left[\frac{t_b \cdot \left(\sigma/40\right)^{0.5} + t_{ob}}{1.248 \cdot \rho_p^{0.5} \cdot \cos\theta} \right]^{18/19} \times \left[1.75 - \frac{\left(v \cdot \cos\theta\right)}{4} \right] .... + \left[\frac{1.071 \cdot t_b^{2/3} \cdot S^{1/3} \left(\sigma/70\right)^{1/3}}{\rho_p^{1/3} \cdot \rho_{ob}^{1/9}} \right] \times \left[\frac{\left(v \cdot \cos\theta\right)}{4} - 0.75 \right] \tag{69}$$

Hypervelocity regime ($v_n \geq 7$ km/s):

$$d_c = \left[\frac{3.918 \cdot t_b^{2/3} \cdot S^{1/3} \left(\sigma/70\right)^{1/3}}{\rho_p^{1/3} \cdot \left(v \cdot \cos\theta\right)^{2/3} \cdot \rho_{ob}^{1/9}} \right] \tag{70}$$

The four different approaches are referred to herein as:

1. Taylor (Taylor et al., 1999);
2. Frost approach 1 (Frost and Rodriguez, 1997);
3. Frost approach 2 (Frost and Rodriguez, 1997);
4. Modified ESA Triple Wall, MET (Schäfer et al., 2004).

The Taylor equation applies the Christiansen / Cour-Palais equation (Eq. (68)-(70)) by calculating the thickness of aluminium plates with the equivalent areal density of the CFRP facesheets. The Al-equivalent rear

wall is then multiplied by a scaling factor based on experimental data (recommended as 0.5). The honeycomb core depth is used as the Whipple shield spacing, S.

Frost and Rodriguez (1997) present two approaches to calculate the ballistic limit of the CFRP/Al HC sandwich panel from the AXAF satellite. In Frost approach 1, the composite material properties and thicknesses are inserted into Eq. (68)-(70) directly. Frost approach 2 calculates equivalent Al-plate thicknesses, similar to the Taylor approach, but the thicknesses are calculated using both the density and yield strength of the CFRP and reference Al materials. The Frost approaches are the only ones which consider properties of the CFRP other than just density.

The MET approach presented by Schäfer et al. (2004) is based on the ESA Triple Wall equation (Drolshagen and Borge, 1992). The approach includes two coefficients (K3S and K3D) which are adjustable for use on structures different to a metallic Whipple shield. It should be noted that the ESA Triple Wall equation is the same as the Christiansen/modified Cour-Palais equation (Eq. (68)-(70)) for the case K3S = 1 and K3D = 0.16. However, the ESA Triple Wall equation does not define a limit angle (i.e. the angle at which the projectile critical diameter does not further increase with increasing impact angle). The MET approach uses the same density-based method as the Taylor approach to calculate the thickness of equivalent aluminium plates for the CFRP facesheets. Furthermore, a multiplier g_i is included to distinguish between different failure types (i.e. detached spallation and clear hole perforation).

Modified parameters of the Whipple shield equation used in the four approaches are given in Table 3-11.

Table 3-11 Whipple Shield equation parameters for CFRP/Al HC SPs.

Frost (1)		*Frost (2)*	*Taylor*	*Schäfer*
t_{ob}	$t_{ob,CFRP}$	$t_{ob,CFRP} \cdot \left(\frac{\rho_{Al}}{\rho_{CFRP}}\right)^{-0.159} \cdot \left(\frac{\sigma_{Al}}{\sigma_{CFRP}}\right)^{-0.236}$	$t_{ob,CFRP} \times \frac{\rho_{CFRP}}{\rho_{Al}}$	$t_{ob,CFRP} \times \frac{\rho_{CFRP}}{\rho_{Al}}$
t_b	$t_{b,CFRP}$	$t_{b,CFRP} \cdot \left(\frac{\rho_{Al}}{\rho_{CFRP}}\right)^{-0.159} \cdot \left(\frac{\sigma_{Al}}{\sigma_{CFRP}}\right)^{-0.236}$	0.5 x t_{ob}	$t_{b,CFRP} \times \frac{\rho_{CFRP}}{\rho_{Al}}$
σ_y	$\sigma_{y,CFRP}$	$\sigma_{y,Al}$	$\sigma_{y,Al}$	$\sigma_{y,Al}$
ρ_{ob}	ρ_{CFRP}	ρ_{Al}	ρ_{Al}	ρ_{Al}
S	t_{HC}	t_{HC}	t_{HC}	t_{HC}

In Figure 3-30 the ballistic limit curves of the RAD1 SP (0°) are shown, calculated using the new BLE, Frost and Rodriguez (approaches 1 and 2), Taylor, and MET approaches. Impact test data is also included in the figure. The differences between the predictions of the various methods can be clearly noted, along with their respective accuracy when applied to the RAD1 SP at normal incidence. The two Frost approaches are shown to predict the most robust shielding (i.e. highest critical diameter) across the range of impact velocities considered. In the LV regime the modified Whipple shield equation provides the most similar predictions to the new equation. All methods predict a greater improvement in the shielding capability of the RAD1 SP during the shatter regime than the new equation. The Taylor and MET approaches provide the best agreement with experimental data of the other methods considered.

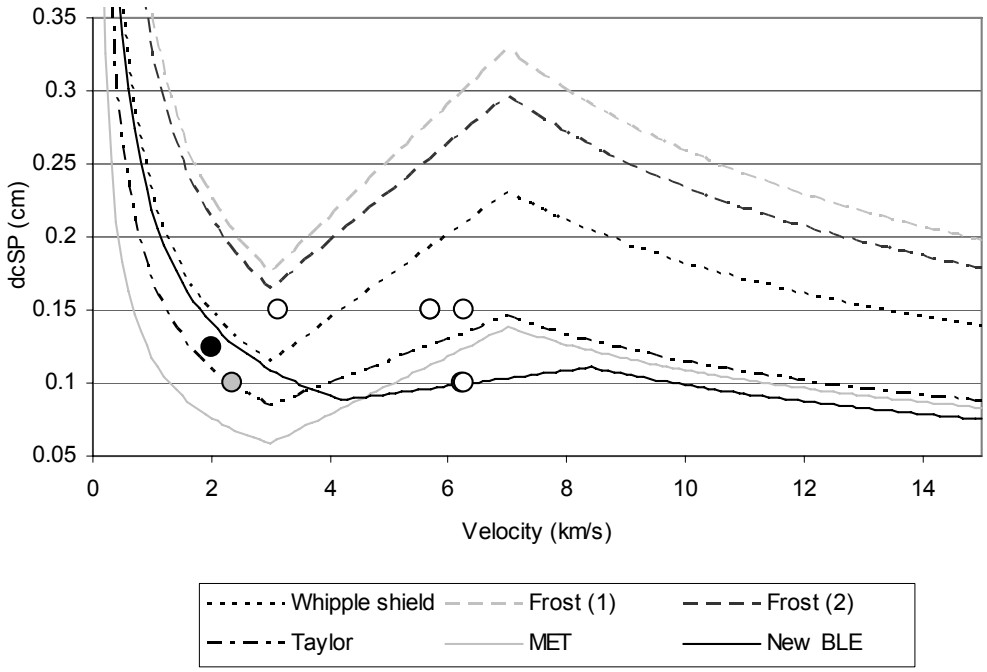

Figure 3-30 Comparison of the predicted ballistic limit curve for RAD1 CFRP/Al HC SP (0°) using various approached.

In Figure 3-31 the various ballistic limit curves are shown for oblique impact (45°) on the RAD3 SP. Again, the two Frost methods significantly over-predict the capability of the shield. The Taylor approach shows good agreement with the test data.

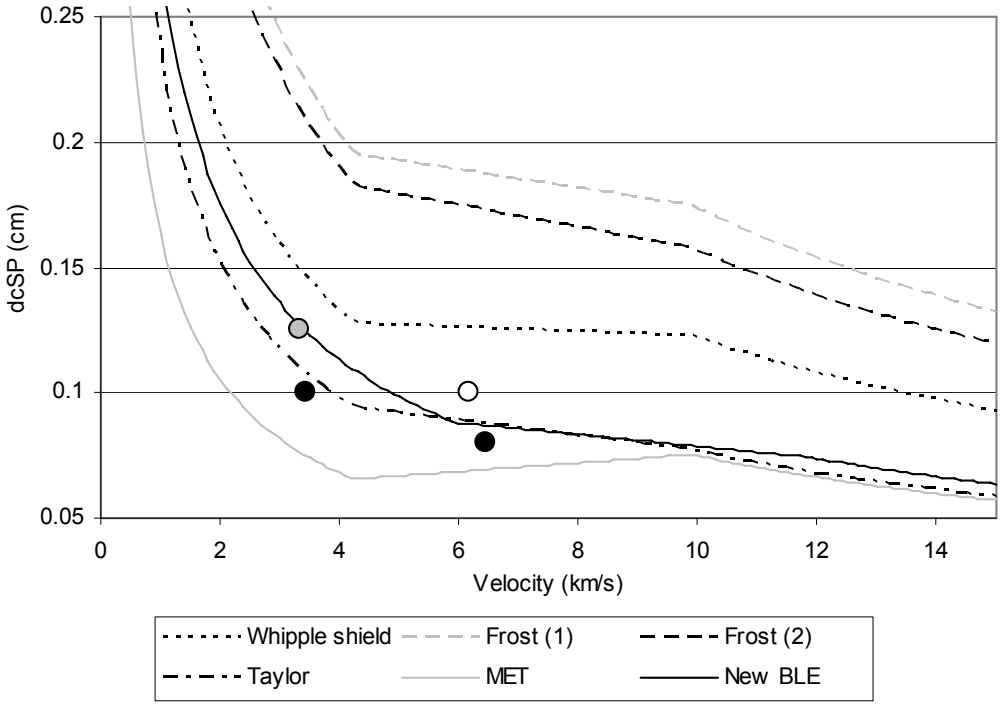

Figure 3-31 Comparison of the predicted ballistic limit curve for RAD3 CFRP/Al HC SP (45°) using various approached.

The modified Whipple shield, Frost, Taylor and MET approaches were used to predict the results of the experiments presented in Table 3-3 as well as those found in the literature (Lambert et al. (2001), Taylor et al. (1999) and Frost and Rodriguez (1997)). An assessment of the predictive accuracy of the various approaches, compared with that of the new BLE is shown in Figure 3-32.

From Figure 3-32 the following observations can be made:

- The modified Whipple-shield approach is non-conservative (50% of all perforating impact experiments were non-conservatively predicted). This characteristic is not structure or parameter specific, i.e. non-conservative predictions are made across the range of structures and parameters (e.g. thin honeycomb, thick facesheet etc). The best performance of this equation is with application on thin-honeycomb structures (RAD3, AXAF) at normal impact. The modified Whipple shield equation was derived by Christiansen (1993) using test data on metallic Whipple shields. This approach was not foreseen for application on composite sandwich panels. It has been included in the analysis of the new BLE as it is the most

widely accepted equation for dual-wall structures and the basis of all current composite-specific approaches.

- The Frost approach 1 is non-conservative (75% of all perforating impact experiments were non-conservatively predicted). This characteristic is not structure or parameter specific. The best performance of this equation is with application on thin-honeycomb structures with MLI attached (AXAF) at normal impact. Frost and Rodriguez (1997) derived their two approaches from tests of the various AXAF composite sandwich panels. This test data is complicated by the presence of different types of thermal insulation blanket, often with large areal densities relative to the composite sandwich panel. Additionally, all AXAF sandwich panels have very thin honeycomb cores, and therefore the fragment cloud expansion within the honeycomb may not be complete.

- The Frost approach 2 is non-conservative (75% of all perforating impact experiments were non-conservatively predicted), providing results very similar to Frost approach 1.

- The Taylor approach shows good agreement with the experimental results (81% of impact test results predicted correctly). Of the 44 perforation/spall impact experiments, only 3 predictions (6.8%) are non-conservative.

- The MET approach shows good agreement with the experimental results (68% of impact test results predicted correctly). Of the 44 perforation/detached spall impact experiments, only 2 predictions (4.5%) are non-conservative.

The new approach gives the best agreement with the experimental results (81% of impact test results predicted correctly) of the approaches considered. Of the 44 perforation/detached spall impact experiments, only 2 predictions (4.5%) are non-conservative (both detached spall).

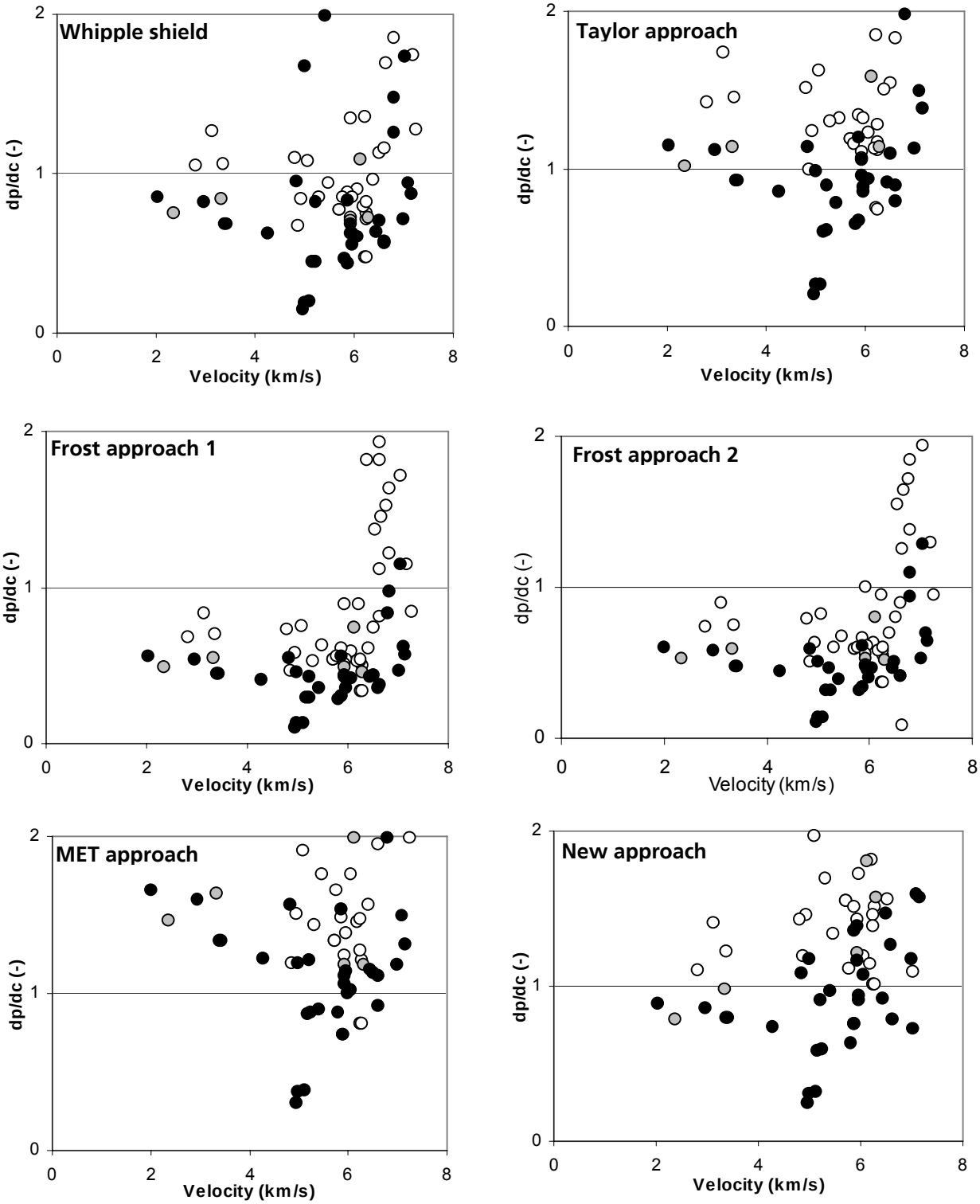

Figure 3-32 Comparing the accuracy of the various BLEs for all sandwich panel experimental data.

3.5 Summary

Disturbances induced in spacecraft structures as a result of space debris impacting at hypervelocity are expected to vary significantly depending on the degree of projectile penetration. To determine penetration limits of the test panel used to assess impact-induced disturbances a ballistic limit equation is required, however no validated equation was previously available for application with CFRP/Al HC sandwich panels.

Ballistic limit equations are analytical/empirical equations which use analytical relationships based on the physical state of the projectile during impact (i.e. intact or fragmented). The analytical expressions are then empirically adjusted to fit test data. An extensive hypervelocity impact test program was performed for six different CFRP/Al HC SPs to provide test data over a wide range of structural configurations. A new ballistic limit equation was defined using this test data and was shown to provide improvements over existing ballistic limit calculation methods for CFRP/Al HC SPs.

In addition to providing an enhancement in accuracy for predicting the ballistic limit of composite sandwich panels, the new equation is also valid for predicting the ballistic limit of a thin Al-plate located at a standoff behind composite sandwich panels. Although not applied for the assessment of space debris impact-induced disturbances, this capability has significant implications for debris shielding design on unmanned spacecraft.

4 Numerical Simulation of Impact-Induced Disturbances in a CFRP/Al HC Sandwich Panel

Space debris impacts on the GAIA satellite can be classified from an operational standpoint (from Guyot, 2005):

- Low level but frequent impact leading to a "noise-like" dynamic disturbance. These impacts generate a mechanical shock wave leading to a low level disturbance on the sensitive measurement equipment. As a consequence, even if the disturbance level is very low, this could continuously degrade the accuracy of the scientific data. This type of impact concerns particles with an impact frequency higher than one per hour.

- Intermediate level and less frequent impacts, which can be considered as discrete events. These impacts lead to a temporary loss of the scientific data, due to a disturbance level relatively high when compared to the equipment accuracy. This concerns particles with an impact frequency between 1 impact per day and 1 impact per month.

- Rare but high level impacts. Such particles lead at least to a temporary loss of the mission. These particles have an impact probability lower than 1 per year.

High level impacts would lead to a loss of spacecraft pointing, and, as such, the effect of impact-induced disturbances on the measurement accuracy caused by this impact type is irrelevant. Therefore, only low and intermediate level impacts are considered in the impact-induced disturbance analysis. For the GAIA spacecraft, these level impacts refer to particles with a mass between 10^{-7} kg and 10^{-11} kg. For spherical aluminium particles, this corresponds to diameters between 20 µm and 400 µm. A velocity range is expected between 11 km/s and 72 km/s, with a mean value of 20 km/s (Guyot, 2005).

These impact conditions are not achievable with current hypervelocity acceleration facilities. As such, numerical simulations are required which can be validated at realisable impact conditions and extrapolated to consider the entire range of relevant in-orbit impact conditions. Finite

Element Analysis (FEA) tools (e.g. NASTRAN) have long been used in structural engineering to determine vibrational response to applied loading, however for highly non-linear events, particularly those involving shocks, these codes are not ideal. Hydrodynamic computer codes, or hydrocodes, are based on explicit finite difference, finite volume, and finite element techniques and use classical continuum mechanics to describe the dynamics of a continuous media. They enable coupling of complex material models with a fluid-structure program that is ideal for simulation of highly dynamic events, particularly those involving shock wave propagation such as hypervelocity impact of space debris (Hiermaier, 2003).

The GAIA spacecraft is constructed of three main modules (shown in Figure 4-1): a 10m wide deployable sunshield (DSA), a service module (SVM), and a payload module (PLM).

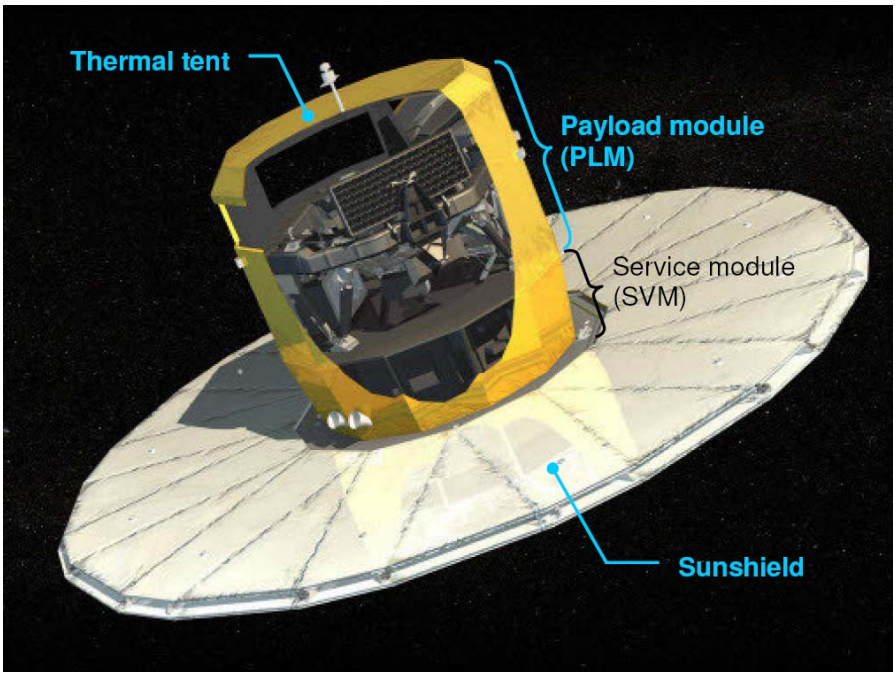

Figure 4-1 General configuration of the GAIA spacecraft (© EADS Astrium).

The DSA is a thin structure deployed in the sun-facing direction of the satellite and made mainly of Multi-Layer Insulation blanket (MLI). The DSA also has a number of solar arrays attached around the edges of the dodecagon-shaped end of the SVM. The SVM is constructed as a dodecagon platform with a hollow cylindrical core. All elements of the SVM are made of CFRP/Al HC sandwich panels with varying thicknesses. Typical dimensions of the SVM sandwich panels are 0.6 mm thick CFRP

facesheets and 30-60 mm thick Al honeycomb cores. The PLM is divided into two sub-modules: the optical bench and the thermal tent. The thermal tent is made mainly from CFRP/Al HC panels with some reinforcing around holes in the tent roof. Typical dimensions of the PLM sandwich panels are 0.5 mm thick CFRP facesheets and 10-30 mm thick Al honeycomb core. A representative panel has been selected for studying the propagation of debris impact-induced disturbances, details of which are given in Figure 4-2.

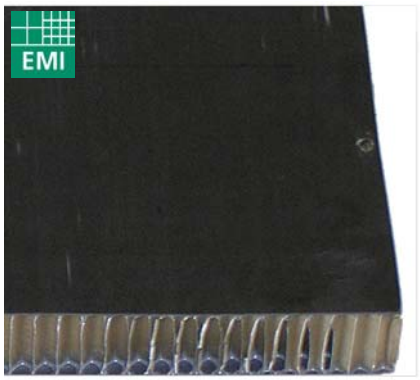

Parameter	*Value*	*Comments*
CFRP skin		
Density	1.48-1.56 g/cm³	Measured at EMI
Thickness	0.5mm	u.d. plies
Stacking	[0°/45°/90°/-45°]	Quasi-isotropic
Fibre	M55J HM carbon	Supplier: Toray
Resin	XU 3508 (hardener 3473)	Supplier: Huntsman
Al HC core		
Designation	3/16-5056-.0007P	Supplier: Hexcel
Thickness	20mm	-

Figure 4-2 Structural details of the representative GAIA CFRP/Al HC sandwich panel selected for testing.

Considering three orders of magnitude exist between the projectile diameters of interest and the spacecraft geometry (i.e. μm → m) it is not possible (nor reasonable) to perform impact simulations on a complete spacecraft model.

In this chapter, hydrocode simulations and experiments are presented to characterise the impact-induced disturbances in the immediate vicinity of the impact. In the absence of experimentally-characterised material data a theoretical approach is used to define dynamic properties of the CFRP facesheets. Sensitivity of the impact-induced disturbances to numerical set-up is investigated and an optimum model is validated via comparison with experimental measurements. The numerical simulations described in this chapter can be used for characterising the dynamic response of a CFRP/Al HC SP representative of those used onboard GAIA.

4.1 Description of the Numerical Model

4.1.1 Material Modelling

4.1.1.1 CFRP Facesheets

The advanced non-linear orthotropic model for composites (Riedel et al., 2003) provides an unparalleled capability in predicting the thermodynamic response in addition to the damage and residual strength of composite materials under shock wave loading in numerical hydrocodes. This continuum model requires the composite properties to be defined macroscopically. Guyot (2006) provides properties of the GAIA CFRP facesheet in terms of the constituent (fibre and resin) properties. In the absence of experimentally-characterised macroscopic properties, a means to derive the laminate elastic performance, equation of state, post-yield hardening and post-yield softening is required.

4.1.1.2 Theoretical Characterisation of CFRP Dynamic Properties

Micromechanics relates the properties of a composite to that of its constituents, thus allowing calculation of the u.d. composite properties from the supplied constituent data. As such, it provides the starting point for derivation of composite laminate mechanical properties. Micromechanical theories can generally be classified into elastic or strength theories. The use of micromechanics in predicting the elastic properties of composite materials is widely accepted, although no single theory receives universal application. For the prediction of composite material strength using micromechanics, there exist significantly more approaches; however they are less accurate in general and subsequently less widely accepted than their elastic counterparts.

Numerous reviews of composite micromechanics theories have been performed (e.g. Christensen (1990)), identifying particular strengths and weaknesses in the main approaches. Constituent properties provided in the literature are often conflicting, for example the tensile strength of carbon fibre type IM6 is provided as: 5589 MPa, 4382 MPa and 2861 MPa by Hexcel (Anon., 2002), Chung (1994) and the University of California (San Diego) (Anon., 2004) respectively. As such a meaningful critical review of the various theories is difficult. One of the better constituent and resulting composite material data sets is provided by Soden et al. (1998) for use in the World Wide Failure Exercise (WWFE)

(Hinton et al., 2004). Even in this multi-national, multi-institutional investigation Soden states that "some of the materials data given will be inaccurate". Additionally, the University of California (San Diego) publish a full experimentally-characterized set of constituent and composite data (experimental values determined from tests on six specimens) for a carbon fibre/epoxy composite (Anon., 2004).

To identify which micromechanical theories are suited for application in predicting the properties for space grade CFRP laminates, six of the most common elastic micromechanics theories were applied to calculate the properties of the three composites previously identified. The techniques considered are:

- Mechanics of materials, Chamis (1984)
- Semi-empirical approach, Halpin-Tsai (Halpin, 1969)
- Self-consistent field, Hermans (1967)
- Equivalent inclusion method, Eshelby (1957)
- Method of cells, Aboudi (1991)
- Bridging method, Huang (2004)

Examples of the predictions are shown in Figure 4-3 for the transverse tensile modulus, E_{22}, and transverse Poisson's ratio, ν_{23}, of composites AS4/3501-6 and T300/BSL914C respectively.

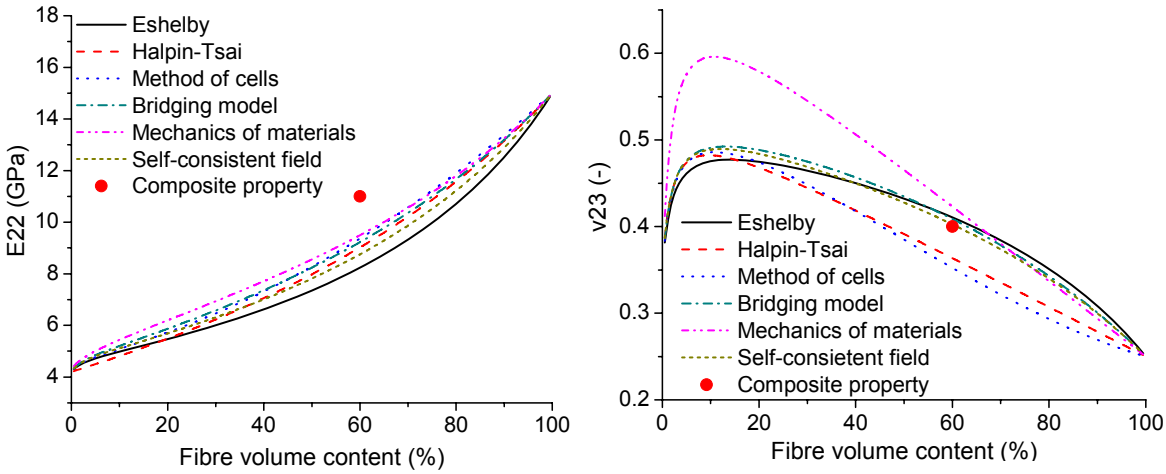

Figure 4-3 Predictions of six elastic micromechanics theories. Left: transverse tensile modulus (E_{22}) of AS4/3501-6 (V_f = 63.5%); Right: transverse Poisson's ration (ν_{23}) of T300/BSL914C (V_f = 60%)

The variance of the micromechanics predictions for the AS4/3501-6, T300/BSL914C, and IM6/3501-6 materials are shown in Figure 4-4 – Figure 4-6. For the longitudinal tensile modulus and major Poisson's ratio the various methods (with the exception of Method of Cells) all effectively produce the rule of mixtures (ROM) result. These properties are predicted to a high degree of accuracy, in agreement with the findings of Rosen and Hashin (1987). Additionally, it appears that the predictive accuracy of the six micromechanics theories is dependent on the material data sets. For example, the transverse tensile moduli of AS4/3501-6 and T300/BSL914C from Soden et al. (1998) are significantly under-predicted. However, the predictions for the IM6/3501-6 material (from Anon., 2004) are reasonably accurate. This data-source dependence is also observed in, for example, the calculated transverse Poisson's ratios, which are significantly over-predicted for the IM6/3501-6 composite, while being accurately predicted for the AS4/3501-6 and T300/BSL914C composites.

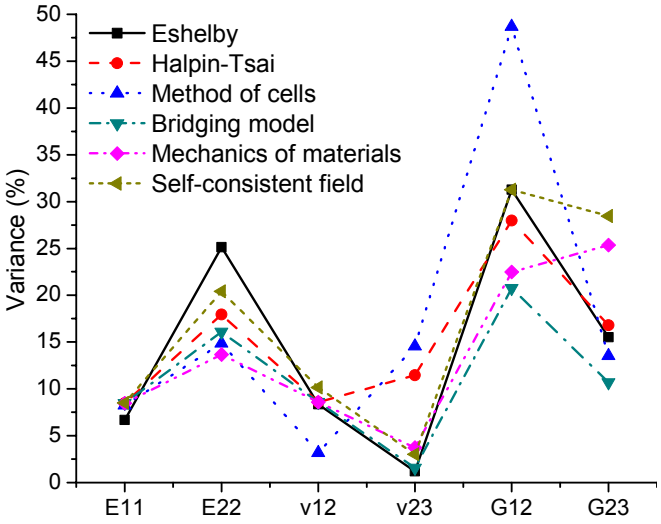

Figure 4-4 Accuracy of various micromechanics methods for predicting the elastic properties of AS4/3501-6 (V_f = 60%).

Of the six analytical techniques investigated, Eshelby's equivalent inclusion method provides the most satisfying mathematical solution as it avoids the gross oversimplifications of stress and strain fields (mechanics of materials) or composite geometry (self-consistent field, method of cells, bridging model) and is not based on empirical factors (Halpin-Tsai). However, Eshelby's method provides poor predictions for the transverse tensile modulus. Across the range of materials considered the bridging model provides the best overall agreement with the reported values.

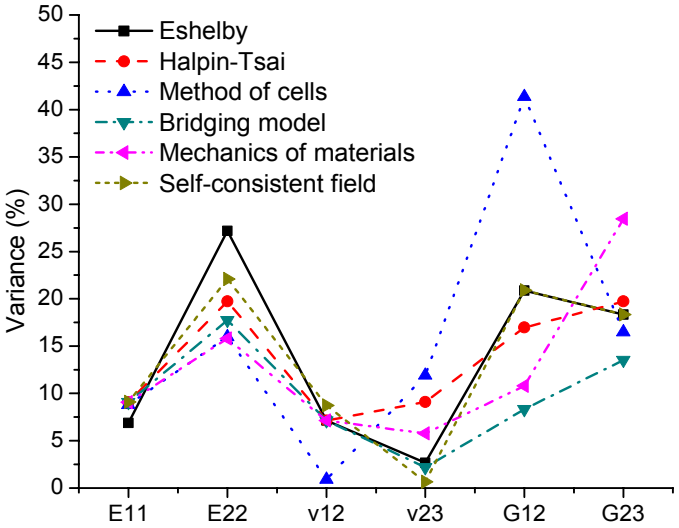

Figure 4-5 Accuracy of various micromechanics methods for predicting the elastic properties of T300/BSL914C (V_f = 60%).

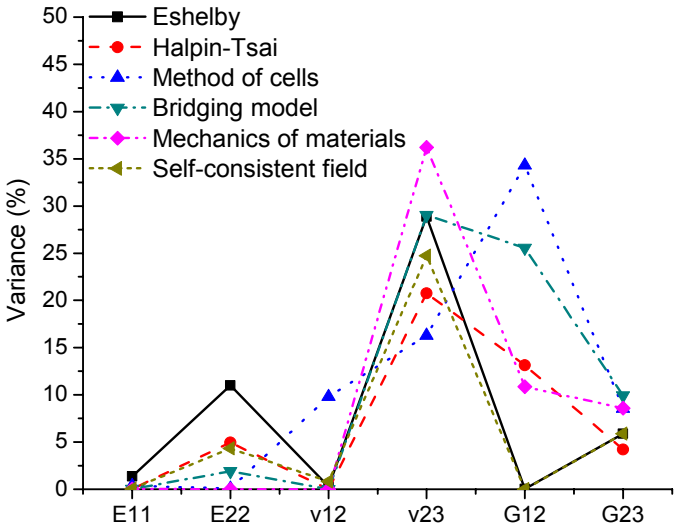

Figure 4-6 Accuracy of various micromechanics methods for predicting the elastic properties of IM6/3501-6 (V_f = 63.5%).

Two strength theories were considered for prediction of composite strength: the strength of materials approach of Chamis (1974), and the continuation of Huang's Bridging Model (Huang, 2004). In the following X, Y and S_{xy} refer to strength in the fibre, transverse, and in-plane shear directions respectively. The subscripts t and c indicate tensile and compressive strengths. Examples of the predictions are shown in Figure 4-7 for the longitudinal tensile strength, X_t, and in-plane shear strength, S_{xy}, of composites AS4/3501-6 and IM6/3501-6 respectively.

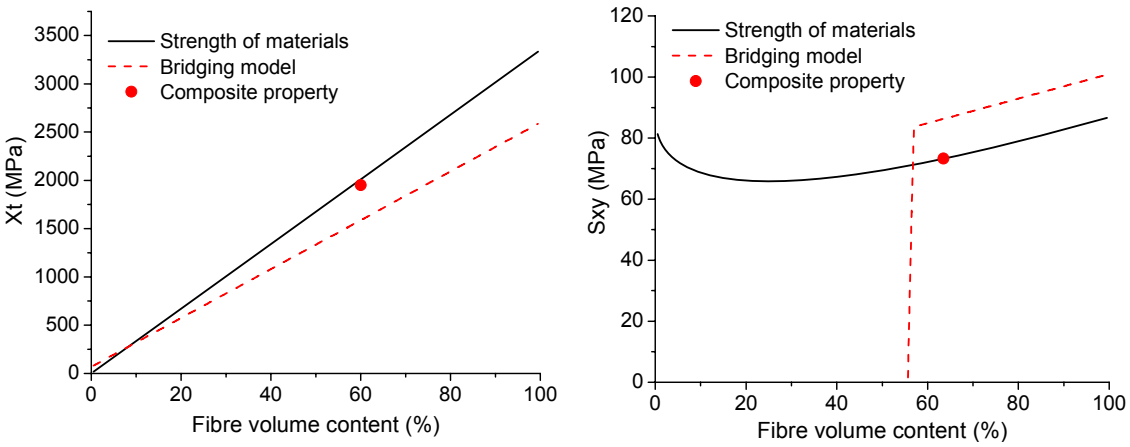

Figure 4-7 Predictions of micromechanics theories for strength. Left: longitudinal tensile strength (X_t) of AS4/3501-6 (V_f = 63.5%); Right: in-plane shear strength (S_{xy}) of IM6/3501-6 (V_f = 60%)

The average variance of the micromechanics strength predictions from the reported composite properties is shown in Figure 4-8. It can be noted in that, with the exception of longitudinal compression strength, X_c, the strength of materials predictions provide better agreement with the reported composite properties than those of the bridging model. Similar to the elastic models, the accuracy of the methods is dependent on the source of the material data.

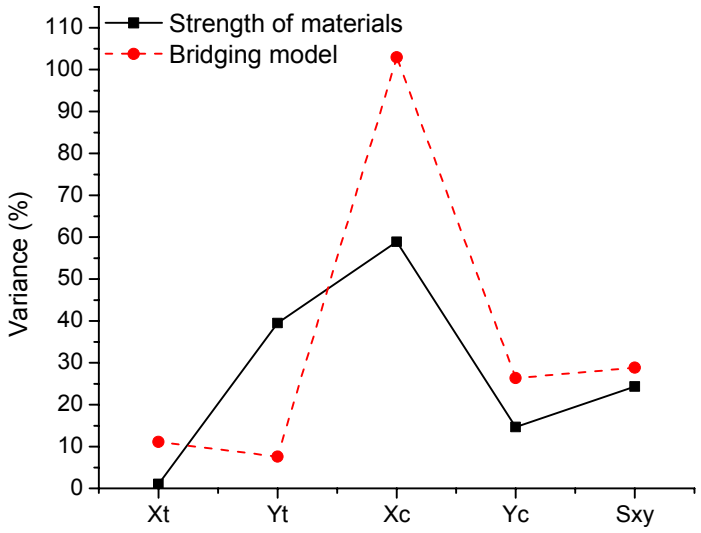

Figure 4-8 Average variance of two micromechanics methods for predicting the strength properties of three carbon fibre/epoxy composites.

The longitudinal compression strength is calculated in the strength of materials approach as the minimum of three different possible failure mechanisms: fibre compression, delamination, and microbuckling. i.e.:

$$X_c = \left\{ \begin{matrix} V_f X_{fc} \\ 10 S_{xy} + 2.5 X_{mt} \\ G_m / \left(1 - V_f \left(1 - G_m / G_{f12}\right)\right) \end{matrix} \right\}_{MIN} \tag{71}$$

In Figure 4-9 the three failure mechanisms are shown for the AS4/3501-6 CFRP. It is apparent that failure is initiated by fibre compression until the volume of fibre reinforcement exceeds ~25%, at which point the failure is initiated by delamination or transverse splitting. By not considering the delamination failure mechanism, the strength of materials approach provides considerably more accurate predictions for the three composite materials considered. As such, for the prediction of CFRP compression strength this failure mechanism is not considered.

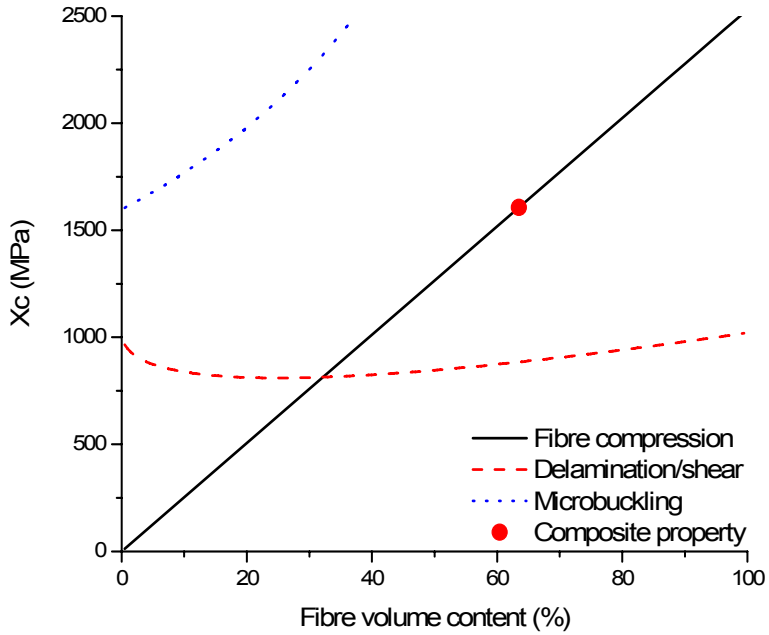

Figure 4-9 Strength of material's failure mechanisms for longitudinal compression strength (IM6/3501-6, V_f = 63.5%).

Defining the Micromechanics Error Bounds

The accuracy of Huang's bridging model and Chamis' strength of materials theory for predicting the respective elastic and strength properties of unidirectional composite materials is summarized in Figure 4-10. The scatter bounds were derived from predictions for three composite materials presented in Soden et al. (1998) and Anon. (2004). It can be clearly observed that the micromechanics techniques show good

agreement with the reported composite values for all elastic properties (~ ± 20%). The failure properties, as expected, show significantly larger error bounds, particularly in the case of transverse and shear failure.

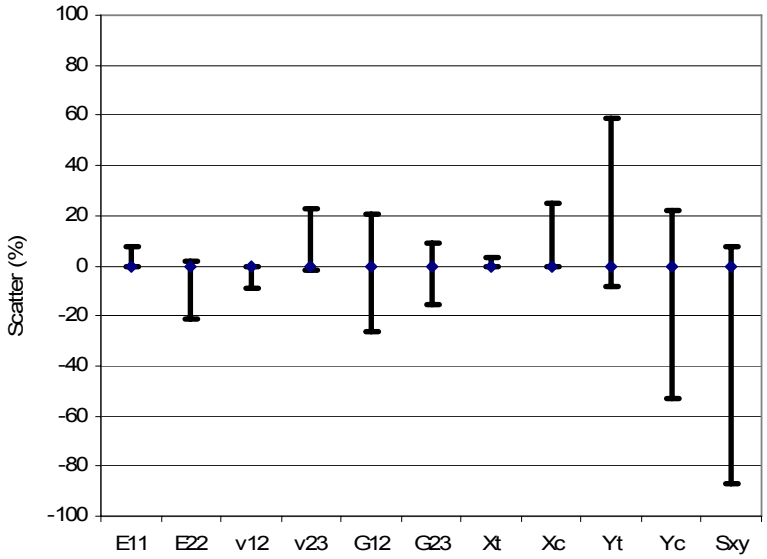

Figure 4-10 Predictive accuracy and scatter bounds for micromechanics predictions of CFRP/epoxy composite properties.

Classical laminate theory and Hooke's law for an orthotropic composite are applied to calculate the elastic properties of the structural laminate from the ply values and laminate stacking.

The shock response of the CFRP laminate is defined by the anistropic formulation of Anderson et al. (1994) which describes a coupled deviatoric and volumetric response. The volumetric response (EOS) is expressed using a polynomial form of the Mie-Grüneisen EOS:

Compression: $$p = A_1\mu + A_2\mu^2 + A_3\mu^3 + (B_0 + B_1\mu)\rho_0 e \quad (72)$$

Tension: $$p = T_1\mu + T_2\mu^2 + B_0\rho_0 e \quad (73)$$

The material average bulk modulus, A_1', is automatically calculated from the orthotropic stiffness matrix. For isotropic materials, the quadratic and cubic terms of the polynomial EOS are determined from the material shock velocity-particle velocity relationship (U_s-u_p), where:

$$A_2 = \rho_0 {c_B}^2 [1 + S(S-1)] \quad (74)$$

$$A_3 = \rho_0 {c_B}^2 [2(S-1) + 3(S-1)^2] \quad (75)$$

Additionally, the Grüneisen gamma is calculated using the approximation proposed by Dugdale and MacDonald (1953):

$$B_0 = B_1 = \Gamma \cong 2S - 1 \tag{76}$$

Flyer plate impact tests on isotropic materials allow shock and particle velocity properties to be deduced, from which the reference curve (generally the Hugoniot) can be defined. However, in the case of anisotropic materials, considering the coupled volumetric and deviatoric material behaviour, these types of measurements do not record the material's pure volumetric response; rather the measurement is that of the coupled response. A theory for the direct derivation of the coefficients in the polynomial EOS, coupled with orthotropic response, is currently not available. Nonetheless, flyer plate impact test measurements are commonly used for the definition of the Hugoniot reference curve for anisotropic materials (e.g. Hiermaier et al. (1999), Riedel et al. (2003)). As a result of the material strain coupling (and in the absence of additional shear measurements), the only truly accurate use of rear side velocity-time measurements made during flyer plate impact tests on anisotropic materials is for validation of complete numerical models.

Three vastly different CFRP laminates subjected to flyer plate impact tests in Riedel and Nahme (2001), Machens et al. (2005), and Wicklein et al. (2007) showed a high level of similarity when normalised in terms of p-wave soundspeed, particularly at particle velocities above ~500 m/s (shown in Figure 4-11). A linear best fit is made to the normalised experimental data (considering particle velocities above 500 m/s). At velocities below 500 m/s significant deviation of the experimental measurements from the linear fit is observed. Fowles (1970) found that the Rankine-Hugniot jump conditions are not strictly applicable at stress levels less than an order of magnitude higher than the elastic limit. At these stress values, shock rise times are appreciable (and sometimes unsteady). Instead, Fowles considers an isentropic stress wave with two wave velocities (stress component and mass velocity component) which can be used to calculate material pressure, volume and internal energy at low stress values.

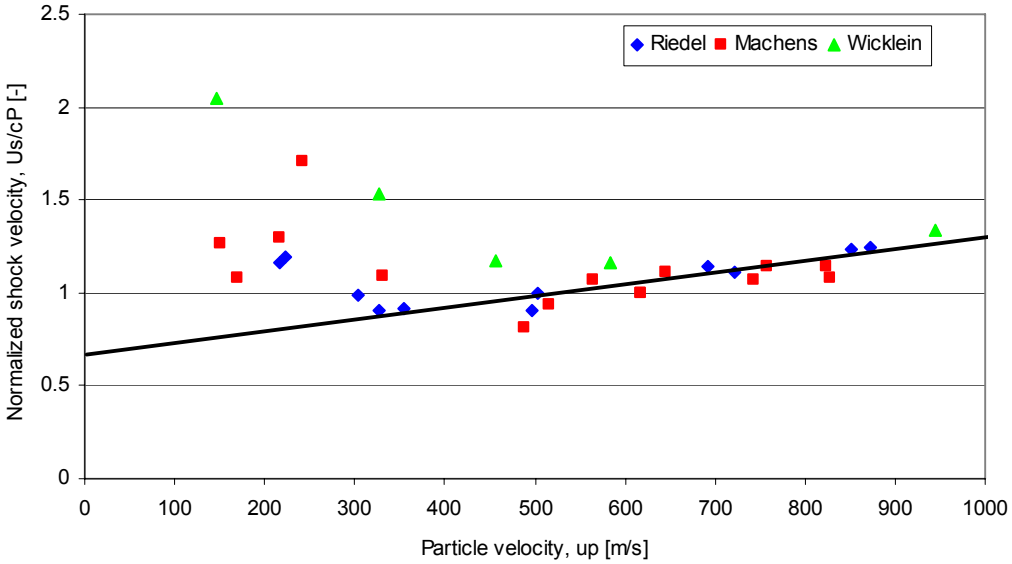

Figure 4-11 A common U_s-u_p curve for CFRP composite laminates.

AUTODYN requires the input of a linear, steadily-increasing shock velocity-particle velocity relationship for all stress levels. As such, the linear curve presented in Figure 4-11 is used. Where:

$$U_s = \left(6.242E-04 \cdot u_p + 6.707E-01\right) \cdot c_p \tag{77}$$

4.1.1.2.1 Non-Linear Hardening

The quadratic yield function of Chen et al. (1997) is used to define the inelastic post-yield performance of the CFRP laminate (hardening). The yield function describes a master effective stress-effective plastic strain curve from which nine so-called plasticity coefficients are used to define the degree of anisotropy of the hardening surface. Generally, the master curve is set to the laminate direction showing the largest amount of plasticity and is approximated by ten coordinates for input into AUTODYN.

The in-plane plastic Poisson's ratios (ν_{12}^p, ν_{21}^p) can be determined from the in-plane stress-strain curves:

$$\nu_{ij}^p = -\frac{d\varepsilon_{jj}^p}{d\varepsilon_{ii}^p} \tag{78}$$

where

$$d\varepsilon_{ii}^p = d\varepsilon_{ii} - d\varepsilon_{ii}^{el} \tag{79}$$

From which the plasticity parameters a_{11}/a_{22} (depending on master curve definition) and a_{12} can be simply calculated:

$$a_{11} = a_{22}\frac{\nu_{21}^{p}}{\nu_{12}^{p}} \qquad a_{22} = a_{11}\frac{\nu_{12}^{p}}{\nu_{21}^{p}} \tag{80}$$

$$a_{12} = -a_{22}\nu_{21}^{p} \tag{81}$$

The in-plane stress-strain performance of the laminate can be determined using Puck's action plane failure criteria (Puck and Schürmann (1988, 2002)). The constants used in Puck's theory are given in Appendix A.

The remaining in-plane and shear plasticity parameters can be defined by simplifying the elastic-plastic stress-strain performance of the material under the relative loading conditions to either perfectly elastic, or perfectly elastic-plastic. Assuming no plasticity the plasticity parameter can be set such that the directional failure stress is achieved prior to the initial yield criterion (1st coordinate of the master curve):

$$a_{ii} = \frac{2}{3}\left(\frac{\bar{\sigma}_{\#1}}{\sigma_{ii,ULT}}\right)^{2} \quad \text{in unidirectional loading (I = 1,2,3)} \tag{82}$$

$$a_{rr} = \frac{1}{3}\left(\frac{\bar{\sigma}_{\#1}}{\tau_{ij,ULT}}\right)^{2} \quad \text{in shear loading (I} \neq \text{j, r = 4,5,6)} \tag{83}$$

Similarly, the parameters can be set ensure the full plasticity curve is reproduced under directional loading by setting the plasticity parameter such that the final yield condition (final coordinate of the master curve) corresponds to the directional failure stress:

$$a_{ii} = \frac{2}{3}\left(\frac{\bar{\sigma}_{\#10}}{\sigma_{ii,ULT}}\right)^{2} \quad \text{in unidirectional loading (I = 1,2,3)} \tag{84}$$

$$a_{rr} = \frac{1}{3}\left(\frac{\bar{\sigma}_{\#10}}{\tau_{ij,ULT}}\right)^{2} \quad \text{in shear loading (I} \neq \text{j, r = 4,5,6)} \tag{85}$$

The parameters a_{13} and a_{23} define coupling between the in-plane directions and can be coarsely derived by adopting the assumption used in derivation of the in-plane plasticity parameters.

4.1.1.2.2 Failure

Puck's action plane criteria are used for prediction of the laminate in-plane strengths. These properties are determined experimentally by Wicklein et al. (2007) using uniaxial quasi-static tensile tests. For definition of the through-thickness tensile strength however, dynamic spall flyer plate impact tests were used in which the loading rate (impact velocity) varied from 159 m/s to 1073 m/s. In Figure 4-12 the measured spall strength for the flyer plate impact tests is shown. It is apparent that the spall strength varies up to 400% for the loading rates considered. Wicklein et al. (2007) calculated an average based on the three experiments with the best spallation signals to define the maximum through-thickness tensile strength (shown in Figure 4-12). This average dynamic tensile strength is significantly higher than what would be expected for a quasi-static though thickness tensile test. Although somewhat arbitrarily defined, the authors assumed that a dynamically-measured strength would ultimately be more accurate than a quasi-statically measured property. This approach is typical of that used during derivation and validation of the advanced orthotropic material model (Hiermaier et al. (1999), Riedel et al. (2003)).

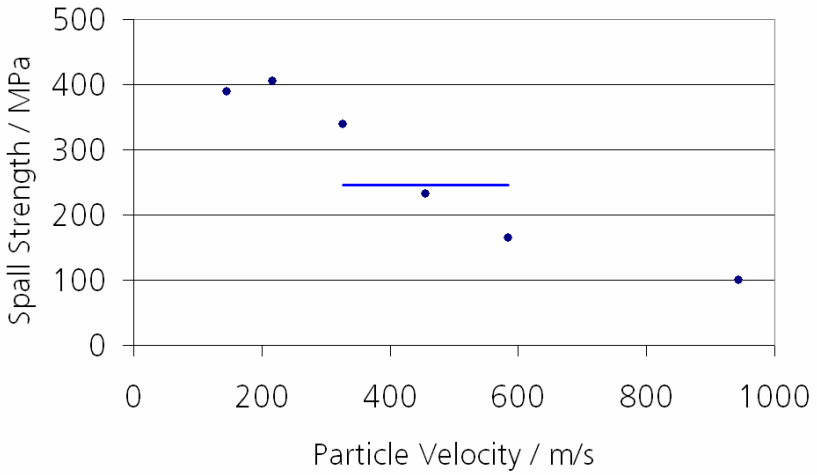

Figure 4-12 Measured spallation strength of the CFRP laminate. The line indicates the average value selected by Wicklein et al. (2007) as σ_{33}.

It is not possible to theoretically predict the dynamic tensile strength of the composite lamina. As the pressures generated during impact are so great, the through-thickness strength is only relevant at positions away from the impact location where the impact shock wave has been sufficiently attenuated. In Figure 4-12 it is shown that an initial increase in strain rate results in increasing through-thickness tensile strength.

Continued increases in strain rate (above 220 m/s) cause a reduction of the directional strength. It is considered that the through-thickness strength is limited by the allowable tensile strain in the matrix. Gilat et al. (2005) found that epoxy resins showed an increase in ductility under tensile loading at low strain rates. An increase in load rate resulted in the epoxy system failing in a brittle manner. Thus, unless dynamic loading conditions equivalent to those induced during hypervelocity impact can be generated, the definition of dynamic tensile strength in the through-thickness direction by experimental spallation measurements is not necessarily an improvement over quasi-static strength values. For the theoretical material derivation, through-thickness strength is estimates as a quasi-static property, based on the methodology for calculating the transverse tensile strength of a unidirectional laminate in Chamis (1974):

$$\sigma_{33,\,fail} = \varepsilon^{m}_{\max} \cdot E_{33} \tag{86}$$

Chamis (1984) defined micromechanics equations for calculating the longitudinal and transverse interlaminar shear strengths of unidirectional composite materials:

Longitudinal:

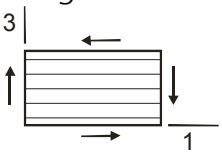

$$S_{13} = \left[1 - \left(\sqrt{V_f} - V_f\right)\left(1 - \frac{G_m}{G_{f12}}\right)\right] S_m \tag{87}$$

Transverse:

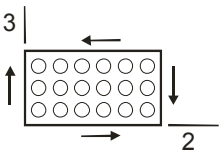

$$S_{23} = \left[\frac{1 - \sqrt{V_f}\left(1 - G_m / G_{f23}\right)}{1 - V_f\left(1 - G_m / G_{f23}\right)}\right] S_m \tag{88}$$

The difference in the two equations arises from the effects of the fibre alignment. For a multi-directional laminate, the through-thickness shear strength is expected to lie between the values calculated using Eqs (87) and (88). A simple scaling between the two limits is made, where the scaling parameter (χ) is dependent on the alignment of the individual layers in the composite laminate:

$$\chi_{ij} = \sum_{k=1}^{no.plies} \cos\varphi_k \frac{t_k}{t} \tag{89}$$

where φ_k – Angle of ply relative to load plane.
T_k – Thickness of ply k.
t – Thickness of laminate.

For $\chi = 1$, all fibres are parallel to the shear plane and the laminate shear strength will correspond to the longitudinal equation (Eq. (87)). For $\chi = 0$, all fibres are perpendicular to the shear plane, and thus the shear strength will correspond to the transverse equation (Eq. (88)). The transverse shear strengths (S_{23}, S_{31}) are then calculated by:

$$S_{ij} = S_{long}\chi_{ij} + S_{trans}\left(1-\chi_{ij}\right) \tag{90}$$

4.1.1.2.3 Non-Linear Softening

For multi-directional laminates loaded under in-plane uniaxial tension the failure occurs progressively through the different ply orientations. As the loading is increased plies are subject to failure which reduces the load-carrying capability of the laminate (realised as softening). Once sufficient plies have failed such that the remaining number of plies are unable to support the applied load, ultimate failure occurs. CFRP laminates exhibit brittle failure under in-plane tensile loading, thus according to the non-linear softening model:

$$G_{f11} = G_{f22} = 0 \;\; J/m^2 \tag{91}$$

Tensile loading in the through-thickness direction is a matrix-dominated failure mode. Experimentally, this fracture energy is determined in a double-cantilever beam (DCB) test. It is been shown by Wicklein et al. (2007) that under this loading type, even for highly brittle epoxy resins, fracture is not instantaneous and therefore $G_{f33} \neq 0$. or For mode-I delamination of the laminate, the fracture energy of the epoxy resin is adopted, thus:

$$G_{f33,ii} = G_{mf,ii} \tag{92}$$

In Figure 4-13 experimental stress-strain curves of a [0/±45] CFRP laminate are shown under tensile loading at 45°. It is apparent that upon reaching the laminate failure stress, the load-carrying capability of the laminate

diminishes immediately to zero. Thus, according to the non-linear softening model:

$$G_{f12} = 0 \;\; J/m^2 \tag{93}$$

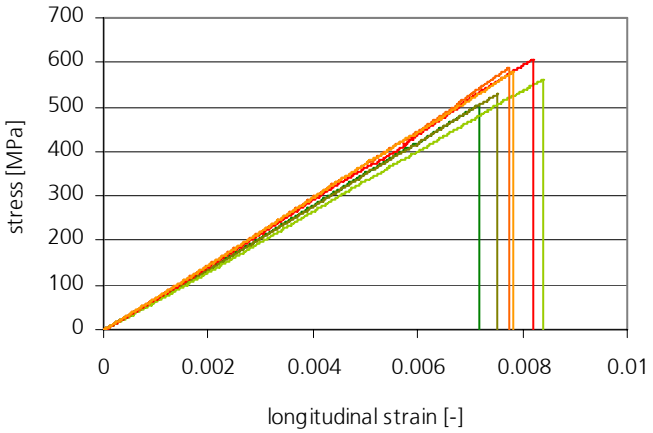

Figure 4-13 Stress-strain curves for tension at 45° on a multi-directional CFRP composite (Wicklein et al., 2007).

For transverse shear failure (mode II) O'Brien (1997) compiled a large databank of delamination fracture toughness values for laminates from multiple resources. The ratio of mode II to mode I fracture toughness for polymer composites is shown in Figure 4-14.

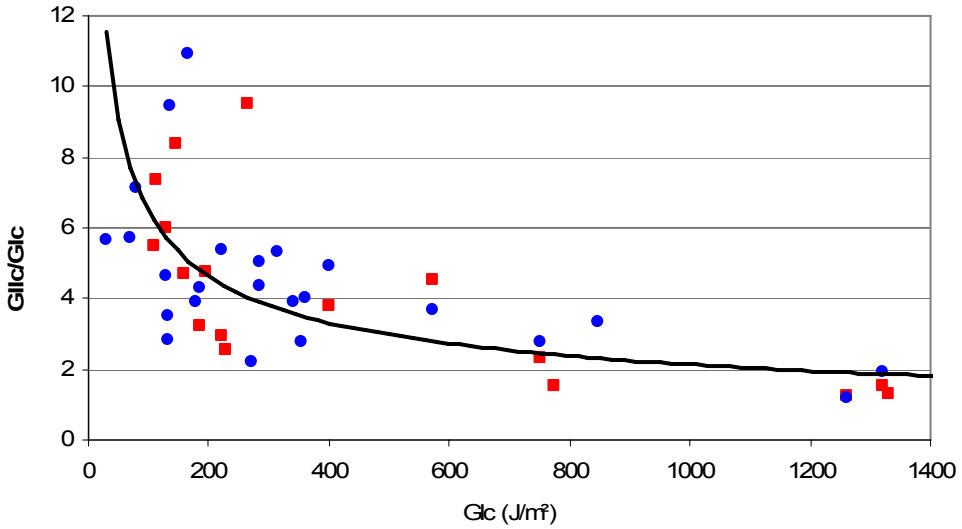

Figure 4-14 Ratio of mode II to mode I toughness for polymer matrix composites (red data points: mode II initiation via pre-crack, blue: mode II initiation via insert).

Although there is a large degree of scatter in the polynomial fit, it is considered to be a reasonable approximation for the transverse (i.e. loading in the through-thickness direction) fracture toughness. The polynomial fit is defined as:

$$\frac{G_{IIc}}{G_{Ic}} = A' \cdot G_{Ic}^{\ -\alpha} \tag{94}$$

where $A' = 59.244$
$\alpha = 0.4811$

4.1.1.3 Validation of the CFRP Material Data Derivation Procedure

Wicklein et al. (2007) performed an extensive experimental characterization campaign on a space representative CFRP/epoxy composite laminate (stacking $[0°/+45°/-45°]_S$) for application in AUTODYN using the advanced non-linear orthotropic material model of Riedel et al. (2003). The theoretical procedure for derivation of CFRP dynamic properties can be validated by a comparison of the experimentally- and theoretically- determined data sets and an assessment of their accuracy in the simulation of hypervelocity impact on a space representative composite structure.

The manufacturer-supplied properties of the composite laminate (referred to herein as the CARMHIS CFRP) are provided in terms of constituent properties, however, they are insufficient for micromechanics analysis using Huang's bridging matrix and Chamis' strength of materials approach for predicting the composite elastic and strength properties respectively. As such, a number of constituent properties must be approximated. The full set of constituents used in the micromechanics analysis is listed in Table 4-1.

Following the procedure outlined in Chapter 4.1.1.2, a full material data set is derived for simulation in AUTODYN using the advanced non-linear composite material model.

The in-plane uniaxial stress-strain curves of the laminate are shown in Figure 4-15 and Figure 4-16 compared to the experimental measurements. It can be noted that there is a significant amount of deviation between the experimental and theoretical stress-strain curves.

Table 4-1 Constituent properties used for micromechanics.

Property	*Symbol*	*Value*	*Source*
Fibre:			
Density	ρ_f	1.79 g/cm³	Tenax data sheet
Longitudinal tensile modulus	E_{f11}	395 GPa	Tenax data sheet
Transverse tensile modulus	E_{f22}	13.33 GPa	E_m relationship (a)
In-plane Poisson's ratio	ν_{f12}	0.2385	Common property
Out-of-plane Poisson's ratio	ν_{f23}	0.2981	Common property
In-plane shear modulus	G_{f12}	24.80 GPa	G_m relationship (a)
Out-of-plane shear modulus	G_{f23}	5.80 GPa	Transverse isotropy
Longitudinal tensile strength	X_{ft}	4560 MPa	Tenax data sheet
Longitudinal compression strength	X_{fc}	2042 MPa	Common property
Resin:			
Density	ρ_m	1.22 g/cm³	Krempel data sheet
Tensile modulus	E_m	3.10 GPa	Average property
Poisson's ratio	ν_m	0.375	Common property
Shear modulus	G_m	1.127 GPa	Isotropy
Tensile strength	X_{mt}	73.82 MPa	Average property
Compression strength	X_{mc}	280.40 MPa	10% rule (b)
Shear strength	S_{mxy}	86.634 MPa	ILSS dominance
Fracture energy	G_{fm}	240 J/m²	Similar material
Maximum tensile strain	$\varepsilon_{m,max}$	2%	Average property

(a) Daniel and Ishai (1994)
(b) Hart-Smith (1992)

Under tension at 0° the curve agrees very well initially, exhibiting an elastic modulus within the range of experimentally-measured values. In the experiments, the laminate failed at ultimate strains of ~0.8-1.0%, while the predicted behaviour continued until a failure strain of ~1.15%, resulting in a larger failure stress prediction.

Under tension at 90°, the predicted elastic modulus is higher than that measured experimentally. Additionally, the ultimate strain measured in experiments was between ~0.9-1.15%, while an ultimate strain of ~1.6% was predicted. A significantly higher degree of plasticity is observed in the experimental curve than that predicted from Puck's action plane failure criteria.

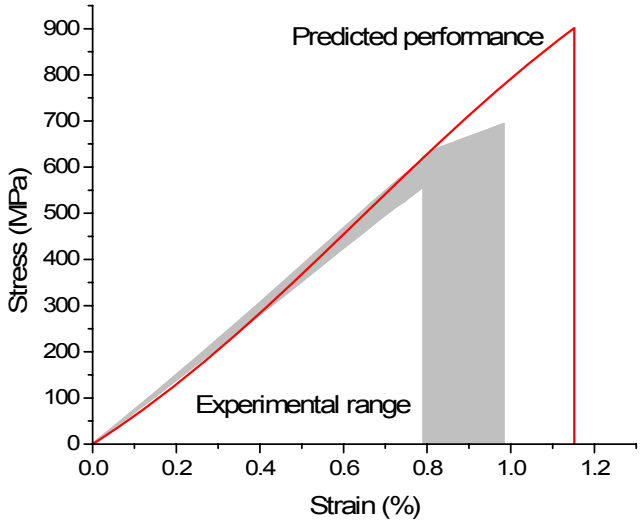

Figure 4-15 Stress-strain curve of the [0/±45] composite laminate under uniaxial tension at 0° (material 11-direction) measured in experiments and predicted using Puck's action plane criteria.

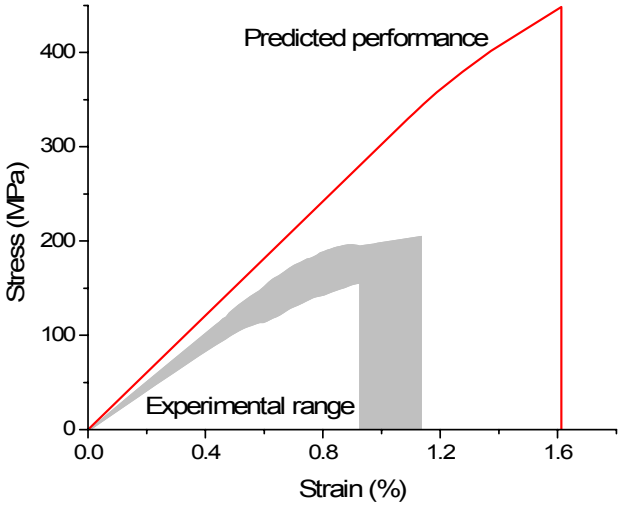

Figure 4-16 Stress-strain curve of the [0/±45] composite laminate under uniaxial tension at 90° (material 22-direction) measured in experiments and predicted using Puck's action plane criteria.

Although in-plane shear stress-strain curves are also derived from Puck's failure criteria, direct comparison with the experimental curves is difficult as the experiment measured the performance under uni-axial stress applied at 45°, which is not a pure in-plane shear strength measurement. The variance between the experimental- and predicted in-plane stress-strain curves was significantly higher than expected. During the WWFE (Hinton et al., 2004), 14 tests cases were considered to assess the

performance of various composite failure theories. Of the tests cases investigated, three considered the performance of multi-directional laminates (both CFRP/epoxy and Glass/epoxy) under uni-axial tension and an additional four cases required a biaxial stress envelope to be derived which included the uniaxial failure strengths. In the three uni-axial stress-strain test cases, Puck's action plane criteria predicted curves which showed, in general, very good agreement with the experimental curves. Indeed, the test considered in the WWFE most similar to this analysis is Test Case 7, which predicted the stress-strain curve of a (0°/±45°/90°) AS4/3501-6 laminate under uni-axial tension at 90°. Puck's action plane criteria provided a result in which the "shape and magnitude of the predicted stress-strain curve (was) in very good agreement with (the) experiment" (Hinton et al., 2002).

The 90° (material 22-direction) is selected as the master stress-strain curve for the quadratic yield function as it provides the highest degree of plasticity (see Figure 4-16). As such, a_{22} is set equal to 1.0. The master effective stress-effective plastic strain curve is shown in Figure 4-17.

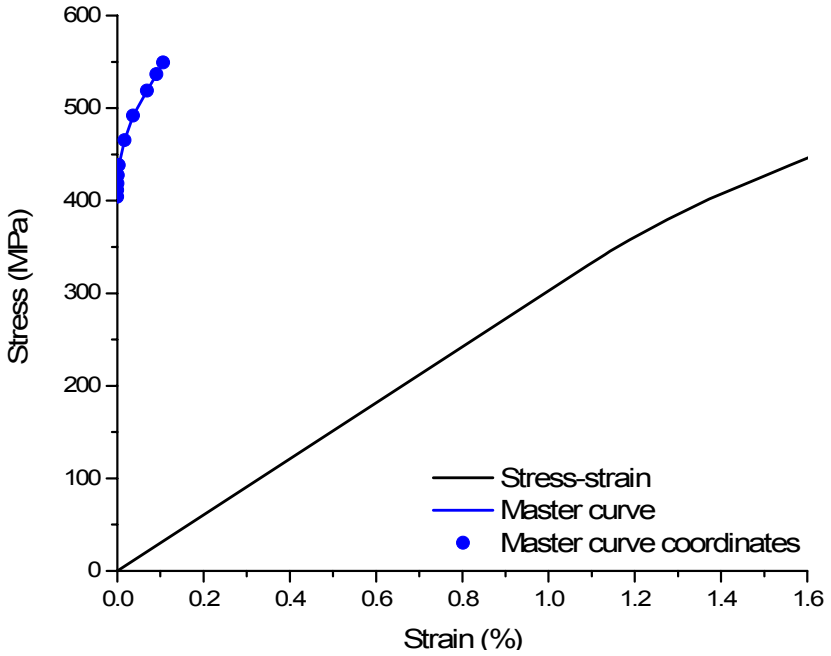

Figure 4-17 Stress-strain curve and derived effective stress-effective plastic strain master curve (22-direction).

The three plasticity coefficients related to uniaxial tension and the three coupling coefficients can be calculated from the plastic Poisson's ratios of the structure using:

$$a_{11} = a_{22}\frac{\nu_{21}^{p}}{\nu_{12}^{p}} \qquad a_{22} = a_{33}\frac{\nu_{32}^{p}}{\nu_{23}^{p}} \qquad a_{33} = a_{11}\frac{\nu_{13}^{p}}{\nu_{31}^{p}}$$
$$a_{12} = -a_{22}\nu_{21}^{p} \qquad a_{23} = -a_{22}\nu_{23}^{p} \qquad a_{13} = -a_{33}\nu_{31}^{p} \tag{95}$$

The plastic Poisson's ratios ν_{12}^{p} and ν_{21}^{p} are determined from the 0° and 90° tensile tests respectively, as shown in Figure 4-18.

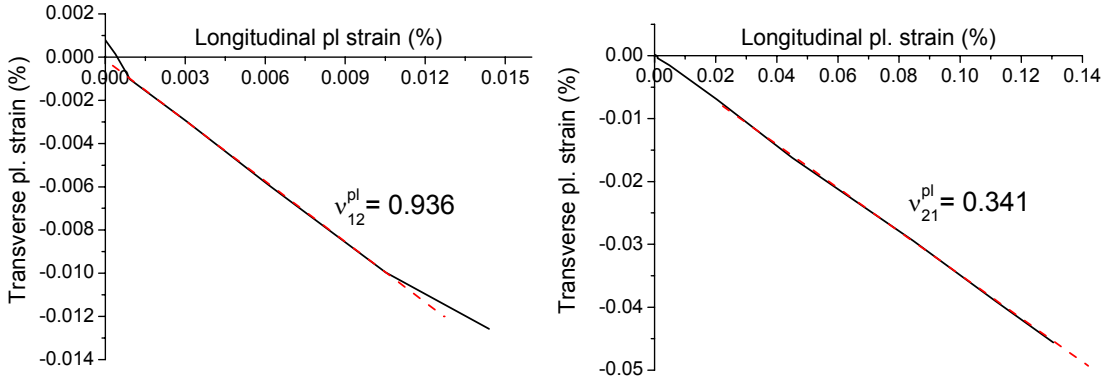

Figure 4-18 Defining the plastic Poisson's ratio ν_{12}^{p} (left) and ν_{21}^{p} (right) from the 0° uniaxial tension test.

The plasticity parameters a_{11} and a_{12} are simply calculated from Eq. (95). The in-plane shear stress-strain analysis showed no discernable plasticity, thus Eq. (83) is applied, i.e.:

$$a_{66} = \frac{1}{3}\cdot\left(\frac{\overline{\sigma}_{\#1}}{\tau_{12}}\right)^{2}$$

Plasticity is assumed in the through-thickness direction; therefore the plasticity parameter a_{33} was determined by setting the final master curve coordinate equal to the directional failure (Eq. (84)). Similarly, shear in the through-thickness direction is expected to exhibit plasticity.

The remaining plasticity coefficients a_{13} and a_{23} cannot be determined using the plastic Poisson ratio relationships as no out-of-plane stress-strain curves can be described using Puck's action plane criteria. As such, it is necessary to make idealized assumptions about the strain performance in

such tensile tests. Under loading in the 22-direction, it is expected that some transverse plastic strain is present. In this case the Poisson's ratio is adopted for the plastic Poisson's ratio, effectively defining a rate of transverse plastic strain in the post-yield regime equal to the transverse strain under elastic loading. As such,

$$a_{23} = -a_{22}\nu_{23}^{p} = -a_{ss}\nu_{23}$$

Under loading in the through-thickness direction, it is reasonable to assume the plastic strain in the 11-direction is minimal (given that under direct tension in the 11-direction very little plastic strain was measured).

Therefore,

$$a_{13} = -a_{33}\nu_{31}^{p}$$

where

$$\nu_{31}^{p} = -\frac{d\varepsilon_{11}^{p}}{d\varepsilon_{33}^{p}}$$

and

$$\varepsilon_{11}^{p} \approx 0$$

Thus,

$$a_{13} \cong 0$$

All coefficients of the yield function have been defined, and conformity to the return algorithm stability requirements (see Chapter 2.2.3.2) is confirmed.

As the quadratic yield function is six-dimensional in stress space, it is difficult to visualize the complete yield surface. However, under only normal stresses the yield function reduces to:

$$f(\sigma_{ij}) = a_{11}\sigma_{11}^{2} + a_{22}\sigma_{22}^{2} + a_{33}\sigma_{33}^{2} + 2a_{12}\sigma_{11}\sigma_{22} + 2a_{23}\sigma_{22}\sigma_{33} + 2a_{13}\sigma_{11}\sigma_{33} = k \qquad (96)$$

Similarly, under only shear stresses the yield function reduces to:

$$f(\sigma_{ij}) = 2a_{44}\sigma_{23}^{2} + 2a_{55}\sigma_{31}^{2} + 2a_{66}\sigma_{12}^{2} = k \qquad (97)$$

The yield surface in the normal and shear stress spaces is shown in Figure 4-19 in addition to the yield surface defined by the experimental parameters. It can be seen that the defined yield surface forms an ellipse in both the normal and shear stress spaces. In normal stress space, the experimentally-derived surface is significantly more elongated than the

theoretical surface. This is a result of differing assumptions applied in derivation of the plasticity parameters. The experimental data set assumes no plastic strain in the 11-direction, thus the surface is defined such that directional failure is initiated prior to the initial yield condition. For the theoretical data set, a small degree of plasticity is predicted in the 0° tensile analysis. In shear stress space, the experimental yield surface is more elongated in the in-plane shear direction than the theoretical data set.

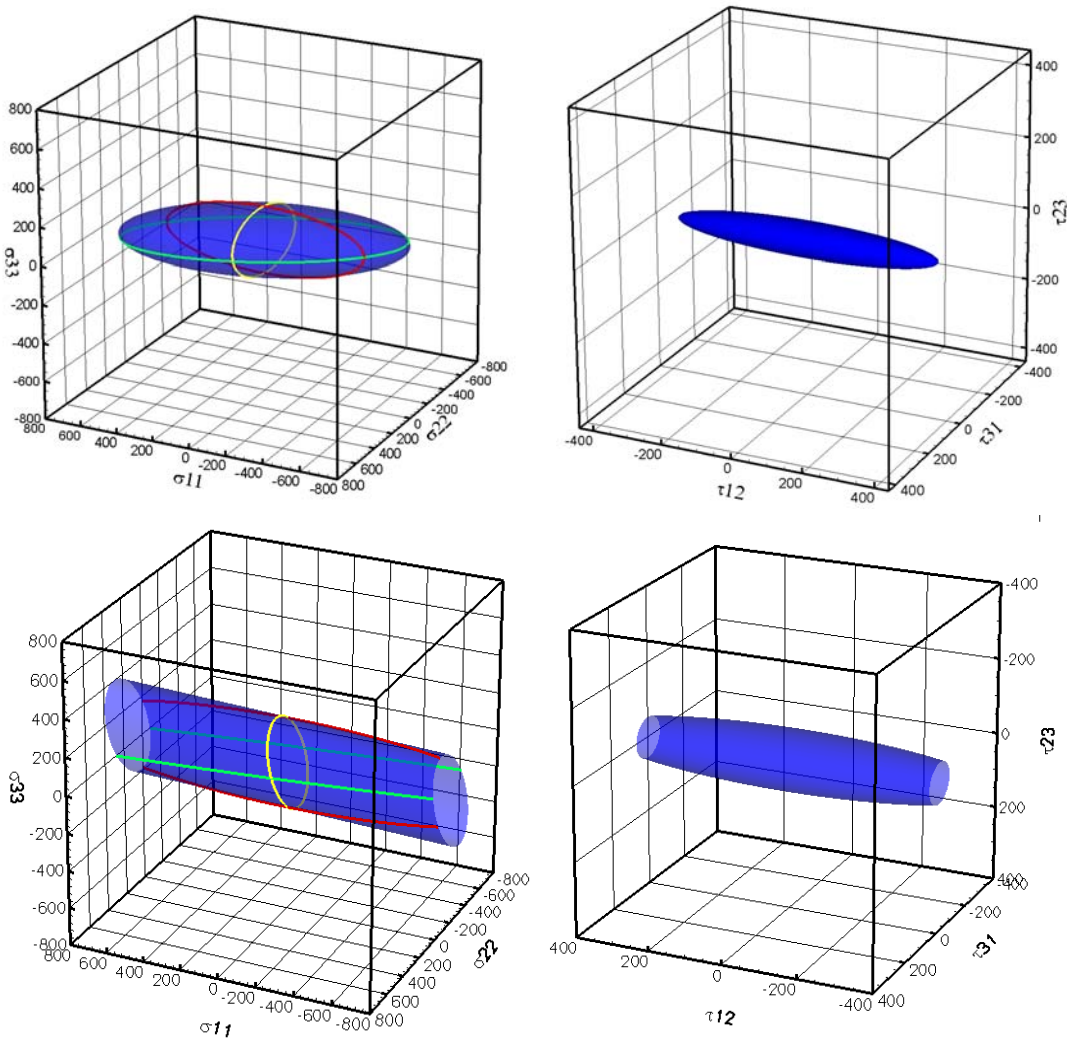

Figure 4-19 Comparison of the laminate yield surfaces defined from the experimentally (bottom) and numerically derived data sets (top). Left: Normal stress space; Right: Shear stress space (stress given in MPa).

The non-linear softening performance of the CFRP laminate is defined in the theoretical data set using the assumption of brittle failure under in-plane tension and shear loading, with the inclusion of non-zero fracture

energies for through-thickness tensile loading (matrix effect) and out-of-plane shear loading (geometrical effect). A comparison of the through-thickness tensile behaviour of the composite laminate is given in Figure 4-20, incorporating the defined elastic behaviour, non-linear hardening, and non-linear softening. Despite the differing means of definition, a good level of agreement is shown between the experimentally- and theoretically defined through-thickness behaviour of the CARMHIS CFRP. The experimentally-defined material shows a slightly higher elastic modulus and less plasticity than the theoretical model. Although both models define non-zero fracture energies for this loading case, the effect is not clearly observable in Figure 4-20.

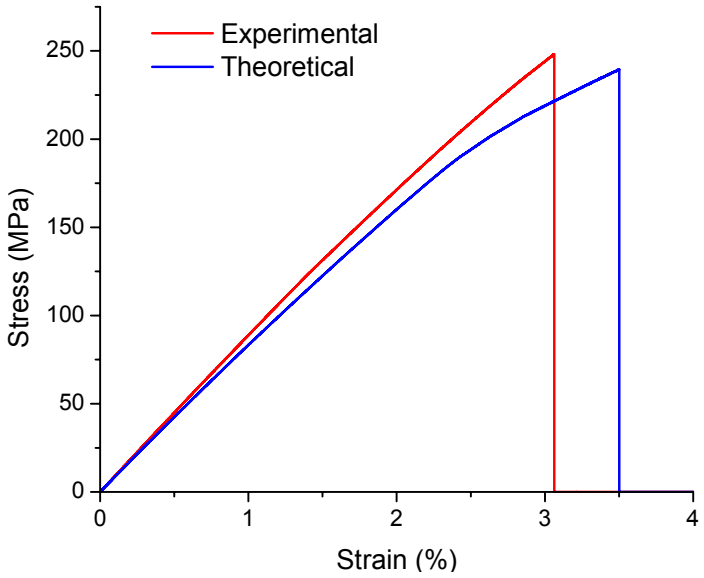

Figure 4-20 Through-thickness stress-strain behaviour of the theoretically- and experimentally defined CARMHIS CFRP laminate.

The equation of state reference curve (Hugoniot) is defined using the polynomial form of the Mie-Grüneisen EOS, shown in Figure 4-21 in terms of Hugoniot pressure versus compression. It can be observed that the theoretically-derived Hugoniot reference curve shows a polynomial increase with increasing compression compared to a constant linear increase for the curve defined in the experimental characterisation study. The theoretically-defined curve describes a decrease in compressibility with increasing shock amplitude while the experimental data set defines a constant level regardless of impact-induced shock amplitude. The polynomial increasing nature of the theoretically-defined curve leads to a description of higher pressures at higher levels of material compression than the experimental curve.

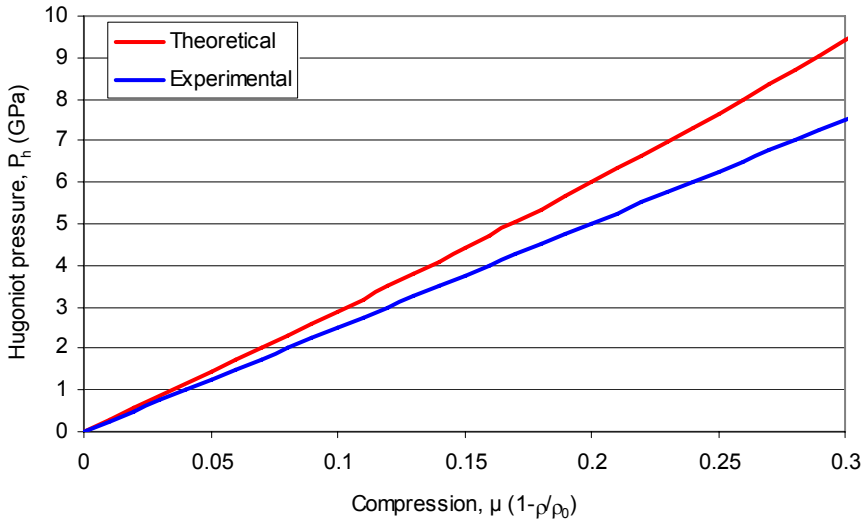

Figure 4-21 Comparison of theoretically- and experimentally defined Hugoniot reference curves for the CARMHIS CFRP.

4.1.1.3.1 Comparing the Experimentally- and Theoretically Derived CFRP Data Sets

A comparison of the properties derived for the CARMHIS CFRP laminate following the theoretical-based procedure and using experimental characterisation (details in Wicklein et al. 2007) is given in Table 4-2.

Table 4-2 Theoretically and experimentally derived material data sets for the CARMHIS CFRP multidirectional laminate.

Parameter	*Theory*	*Experiment*
Equation of State: Ortho		
Reference density [g/cm^3]	1.516	1.563
Young's Modulus 11 [GPa]	79.24	72.90
Young's Modulus 22 [GPa]	30.25	22.89
Young's Modulus 33 [GPa]	8.71	9.07
Poisson's Ratio 12	0.84	0.77
Poisson's Ratio 23	0.33	0.55
Poisson's Ratio 31	0.0071	0.0187
Shear Modulus 12 [GPa]	36.32	48.35
Shear Modulus 23 [GPa]	2.87	0.558
Shear Modulus 31 [GPa]	3.36	0.873
Bulk Modulus A1 [GPa]	28.24	25.04
Parameter A2 [GPa]	5.35	0
Parameter A3 [GPa]	16.97	0

Parameter B0	2.496	1.098
Parameter B1	2.496	1.098
Parameter T1 [GPa]	28.24	25.04
Parameter T2 [GPa]	5.35	0
Strength: Orthotropic Yield		
A11	0.364	0.025
A22	1	1
A33	3.576	0.660
A12	-0.341	-0.1285
A13	0	0
A23	-0.3345	-0.473
A44	23.066	3.157
A55	21.405	2.128
A66	0.388	0.061
Eff. Stress #1 [MPa]	404.277	120.025
Eff. Stress #2 [MPa]	411.432	145.745
Eff. Stress #3 [MPa]	418.587	168.157
Eff. Stress #4 [MPa]	427.416	186.774
Eff. Stress #5 [MPa]	438.265	199.633
Eff. Stress #6 [MPa]	465.098	210.166
Eff. Stress #7 [MPa]	491.930	218.984
Eff. Stress #8 [MPa]	518.763	227.068
Eff. Stress #9 [MPa]	536.651	232.702
Eff. Stress #10 [MPa]	549.173	238.825
Eff. Plastic Strain #1	0	0
Eff. Plastic Strain #2	2.701E-6	1.7236E-4
Eff. Plastic Strain #3	8.295E-6	3.4473E-4
Eff. Plastic Strain #4	1.697E-5	5.1709E-4
Eff. Plastic Strain #5	3.997E-5	6.8945E-4
Eff. Plastic Strain #6	1.670E-4	8.6140E-4
Eff. Plastic Strain #7	3.676E-4	0.00103
Eff. Plastic Strain #8	6.907E-4	0.00121
Eff. Plastic Strain #9	9.088E-4	0.00138
Eff. Plastic Strain #10	1.070E-3	0.00155
Failure: Orthotropic Softening		
Tensile Failure Stress 11 [MPa]	901.177	619
Tensile Failure Stress 22 [MPa]	448.398	195
Tensile Failure Stress 33 [MPa]	217.75	245.7
Maximum Shear Stress 12 [MPa]	374.639	280.5
Maximum Shear Stress 23 [MPa]	66.018	39.0
Maximum Shear Stress 31 [MPa]	68.524	47.5
Fracture Energy 11 [J/m^2]	1E-6	1E-6
Fracture Energy 22 [J/m^2]	1E-6	1E-6
Fracture Energy 33 [J/m^2]	240	333.5
Fracture Energy 12 [J/m^2]	1E-6	1E-6
Fracture Energy 23 [J/m^2]	1018	1378
Fracture Energy 31 [J/m^2]	1018	747

From Table 4-2 it is apparent that the laminate elastic properties (E, ν, G) are predicted to a good degree of accuracy using micromechanics and laminate theories. The agreement of the predictions is greater for in-plane properties (E_{11}, ν_{12}, G_{12}) than transverse (E_{22}, ν_{31}, G_{23}). However, given the uncertainties in estimating unknown constituent properties, the agreement is considered as good.

The principal differences between the equation of state parameters lie in the quadratic and cubic bulk moduli (A_2, A_3), and the Grüniesen gamma (B_0, B_1). Wicklein et al. (2007) selected zero values for A_2 and A_3 based on comparison of flyer plate impact test signals. Manual adjustment of these parameters was unable to provide a more satisfactory agreement with the experimental velocity-time signal, and as such they were set to zero. This results in a linear Hugoniot curve, defining a constant degree of material compressibility regardless of shock amplitude. In the theoretically-derived data set, it is considered that a more realistic representation of material behaviour is obtained by giving positive, non-zero values to the A2 and A3 terms, resulting in a Hugoniot which describes a decrease in material compressibility with increasing shock pressures. An isotropic assumption was used to calculate these parameters, based on a common shock velocity-particle velocity relationship defined from existing flyer plate impact test data. The Grüniesen gamma terms (B_0 and B_1) are also approximated using an isotropic assumption (i.e. the slope of the U_s-u_p curve is constant in all material directions) and are calculated using the Dugdale and MacDonald (1953) simplification based on the slope of the U_s-u_p relationship (Eq. (76)).

The failure properties show a reasonable degree of agreement with the exception of tensile failure stress in the 22-direction. In this direction Puck's theory predicted a failure strength more than double that of the experimentally measured value. As discussed previously, this result was unexpected given the favourable results obtained by Puck in the WWFE (Hinton et al., 2002) for multi-directional laminates loaded in uniaxial tension.

The plasticity parameters and master effective stress-effective plastic strain curve are considered secondary properties as they are based on the pre-defined elastic-plastic stress-strain behaviour. The theoretically-derived master curve shows significantly higher effective stress values than the experimentally-determined values as a result of the higher stress-strain capability calculated in the material 22-direction using Puck's action plane

criteria. These higher effective stress values result in higher out-of-plane shear stress plasticity parameters (a_{44} and a_{55}) as well as a higher through-thickness plasticity parameter (a_{33}). Some phenomenological differences in the experimental and theoretical derivation are also the cause of variance in the two data sets, namely the assumption of no plastic strain in the material 11-direction for the experimental data set.

A good degree of agreement is found for the non-linear softening parameters. The experimentally-derived data set shows an increased fracture energy for out-of-plane shearing 23 than 31 (derived from ENF tests), probably as a result of the decreased fibre alignment in the 22-direction. The theoretical assumption, based on a relationship between mode I and mode II fracture energies of CFRP composites, is unable to reproduce this difference.

4.1.1.3.2 Comparing HVI Simulation Results using the Experimentally- and Theoretically Derived CFRP Data Sets

Verification of the material parameter derivation procedure can be further made through application of the derived data set in hypervelocity impact simulations. The two structures considered for the analysis are shown in Figure 4-22.

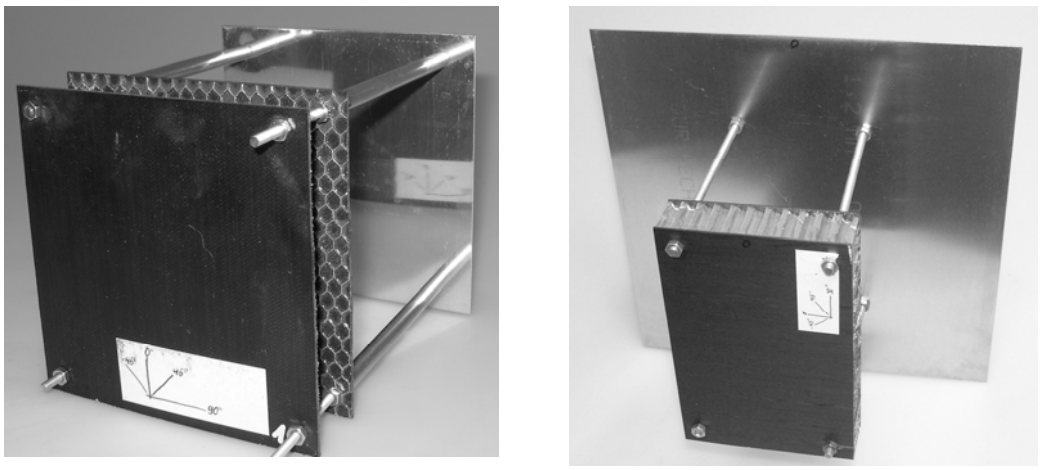

Figure 4-22 Targets subject to hypervelocity impact testing and numerical simulation. Left: Spaced CFRP facesheets; Right: CFRP/Al HC SP.

In Figure 4-23 a comparison between the experimental (both visual and ultrasonic) and numerical damage caused by oblique (60°) impact of a 1.775mm Al-sphere at 6.095 km/s is shown. In the experiment a roughly circular perforation is observable on the front facesheet. On the rear

facesheet a number of small cracks are visible in the photograph of the target. The ultrasonic scan reveals widespread internal damage (delamination). The honeycomb core shows a damage cone biased to one side relating to the oblique impact velocity vector (to right of page). A comparison of the numerical damage shows little difference. The numerical simulation applying the experimentally-characterised data set shows a near-triangular shaped perforation hole in the front facesheet. Two separate areas of damage are observable on the rear facesheet, with one large perforation hole corresponding to the debris ejected normally from the front facesheet, and a second smaller perforation biased in the direction of the impact velocity vector. The damage to the honeycomb core is significantly less that that observed in the experiment. The numerical simulation applying the data set derived from theoretical principles and generalised properties also shows a non-circular perforation hole in the front facesheet (although dimensions of the perforation hole are comparable with the experiment). The rear facesheet also shows two separate perforation holes, with similar dimensions and location as the experimentally-characterised model. The honeycomb core shows considerably more damage in the model with the theoretically-characterised CFRP material than that using the experimental characterisation, however it is still much less than that observed in the experiment.

The damage induced by the normal impact of a 1.179mm Al-sphere at 4.935 km/s on the spaced CFRP facesheets is shown in Figure 4-24 compared to simulated damage using both the experimentally- and numerically-characterised data sets. The experiment shows a clear perforation hole in the front facesheet and very minimal cracks on the rear facesheet. Again, ultrasonic scans of the rear facesheet show a degree of internal damage (delamination) in the rear CFRP sheet. Both numerical models again show very similar predictions, both providing a circular perforation hole in the front facesheet and no noticeable damage on the rear side of the rear facesheet. As with simulation of the oblique impact experiment, the numerical simulation using the experimentally-characterised data set shows significantly more damage than the theoretically-characterised model in the front facesheet about the perforation hole. This represents the major difference between the two models.

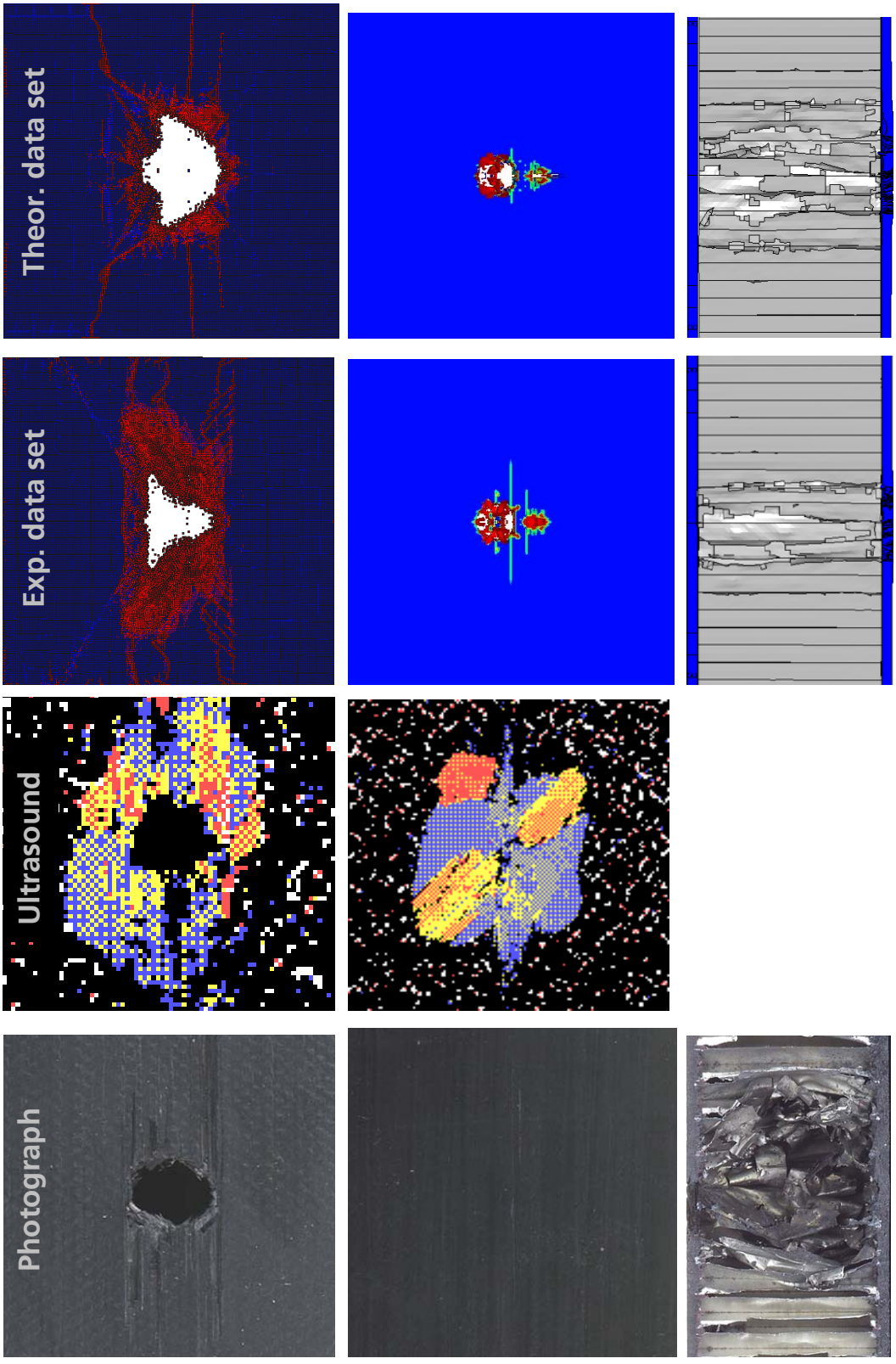

Figure 4-23 Comparison of damages after oblique (60°) impact of a 1.775mm Al-sphere at 6.095 km/s.

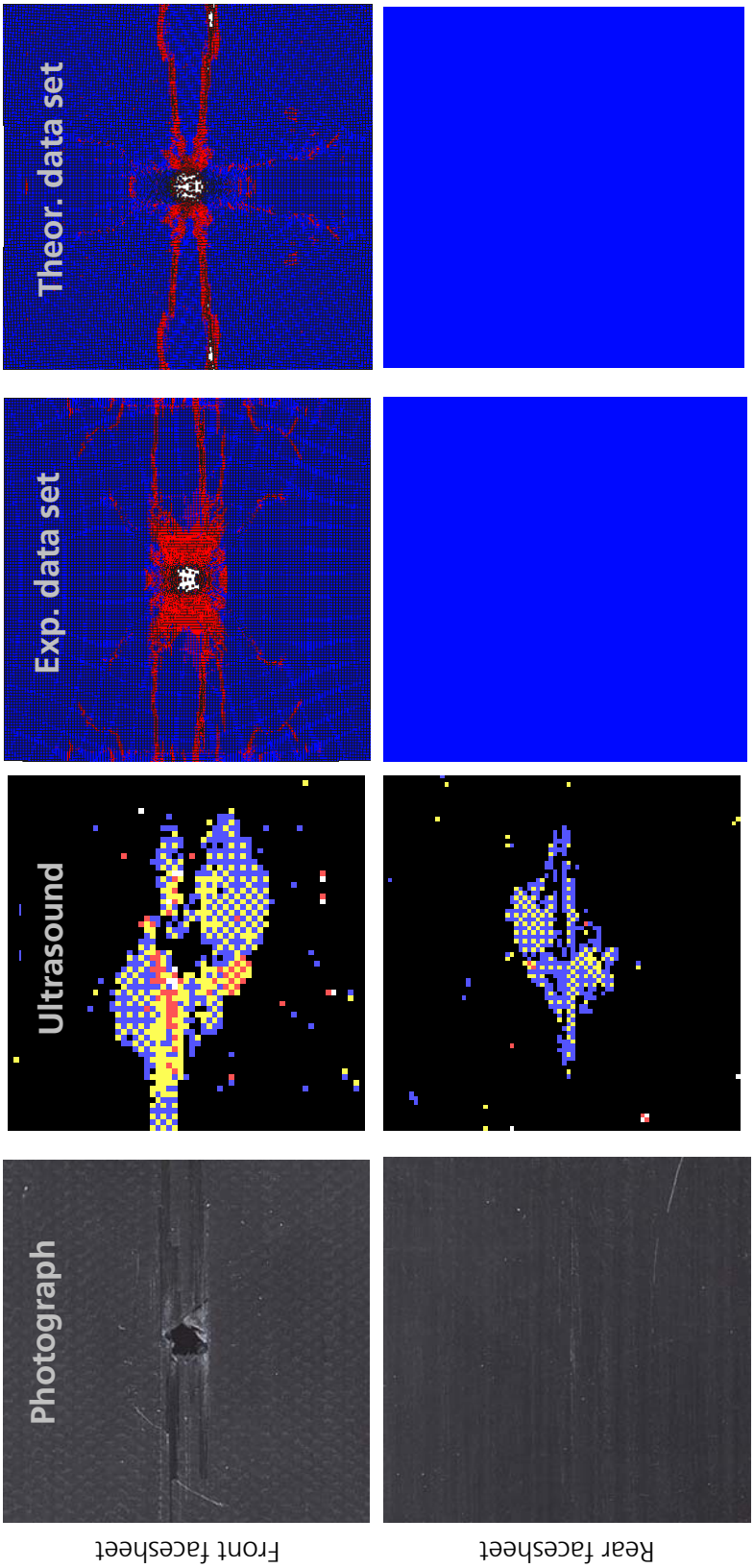

Figure 4-24 Comparison of damages after normal impact of a 1.179mm Al-sphere at 4.935 km/s.

For simulation of oblique impact, both numerical models over-predict the level of damage to the rear CFRP facesheet. In the experiment small cracks and delamination is observed, while the numerical simulations predict clear perforation. This over-prediction of damage could be the result of overly capable honeycomb core foils, which act to channel the fragment cloud more severely in the numerical simulations than in the experiment (notable in the extension of damage in the honeycomb core). For simulation of normal impact, the simulations slightly under-predict the damage. In the experiment slight cracking and internal delamination are observable. In both numerical simulations damage can be seen on the front side of the rear facesheet; however the rear side remains damage free. Nonetheless it is considered that both numerical simulations provide a reasonable prediction of the experimental damage induced by hypervelocity impact of debris particles. There is no discernable improvement provided by experimental-characterisation of the composite material even though some significant differences were input into the numerical model (see Table 4-2).

As such, the derivation procedure is considered reasonable for the prediction of CFRP material properties for application in the advanced orthotropic material model of Riedel et al. (2003).

4.1.1.4 Derivation of CFRP Material Data for Impact-Induced Disturbance Simulations

The derivation procedure is applied to the 0.5mm thick, quasi-isotropic CFRP laminate representative of those used on-board GAIA (see Figure 4-2 for details). This laminate will be referred to as the GAIA CFRP herein. For micromechanics a number of the constituent properties must be estimated. An overview of the constituent data used for the micromechanics analysis is given in Appendix B.

From micromechanics and Classical Laminate Theory the in-plane elastic properties of the laminate are determined as:

$$E_{11} = 23.64 \text{ GPa} \qquad E_{22} = 49.124 \text{ GPa}$$
$$\nu_{12} = 0.0.0538 \qquad G_{12} = 14.88 \text{ GPa}$$

Although the laminate is quasi-isotropic, there is a significant difference in the in-plane stiffness properties E_{11} and E_{22}. The elastic properties are

calculated in CLT by determining the stiffness matrices of the individual layers in a global coordinate system $[\overline{Q}_{ij}]_k$, from which the stiffness matrix of the structure is determined. However, the laminate stiffness matrix is not merely a summation of the contributions of each individual ply to the principle directions; it is a function of the geometry, material properties and stacking sequence of the individual plies. The elastic properties of the composite laminate are calculated from the laminate compliance matrix, where the compliance matrix is simply the inverse stiffness matrix. The stiffness matrix is of the form:

$$[C]=\begin{bmatrix} A_{xx} & A_{xy} & A_{xs} & B_{xx} & B_{xy} & B_{xs} \\ A_{yx} & A_{yy} & A_{ys} & B_{yx} & B_{yy} & B_{ys} \\ A_{sx} & A_{sy} & A_{ss} & B_{sx} & B_{sy} & B_{ss} \\ B_{xx} & B_{xy} & B_{xs} & D_{xx} & D_{xy} & D_{xs} \\ B_{yx} & B_{yy} & B_{ys} & D_{yx} & D_{yy} & D_{ys} \\ B_{sx} & B_{sy} & B_{ss} & D_{sx} & D_{sy} & D_{ss} \end{bmatrix} \tag{98}$$

For symmetric laminates, the coupling-stiffness coefficients (B coefficients) are equal to zero as:

$$B_{ij} = \frac{1}{2}\sum_{k=1}^{n} Q_{ij}^{k}\left(h_k^2 - h_{k-1}^2\right) \tag{99}$$

and $h_k^2 \cong h_{k-1}^2$

In the case where the laminate is not symmetric, in-plane forces produce flexural and twisting deformations while moments produce extension of the middle surface in addition to flexure and twisting. Analytically this is represented in the [B] matrix terms, which are non-zero for the 0.5mm thick laminate. In the inversion of the stiffness matrix, these non-zero terms are then included in the calculation of the coefficients which define the elastic properties. In practice this means that when a non-symmetric laminate is loaded by an in-plane force, flexural and twisting deformations are produced as a result of strain mismatch through-the-thickness of the laminate (each layer with a different stiffness has therefore a different strain response to the applied load). The amplitude of the flexural and twisting deformations is dependent on how severe the strain mismatch is, which is dependent on the stacking sequence.

As the GAIA CFRP laminate is non-symmetric, flexural and twisting deformations produced under in-plane loading mean that Hooke's law, as

applied in Chapter 4.1.1.2 for derivation of the out-of-plane composite properties, is not valid. In this case, the material through-thickness elastic stiffness is approximated from the u.d. ply transverse stiffness, i.e.:

$$E_{33} = E_{c,22} \tag{100}$$

The out-of-plane Poisson's ratios (ν_{23}, ν_{31}) and stiffness moduli (G_{23}, G_{31}) are determined in Puck's action plane failure theory analysis.

The stress-strain response of the laminate under uni-axial tension at 0° and 90° is calculated using Puck's action plane criteria. In Figure 4-25 it is shown that under tensile loading in the 22-direction, the laminate is predicted to exhibit negative transverse plastic strain. The quadratic yield function of Chen et al. (1997) is not suitable for materials showing a transverse expansion in the post-yield regime under longitudinal loading. This type of performance is very rarely observed, and in fact, it should be noted that in the course of the World-Wide Failure Exercise, no non-symmetric laminate was considered. The accuracy of Puck's action plane failure criteria and degradation parameters have therefore not been (to the knowledge of the author) validated for non-symmetric laminates, and as such, the negative transverse plastic strain should be considered with some scepticism. For this analysis, the predicted negative plastic strain is inverted to provide positive transverse plastic strain (and thus a positive plastic Poisson's ratio).

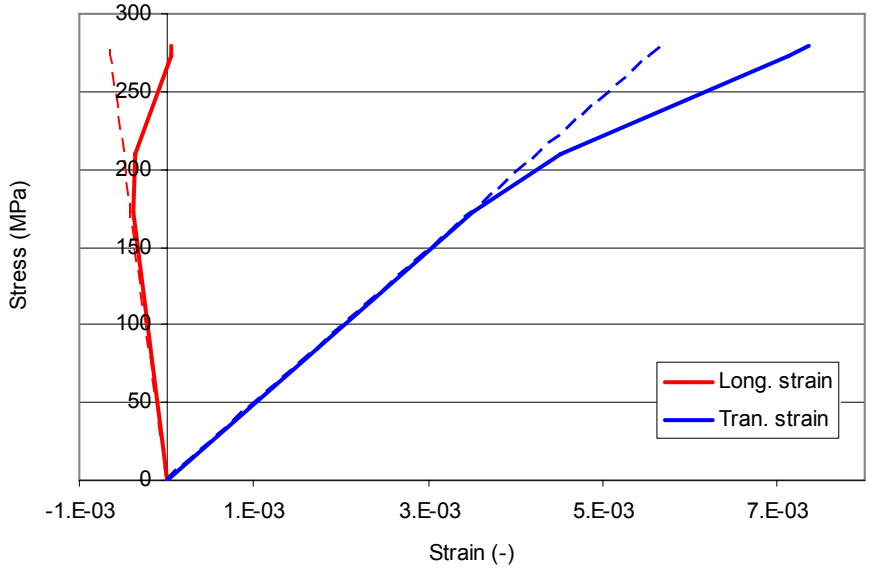

Figure 4-25 Stress-strain curves of the GAIA CFRP laminate under: Upper: tension at 0°; Middle: tension at 90°; Lower: in-plane shear.

The most plastic strain is predicted to occur under uniaxial loading at 0°. As such, this response is used to define the master curve of the GAIA CFRP laminate, shown in Figure 4-26.

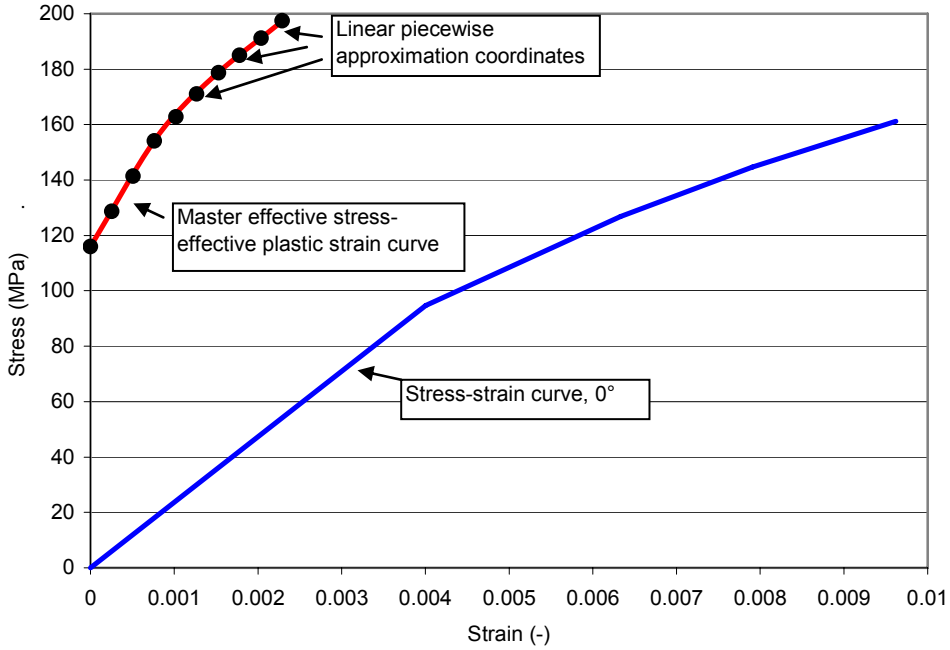

Figure 4-26 Definition of the effective stress-effective plastic strain curve for the GAIA CFRP laminate under uniaxial tension at 0°.

The plastic Poisson ratio's ν_{12}^{p} and ν_{21}^{p} are defined in Figure 4-27 from the predicted in-plane stress-strain curves.

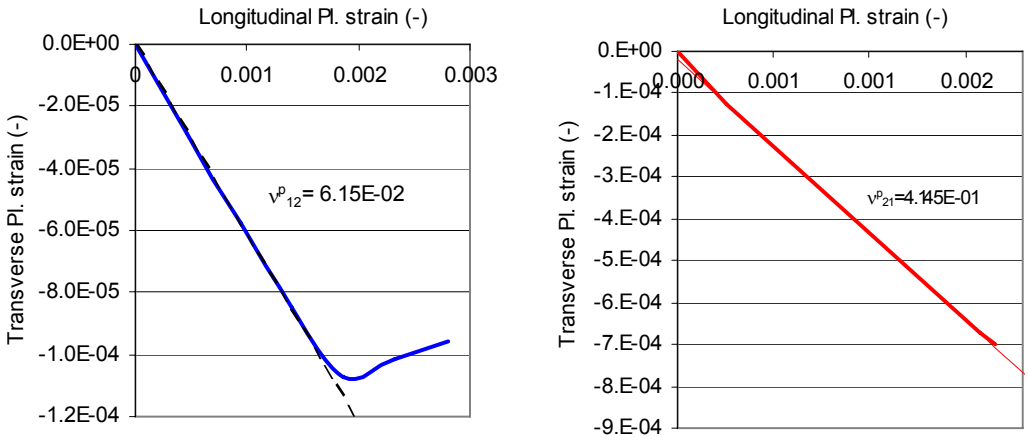

Figure 4-27 Defining the plastic Poisson's ratio ν_{12}^{p} (left) and ν_{21}^{p} (right) from the 0° uniaxial tension test.

The plasticity parameters a_{22} and a_{12} can be simply calculated using:

$$a_{22} = a_{11}\frac{\nu_{12}^p}{\nu_{21}^p} \qquad a_{12} = -a_{22}\nu_{21}^p$$

Under in-plane shear loading it is apparent in Figure 4-25 that the laminate behaviour is linear-elastic until failure, i.e. there is no plasticity. Thus the plasticity parameter a_{12} is calculated from Eq. (83):

$$a_{66} = \frac{1}{3}\left(\frac{\bar{\sigma}_{\#1}}{\tau_{12}}\right)^2$$

For uni-axial tension in the through-thickness direction and transverse shear, plasticity is expected due to yielding of the polymer matrix.

In the absence of stress-strain data it is not possible to calculate the plastic Poisson's ratio, ν_{23}^p. It is assumed that the elastic Poisson's ratio can be adopted for the plastic loading phase. It is further assumed that during through-thickness tensile loading the transverse strain in the 11 direction would be minimal, therefore:

$$a_{13} = -a_{33}\nu_{31}^p \tag{101}$$

where $\nu_{31}^p = -\frac{d\varepsilon_{11}^p}{d\varepsilon_{33}^p}$. Assuming $d\varepsilon_{11}^p \approx 0$:

$$\rightarrow a_{13} \approx 0$$

The yield surface of the GAIA CFRP laminate in normal and shear stress space is shown in Figure 4-28 and Figure 4-29 respectively. In normal stress space the yield surface forms a closed ellipsoid as required to ensure stability of the return algorithm. In comparison to the derived hardening surface of the CARMHIS CFRP (Figure 4-19) the ellipsoid is much fuller in the through-thickness direction relative to the in-plane directions. This is a result of the lower in-plane yield values of the GAIA CFRP. In shear stress space the hardening surface also forms a closed ellipsoid. As the in-plane shear yield stress is higher than the out-of-plane property the ellipsoid is extruded in the τ_{12} direction.

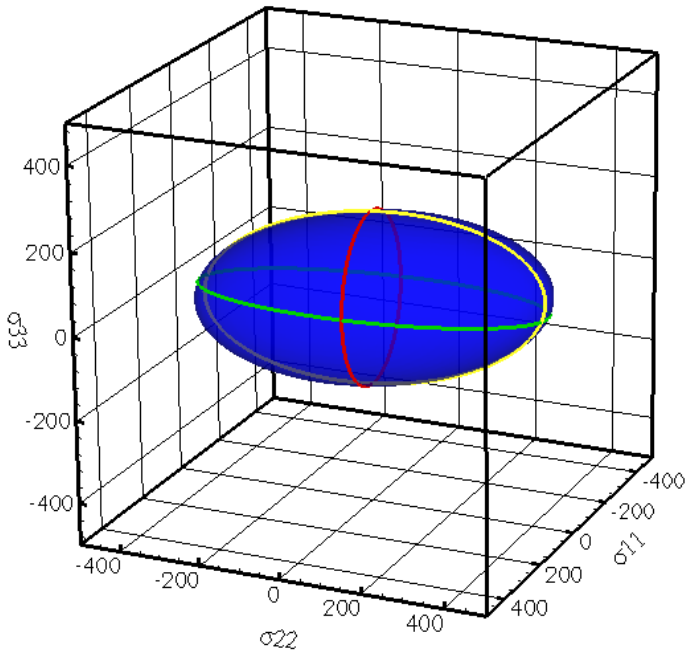

Figure 4-28 Yield surface of the GAIA CFRP laminate using the theoretically-derived plasticity parameters (stress given in MPa) in normal stress space. Curves correspond to cross-section plots.

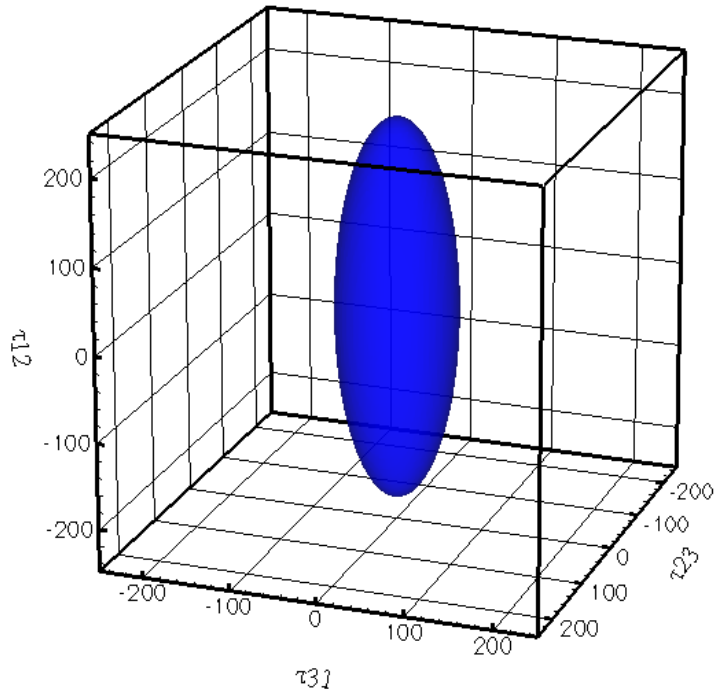

Figure 4-29 Yield surface of the composite laminate using the theoretically-derived plasticity parameters (stress given in MPa) in normal stress space.

The yield surface and the loading cases under which plasticity is active can be more clearly examined in normal stress space by considering the cross-section plots of the normal stress space yield body. The yield surface cross-section for $\sigma_{33} = 0$ is shown in Figure 4-30. It can be seen that under uniaxial loading in the 11-direction, the material will deform elastically until the initial yield condition is met. Following this, in addition to elastic deformation the material will begin to deform plastically at a rate defined by the master curve until reaching the final yield condition, which, in this case corresponds exactly to the directional failure stress. Under tension in the 22-direction, the material reaches its directional failure stress prior to the final yield condition.

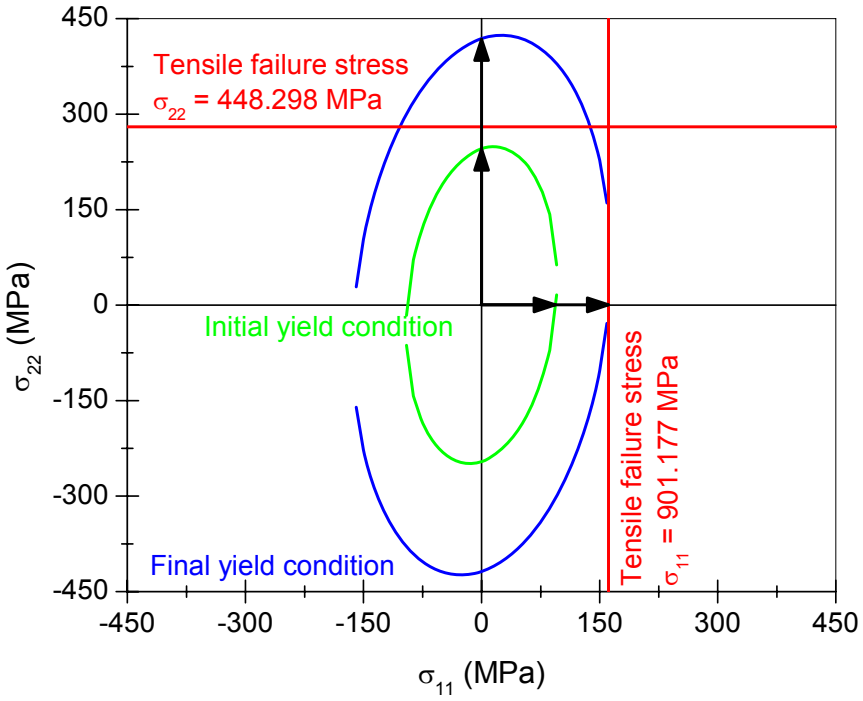

Figure 4-30 Yield surface cross section in normal stress space shown for $\sigma_{33} = 0$ (corresponds to green curve in Figure 4-28).

In Figure 4-31 and Figure 4-32 it can be seen that the directional failure stress σ_{33} is located outside the final yield condition. This is a constraint of the quadratic yield function, which only allows definition of a single parameter to relate the material anisotropy to the defined master curve.

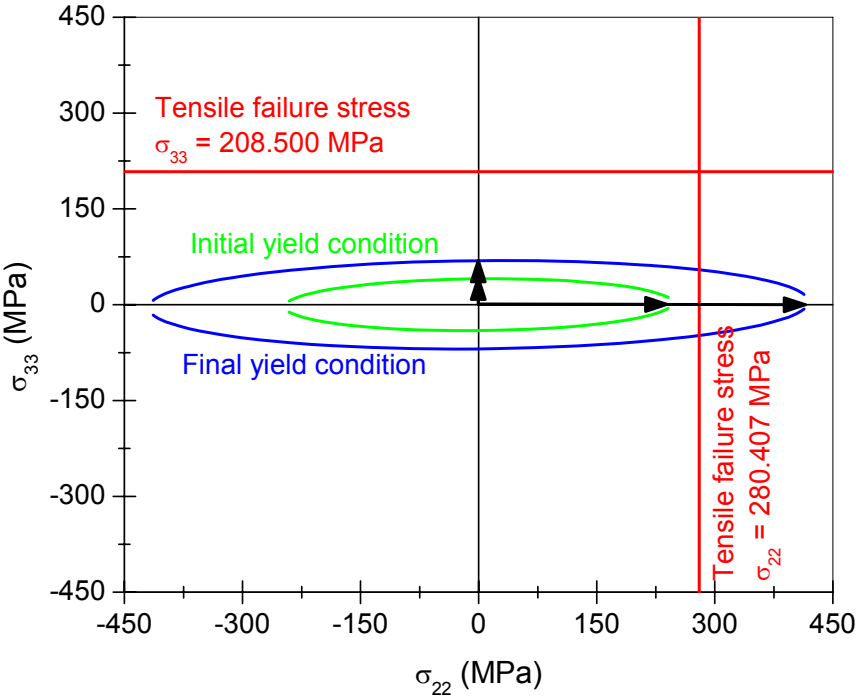

Figure 4-31 Yield surface cross section in normal stress space shown for $\sigma_{11} = 0$ (corresponds to yellow curve in Figure 4-28).

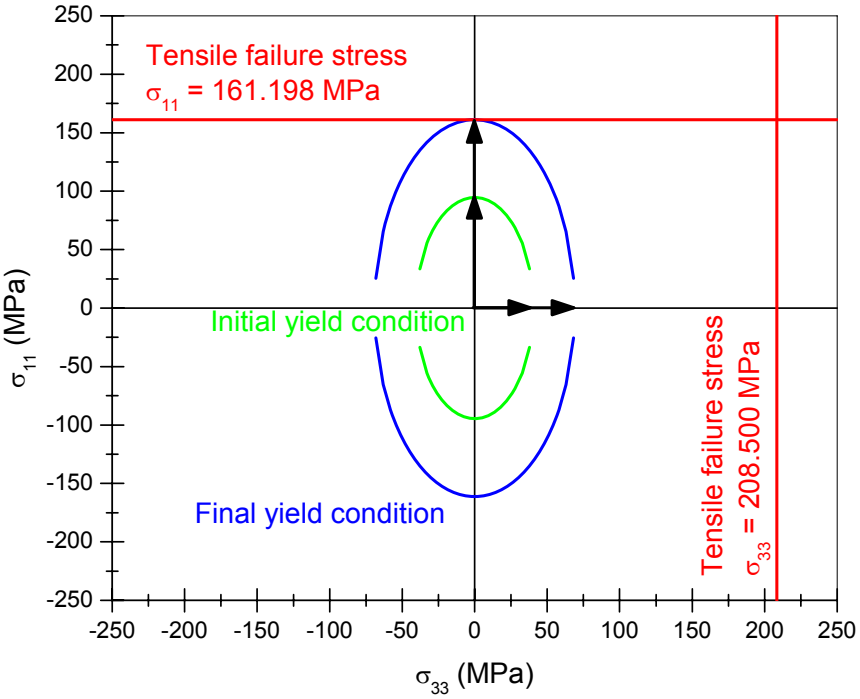

Figure 4-32 Yield surface cross-section in normal stress space shown for $\sigma_{22} = 0$ (corresponds to red curve in Figure 4-28).

The effect of the failure surface being located outside the limits of the hardening surface is that once the final yield condition has been met, the material will continue to deform plastically at this rate until the directional failure stress has been exceeded. This is clearly observable in Figure 4-33 which presents the results of a single element uni-axial tension test loaded in the 33-direction.

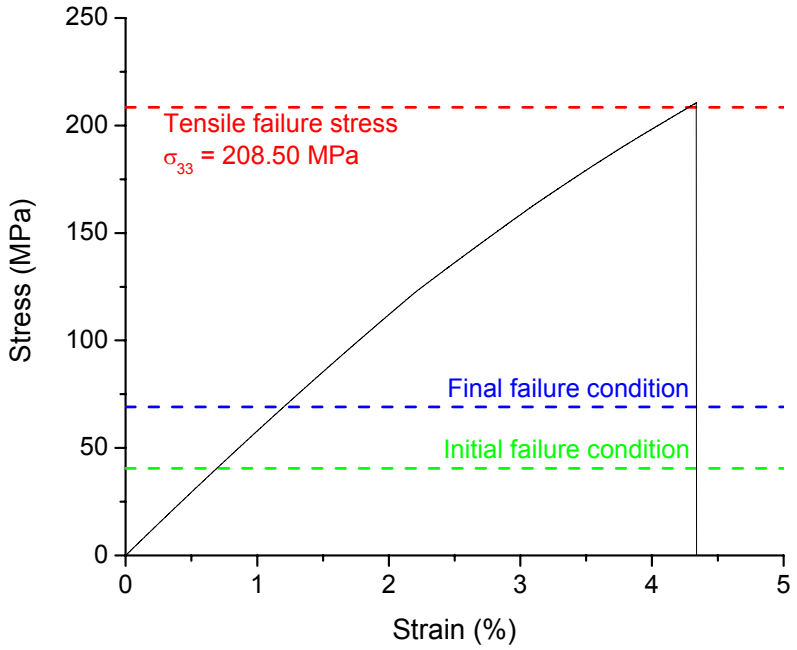

Figure 4-33 Stress-strain curve under uniaxial tension in the 33-direction. Initial and final yield conditions defined by the quadratic yield function are shown.

The equation of state parameters are defined from the orthotropic stiffness matrix (A_1) and using an isotropic assumption with the generalised U_s-u_p relationship based on existing flyer plate impact test data on CFRP laminates. The p-wave soundspeed of the GAIA CFRP laminate was measured using ultrasound as 2800 m/s.

The derived material data set for the GAIA CFRP laminate is listed in Table 4-3, along with the source of the specific values.

Table 4-3 Material data set for M55J/XU3508 (hardener 3473) 0.5mm thick laminate.

Parameter	*Value*	*Source*
Equation of State: Ortho		
Reference density [g/cm^3]	1.52	Measured
Young's Modulus 11 [GPa]	23.638	CLT
Young's Modulus 22 [GPa]	49.124	CLT
Young's Modulus 33 [GPa]	5.981	Micromechanics
Poisson's Ratio 12	0.054	CLT
Poisson's Ratio 23	0.421	Puck's action plane criteria
Poisson's Ratio 31	0.0085	Reciprocation
Shear Modulus 12 [GPa]	14.878	CLT
Shear Modulus 23 [GPa]	2.856	Puck's action plane criteria
Shear Modulus 31 [GPa]	2.856	Puck's action plane criteria
Bulk Modulus A1 [GPa]	10.224	From [C]
Parameter A2 [GPa]	6.8773	Linear U_s-u_p, general c_B
Parameter A3 [GPa]	6.8549	Linear U_s-u_p, general c_B
Parameter B0 [-]	1.9962	Γ, from linear U_s-u_p
Parameter B1 [-]	1.9962	Γ, from linear U_s-u_p
Parameter T1 [GPa]	20.327	Assumed EOS same in tension
Parameter T2 [GPa]	6.8773	and compression
Strength: Orthotropic Yield		
A11	1	Master direction
A22	0.1484	PPR12, PPR21
A33	0.5979	Assuming full plasticity
A12	-0.0615	PPR21, A22
A13	0	Assuming PPR31 $\rightarrow$ 0
A23	-0.0625	ν_{23} (elastic)
A44	2.726	Assuming full plasticity
A55	2.726	Assuming full plasticity
A66	0.2647	Assuming no plasticity
Eff. Stress #1 [MPa]	115.92945	From $(\sigma$-$\varepsilon)_{11}$, Puck's AP
Eff. Stress #2 [MPa]	128.63707	From $(\sigma$-$\varepsilon)_{11}$, Puck's AP
Eff. Stress #3 [MPa]	141.34468	From $(\sigma$-$\varepsilon)_{11}$, Puck's AP
Eff. Stress #4 [MPa]	154.0523	From $(\sigma$-$\varepsilon)_{11}$, Puck's AP
Eff. Stress #5 [MPa]	162.7666	From $(\sigma$-$\varepsilon)_{11}$, Puck's AP
Eff. Stress #6 [MPa]	171.02516	From $(\sigma$-$\varepsilon)_{11}$, Puck's AP
Eff. Stress #7 [MPa]	178.76225	From $(\sigma$-$\varepsilon)_{11}$, Puck's AP
Eff. Stress #8 [MPa]	184.99356	From $(\sigma$-$\varepsilon)_{11}$, Puck's AP
Eff. Stress #9 [MPa]	191.22487	From $(\sigma$-$\varepsilon)_{11}$, Puck's AP
Eff. Stress #10 [MPa]	197.45618	From $(\sigma$-$\varepsilon)_{11}$, Puck's AP
Eff. Plastic Strain #1	0	From $(\sigma$-$\varepsilon)_{11}$, Puck's AP
Eff. Plastic Strain #2	2.54E-04	From $(\sigma$-$\varepsilon)_{11}$, Puck's AP
Eff. Plastic Strain #3	5.09E-04	From $(\sigma$-$\varepsilon)_{11}$, Puck's AP
Eff. Plastic Strain #4	7.63E-04	From $(\sigma$-$\varepsilon)_{11}$, Puck's AP
Eff. Plastic Strain #5	0.00102	From $(\sigma$-$\varepsilon)_{11}$, Puck's AP

Eff. Plastic Strain #6	0.00127	From $(\sigma\text{-}\varepsilon)_{11}$, Puck's AP
Eff. Plastic Strain #7	0.00153	From $(\sigma\text{-}\varepsilon)_{11}$, Puck's AP
Eff. Plastic Strain #8	0.00178	From $(\sigma\text{-}\varepsilon)_{11}$, Puck's AP
Eff. Plastic Strain #9	0.00204	From $(\sigma\text{-}\varepsilon)_{11}$, Puck's AP
Eff. Plastic Strain #10	0.00229	From $(\sigma\text{-}\varepsilon)_{11}$, Puck's AP
Failure: Orthotropic Softening		
Tensile Failure Stress 11 [MPa]	161.198	Puck's failure criteria
Tensile Failure Stress 22 [MPa]	280.407	Puck's failure criteria
Tensile Failure Stress 33 [MPa]	208.500	Epoxy maximum tensile strain
Maximum Shear Stress 12 [MPa]	130.101	Puck's failure criteria
Maximum Shear Stress 23 [MPa]	60.376	Modified u.d. equation
Maximum Shear Stress 31 [MPa]	60.376	Quasi-isotropic
Fracture Energy 11 [J/m^2]	1E-06	Instantaneous failure in 11
Fracture Energy 22 [J/m^2]	1E-06	Instantaneous failure in 22
Fracture Energy 33 [J/m^2]	420	From resin G_{Ic}
Fracture Energy 12 [J/m^2]	1E-6	Not measurable
Fracture Energy 23 [J/m^2]	1360	G_{Ic}:G_{IIc} ratio
Fracture Energy 31 [J/m^2]	1360	G_{Ic}:G_{IIc} ratio

4.1.1.5 Aluminium Honeycomb Core

The aluminium honeycomb core foils are of Al 5056 and have been modelled using a linear equation of state, Johnson-Cook strength, and plastic strain failure model. An overview of the material parameters is given in Table 4-4.

Table 4-4 Linear EOS and Johnson-Cook strength parameters for Al 5056.

Equation of state: Linear		*Strength: Johnson-Cook*	
Density, ρ [g/cm³]	2.780	Shear modulus, G [GPa]	27.6
Bulk modulus, K [GPa]	79.06	Yield stress, A [MPa]	140.0
Reference temp., T_{ref} [K]	293.0	Hardening constant, B [MPa]	426.0
Specific heat, c [J/kgK]	875.0	Hardening exponent, n [-]	0.34
		Strain rate constant, C [-]	0.015
		Thermal soft. comp. m [-]	1.00
		Ref. strain rate, $\dot{\varepsilon}_{ref}$ [s^{-1}]	1.00
		Strain rate correction, ε_{pl} [-]	0.70

4.1.1.6 Projectile

An Al 2017-T4 projectile is used in all simulations modelled using a Mie-Grüneisen shock EOS, Johnson-Cook strength, and principal stress failure model. An overview of the material parameters is given in Table 4-5.

Table 4-5 Shock EOS and Johnson-Cook strength parameters for Al 2017-T4.

Equation of state: Shock		*Strength: Johnson-Cook*	
Density, ρ [g/cm³]	2.780	Shear modulus, G [GPa]	27.6
Grüneisen coeff., Γ [-]	2.0	Yield stress, A [MPa]	140.0
Parameter C1 [m/s]	5328	Hardening const, B [MPa]	426.0
Parameter S1 [-]	1.338	Hardening exponent, n [-]	0.34
Reference temp., T_{ref} [K]	293	Strain rate constant, C [-]	0.015
		Thermal soft. comp. m [-]	1.00
		Ref. strain rate, $\dot{\varepsilon}_{ref}$ [s^{-1}]	1.00
		Strain rate correction, ε_{pl} [-]	0.70

4.1.2 Numerical Set-Up

Numerical simulations have been performed in the commercial Hydrocode AUTODYN (Anon., 2005). Prior to simulation of hypervelocity impacts, sensitivity of the simulation results to the model set-up was investigated. The sensitivity study included solver type, discretisation of the CFRP facesheets, and parallel discretisation.

4.1.2.1 Numerical Model Sensitivity Study

4.1.2.1.1 Facesheet Solver

All hydrocodes utilize a set of differential equations established through application of the conservation of mass, momentum, and energy to describe the shock compression and release of continuous media:

Conservation of mass:

$$\rho_0 U_s = \rho\left(U_s - u_p\right) \tag{102}$$

Conservation of momentum:

$$\left(P - P_0\right) = \rho_0 U_s u_p \tag{103}$$

Conservation of energy:

$$E - E_0 = \frac{1}{2}\left(P + P_0\right)\left(V_0 - V\right) \tag{104}$$

where:

$$V = \frac{1}{\rho}$$

The differential equations derived from the conservation equations can be described in Lagrangian (body fixed) or Eulerian (space fixed) coordinates. The Lagrangian technique is a spatial description in which the material is described in geometric cells. Under deformation the grid moves and distorts with the material it models and the conservation of mass is therefore automatically satisfied. The Lagrangian descriptions of the differential equations are:

Lagrangian conservation of mass

$$\frac{d\rho}{dt} = -\rho \frac{\partial u_\alpha}{\partial x_\alpha} \tag{105}$$

Lagrangian conservation of momentum

$$\frac{du_a}{dt} = -\frac{1}{\rho} \frac{\partial \sigma_{\alpha\beta}}{\partial x_\beta} \tag{106}$$

Lagrangian conservation of energy

$$\frac{de}{dt} = -\frac{\sigma_{\alpha\beta}}{\rho} \frac{\partial u_\alpha}{\partial x_\beta} \tag{107}$$

To describe the dynamics of a continuous medium numerically, the differential equations describing the continuum must be discretized using a finite grid technique. The major limitation of the Lagrangian discretisation approach occurs in cases of high grid distortion (Anon., 2005b), as a result of which mesh lines can cross over one another or zones become re-entrant (see Figure 4-34). As a result, many large deformation problems are calculated using Eulerian techniques, which do not suffer from grid entanglement but have some limitations in terms of modelling material interfaces. Eulerian techniques are also numerically intensive in relation to grid-based Lagrangian techniques.

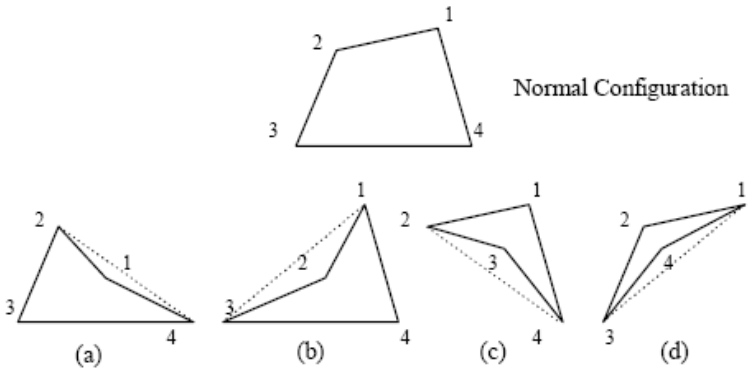

Figure 4-34 Typical Lagrangian mesh tangling (from Anon., 2005).

Smooth Particle Hydrodynamics (SPH) is another alternative for high-deformation problems. SPH is a grid-less technique which uses a set of interpolation points to model a continuum (shown in Figure 4-35) while still using the Lagrangian description of the conservation equations. Despite the known problems of SPH (e.g. Anderson, 1987), promising results have been obtained using the SPH solvers for a number of applications including hypervelocity impact (e.g. Riedel et al., 1999). SPH is a computationally-expensive approach when compared to typical cell-based discretisation techniques, and therefore generally its application should be minimized to structural areas subject to large deformation forces. AUTODYN-3D allows coupling of SPH and Lagrange solvers.

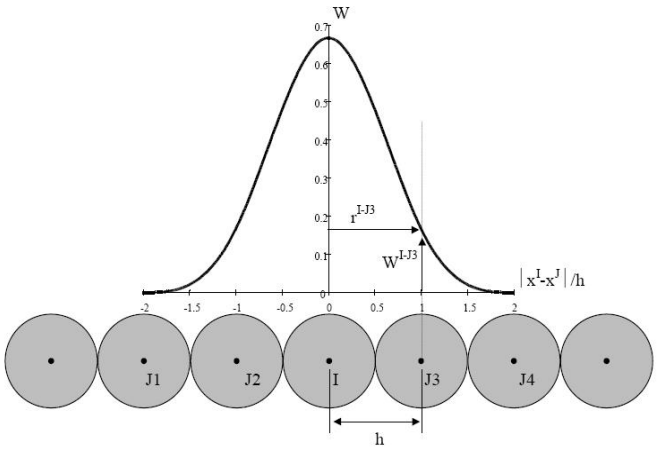

Figure 4-35 SPH processor – Interpolation 'particles' for calculating density at particle I (from Anon., 2005b).

To investigate the sensitivity of the model to the facesheet solver, and in the case of a coupled SPH/LAG set-up the extension of the SPH zone, simulations of a 0.8mm Al-projectile impacting at 6.0 km/s on the GAIA CFRP facesheet were performed. An overview of the sensitivity simulations is given in Table 4-6.

Table 4-6 Overview of the simulations performed to assess the sensitivity of transverse velocity measurements to solver type. NOTE: d_p = projectile diameter

Description	*Details*
SPH	Facesheet discretized purely using SPH
SPH/LAG 1	Coupled SPH/LAG facesheet, SPH extension = 5 x d_p
SPH/LAG 2	Coupled SPH/LAG facesheet, SPH extension = 10 x d_p
SPH/LAG 3	Coupled SPH/LAG facesheet, SPH extension = 15 x d_p
SPH/LAG 4	Coupled SPH/LAG facesheet, SPH extension = 20 x d_p
LAG	Facesheet discretized purely using LAG

Figure 4-36 shows a comparison of pressure contours at 3 µs after impact for the various models described in Table 4-6. It is apparent that significant differences are present in the propagation and reflection of the impact-induced shock. To quantify the sensitivity of out-of-plane velocity signals to solver type and SPH zone extension, sensitivity, gauge measurements were made 10mm from the impact location in the material 22-direction. The measurements are shown in Figure 4-37.

Generally, SPH is a more dispersive numerical technique than grid-based solvers. This can be observed in the propagation of the shock wave front in the simulation models, in which the initial compression wave has a much broader front in the SPH model than the LAG model. Upon reflection at the free-boundaries, the broader wave-front results in a less-clearly defined release wave. In comparison to the in-plane values, out-of plane velocities are significantly smaller. As such, any numerical "noise" in the in-plane velocity will translate into comparatively large changes in the out-of-plane velocities. Due to the dispersive nature of the SPH technique, these models are more susceptible to numerical noise and therefore the out-of-plane measurements are more susceptible to numerical inaccuracies.

It is considered that although SPH solvers are ideal for simulations involving high deformation and fracture/fragmentation, they are poor at reproducing low magnitude vibration. In the case of a simple facesheet, therefore, it is recommended that a purely Lagrangian discretisation is used. However, in the case of a sandwich panel structure, the fragmentation cloud generated by projectile impact on the front facesheet which further impacts upon the rear facesheet would preferably be modelled with some degree of SPH in the impact locality (i.e. the couple SPH/LAG models).

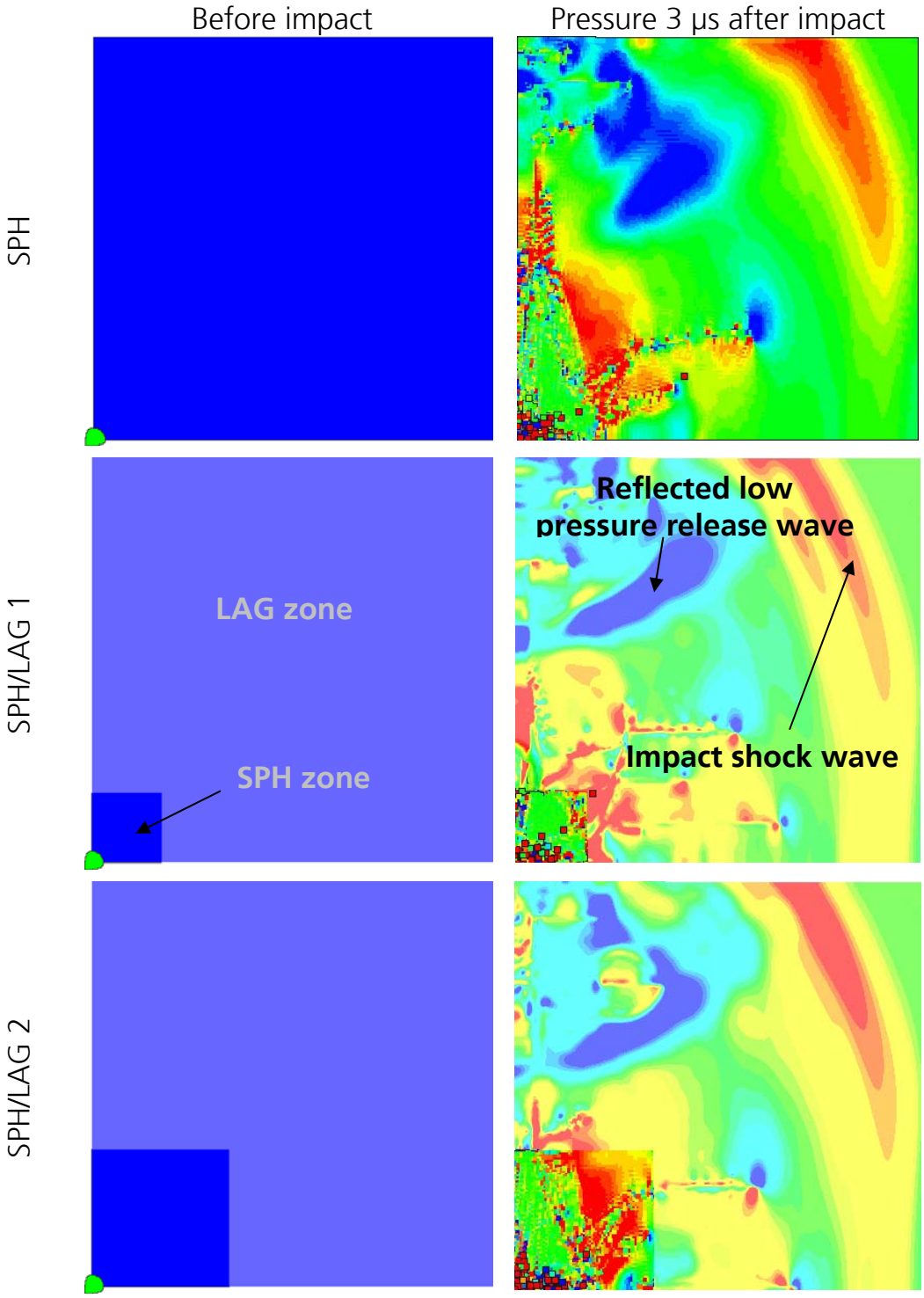
Before impact
Pressure 3 µs after impact
SPH
SPH/LAG 1
SPH/LAG 2
LAG zone
SPH zone
Reflected low pressure release wave
Impact shock wave

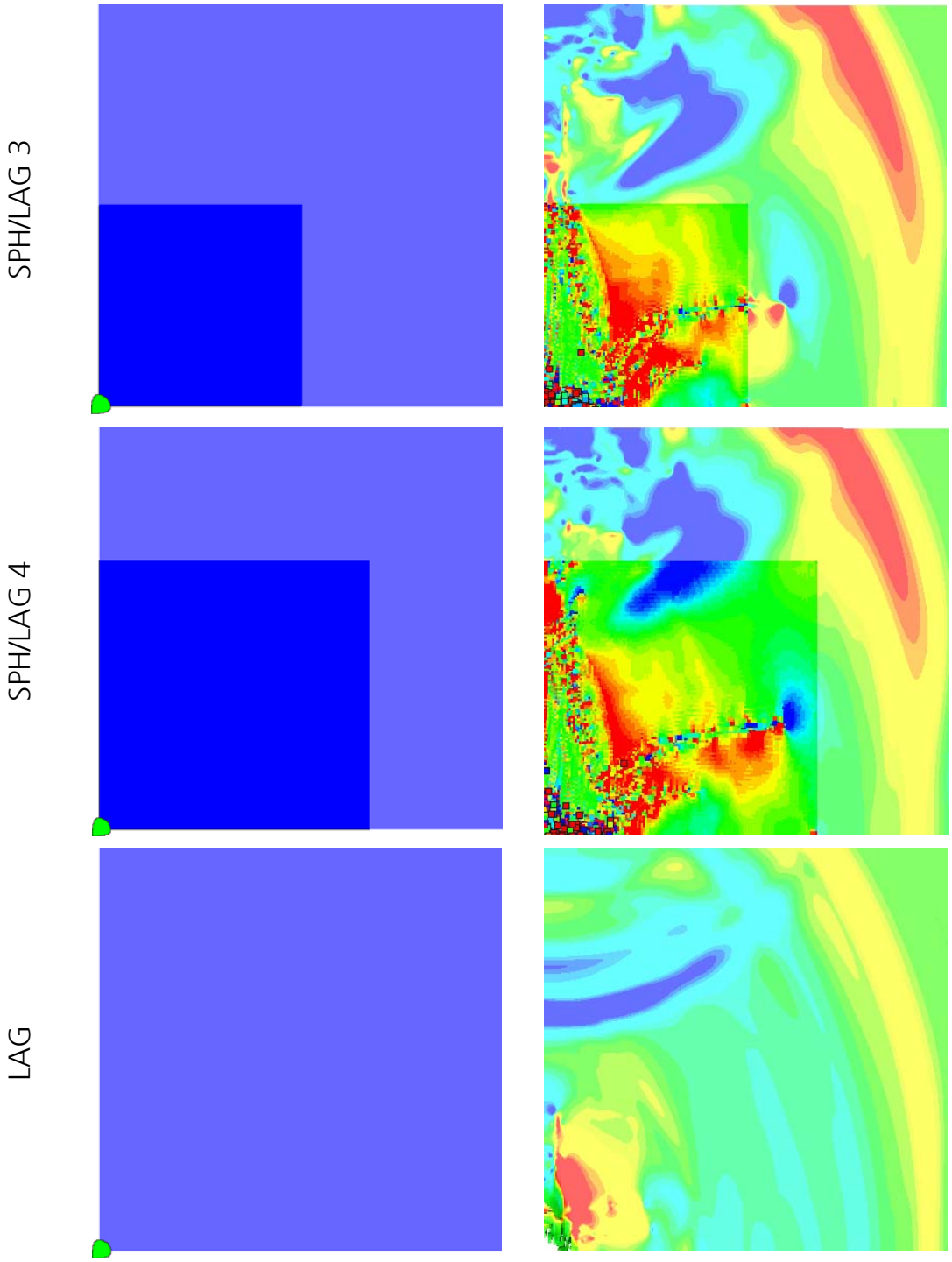

Figure 4-36 The sensitivity of wave propagation in CFRP to solver type, showing pressure contours 3 µs after impact (red – high pressure, blue – low pressure).

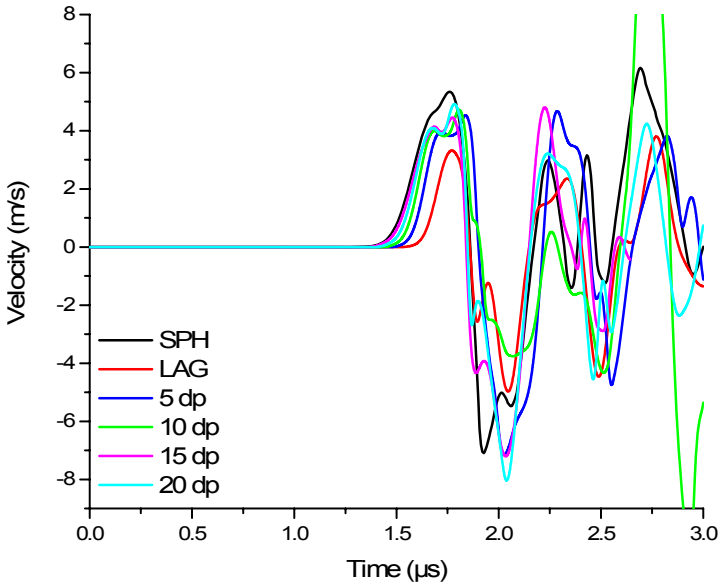

Figure 4-37 Out-of-plane velocity measurements (10 mm from impact in material 22-direction) from solver-type sensitivity simulations.

In AUTODYN, coupling of the grid-based solvers and SPH parts is an approximate technique. An assumption made in this coupling is that the parts across the join remain plane, i.e. there is no out-of-plane distortion. As such, it is recommended that this join be placed far enough from the impact location that very little out-of-plane deformation is present. Subsequently, this suggests a larger SPH zone, which returns to the problem of shock wave dispersion discussed previously. Additionally, it has been noted that propagation of a shock wave across the numerical coupling interface introduces some inconsistencies in the form of the shock wave. For example, in Figure 4-38 partial reflection of the low pressure trough following the shock wave front is shown at the SPH/LAG interface.

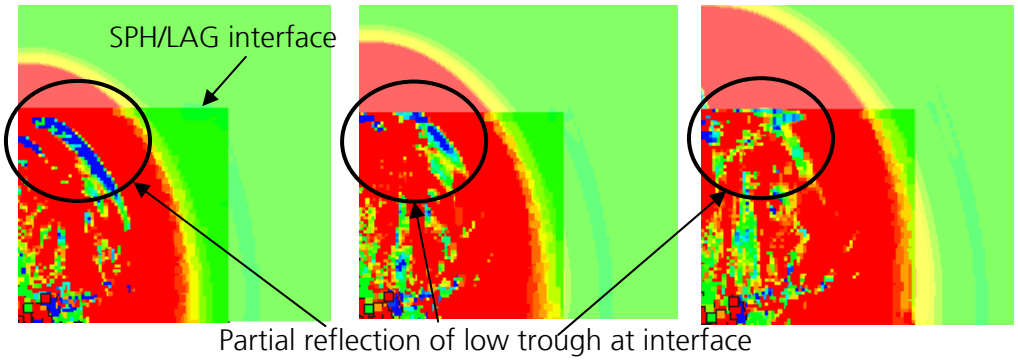

Figure 4-38 Imperfect transmission of a pressure wave across coupled SPH/LAG interface (0.8 mm Al projectile at 6.0km/s).

It has been observed in previous hypervelocity impact experiments on CFRP/Al HC sandwich panels (e.g. Schäfer et al., 2005) that the majority of mechanical damage in the rear facesheet is caused by fragments of the projectile, and indeed the damage potential of the CFRP fragments is very low. Assuming that the mechanical damage potential is proportional to the impulse which is imparted by the fragment cloud on the rear facesheet, it can then be assumed that the CFRP constituent of the fragment cloud plays little role in the excitation of the rear facesheet. Thus, modelling of the CFRP facesheet with a Lagrangian grid and incorporating an erosion model in the material definition to prevent grid entanglement problems should not have a significant effect on the transient response of the rear facesheet provided the projectile is discretized using SPH.

Modelling of Material Erosion

To prevent entanglement of the Lagrangian grid in the impact zone, an erosion model is required which can ensure that cells under high levels of deformation are removed from the simulation. The type of erosion model implemented with the CFRP facesheet model is instantaneous geometric strain, which states that when the deformation of an individual cell exceeds a predefined value at any stage then the cell is eroded. Instantaneous geometric strain is calculated from strain in the principal material directions using (from Anon., 2005):

$$\varepsilon_{eff} = \frac{2}{3}\left[\left(\varepsilon_1^2 + \varepsilon_2^2 + \varepsilon_3^2\right) + 5\left(\varepsilon_1\varepsilon_2 + \varepsilon_2\varepsilon_3 + \varepsilon_3\varepsilon_1\right) - 3\varepsilon_{12}^2\right]^{1/2} \qquad (108)$$

Instantaneous geometric strain erosion will only be activated in the case when a cell deforms out of shape. In preliminary models, it was observed that a number of front facesheet cells in the impact locality expanded isotropically following impact up to 100 times their original dimensions, for example see Figure 4-39. Given that these cells expanded isotropically and did not change shape significantly, they did not exceed the defined instantaneous geometric strain limit of 100%. These expanded cells acted by reducing the speed of the simulations significantly, and it is expected that in simulations of impact on the honeycomb sandwich panel, the generation of such cells following projectile impact on the front facesheet will cause problems.

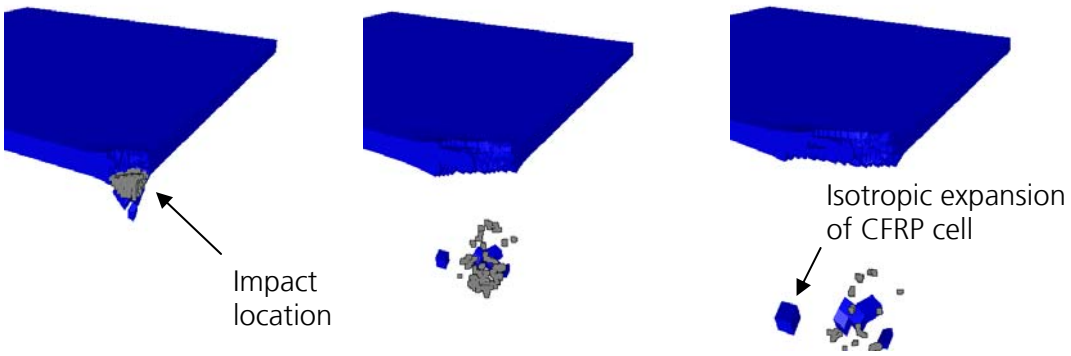

Figure 4-39 Isotropic expansion of Lagrangian cells in the fragment cloud generated during impact with the front facesheet (2, 12 and 18 µs after impact).

To account for this, a user-defined subroutine was implemented which combined the instantaneous geometric strain criteria for cells changing shape, and a density-based cut-off criteria for cells expanding isotropically.

4.1.2.1.2 Discretisation of the Targets

Meshing

To minimize the required processing time of the numerical simulations, the number of cells and the complexity of grid discretisation should be minimized such that the most efficient numerical model is defined while maintaining the integrity of the numerical solution. One way to reduce the number of cells is to increase the size of the facesheet elements proportionally to their respective distance from the impact location. This is referred to in AUTODYN as grading.

The two options considered initially to examine the numerical sensitivity to the grading of the grid was a quadrilateral part with grading bias in the two in-plane directions towards the impact location, and a cylindrical facesheet in which the facesheet was separated into two parts: an inner, finely meshed cylinder, and; an outer hollow cylinder with radial grading. The two models are shown in Figure 4-40. For both models, the cells in the impact locality were the same size as the projectile cells.

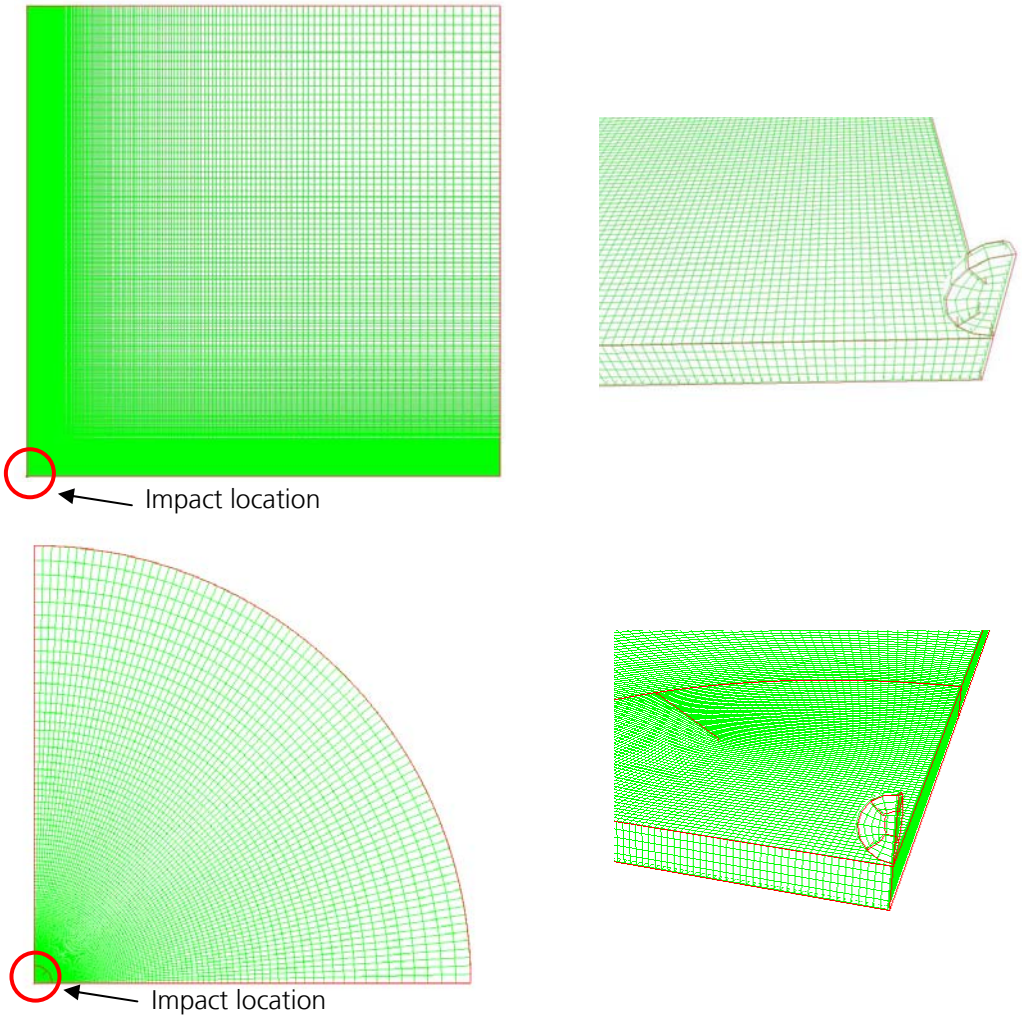

Figure 4-40 Upper: Square facesheet with grading in the two in-plane directions; Lower: Cylindrical facesheet with inner cylinder and radially graded outer hollow cylinder.

Simulation of a 0.75 mm Al-sphere impacting at 3.0 km/s on a 2 mm thick Al-7075-T3 plate was considered, the results of which are shown in Figure 4-41. At 45 µs after impact the square model incorporating rectangular cells with grading in the two in-plane directions shows a large disruption in the propagating disturbance waves at an angle ~45° from impact. This phenomenon is not apparent in the cylindrical model. The impacted material is isotropic and, as such, impact-induced disturbance waves should theoretically show a uniform dispersion. The undisturbed zone in the square simulation model is considered to be an effect of the inaccuracy of a square discretisation in properly propagating a radially-expanding disturbance wave. As such, it is considered that the cylindrical plate, graded in the radial direction, provides a superior result than the quadrilateral model.

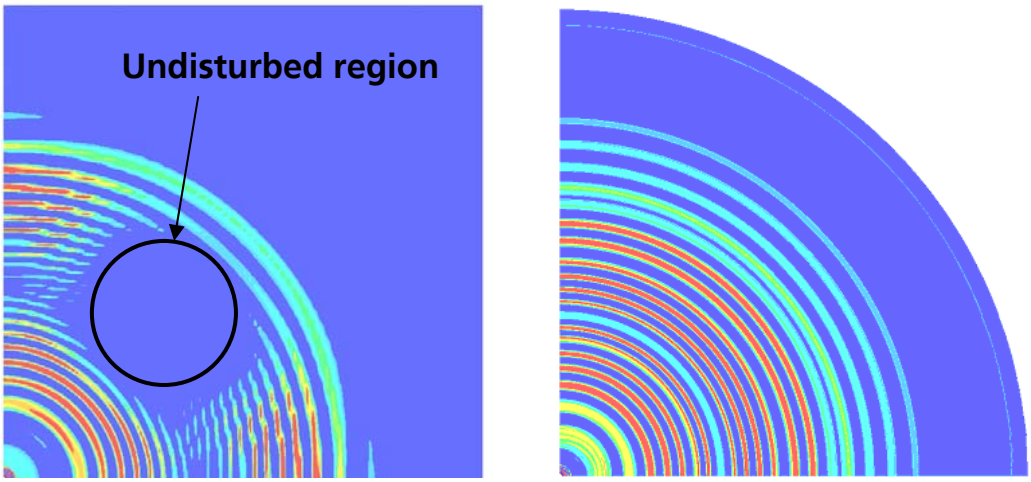

Figure 4-41 Shock wave propagation in an Al plate (note: pressure contours in square plate at 45 µs after impact, in cylindrical plate at 75 µs after impact).

In addition to the definition of facesheet grading type, the sensitivity of the numerical result to the rate of radial grading was investigated. An overview of the sensitivity simulations is given in Table 4-7.

Table 4-7 Overview of the simulations performed to assess the sensitivity of the numerical model to radial grading rate.

Description	*Details*
Grad_01	Radial grading at rate: 1.0%
Grad_025	Radial grading at rate: 2.5%
Grad_05	Radial grading at rate: 5.0%
Grad_075	Radial grading at rate: 7.5%
Grad_10	Radial grading at rate: 10.0%

Simulations were performed considering a 0.8 mm Al-sphere impacting at 6.0 km/s on the GAIA CFRP facesheet with 75 mm lateral extension modelled. A comparison of the pressure contours, recorded at 9 µs and 19 µs after impact, is given in Figure 4-42. The rate of radial grading is seen to have a significant effect on shock wave propagation and reflection in the GAIA CFRP laminate. Under lower grading rates (1%, 2.5%) the wave front is clearly defined at 9 µs post-impact, and its reflection from the free boundary can also be clearly seen. As the rate of grading increases the pressure contours appear progressively less well defined. Propagation rate of the shock wave is dependent on the material direction, i.e. it propagates faster in the 22- than the 11-direction due to differences in the in-plane elastic moduli of the laminate. At 19 µs after

impact a second waveform can be observed in the 1% grading rate simulation (marked in Figure 4-42).

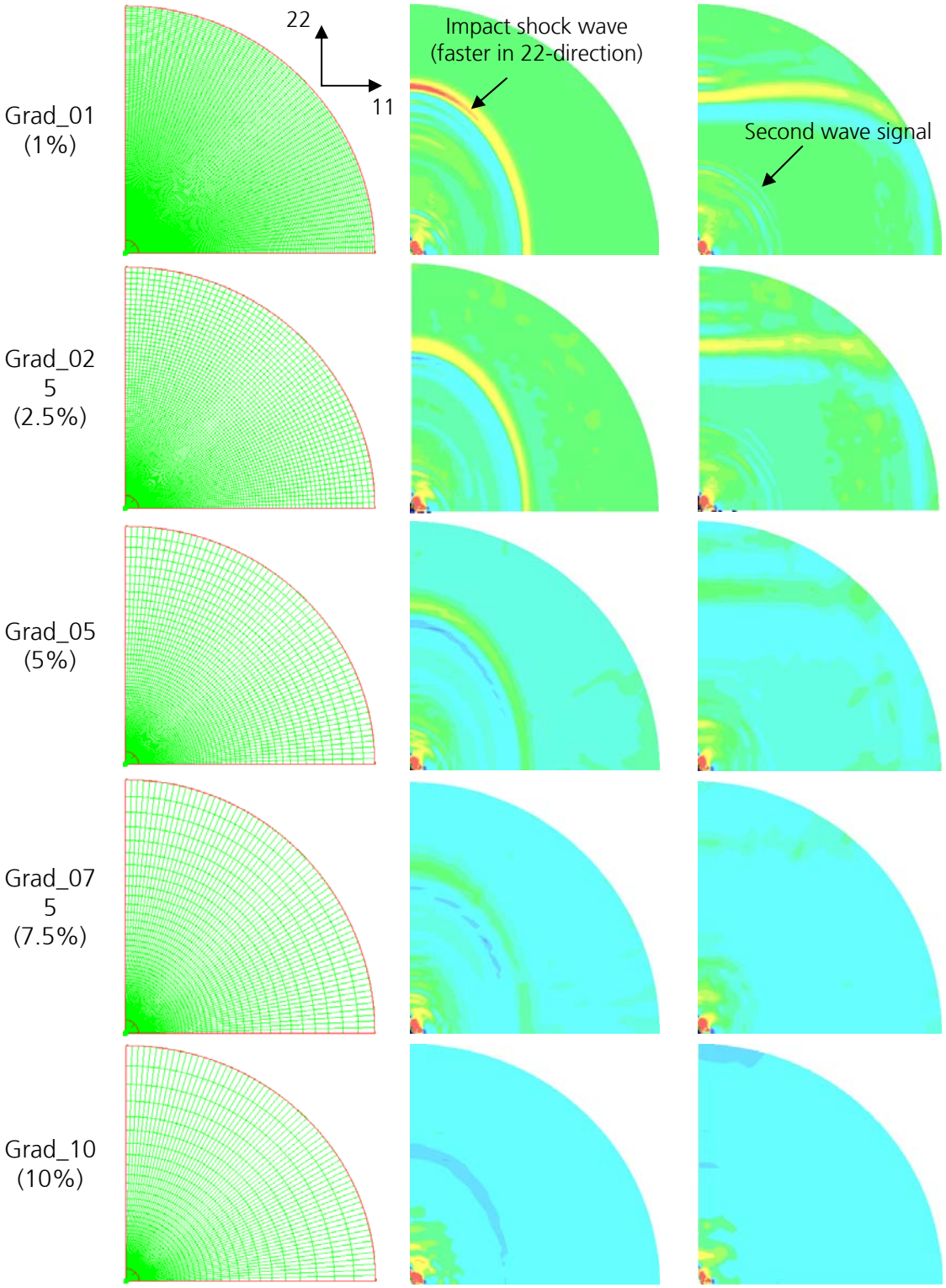

Figure 4-42 Sensitivity of the shock wave propagation to the rate of radial grading (from left to right: 0, 9, 19 µs after impact).

The out-of-plane velocity measurements, made at 50 mm offset in the material 22-direction, are shown in Figure 4-43 for the various radial grading rate sensitivity models. The model with 1% radial grading shows a high-amplitude, high-frequency waveform beginning at ~8 µs after impact. A second high amplitude wave, this time with a much lower frequency is observable approximately 35 µs after impact. These characteristics are reproduced in all other grading rate models with the exception of 7.5%, which shows a very large disturbance at 30 µs after impact.

Number of Cells through the Facesheet Thickness

The sensitivity of the numerical result to the number of cells in the through-thickness direction of the composite facesheet has also been investigated. Models using 4, 6 and 8 cells in the though-thickness direction were considered. The lateral dimensions of the cells were also modified to ensure stable element shapes in the impact axis. The sensitivity simulations were performed for impact of a 0.8 mm Al-sphere at 6.0 km/s on the GAIA CFRP facesheet. A comparison of the pressure contours, recorded 10 µs and 24 µs after impact, is given in Figure 4-44. It can be seen that the number of cells in the through-thickness direction does not, in comparison to grid shape and grading rate, play a major role in the propagation of impact-induced disturbances. In the three models considered, all show propagation and reflection of a clearly defined shock wave. The width of the wave front is sensitive to the cell size, with the more finely discretized models showing a thinner wave front. Additionally, for the 6- and 8-cell models, at 19 µs after impact a second waveform can be clearly identified as it crosses the reflected shockwave.

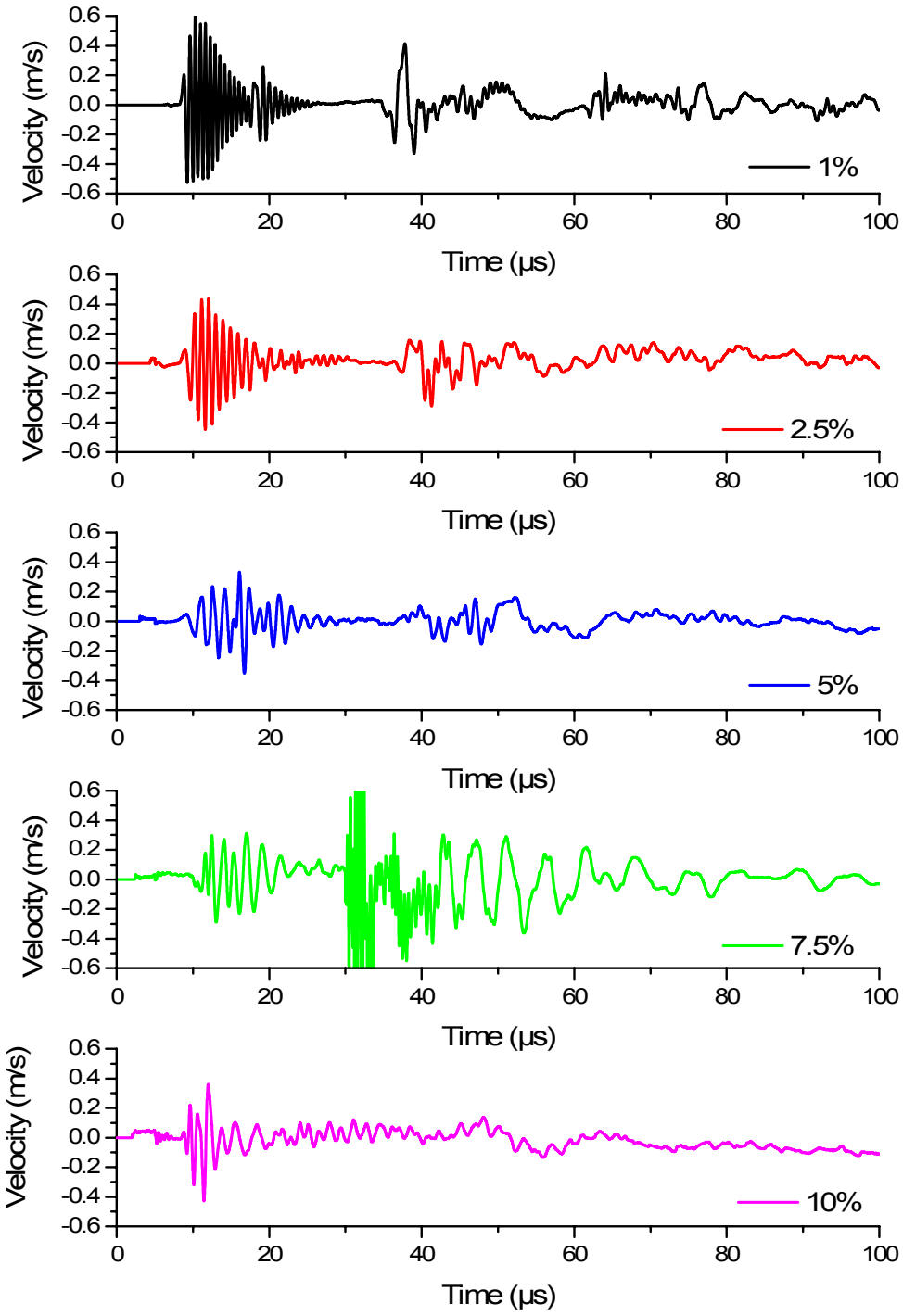

Figure 4-43 Out-of-plane velocity measurements made at 50 mm from the impact location (in 22-direction) in radial grading rate sensitivity simulations.

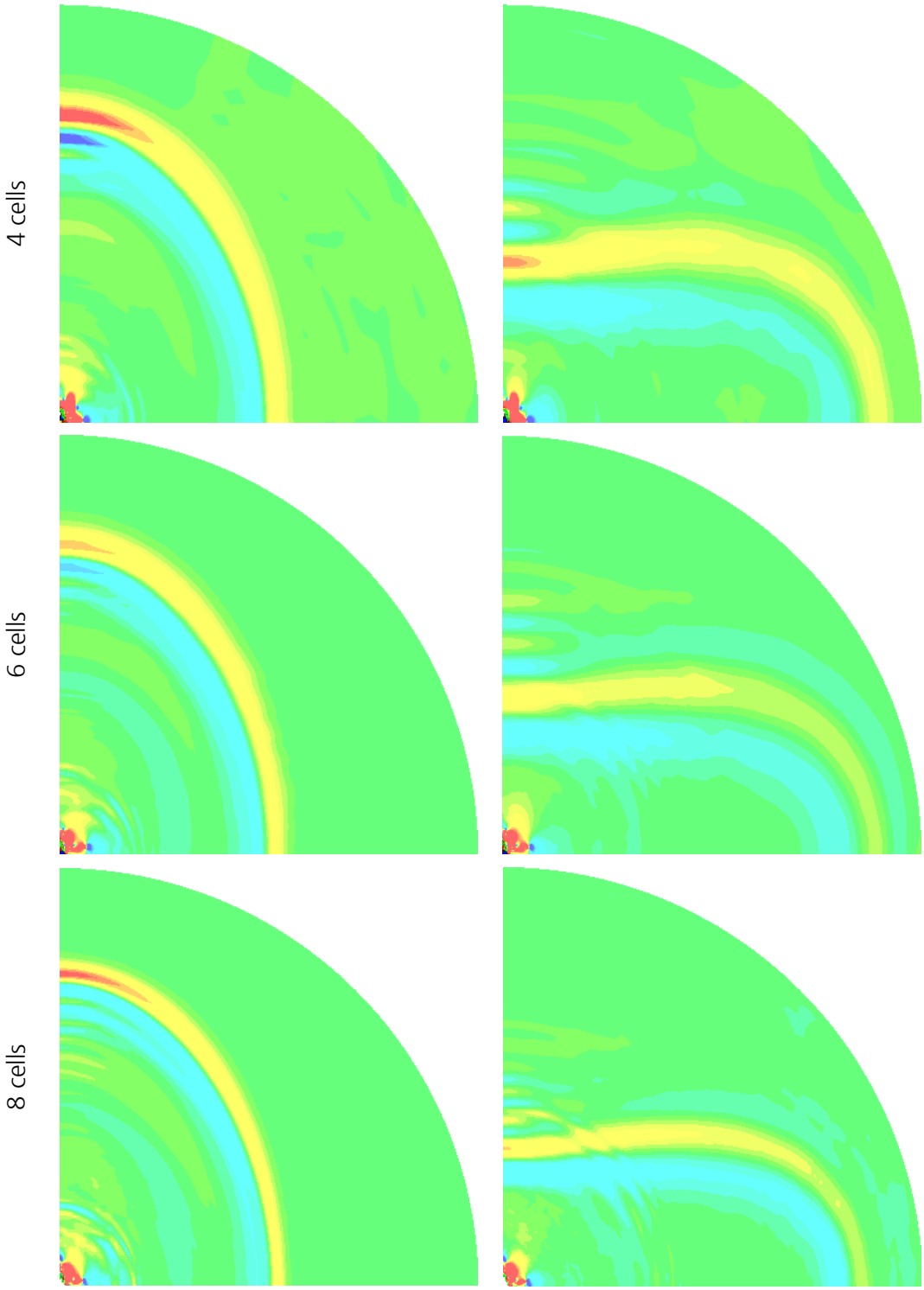

Figure 4-44 Sensitivity of the shock wave propagation to the number of cells through the facesheet thickness (shown: pressure contours).

The out-of-plane velocity measurements, recorded at 50 mm offset in the material 22-direction are compared in Figure 4-45. In agreement with the

pressure contours of Figure 4-44 it can be noted that the number of cells in the through-thickness direction of the laminate does not significantly effect the lateral disturbance wave propagation. All measured wave signals show comparable phenomena, with a high-amplitude, high-frequency waveform at ~10 µs after impact, followed by a second signal ~35 µs after impact.

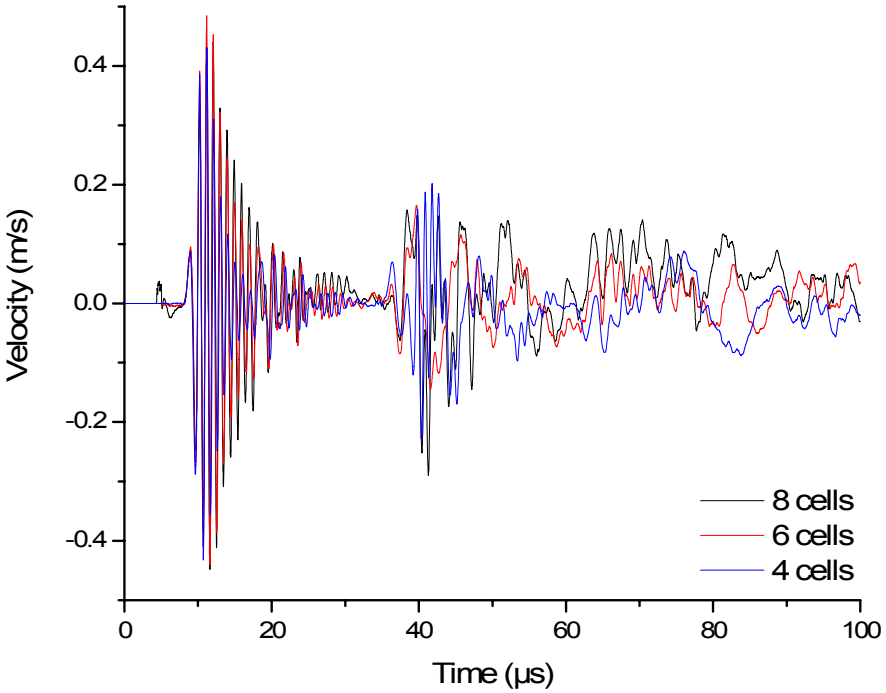

Figure 4-45 Out-of-plane velocity measurements made at 50mm from the impact location (in 22-direction) sensitivity simulations considering the number of cells through the facesheet thickness (grading rate 1%).

Lateral Extension

Given the very small projectiles under consideration, the relatively large structures used in the experimental testing campaign, and the high sensitivity of the disturbance propagation signal to the degree of grid refinement, the numerical models required to allow validation via comparison of disturbance signals with experimental measurements will be computationally expensive. In order to minimize the size of the numerical model, it is advantageous to restrict the lateral extension of the models. In the experiments, velocity measurements are made at 50 mm offset from the impact location, thus an absolute minimum length of 50 mm is required in the numerical model. Additionally, placement of the measurement point on the extreme outer edge of the facesheet is expected to provide numerically-sensitive results, thus a model with

greater than 50 mm lateral extension is required. AUTODYN provides the option for a transmitting boundary condition which "allows outwards travelling waves to pass through it without reflecting energy back into the computational grid" (Anon., 2005). This boundary condition is approximate, and so a number of simulations were performed to examine the sensitivity of the numerical out-of-plane velocity measurement to the transmit boundary condition.

Three simulations were performed for impact of a 2 mm Al-sphere on a 2 mm thick Al 7075-T3 plate at 6.0 km/s. The base model extended to 300 mm from the impact location. Two reduced models, with a lateral extension of 75 mm, were also defined, with one model utilizing the transmit boundary condition. The out-of-plane velocity measurements, made at 50 mm offset form the impact location, are shown in Figure 4-46. The effect of the transmit boundary condition is seen to be minimal, providing a slight decrease (~20%) in the amplitude of the reflected wave. The amplitude of the reflected signal, in comparison to the propagating bending wave, is relatively high. This suggests that validation of the numerical model via comparison with experimental measurements at 50 mm offset from the impact location is highly sensitive to the lateral extension of the model.

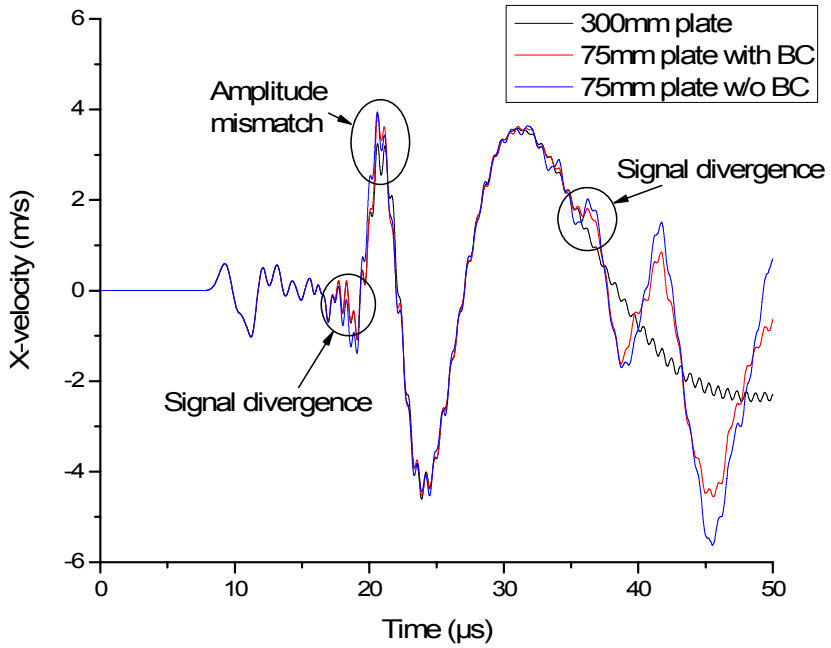

Figure 4-46 Out-of-plane velocity measurements made at 50 mm from the impact location to determine the sensitivity of the numerical result to the model lateral expansion.

Ideally, the model would be large enough such that the initial waveform, when reflected, arrived at the velocity measurement point much later than the high-amplitude low-frequency wave. However, from Figure 4-46 the initial signal arrives at ~9 µs after impact, compared to ~31 µs for the high-amplitude low-frequency wave. This corresponds to propagation velocities of ~5550 m/s and ~1610 m/s respectively. Thus, a plate sufficiently large enough to enable the low frequency wave to propagate to the 50 mm-offset point without disturbance from the reflected longitudinal wave would need to extend over 110 mm. To ensure that the complete low-frequency signal was not disturbed, an extension of over 200 mm would be required. It is considered that such a model would require computing power and computational durations beyond reasonable limits. As such, a nominal lateral extension of 75 mm from the impact location is used in all further simulations.

4.1.2.2 Overview of the Final Numerical Discretisation

Details of the numerical model discretisation are given in Table 4-8 and Table 4-9.

Table 4-8 Overview of the final CFRP facesheet model set-up.

Description	*Details*
No. cells through the thickness	4
Solver type	Lagrangian FE
Extension of the inner zone	8mm
No. cells in circumference	32
Radial grading rate	10%
Inner cell size	0.125

Table 4-9 Overview of the final honeycomb model set-up.

Description	*Details*
No. cells per HC segment	1
No. cells in SP thickness-direction	8
Solver type	Shell

4.2 Validation of the Numerical Set-Up

Validation of the numerical model is performed through comparison of the measured disturbance signal with experimental measurements.

4.2.1 Experimental Measurement of Impact-Induced Disturbances

4.2.1.1 Test Set-Up

Two target sizes are used for the impact tests: smaller panels with lateral extensions of 250 x 250mm and larger panels measuring 500 x 400mm. Along the top edges of each of the target panels, 2 small holes with a diameter of ~ 3 mm are drilled to allow suspension of the target from the ceiling of the target chamber. The target is suspended from adjustable eyelets mounted on sliding tracks fixed in place with position screws using 20 lb. (9 kg) weight capacity, 0.45 mm diameter, braided polymer twine. A unit piece of twine, whose length is 10 cm, has a weight of 0.016 grams. The twine is doubled over to provide extra strength. This method of target setup is used to reduce the transmission of facility noise signals to the target.

As some impact experiments are expected to result in complete perforation of the SP target, witness plates were placed at a suitable distance behind the SP to catch ejected fragments.

Disturbance measurements are made 50 mm below the shot axis (expected impact location), shown in Figure 4-47. To minimise target materials, multiple impact tests have been performed on the panels. The first impact location was always in the target centre, followed by a 5cm horizontal offset to the left (or right), subsequently followed by a 5cm horizontal offset in the opposite direction (shown in Figure 4-47).

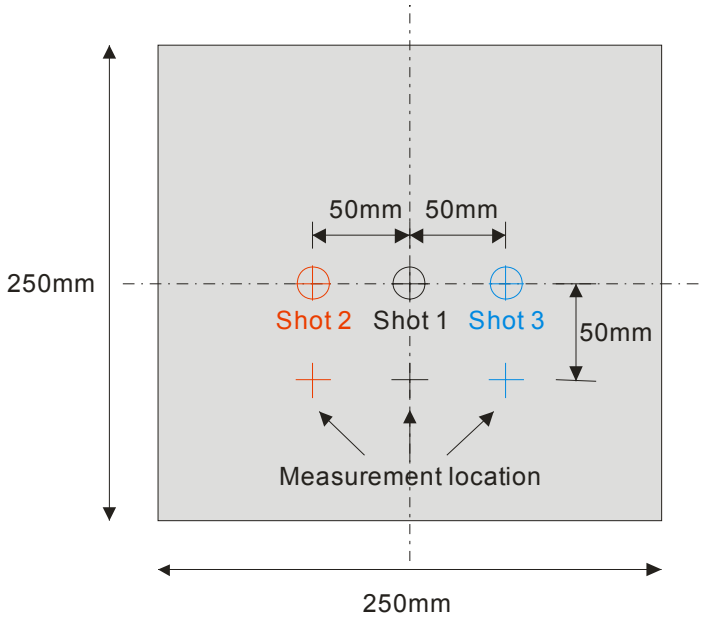

Figure 4-47 Small test panel with multiple impact and measurement locations.

4.2.1.2 Instrumentation

A Polytec Laser Vibrometer (LV) measurement system which can measure both velocity and displacement simultaneously at a single point on an object is used to record the hypervelocity impact-induced disturbance wave. The device uses a high frequency carrier generated on a photo detector with the aid of a Bragg cell. This is used with a helium-neon laser, of wavelength 633 nm (Class II He-Ne Laser, < 1mW), to obtain velocity and displacement measurements. The laser is pointed at the structure and then the beam is scattered back at the laser source where it is collected. A frequency and phase modulation are generated by the vibrating object as a result of the Doppler Effect. Through the use of decoders, the velocity information is captured via the frequency modulation, while the displacement data is obtained through the phase modulation. The Laser Vibrometer was used to instrument the target due to its unique measurement capabilities. Simulation models use massless measurement points to monitor progress, which makes this device useful for simulation and experimental comparisons as its almost massless nature does not significantly influence the motion of the target surface. The minimum measurement range of the Laser Vibrometer is 530 mm (standoff distance between target and laser) and the focal point is approximately 18 μm in diameter. This size increases slightly as the

standoff distance increases (1000 mm = 62 μm, 2000 = 135 μm, 5000 = 354 μm).

Each decoder (velocity and displacement) has an independent frequency range (bandwidth). The velocity decoder (VD-02) has a range of 0.5 Hz to 1.5 MHz, while the displacement decoder (DD-200) has a range of 0 to 250 kHz. Table 4-10 shows the calibration accuracy for amplitude error of measurements based on temperature. The Laser Vibrometer also has an amplitude linearity error of ± 1.0 % of the rms reading for one particular range or ± 2.5 % of rms reading of the overall measurement.

Table 4-10 VD-02 laser vibrometer sensitivity values.

Measurement Range $\frac{mm}{s}\Big/V$	*Amplitude Error @ T = (25±5)°C % of rms reading*	*Amplitude Error 5°C ≥ T ≥ 40°C % of rms reading*
5	± 1.0	± 1.5
25	± 1.0	± 2.0
125	± 1.0	± 2.5
1000	± 1.0	± 2.5

In addition to this calibration data, the Laser Vibrometer has an Amplitude Frequency Response, referred to as its flatness, for each of the four measurement ranges in Table 4-10. This information is displayed in Table 4-11. Transforming the units from dB to voltage ratio, the error associated with the 0.1 dB is a voltage ratio of 1.01158, or approximately 1.2%. The error of 0.5 dB converted is approximately a voltage ratio of 1.06, or 6%.

Table 4-11 VD-02 laser vibrometer amplitude frequency response.

Frequency Range	*Measurement Range,* $\frac{mm}{s}\Big/V$			
	5	*25*	*125*	*1000*
0.5 Hz – 10 Hz	± 0.5 dB	± 0.5 dB	± 0.5 dB	± 0.5 dB
10 Hz – 100 kHz	± 0.1 dB	-	-	-
10 Hz – 250 kHz	-	± 0.1 dB	± 0.1 dB	± 0.1 dB
100 kHz – 250 kHz	+ 0.1/-0.1 dB	-	-	-
250 kHz – 1.5 MHz	-	+ 0.5/-0.1 dB	+ 0.5/-0.1 dB	+ 0.5/-0.1 dB

To achieve a high-quality backscatter signal from the Laser Vibrometer, a reflective foil must be applied to the area of the structure where the

measurement is taken. The reflective foil used is 5 mm by 5 mm, and has a thickness of 0.1 to 0.12 mm. A foil this size has a weight of 0.0063 grams, resulting in an aerial weight of ca. 0.025 g/cm^2. The foil has adhesive on its backside for application to the target. Once applied, a mirror is positioned behind the target, directly in-line with the reflective foil. It is rotated towards the laser, which is positioned outside the target chamber beaming in through a window. This mirror is rotated until the laser beam is centred in the reflective foil and focused to achieve optimal backscatter for accurate measurements. This is illustrated in Figure 4-48.

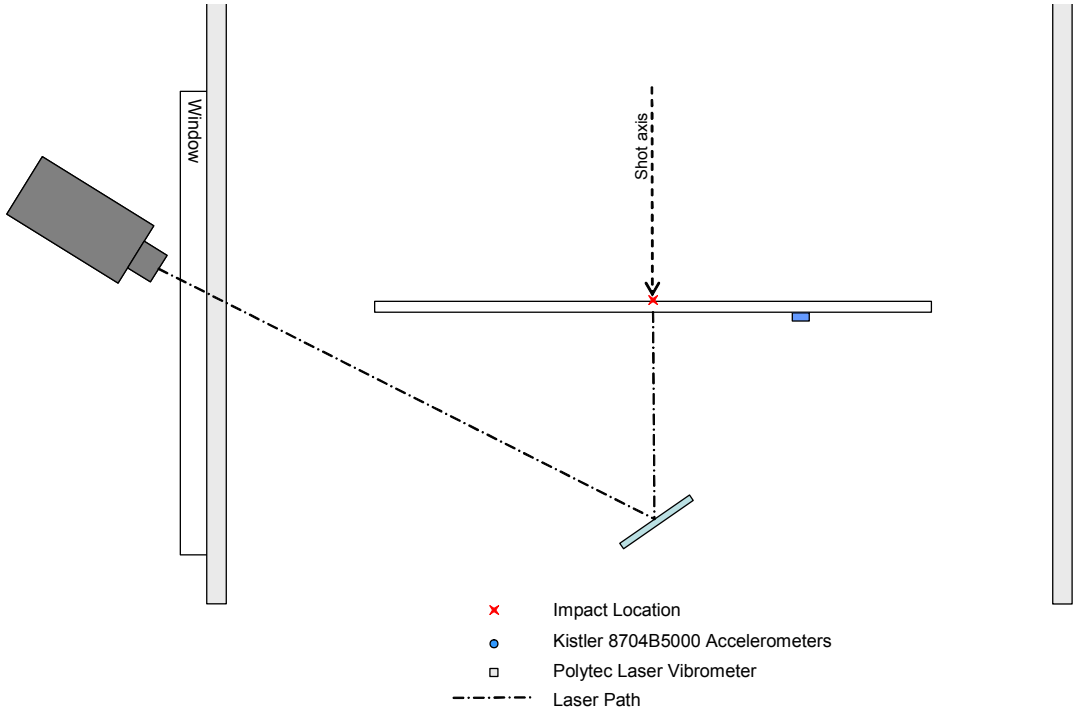

Figure 4-48 Laser Vibrometer set-up.

4.2.1.3 Perturbations Induced by the Acceleration Facility

Two major sources of perturbations were considered to be relevant for contributing to undesired accelerations of the target. Firstly, mechanical shocks and vibrations transmitted to the whole impact facility including the impact chamber and the foundation of the facility. Secondly, the action of the blast wave transmitted to the location of the target through the ambient atmosphere contained in the tanks of the facility.

It was assumed that the transmitted shocks and vibrations are induced by: ignition and combustion of the gun powder in the powder chamber; the

detachment, acceleration and deceleration of the piston in the conical part of the high pressure-section; the sabot parts impacting on the sabot catcher, and; the interaction (i.e. encounter) of the blast wave with the facility's tank walls. The second source of perturbations is induced by the hot hydrogen gas that is expelled into the blast tank and combusts when it mixes with the oxygen contained in the tank's residual atmosphere. This gas contains a considerable momentum traveling in the shot direction. Thus, a strong pressure wave is generated that propagates towards the target, and induces out-of plane accelerations on the target.

These sources of perturbations have been investigated in detail for both two-stage light-gas gun facilities used in this campaign i.e., Space Gun and Baby Gun (see Spencer et al. (2007) for details). To this purpose, high-g accelerometers and ultrasonic transducers with a broad bandwidth were fixed to the target chamber right next to connection point of threads used to suspend the target. The instrumentation was used to measure the out-of-plane accelerations of the target chamber wall and the arrival time of the disturbance waves in the facility. The frequency spectrum of the facility perturbation was also assessed.

For investigating the perturbations induced by the blast wave on the target, pressure transducers were placed in the target chamber to measure the head-on amplitude of the pressure wave prior to interaction with the target. Additionally, the target was instrumented with accelerometers and ultrasonic transducers to measure the induced vibrations and to define the arrival time of the perturbation. Again, the frequency spectrum of the perturbation was also investigated.

Other sources such as electromagnetic noise have been neglected, as the types of measurements performed are mainly mechanical.

In general, it was observed that the arrival time of the blast wave at the target location was later than the sound wave that travels through the walls of the impact facility's tanks. Furthermore, as the projectile's velocity is in the order of the sound speed in the tanks walls (or faster), the time sequence for a typical impact at upper hypervelocity is:

1. Impact of the projectile on the target,
2. Arrival of the sound wave transmitted through the facility body at the target chamber,
3. Arrival of the blast wave at the target.

From this time sequence, it is possible to define two measurement time windows: the first time window covers the time span between projectile impact and arrival of the sound wave in the target chamber, while the second window covers the time span after the arrival of the sound wave. The first time window is referred to as the "perturbation-free" window during which no perturbations are recorded on the target surface. This time window is typically several tens or hundreds of microseconds long, allowing high-quality measurements of impact-induced disturbance waves to be made. In the second measurement time window some perturbations are introduced in the disturbance signal, stemming from the facility body. These perturbations may be avoidable; however the effort to remove them is considerable. The perturbation environment has been characterized for both LGG facilities.

(a) Space Gun (SLGG)
During the dedicated impact tests performed with the Space Light Gas Gun, the maximum peak acceleration observed on the target chamber wall was 6 g. The FFTs of the signals showed that the frequency range with the largest acceleration component is located between 0.5 and 2 kHz, with the dominant frequency of this signal located at 0.6 kHz. Frequencies below 0.3 kHz are not significant contributors to the noise.

After having introduced several blast reduction shields in the tanks along the flight path of the projectile, the peak acceleration from the blast wave measured on the target surface amounted to ca. $\pm$ 4 g. From the tests conducted during the noise environment characterization campaign, a conservative window for performing target measurements prior to acoustic noise interference is approximately 300 µs ("perturbation-free" time window).

(b) Baby Gun (BLGG)
During the tests performed for noise environment characterization of the Baby Light Gas Gun, peak accelerations of the baby gun wall of up to 50 g were recorded. The FFTs had a negligible amplitude in the low frequency range (<1.0 kHz) and peaked at approximately 3.7 kHz. The accelerations induced by the blast wave using accelerometers placed directly on the target plate amounted to about 5 g.

4.2.1.4 Defining Experimental Measurement Scatter

In the course of the experimental campaign nine impact tests were performed on the CFRP/Al HC SP, defined in Table 4-12.

Table 4-12 Impact experiments performed on the CFRP/Al HC SP.

Exp. No.	*EMI No.*	d_p *(mm)*	V_{imp} *(km/s)*
SDHI 1	296	0.8	3.36
SDHI 2	297	0.8	4.38
SDHI 3	252	0.8	5.25
SDHI 4a	4860	1.5	5.62
SDHI 4b	4861	1.5	5.70
SDHI 5*	4862	1.5	5.76
SDHI 6*	4875	1.5	6.21
SDHI 7*	4873	1.5	6.32
SDHI 8*	4865	1.5	6.71

* Tests performed on large panel (600 x 400)

Tests SDHI 4a and 4b were performed at nominally-identical conditions with measurements made on the front and rear side of the SP respectively. A comparison of disturbance measurements, made during tests with similar impact conditions, can be used to assess the magnitude of scatter. In Figure 4-49 disturbance waveforms measured in SDHI 4a (4860) and SDHI 5 (4862) are considered. The significant difference between the two signals indicates a large degree of experimental scatter.

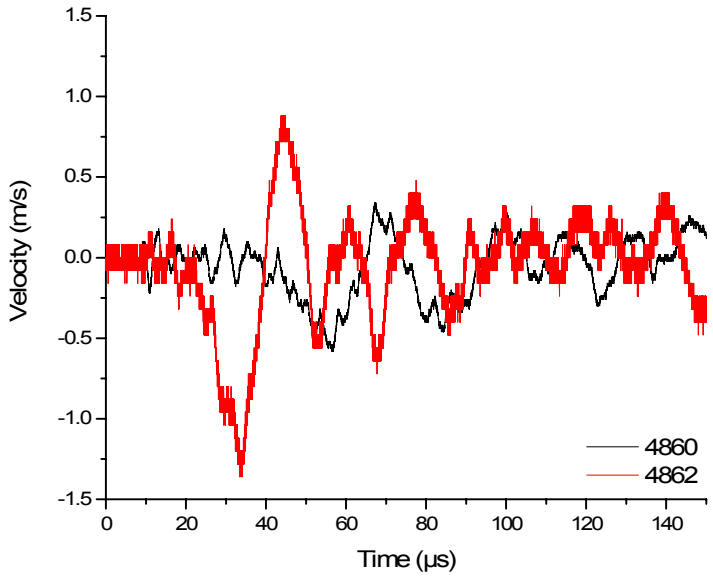

Figure 4-49 Disturbance signals measured during impact of a 1.5mm Al-sphere on the GAIA CFRP/Al HC SP target at ~5.70 km/s.

Scatter has been assessed for the five impact experiments defined in Table 4-12 with 1.5 mm projectiles (excluding SDHI 4b), which have impact velocities ranging from 5.62 to 6.71 km/s. The high-amplitude, low-frequency wave is considered the critical feature of the disturbance waveform, and therefore the scatter is assessed in terms of this characteristic. Figure 4-50 shows the experimental measurements of the 1.5 mm projectile impact tests.

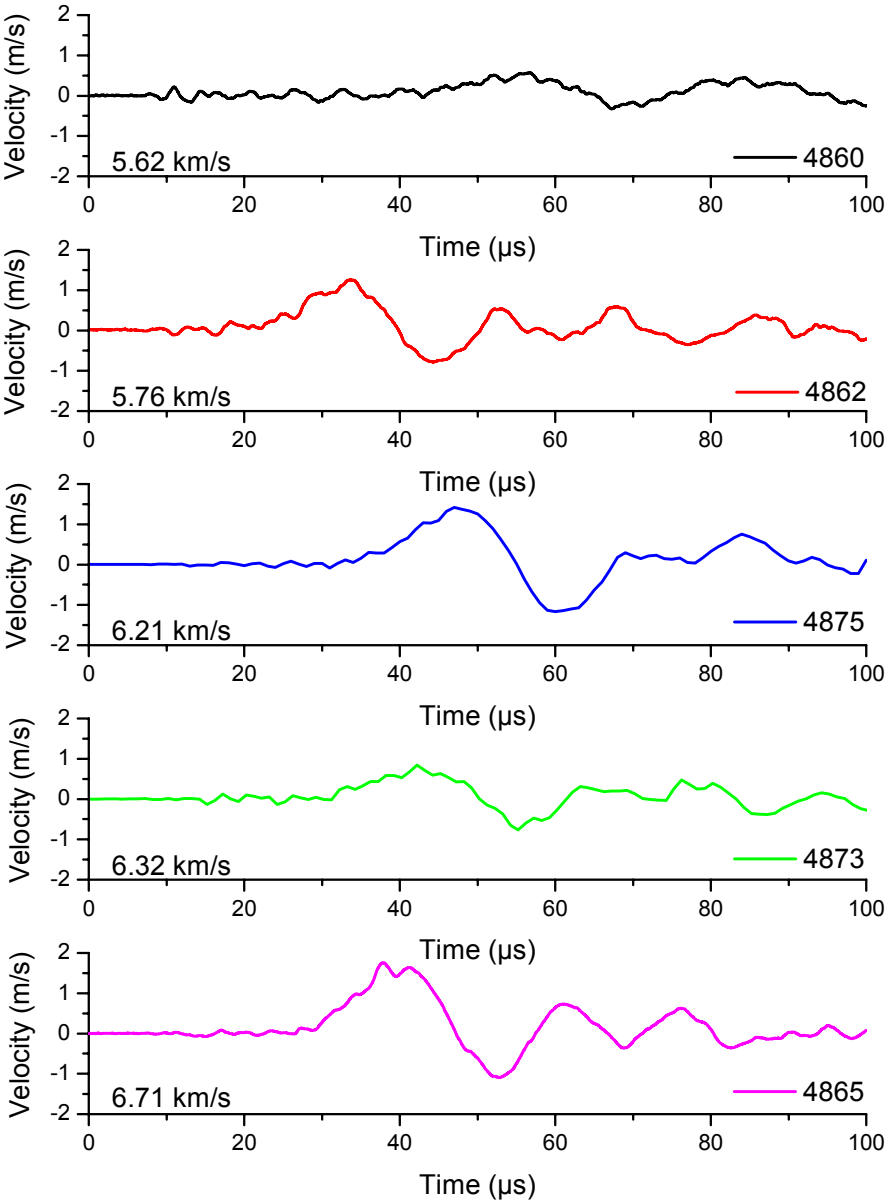

Figure 4-50 Experimental disturbance signals measured during impact of a 1.5mm Al-sphere on the GAIA CFRP/Al HC SP.

Although all experimental measurements were made at a nominally identical offset from the impact location, the actual impact location in the hypervelocity impact tests was subject to mm-sized scatter. From a post-impact inspection of targets, it is apparent that the impact location is not constant for all experiments. A list of impact locations, relative to the measurement location, is given in Table 4-13.

Table 4-13 Distance of laser vibrometer measurement point from the impact location.

EMI No.	*Vertical (mm)*	*Horizontal (mm)*
4860	51	0
4862	44	1.5
4865	49.3	2.2
4873	52.6	5
4875	56.5	3

The experimental signals can be adjusted to account for the slight scatter in impact location by adding or subtracting the time it would take the disturbance signal to propagate the difference in planned and actual offsets. This assumes that the effect of any horizontal offset of the laser vibrometer measurement point is negligible. Eq. (108) was used to calculate a propagation velocity of 5693 m/s for the longitudinal wave. The time used to adjust the signals shown in Figure 4-50 is calculated as:

$$\Delta t_{IL} = t - \left(\frac{S_{act} - 50}{c_{L,22}} \right) \tag{109}$$

where t – time (μs),
S_{act} – vertical measurement offset from impact location (mm),
$c_{L,22}$ – longitudinal wavespeed in material 22-direction (km/s).

Given that the adjustment is made based on the longitudinal wavespeed, some discrepancy will still be present for the remainder of the disturbance signal (i.e. waveforms with lower propagation velocities). Figure 4-51 shows the dependency of the critical wave feature on impact velocity. There is no discernable relationship between impact velocity and wave arrival time, and between impact velocity and wave peak amplitude, or rather if there is a relationship then the scatter is so large that the trend is not obvious.

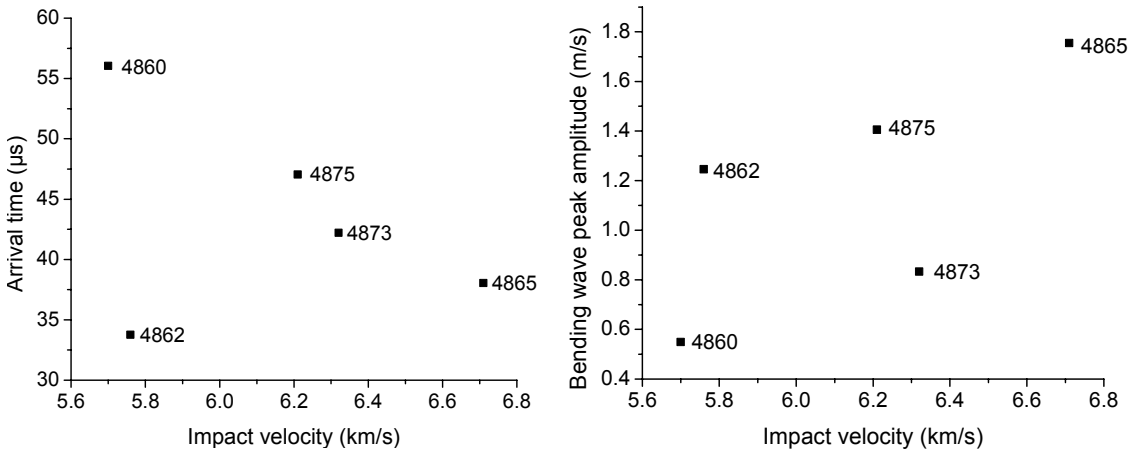

Figure 4-51 Dependence of critical wave feature peak amplitude and arrival time for 1.5mm projectile impact experiments on the CFRP/Al HC sandwich panel.

Experiments SDHI 4a and 5 (EMI no. 4860 and 4862 respectively) have the closest impact velocities, and as such, scatter will be assessed using measurements made during these tests. The properties of the peak critical wave feature, induced by impact of a 1.5 mm Al-sphere at 5.69 ± 0.07 km/s are:

- Arrival time: 44.90 ±11.14 µs (velocity = 1113.48 ± 376.52 km/s)
- Peak amplitude: 0.898 ± 0.349 m/s
- Frequency: 27.85 ± 2.75 kHz

These properties will be used to assess the validity of the numerical model.

4.2.2 Comparison of the Numerical and Experimental Disturbance Signal

A comparison of the experimental and numerical impact-induced disturbance measured 50 mm from impact (material 22-direction) on the sandwich panel rear facesheet is shown in Figure 4-52 for a 1.5 mm Al-sphere impacting at 5.69±0.07 km/s. The numerical signal shows good agreement with both the amplitude and arrival time of the initial disturbance signal, as well as reproducing the disturbance trends between 10-30 µs after impact (albeit the amplitudes are generally higher). The

high-amplitude, low-frequency wave feature is also reproduced in the numerical simulation, although the negative velocity prior to the signal is not present in the experiment and the frequency of the experimental bending wave is slightly higher.

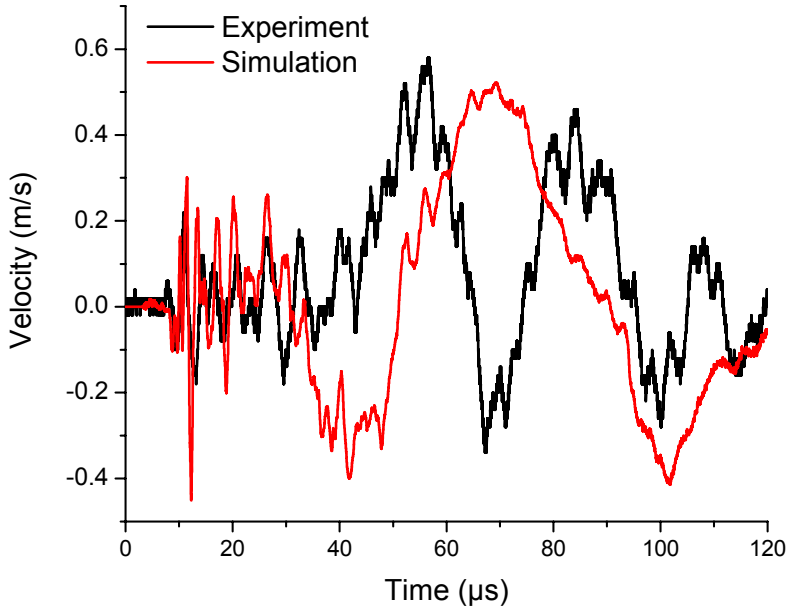

Figure 4-52 Comparison of experimental and numerical signals for impact of a 1.5mm Al-sphere at 5.69 ± 0.07 km/s on the GAIA CFRP/Al HC SP.

The critical wave feature recorded in the numerical simulation has a peak amplitude of 0.498 m/s and a propagation velocity of 772.8 m/s (arrival time 64.7 µs). The signal arrival time/propagation velocity is within the defined experimental scatter bounds; however the peak amplitude is slightly below the lower limit. It can be noted in Figure 4-52 that prior to the large amplitude low-frequency waveform the numerical signal records a negative wave which is not seen in the experimental signal. If the peak amplitude is taken as peak-to-peak measured from this negative feature, the amplitude corresponds to 0.892 m/s, which lies directly in the centre of the experimental bounds.

4.3 Numerical Simulation of Hypervelocity Impact-Induced Disturbance Propagation

In Chapter 3, four degrees of penetration were identified for impact on a sandwich panel structure. The four cases, each expected to induce different modes of momentum transfer (excitation), were defined as:

1. Non-penetration case: projectile does not penetrate the outer facesheet of the SP.

2. Penetration case 1: projectile penetrates the SP structure and is stopped inside the SP

3. Penetration case 2: projectile minimally penetrates the SP

4. Penetration case 3: projectile penetrates the SP completely

The limit of front facesheet perforation is determined using the ballistic limit equation for a thin CFRP plate defined by Schäfer et al. (2004):

$$d_c = \frac{t_{CFRP} + K2 \cdot \frac{\rho_{AD,MLI}}{\rho_{CFRP}}}{k \cdot K_{CFRP} \cdot \rho^{\alpha} \cdot v_n^{\beta}} \tag{110}$$

Constants used in Eq. (110) are given in Table 4-14.

Table 4-14 Values used with Eq. (110) when applied to the front CFRP facesheet.

Parameter	*Description*	*Value*
K2	Fit factor describing the protection enhancement of MLI [-]	4.5
k	Constant describing the type of failure [-]	3.0
K_{CFRP}	Constant describing the target material [-]	0.52
α	Density coefficient [-]	0.5
β	Density coefficient [-]	2/3

The limit of rear facesheet perforation (sandwich panel perforation) is determined using the ballistic limit equation derived in Chapter 3.4.

In terms of the ballistic limit of the sandwich panel structure, the four penetration cases are shown in Figure 4-36.

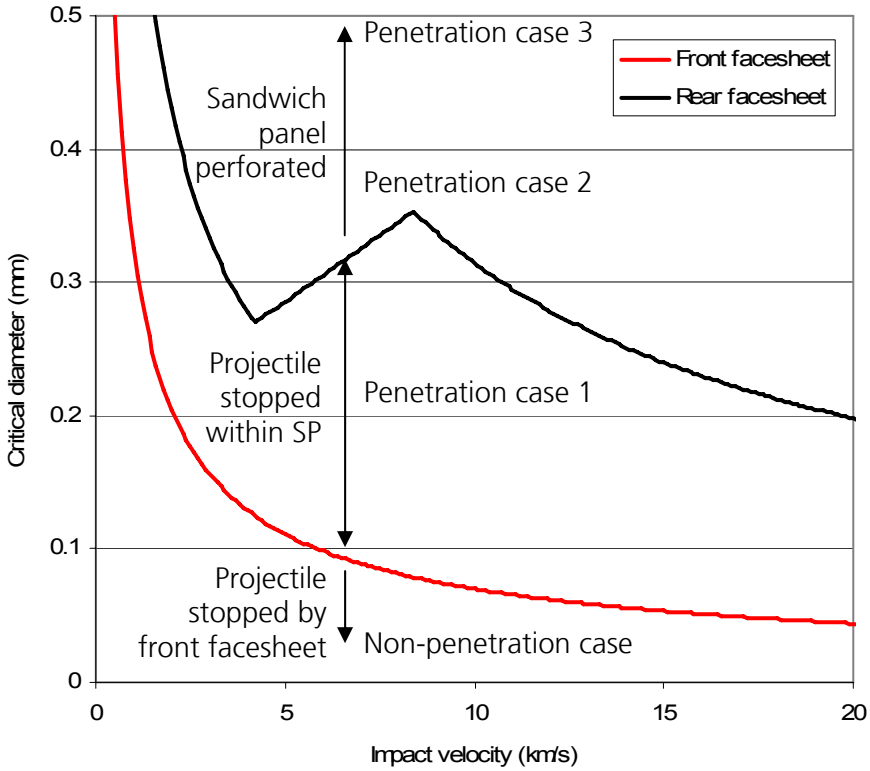

Figure 4-53 Ballistic limit curves of the front CFRP facesheet and complete sandwich panel showing the four penetration cases.

Numerical simulations were performed to consider all four types of penetration. For impact in which the majority of excitation was expected to occur on the sandwich panel front facesheet (non-penetration case, penetration case 1) only the front facesheet was modelled. An overview of the facesheet simulations is given in Table 4-15.

Table 4-15 Details of the CFRP facesheet HVI simulations.

Sim No.	*Projectile diameter (mm)*	*Projectile mass (mg)*	*Impact velocity (km/s)*	*Impact momentum (g.m/s)*
FS-1	0.05	1.8326E-04	4.9	8.9797E-04
FS-2	0.05	1.8326E-04	10.0	1.8326E-03
FS-3	0.2	0.0117	4.9	0.0575
FS-4	0.2	0.0117	10.0	0.1173
FS-5	0.4	0.0938	4.9	0.4598
FS-6	0.4	0.0938	10.0	0.9383
FS-7	0.8	0.7506	4.9	3.6518

For impact conditions in which the majority of excitation was expected to be realised on the sandwich panel rear facesheet (penetration case 2,

penetration case 3) the full sandwich panel was modelled. An overview of the sandwich panel simulations is given in Table 4-16.

Table 4-16 Details of the CFRP/Al HC SP HVI simulations.

Sim No.	*Projectile diameter (mm)*	*Projectile mass (mg)*	*Impact velocity (km/s)*	*Impact momentum (g.m/s)*
SP-1	0.4	0.0938	6.0	0.5590
SP-2	0.4	0.0938	10.0	0.9316
SP-3	0.4	0.0938	20.0	1.8632
SP-4	0.6	0.3167	16.0	5.0306
SP-5	0.8	0.7506	10.0	7.4527
SP-6	0.7	0.5029	20.0	9.9855
SP-7	0.8	0.7506	17.5	13.042
SP-8	0.8	0.7506	20.0	14.905

Compared to the ballistic limit curves of the structure, the numerical simulation impact conditions are shown in Figure 4-54.

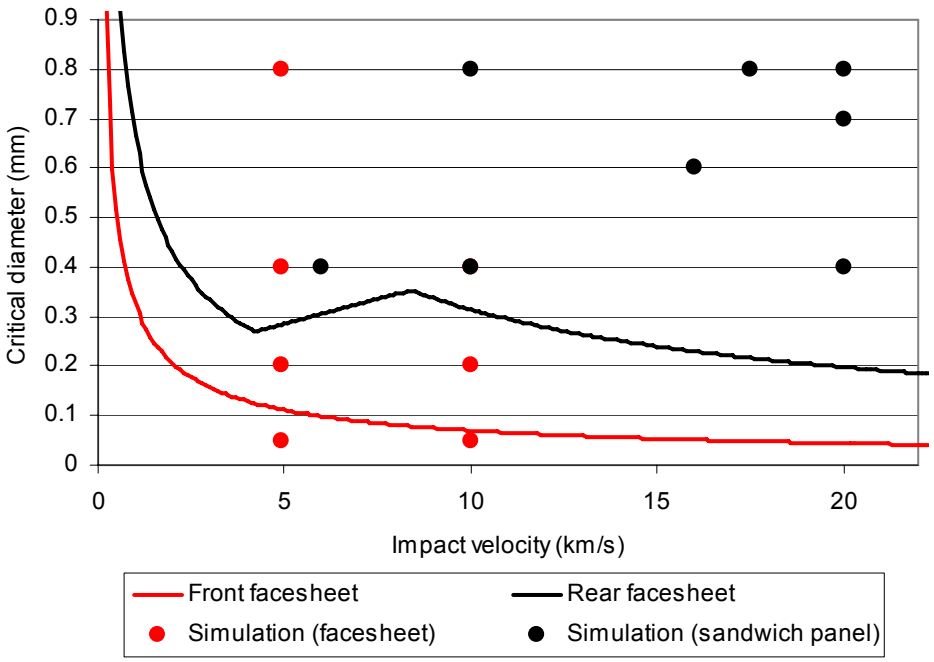

Figure 4-54 Impact-induced disturbance simulation matrix.

The simulation models are highly instrumented through the application of numerical gauges at various locations on the CFRP facesheet outer surfaces. These mass-less numerical points are capable of recording the time history of the applied numerical cell for user-specified variables (such as out-of-plane velocity). In all simulations, arrays of gauges were placed

along the material in-plane principle directions (11 and 22) on both the front and rear side of the numerical structure, i.e. front and rear surface of the facesheet, and front and rear facesheet of the SP for the facesheet and SP simulations respectively. Figure 4-55 shows the numerical gauge locations for the SP numerical model.

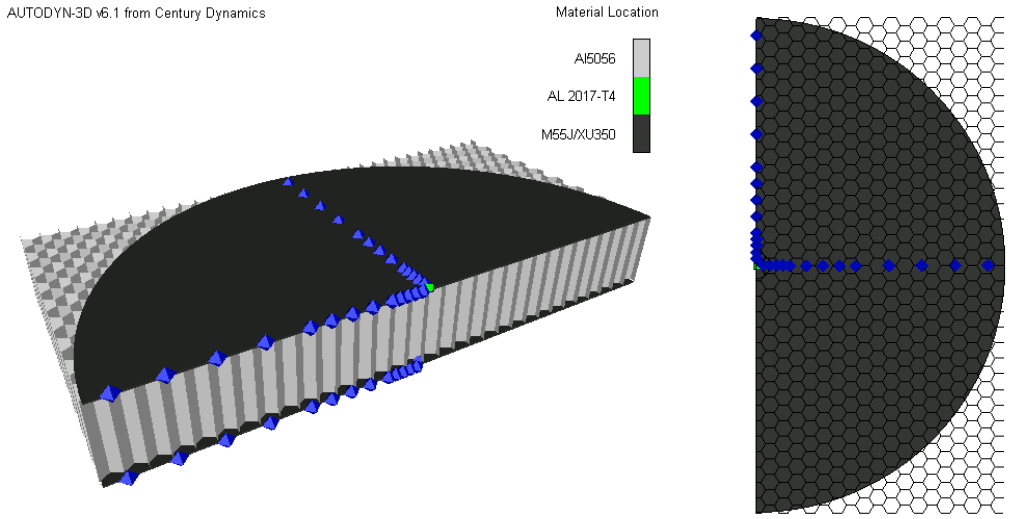

Figure 4-55 Placement of the numerical gauges on the sandwich panel numerical model.

4.4 Summary

Numerical codes are required for simulation of on-orbit impact conditions representative of those expected for the GAIA mission. For these type of loading conditions, hydrocodes are ideal as they allow coupling of complex material models with a fluid-structure program. A new advanced material model for simulation of composite materials during hypervelocity impact is available within the commercial hydrocode AUTODYN. In the absence of experimentally-characterised material data a procedure has been developed which applies a number of composite mechanics theories (e.g. micromechanics, classical laminate theory) in combination with generalised material properties to derive a full CFRP material data set suitable for application in the new material model. An experimentally-characterised material data set has been used to assess the validity of this derivation procedure, allowing comparison of material performance in element tests and in the simulation of hypervelocity impact events on sandwich panel structures with CFRP facesheets. A good level of agreement was found between the experimentally- and theoretically-

developed simulation models. The procedure has further been applied for derivation of a data set for the GAIA CFRP laminate.

A sensitivity study has been performed to optimise the numerical model and minimise sensitivity of the results to the numerical set-up prior to execution of the impact-induced disturbance simulation campaign. It has been found that the out-of-plane velocity measurements are highly sensitive to discretisation type (Lagrangian or Smooth Particle Hydrodynamics), cell configuration and grading rate. The number of cells in the laminate through-thickness direction was shown to have little effect; however this parameter is expected to be important in capturing fragmentation ejecta for sandwich panel simulations.

An assessment of the scatter present in experimental disturbance measurements was made, and the characteristics of the critical waveform feature were defined. The experiment was numerically reproduced using the derived material data set and numerical set-up defined in the sensitivity study, and the out-of-plane velocity waveform was compared to the experimental measurement. Good overall agreement was achieved for the disturbance waveform and the critical features of the numerical signal were found to lie within the experimental range.

Using the ballistic limit equations for a CFRP plate and CFRP/Al HC SP, a numerical simulation campaign was defined in which all four penetration cases were considered. The simulation models are highly instrumented to allow characterisation of the impact-induced disturbance signal.

5 An Excitation Function for Hypervelocity Impact-Induced Disturbances

Hypervelocity impacts (HVI) of M/SD particles on a satellite induce transient disturbances which propagate from the impact site through the satellite structure leading to disturbances at locations of critical stability, e.g. measurement devices. Considering the impact process, a high amplitude shock wave is initially generated at the impact location resulting in a large amount of plastic deformation and permanent damage (e.g. cratering in the front surface of the target). As the shock wave propagates into the surrounding structure, the plastic wave is rapidly dampened, evolving into an elastic wave. It is considered that under perpendicular impact, the excitation induced in the surface of the satellite debris shield (expressed as velocity vs. time) will be a single pulse with velocity in the direction of the projectile flight vector. This excitation pulse can be simplified by a mathematical function.

In this chapter numerical simulations are presented in which the shock disturbance generated during impact is characterised as it propagates into the GAIA CFRP/Al HC SP. Additionally, simulation of impact by different projectile sizes and at different impact velocities is made, from which a function is defined for the elastic excitation of the GAIA CFRP/Al HC SP that is general in terms of impact conditions.

5.1 Methodology

To characterise the elastic excitation of the impacted structure, numerical simulations are performed in which a series of disturbance measurements are made at intervals away from the impact site. The measured disturbance waveforms can then be used to characterise the evolution of the disturbance waveform in terms of distance from the impact axis. This characterization can then be extrapolated back to the impact site to define the initial elastic excitation. For example, if we know how the disturbance appears at say 4, 6, 8 and 10 mm from the impact site, we can see how it changes with propagation distance and use this understanding to predict the original elastic excitation.

Repeating the characterization procedure for multiple impact conditions (varying projectile diameter and impact velocity), the elastic excitation waveform can then be characterized in terms of impactor momentum, defining a generalized elastic-equivalent excitation for a specific structure

impacted by debris at hypervelocity. The characterisation will take the form of a mathematical function, referred to as the excitation function, which represents a simplification of the measured waveform suitable for application in structural FE codes for propagation of the disturbance in complete satellite models (such as that shown in Figure 5-1).

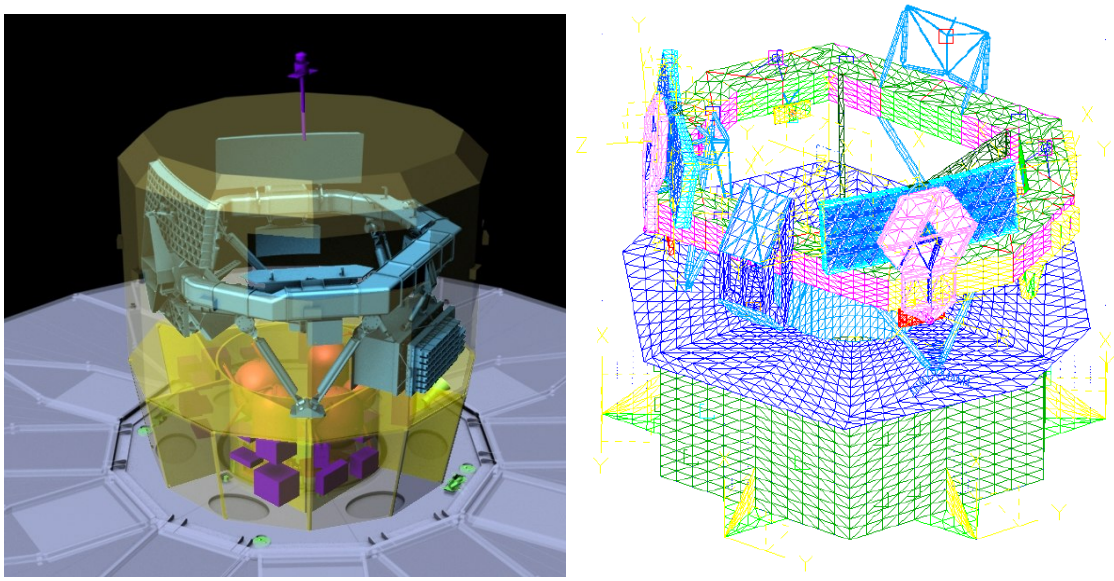

Figure 5-1 GAIA service module and payload module internal configuration, Left: artist's impression © ESA, Right: Finite element model © EADS-Astrium.

For application in structural analysis codes the excitation function needs to be expressed in terms of force magnitude as a function of time, F(t), where excitation is considered perpendicular to the body surface:

$$F(t) = m \cdot a(t) \tag{111}$$

An overview of the methodology used for derivation of the excitation function is shown in Figure 5-2.

It has been shown in Chapter 3 that for the range of impact conditions under consideration, four penetration cases are relevant to the induced-disturbance: no penetration of the front facesheet, minimal penetration of the front facesheet, significant penetration of the front facesheet, significant penetration of the rear facesheet. Each of these penetration cases results in a different mode of momentum transfer to the sandwich panel structure and, subsequently, a different type of excitation.

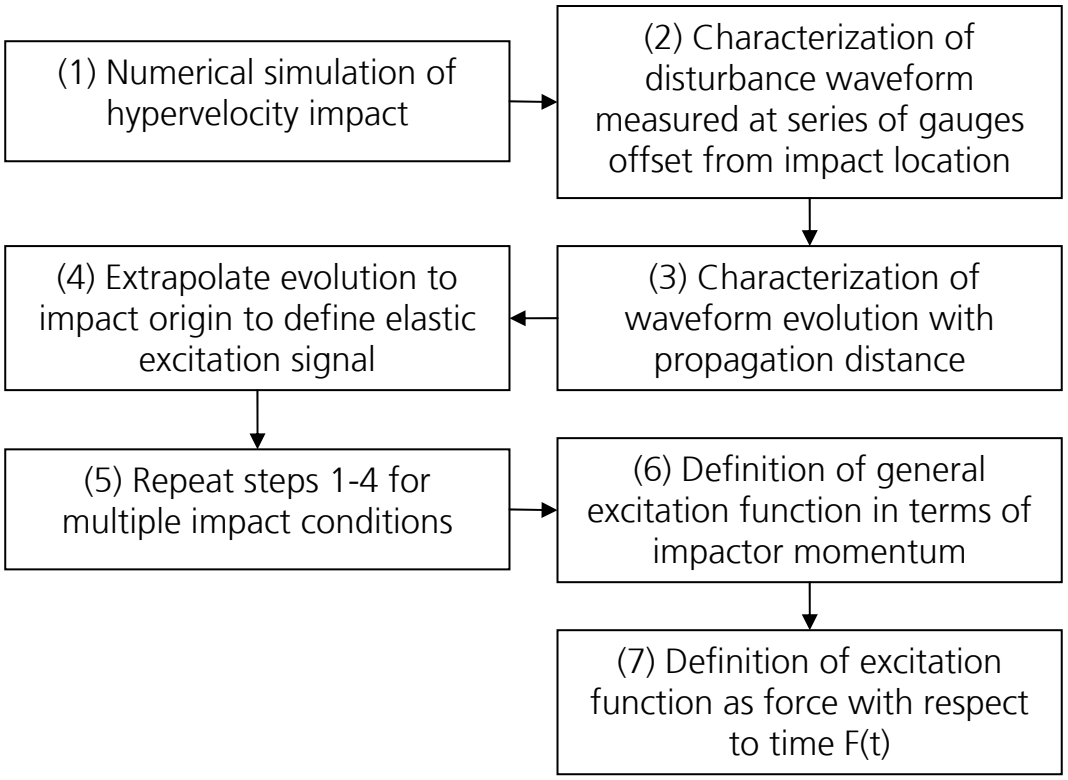

Figure 5-2 Methodology applied in derivation of the excitation function.

The sandwich panel facesheet on which the highest amplitude disturbance is induced will represent the critical excitation. Thus, for impacts which lead to perforation of (at least) the front facesheet, the excitation function will only consider the facesheet to which the most elastic energy is transferred. It is necessary, therefore, to define separate excitation functions for the front and rear facesheet, and provide guidelines to define which excitation function should be applied for which impact conditions. This methodology is outlined in Figure 5-3.

Significant perforation is defined as the degree of penetration at which an increase in projectile momentum will not result in an increase of momentum transfer to the respective facesheet.

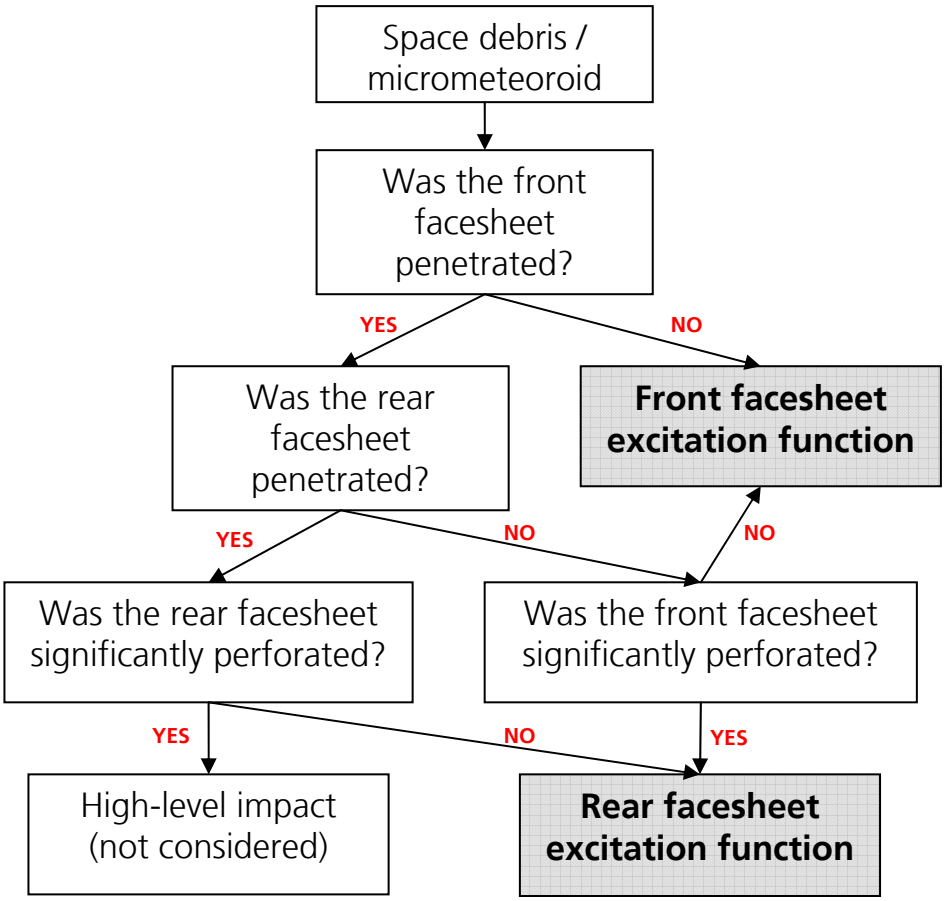

Figure 5-3 Methodology for application of the excitation function.

5.2 Characterisation of Impact-Induced Wave Evolution in CFRP/Al HC Structures

In order for the waveform to be approximated by an empirical function it must be simplified. Thus, only components of the measured signal key to the impact-induced disturbance threat are considered. The disturbance induced by impact of a 0.2mm Al-sphere at 10 km/s on the CFRP/Al HC SP is shown in Figure 5-4. The disturbance was measured 8 mm from the impact site on the front surface of the sandwich panel. The disturbance waveform can be separated into three distinct phases corresponding to different types of wave phenomena, namely: longitudinal, shear, and flexural. For impact tests on metallic targets, these phenomena are clearly separable and identifiable (Ryan et al., 2006); however for composite sandwich panels the distinction is more ambiguous.

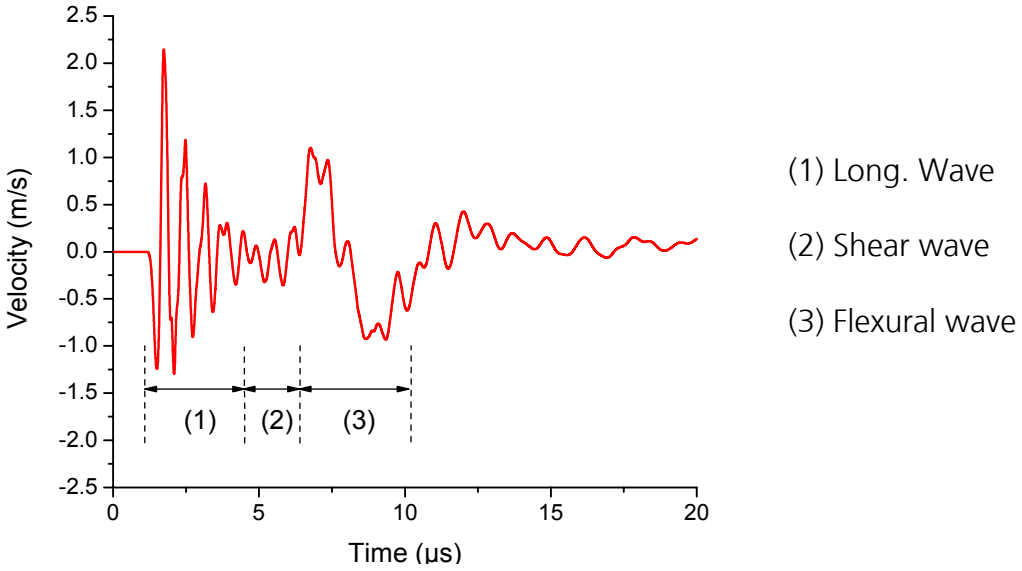

Figure 5-4 Classification of wave types in the disturbance signal.

In Figure 5-4 the initial high amplitude, high frequency waveform is classified as the longitudinal wave. Longitudinal waves oscillate in the direction of propagation. Perfect longitudinal waves occur only in quasi-unbounded solids, i.e. when the lateral extension of the structure is large compared to the wavelength. This is characteristic for a uni-axial stress state, in which the wave propagation speed is determined by:

$$c_L = \sqrt{\frac{K}{\rho}} \tag{112}$$

where c_L- long. wave propagation velocity in unbounded solids (m/s)
K – bulk modulus (Pa)
ρ - density of the material (kg/m³)

In bounded solids, wave propagation is influenced by the boundaries of the solid, resulting in wave propagation velocities lower than those of unbounded solids. These waves are referred to as quasi-longitudinal. Two different modes of quasi-longitudinal wave propagation can be distinguished: wave propagation in solids that are bounded in one plane (e.g. plates) and wave propagation in solids that are bounded in two planes (e.g. rods). For solids bounded in two planes, the longitudinal wave propagation velocity is reduced as a function of the ratio between the stiffness of the bulk material (K) and that of the bounded one (E):

$$c_{L,ii} = \sqrt{\frac{E_{ii}}{\rho}} \qquad ii = 1,2,3 \tag{113}$$

where $c_{L,ii}$- long. wave.velocity in solids bounded in two planes (m/s)
E – Young's modulus (Pa) $\rightarrow E = K \cdot 3(1-2\nu)$

Wave propagation in plates (bounded in one plane) is characterized by a bi-axial state of stress: for the in-plane direction, no contraction and elongation occurs. Thus, the Young's modulus is reduced by a factor (1-ν^2), defining a wave propagation velocity of (from Schäfer et al., 2006b):

$$c_{L,i} = \sqrt{\frac{E}{\rho(1-\nu^2)}} \qquad i - 1,2 \tag{114}$$

The propagation velocity of flexural waves is dispersive (i.e. frequency dependent) and can be determined using (from Schäfer et al., 2006b):

$$c_B = \sqrt{2 \cdot \pi \cdot f} \cdot \sqrt[4]{\frac{B}{\rho_A}} \tag{115}$$

where f – wave frequency (Hz)
B – bending stiffness (Nm)
ρ_A – areal weight (kg/m^2)

Considering the facesheet thickness, Eq. (115) can be simplified to:

$$c_B \cong \sqrt{1.8 \cdot c_L \cdot t \cdot f} \tag{116}$$

Shear wave propagation velocity is governed by the shear modulus, G:

$$c_S = \sqrt{\frac{G}{\rho}} \tag{117}$$

Using the laminate properties previous defined in Table 4-3, the longitudinal wave propagation velocity of the CFRP laminate was calculated as 5693 m/s in the material 22-direction. Using Eq. (117) a shear propagation velocity of 3128 m/s is determined. In Figure 5-4 the low frequency, high-amplitude wave feature recorded ~6.5 µs after impact has an approximate frequency of 210 kHz. As such, an approximate bending wave propagation velocity at this measurement location is determined as 1038 m/s. Theoretical arrival times of the three

wave features are subsequently calculated as 1.4, 2.6, and 7.7 μs after impact for the longitudinal, shear and bending waves respectively. From Figure 5-4 is it considered that arrival of the shear wave occurs later than 2.6 μs after impact. Eq. (117) is used for isotropic materials. In this instance, the in-plane shear modulus (G_{12}) has been used in the calculation, however as out-of-plane velocities are measured it is considered that the transverse shear modulus G_{23} will also affect the shear wave propagation velocity. The longitudinal and flexural signals agree well with the theoretical calculations.

Figure 5-5 shows out-of-plane velocity measurements of the impact-induced disturbance propagation from a 0.2 mm projectile impacting the 0.5 mm thick CFRP facesheet at 10 km/s. At 2 mm from the impact site, the amplitude of the longitudinal wave is ~6 m/s. As the disturbance propagates away from the impact axis, this feature is rapidly reduced. By 25 mm from the impact axis, the longitudinal waveform is hardly discernable.

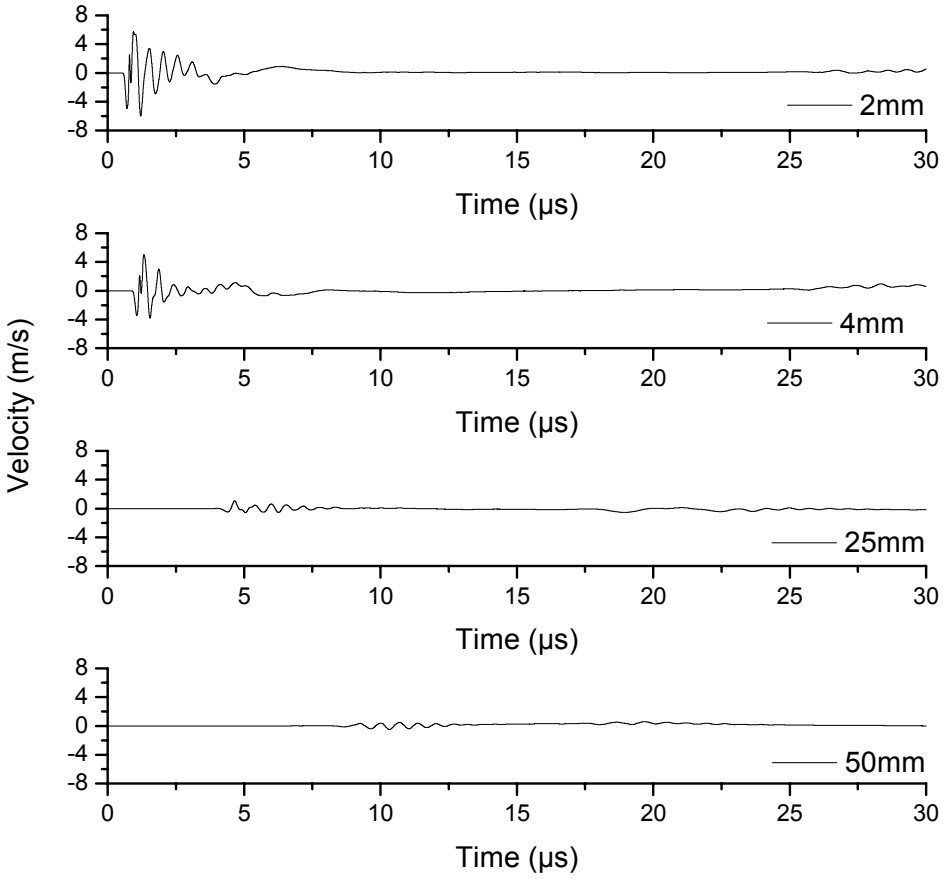

Figure 5-5 Out-of-plane velocity measurements made 2, 4, 25 and 50 mm from the impact of a 0.2mm Al-sphere at 10km/s on the GAIA CFRP facesheet.

The excitation function provides a local characterisation of the sandwich panel elastic excitation induced by impact of a particle at hypervelocity suitable for application in a structural code. The expected valid frequency range of the structural code has a maximum of ~500 kHz and will therefore be unable to propagate features of the characterised disturbance waveform with higher frequencies. The longitudinal feature of the disturbance waveform shown in Figure 5-5 has a frequency of ~1 MHz and is therefore not be transferable to the FE simulations. As such, a 500 kHz low-pass filter will be applied to the disturbance waveform measured in the numerical simulations prior to characterisation. An example of the low-pass filter effect is shown in Figure 5-6.

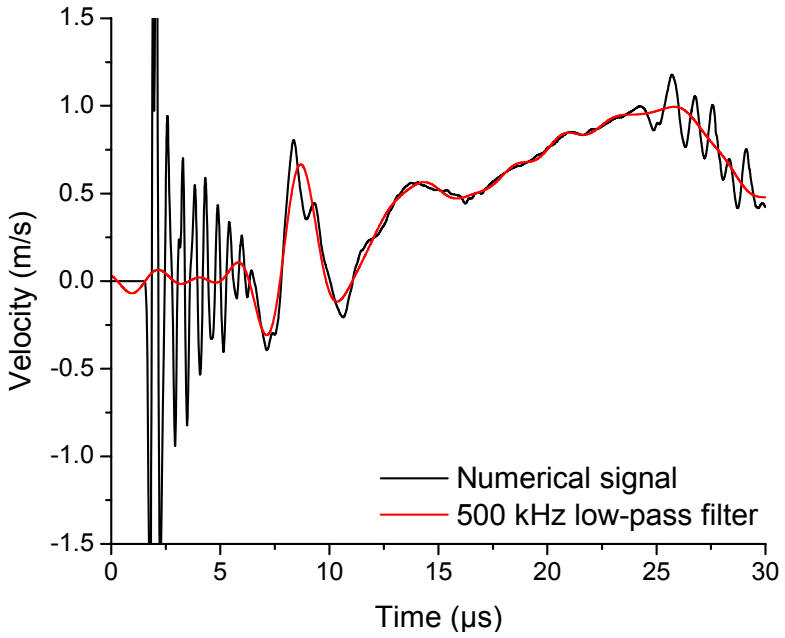

Figure 5-6 The effect of a 500 kHz low-pass filter on the out-of-plane velocity measurement made at 10 mm offset from the impact of a 0.2 mm Al-sphere at 10.0 km/s on the 0.5 mm thick CFRP facesheet.

Considering the rapid damping of the longitudinal wave in the CFRP facesheets and the effect of the low-pass filter representing the structural code upper frequency limit, it is apparent that the flexural feature of the disturbance waveform is the key feature. Therefore, this feature will be the subject of characterisation.

At the impact site, the excitation of the panel is expected to be a single pulse in the flight direction of the projectile. The rate of acceleration is expected to be in the same order of magnitude as the impact velocity. At the excitation maxima, the projectile will have either perforated or been

halted by the CFRP sheet, and therefore the excitation will return to zero. It is considered that this type of behaviour is best approximated by a polynomial-exponential decay function of the form:

$$V(t) = A \cdot (t - t_0)^2 \cdot e^{-\beta(t-t_0)} \tag{118}$$

where A –amplitude scaling factor
β – rate of the exponential decay factor
t – time (μs)
t_0 – arrival time at gauge location (μs)

Eq. (118) represents an empirical fit of the excitation pulse. Given the complexity of the problem, it is not possible to calculate the panel response from first principles – a common problem in hypervelocity impact research. The space community, recognising this, uses analytical-empirical equations which although based on a physical description use experimental data and observations to empirically adjust the analytical expression (Ballistic Limit Equations for example). Eq. (118) describes an ideal single-pulse excitation of the impacted panel, the constants of which are empirically-adjusted to fit the measured curve.

A series of out-of-plane velocity measurements made on the CFRP facesheet following impact of a 0.2 mm Al-sphere at 10 km/s are shown in Figure 5-7. The signals are measured at intervals from the impact location. The low-pass filter has been applied to the numerical data, and the flexural wave peak can be clearly observed. Measurements shown in Figure 5-7 are made at a minimum of 4 mm from the impact site, thus the ideal single polynomial-exponential peak has evolved into a more dispersive flexural wave, observable in the 4 mm signal (two peaks at ~2.5 and ~7.5 μs) and even more significantly in the 10 mm signal which shows after 10 μs a long duration, highly uneven velocity pulse in the impact velocity direction.

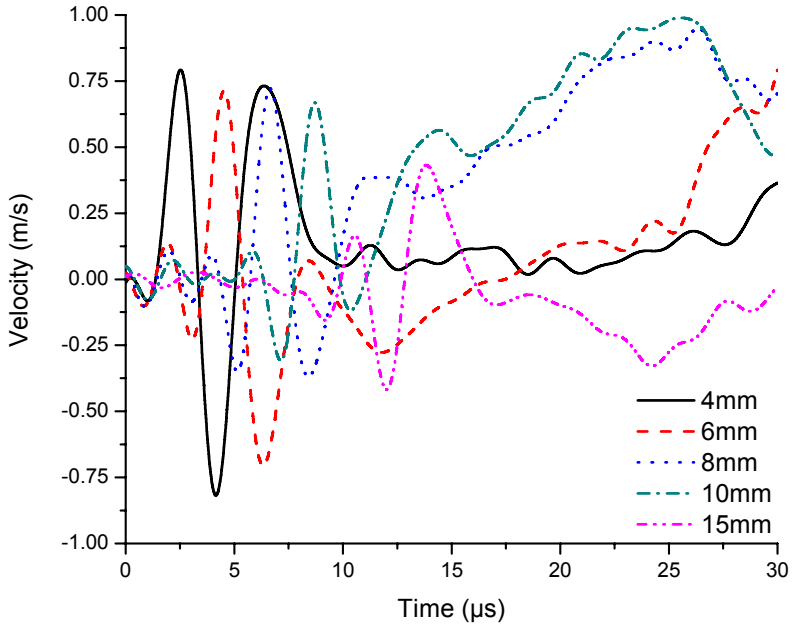

Figure 5-7 Filtered velocity measurements showing signal evolution with distance from impact location.

The polynomial-exponential fit function is applied to a series of disturbance signals in Figure 5-8 that are numerically measured on the rear side of the GAIA CFRP/Al HC SP following impact of a 0.6mm Al-sphere at 16 km/s. It can be seen that as $t \rightarrow 0$, the fit function (Eq. (118)) approaches infinity. As the excitation function will provide the elastic response of the structure *at the impact location*, i.e. $t_0 \equiv 0$, the rapid increase of velocity for times $< t_0$ will not be considered. Furthermore, it can be observed that at increasing distance from the impact location the disturbance measurements show an initial negative velocity pulse. This is an evolutionary characteristic of the flexural waveform, however to fit the polynomial-exponential decay to such a curve a vertical offset must be included in Eq. (118). The result is that instead of asymptoting at V = 0 m/s (i.e. rest condition), the equation then describes a negative velocity at late times. Again, as the characterisation signals at offset measurement locations are only used to characterise the evolution of the flexural waveform to allow extrapolation back to the impact origin, this will not be problematic.

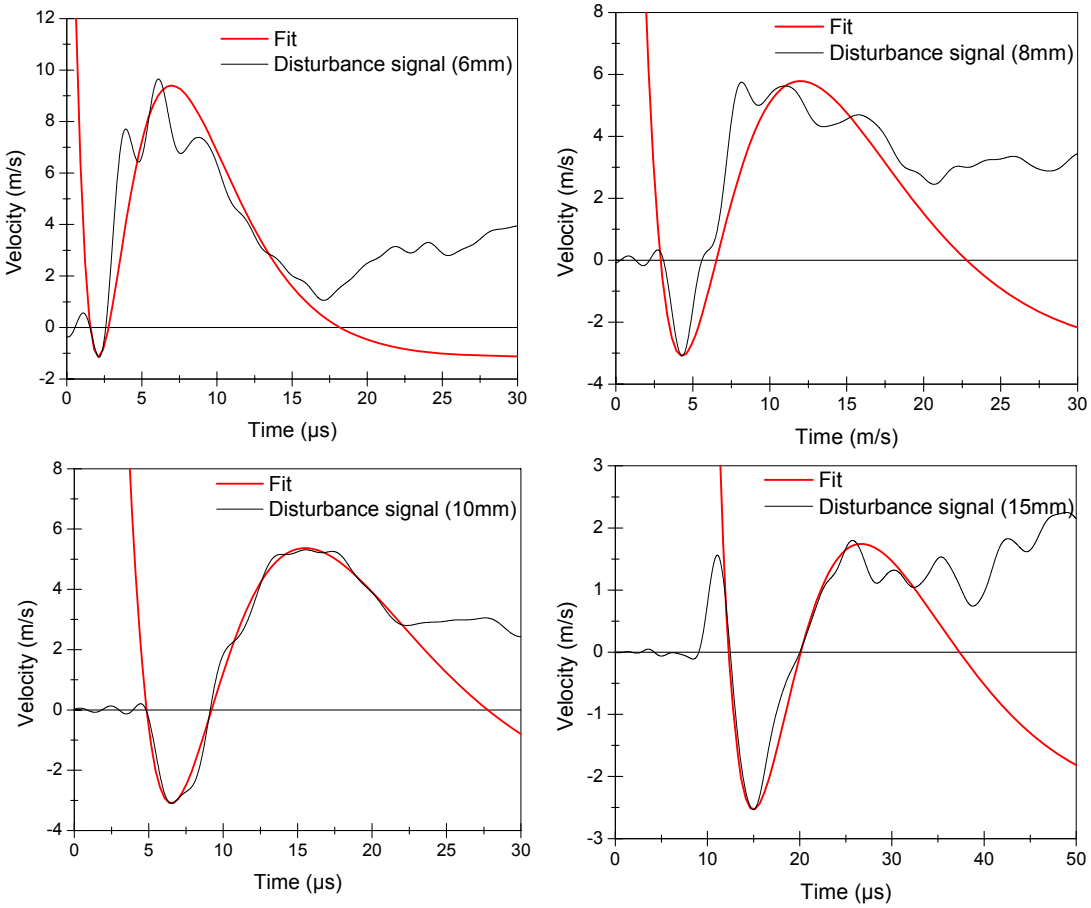

Figure 5-8 Disturbance signals and polynomial-exponential bending wave fit for impact of a 0.6mm Al-sphere at 16.0 km/s measured on the SP rear side.

The evolution of the disturbance flexural wave can be characterized in terms of the constants in Eq. (118), as shown in Figure 5-9. It can be seen that the t_0 term does not approach the origin at x=0 mm. This indicates that the excitation measured on the rear facesheet is not induced on a point-source impact, but rather over a finite area with radius defined by the intercept of the t_0 linear relationship.

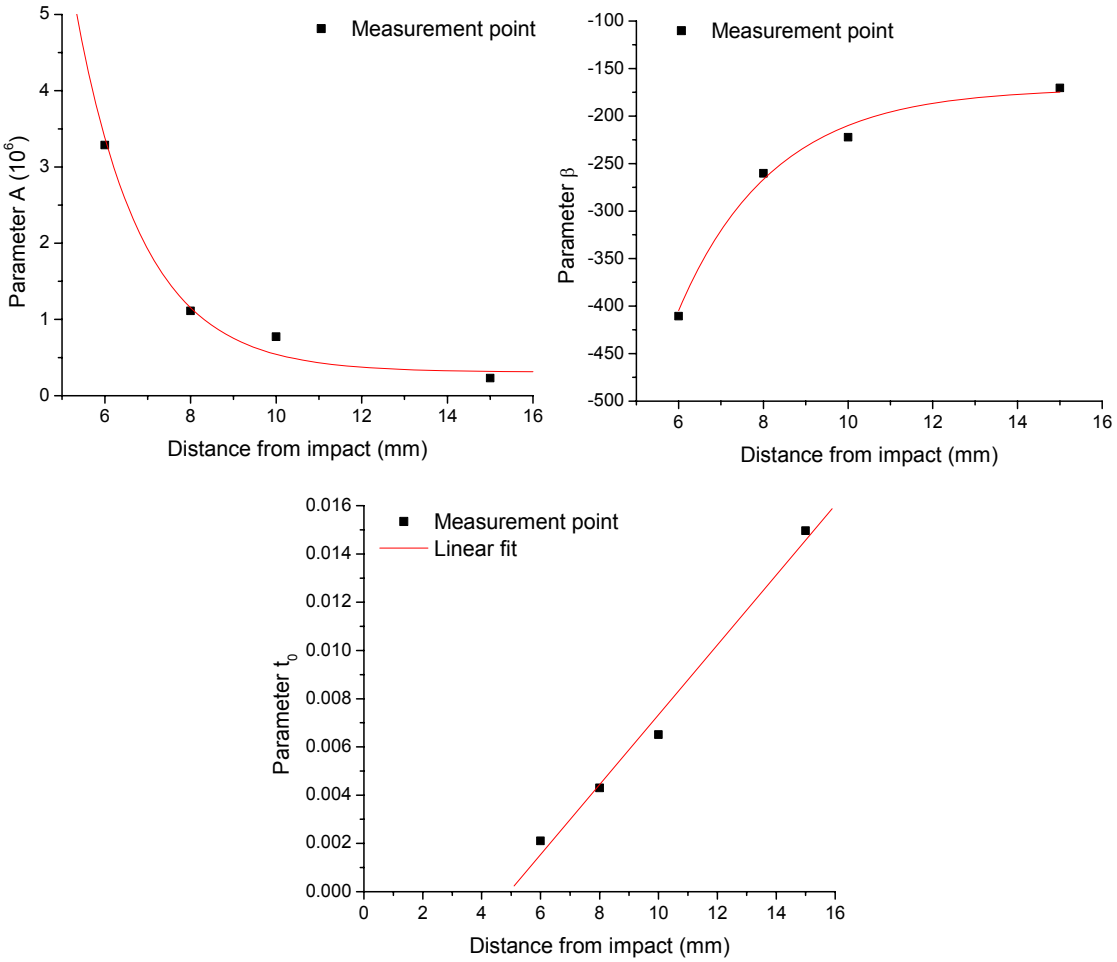

Figure 5-9 Characterizing the evolution of the simplified disturbance signal for impact of a 0.6mm Al-sphere at 16.0 km/s.

The radius of the excitation area for the impact conditions shown in Figure 5-9 is calculated as:

$$x(t_0 = 0) = x_e = \frac{7.14 \times 10^{-3}}{1.45 \times 10^{-3}}$$
$$\rightarrow x_3 = 4.924 \text{ mm}$$

For rear facesheet excitation, this finite area represents impact of the expanded fragment cloud. The expanded fragment cloud is shown in Figure 5-10 during impact on the rear facesheet along with the final facesheet damage profile.

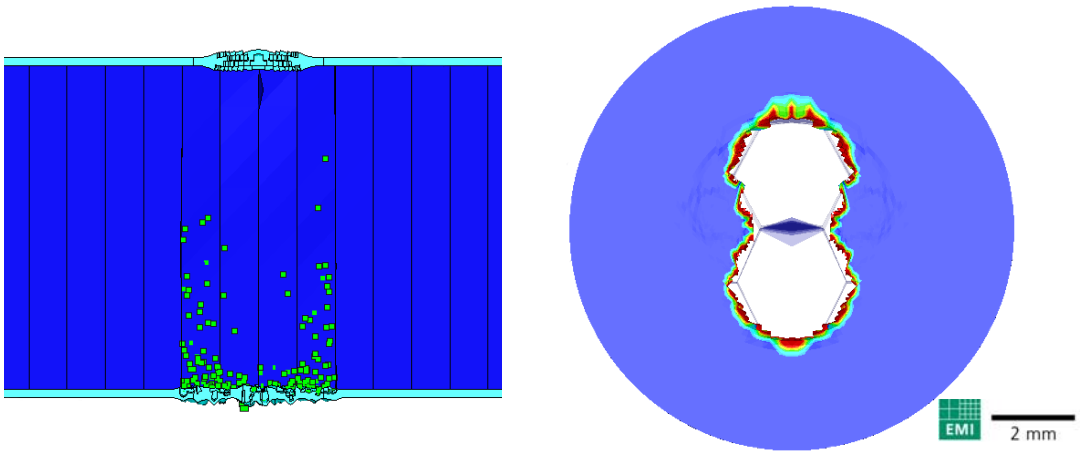

Figure 5-10 Channelling of the fragment cloud and the resultant damage on the SP rear facesheet (impact conditions: 0.6mm Al-sphere at 16.0 km/s).

Expansion of the fragment cloud is restricted, or "channelled", by the honeycomb cell walls. It can be seen in Figure 5-10 that for this case, all fragments are channelled within 2 honeycomb cells.

For the front facesheet, the excitation area approximately represents the plastic damage zone. Initially, as the projectile impacts the target, shock waves are generated which propagate into both the target and projectile. In the case where the impact velocity is higher than the sound speed of the target material, the projectile initially penetrates the target at a faster rate than the impact-induced shock wave is able to propagate. As the target is slowed by the plate, the shock wave overtakes the penetrating particle. Initially, the magnitude of the impact-induced shock wave is sufficient to plastically damage the facesheet material (realized as permanent deformation and delamination). Tennyson and Shortliffe (1997) provide equations for predicting the extent of delamination in composite laminates subject to hypervelocity impact. The damage equation is derived from impact tests on CFRP/PEEK composites and is independent of lay-up. The equation was derived from experimental data with a velocity range of 4.0 to 7.5 km/s, and is given as:

$$D_{delam} = 4.04 \cdot \sqrt[3]{KE \frac{t}{d_p}} \tag{119}$$

This expression can be used to verify the justification of a finite excitation area on the sandwich panel front facesheet.

The constants of the polynomial-exponential decay function are characterised in Figure 5-9 as:

$$A = A_1 \cdot e^{-x/A_2} + A_3 \tag{120}$$

where x – Distance from impact (mm)
A_1 = 146.62E+06
A_2 = 1.552
A_3 = 0.3097E+06

$$\beta = \beta_1 - \beta_2 \cdot \beta_3^{\,x} \tag{121}$$

where β_1 = -170.57
β_2 = 3393.27
β_3 = 0.640

$$t_0 = t_1 + t_2 \cdot x \tag{122}$$

where t_1 = -7.14E-03
t_2 = 1.45E-03

Extrapolated back to the excitation area (x=4.924 mm), the excitation function takes the form:

$$V(t) = A \cdot t^2 \cdot e^{-\beta \cdot t} \tag{123}$$

where $A = 6.452 \cdot 10^6$
$\beta = 0.5488 \cdot 10^3$
V – mm/ms (m/s)
t – ms

The simplified disturbance waveforms (SP rear side) for impact of a 0.6mm Al-sphere at 16.0 km/s are shown in Figure 5-11 in addition to the original elastic excitation waveform defined by extrapolation of the polynomial-exponential decay function constants to the limit of the excitation area. The figure therefore shows the evolution of the (simplified) waveform as it propagates away from the impact location. As shown previously for the numerical measurements, the amplitude of the flexural wave decreases with increasing distance from the impact axis. Additionally, the rate of acceleration (i.e. the positive slope of the waveform) is more rapid closer to the impact site. This is to be expected as the waveform will disperse and the shock wave is attenuated with increasing distance from the impact site. In addition to a decreased rate of acceleration, waveform dispersion causes a significant decrease in the

flexural waveform frequency, which is realised in Figure 5-11 as a spreading of the excitation pulse. In this figure the simplified waveforms do not include the negative vertical offset of the velocity signals discussed in Figure 5-8.

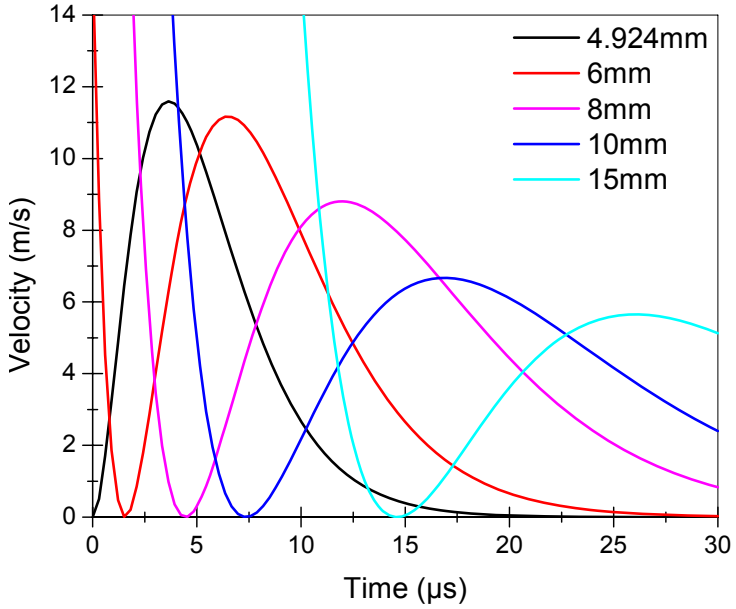

Figure 5-11 Fit curves of the disturbance signals induced by impact of a 0.6mm Al-sphere at 16 km/s measured on the SP rear side and the elastic-equivalent excitation signal at the excitation area.

5.3 Definition of a Generalised Excitation Function

A general excitation function is required which incorporates the effects of projectile diameter and impact velocity. It is considered that these can be accounted for by defining the excitation function in terms of the impactor momentum, where:

$$P_p = m_p \cdot V_{imp} \tag{124}$$

where m_p – projectile mass (kg)
V_{imp} – impact velocity (m/s)

The excitation area must be constant to allow comparison between the excitation function constants derived for different impact conditions. An overview of the derived excitation area radius for the numerical simulations defined in Chapter 4.3 is given in Table 5-1.

Table 5-1 Radius of the excitation area in the numerical simulations.

Sim No.	*Proj. diameter (mm)*	*Impact velocity (km/s)*	*Impact momentum (g.m/s)*	*Radius of exc. area (mm)*
FS-1	0.05	4.9	8.9797E-04	n/a
FS-2	0.05	10.0	1.8326E-03	n/a
FS-3	0.2	4.9	0.0575	2.3033
FS-4	0.2	10.0	0.1173	2.606
FS-5	0.4	4.9	0.4598	2.416
FS-6	0.4	10.0	0.9383	1.396
FS-7	0.8	4.9	3.6518	3.765
SP-1	0.4	6.0	0.5590	0.2277
SP-2	0.4	10.0	0.9316	1.013
SP-3	0.4	20.0	1.8632	2.756
SP-4	0.6	16.0	5.0306	4.924
SP-5	0.8	10.0	7.4527	3.043
SP-6	0.7	20.0	9.9855	4.810
SP-7	0.8	17.5	13.042	1.981
SP-8	0.8	20.0	14.905	2.352

Of the seven facesheet simulations performed, only five are considered for derivation of the generalized excitation function. The two simulations considering impact of 0.05 mm Al-sphere provided results which are deemed overly sensitive to the numerical model. Validation of the numerical model was performed with a 1.5 mm Al-sphere projectile, which represents four orders of magnitude difference in projectile mass. For such small particles it is considered that a higher-resolution numerical model is required, however experimental validation through direct signal comparison is not possible with available facilities (two-stage light-gas guns).

From the simulations a maximum excitation area radius of 3.765 mm and 4.810 mm was recorded for the front and rear facesheets, respectively. A constant excitation area was thus conservatively defined at 4 mm and 6mm for the front and rear facesheets. The front and rear facesheet excitation function constants determined from the numerical simulations are characterized in Figure 5-12 in terms of impactor momentum.

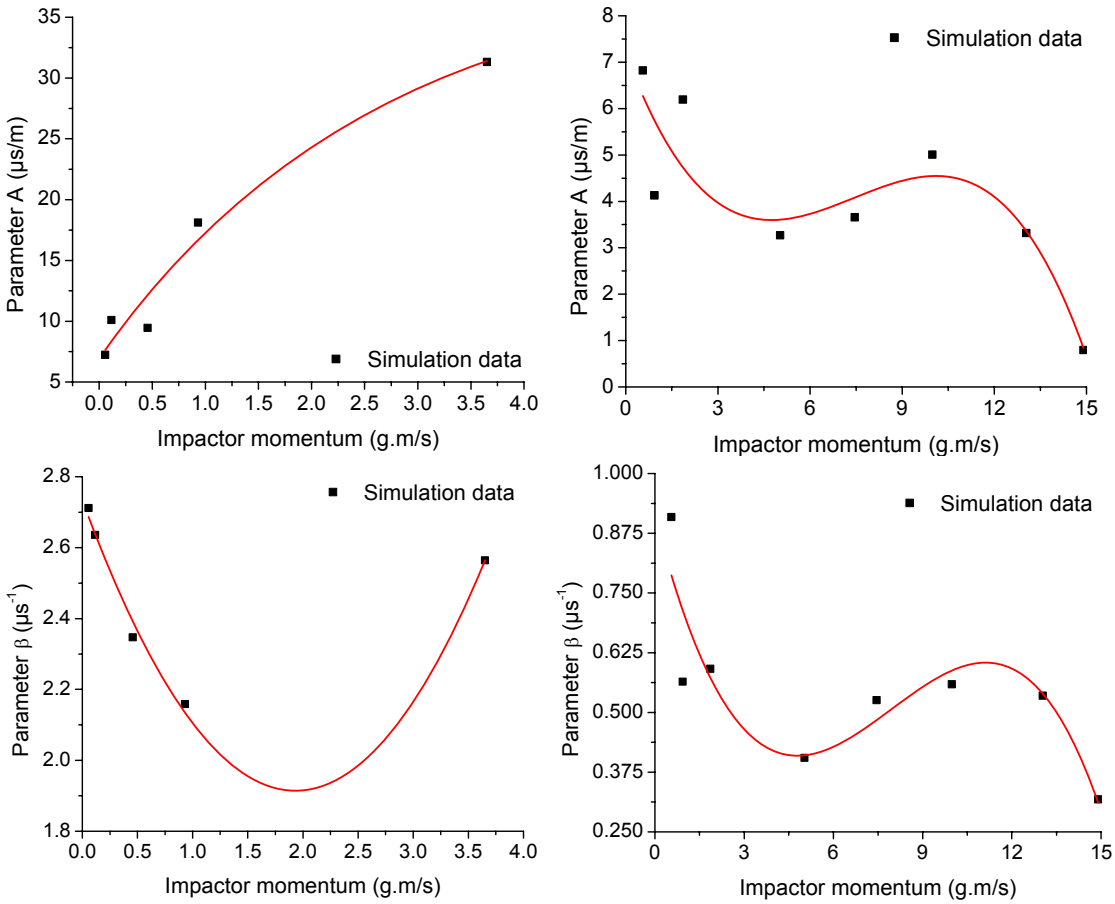

Figure 5-12 Characterization of the excitation function constants. Left: front facesheet (solved for x=4mm), Right: rear facesheet (solved for x=6mm).

The generalized excitation function, expressed as velocity with respect to time, is defined as:

$$V(t) = A \cdot t^2 \cdot e^{-\beta t} \tag{125}$$

Parameters A and β are determined empirically using curve fit functions:

Front facesheet:

$$A = 39.491 - 32.551 \cdot 0.683^{P_p}$$

$$\beta = 2.7347 - 0.8494 \cdot P_p + 0.2199 \cdot P_p^{\,2}$$

Rear facesheet:

$$A = 7.189 - 1.794 \cdot P + 0.278 \cdot P^2 - 0.0125 \cdot P^3$$

$$\beta = 0.913 - 0.245 \cdot P + 0.037 \cdot P^2 - 1.54E - 03 \cdot P^3$$

Figure 5-13 shows the peak excitation velocities of the excitation waveform for the front and rear facesheets, defined in terms of impactor momentum. For both facesheets it is apparent that with increasing impactor momentum there in an initial rise in peak excitation velocity (i.e. magnitude of the impact-induced disturbance). The maxima of the peak excitation velocity curves define the onset of "significant perforation". Following this peak, both excitation functions predict a decrease in peak excitation velocity with increasing impactor momentum as a result of the change in penetration mechanism. It should be noted that the peak excitation velocity described by the front excitation function reaches higher values than the rear facesheet function. The front facesheet excitation function is defined 4 mm from the impact axis, compared to 6 mm for the rear facesheet. Thus, the magnitudes of these curves should not be directly compared. In the rear facesheet peak excitation velocity curve a very sharp decrease can be observed after ~14 g·m/s. This impactor momentum (from simulation of a 0.8 mm Al-sphere at 20 km/s) indicates the limit of validity of the excitation function.

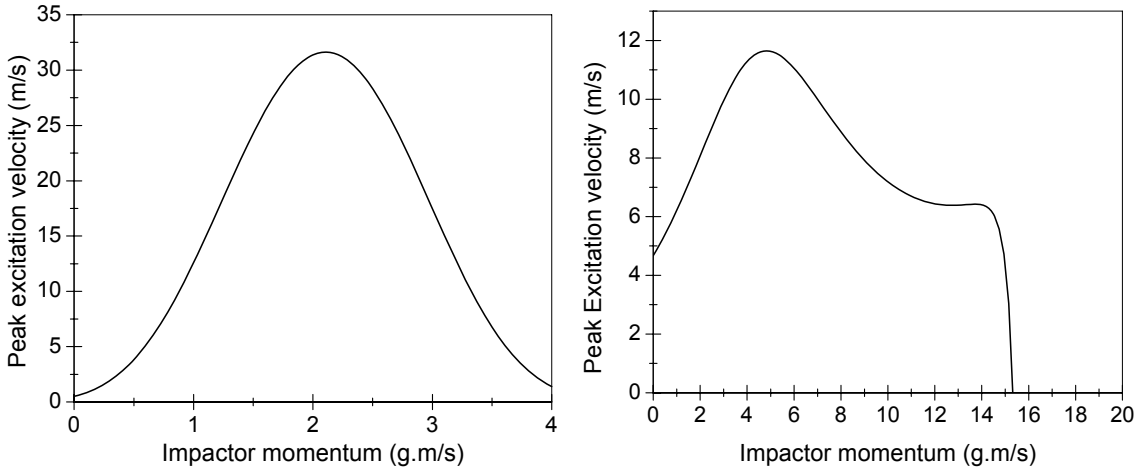

Figure 5-13 Peak excitation velocities for the front (left) and rear (right) facesheet excitation functions.

5.3.1 An Excitation Function Suitable for Application in Structural Analysis Codes

For application of the excitation function in a structural FE code it must be expressed as force with respect to time. The acceleration is determined by taking the time derivative of the velocity excitation function:

$$a = \frac{dV(t)}{dt}$$

$$\rightarrow a = 2A \cdot t \cdot e^{-\beta \cdot t} - A \cdot t^2 \cdot \beta \cdot e^{-\beta \cdot t} \quad (126)$$

The excited mass is defined by the area of excitation on the corresponding facesheet. Considering the radius of the excitation area was set as 4mm and 6mm for the front and rear facesheet function, the excited mass is calculated as 0.0382g and 0.0597g respectively (0.5mm thick CFRP facesheets having 1.52 g/cm³ volumetric density). The front and rear facesheet excitation functions, for application of force with respect to time, are expressed as:

$$F(t) = ma(t) \quad (127)$$

where $a(t) = 2A \cdot t \cdot e^{-\beta \cdot t} - A \cdot t^2 \cdot \beta \cdot e^{-\beta \cdot t}$

Front facesheet	Rear facesheet
$m = 0.0382E-03$ kg	$m = 0.0860E-03$ kg
$A = 39.491 - 32.551 \cdot 0.683^{P_p}$	$A = 7.189 - 1.794 \cdot P_p + 0.278 \cdot P_p^{\,2} \ldots - 0.0125 \cdot P_p^{\,3}$
$\beta = 2.7347 - 0.8494 \cdot P_p + 0.2199 \cdot P_p^{\,2}$	$\beta = 0.913 - 0.245 \cdot P_p + 0.037 \cdot P_p^{\,2} \ldots - 1.54E-03 \cdot P_p^{\,3}$

Units a – 1×10^6 m/s² t - µs m – kg F – N

The peak excitation force is shown in Figure 5-14 for the front and rear facesheet excitation functions. The range of application for the facesheet functions is defined about an impactor momentum of 2.64 g·m/s. This point represents the condition of significant perforation in the front facesheet upon which the majority of momentum transfer changes from the front to rear facesheet. It can be noted that as the impactor momentum approaches zero, the rear facesheet excitation function does not return to the origin. This is due to the rear facesheet excitation function being derived from disturbance signals measured for impact of projectiles with 0.56 g·m/s momentum or higher. Additionally, for impactors with momentum less than ~4.5 g·m/s there is significant scatter in the fit of the rear facesheet excitation function constants (Figure 5-12). Ideally there would be a smooth transition of the peak excitation force of the front facesheet function to the rear facesheet function at the limit of

2.64 g·m/s. It is considered that the current derivation provides conservative solutions in the 2.64-4.5 g·m/s momentum range.

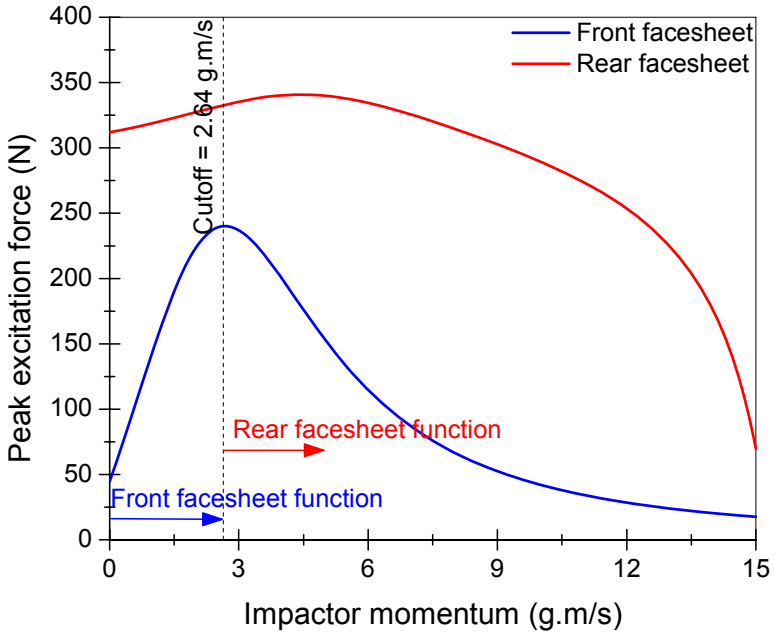

Figure 5-14 Excitation function profile peak force defined in terms of impactor momentum.

A comparison of the force-time excitation profile defined for the front- and rear facesheet at the transition momentum (2.64 g·m/s) is shown in Figure 5-15. It can be seen that the rear facesheet excitation function gives a higher peak excitation force (as expected from Figure 5-14). Additionally, the force is applied over a longer duration (4 µs compared with 1 µs) leading to a significantly larger impulse. A series of excitation function force profiles are also given in Figure 5-15 that show the effect of increasing projectile diameter on impact excitation (all projectiles impacting at 20 km/s). Again, the peak excitation force increases with projectile diameter due to the increase in impulse.

5.4 Summary

A series of highly-instrumented numerical simulations defined in Chapter 4 have been performed in order to characterise the transient disturbance waveform induced by impact of projectiles at hypervelocity on a space-representative CFRP/Al HC sandwich panel. Four penetration cases have previously been defined which are expected to induce significantly different excitation modes. Through the application of the new predictive

ballistic limit equation, the numerical simulation program was defined to encompass all degrees of structural penetration.

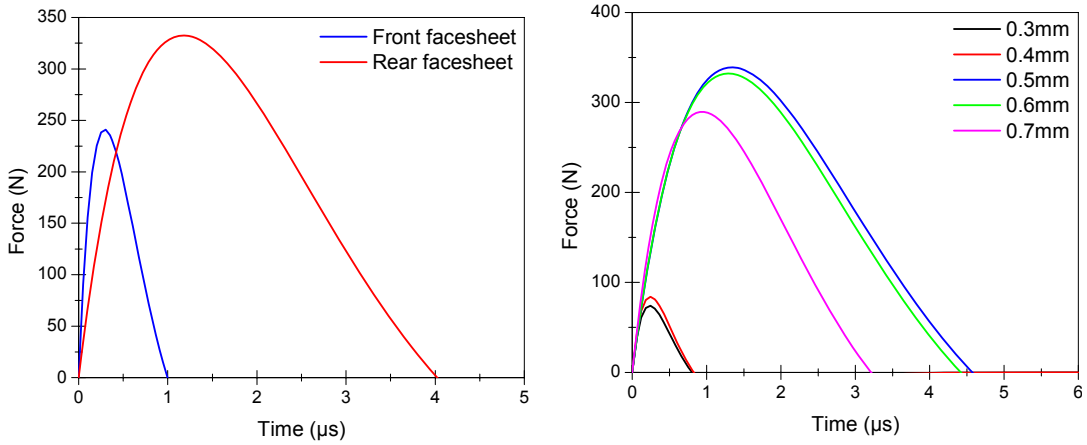

Figure 5-15 Excitation force profile. Left: Comparison of the front and rear facesheet excitation functions at the transition momentum. Right: The effect of increasing projectile diameter on excitation profile (all projectiles at impact velocity of 20 km/s).

The impact-induced disturbance has been measured in the numerical simulations via massless sensing points at spaced offsets from the impact axis. By recording the transient waveform at increasing offsets from the impact site, the evolution of the waveform characteristics is characterised in terms of propagation distance. The excitation waveform is simplified using a polynomial-exponential decay function. This function is able to describe an origin at zero followed by a single, rapidly increasing pulse which reaches a positive maxima and then asymptotes at zero. This is representative of the physical effect of the projectile on the local facesheet area.

The waveform evolution characterisation is then used to extrapolate the simplified excitation signals back to the impact origin, thus defining the original elastic excitation. It was found that excitation of the facesheets is not induced by a point-source, rather a finite area. For the front facesheet this area represents the extent of plastic damage (delamination), while for the rear facesheet it is defined by the expansion of the fragment cloud.

Given the range of impact conditions relative to the GAIA mission (impactor mass, impact velocity), a general excitation function has been derived which accounts for the impact parameters in terms of momentum. This generalized function, expressed in two parts (front- and rear facesheet) allows the derivation of an excitation function for any

combination of impactor diameter and velocity within the range of validity (maximum projectile diameter 0.8 mm).

For implementation of the excitation function in global satellite finite element models, the impact excitation is expressed as force in terms of time. Furthermore, the area and mass of the relevant facesheet subject to acceleration is defined to ensure consistency between the numerical methods (hydrocode, FE packages).

6 Summary and Conclusions

6.1 Research Outcomes

The problem of a polluted space environment is one that the space industry must fully come to terms with in the near future. Unless binding preventative measures are implemented to mitigate the generation of space debris, and active removal of existing debris is performed, the saturation of key orbital altitudes (or critical debris mass) will threaten their use for future generations.

Although the threat of meteoroids and space debris impacts on spacecraft has long been recognised and subsequently addressed, the space industry has survived this long without a catastrophic debris impact-induced failure only with a large measure of luck. Indeed, that space debris has succeeded this long in remaining a topic of somewhat peripheral interest to mission designers is purely due to the lack of major impact events. Nonetheless, space debris is garnering an ever-increasing level of awareness in the space community, primarily as a result of the International Space Station. In a list of safety hazards and technical risks maintained by the ISS safety office during station development and construction, the sixth ranked risk is directly related to meteoroids and debris: "The risk from meteoroids and debris is unacceptably high, primarily because of the inadequate shielding of the Russian modules".

For unmanned satellites, particularly the next generation of European scientific satellites which employ extremely sensitive measurement devices, current micrometeoroid/space debris (M/SD) risk analysis procedures are inadequate. Recognising that a degradation of measurement accuracy represents a mission failure equally as effective (yet not nearly as sensational) as catastrophic failure, an effort is being made to assess the structural vibration environment induced by the regular impact of debris particles. Towards this goal, this thesis presents a means of characterising the local structural disturbance induced by impact of M/SD particles at hypervelocity. The platform stability requirements of the next generation ESA satellites (e.g. GOCE, GAIA, LISA, μScope etc) demand use of CFRP/Al HC sandwich panels as the primary structure. Although these panels are amongst the most commonly used structures in unmanned spacecraft, their response to hypervelocity impact was previously relatively unknown.

Four levels of penetration were defined for the sandwich panel, each one expected to induce a significantly different excitation. The penetration cases were: (1) no penetration of the front facesheet; (2) minimal penetration of the front facesheet, no penetration of the rear facesheet; (3) minimal penetration of the rear facesheet, and; (4) significant perforation of the rear facesheet. The Global Astrometric Interferometer for Astrophysics (GAIA) satellite was selected as a representative platform to investigate disturbances induced by hypervelocity impacts. GAIA will operate in a Lissajous orbit about the Earth-Sun L2 Lagrangian point, at which the debris environment will be dominated by meteoroids with a mass between 10^{-11} and 10^{-7} kg travelling at between 11 and 72 km/s with a mean of 20 km/s. As hypervelocity acceleration test facilities are unable to reproduce these impact conditions, numerical simulations are required.

To ensure the complete range of penetration conditions were simulated in the numerical program, an extensive test campaign was performed on six different CFRP/Al HC sandwich panel structures to determine their shielding capability. A new equation was defined which can be used to predict the penetration thresholds of composite sandwich panels. The equation was validated by comparing the predictions to additional impact test data available in literature. The equation provided an improvement over existing predictive techniques. Additionally, the new ballistic limit equation can be used to predict the penetration thresholds of thin metallic plates located behind the shielding wall, representative of electronic-box lids, battery casings and metallic pressure vessels. Although not directly applicable in the analysis of hypervelocity impact-induced vibrations, this capability can be very useful in the assessment of M/SD penetration-based risk criteria.

Recent advances in the capability of reproducing composite material behaviour during hypervelocity impact allow the definition of orthotropic constitutive behaviour, non-linear equation of state, orthotropic non-linear hardening, and individual material failure plane initiation criteria. In the absence of experimentally-characterised material data, a derivation procedure has been developed which applies a number of traditional composite mechanics theories (micromechanics, classical laminate theory, Hooke's law) in conjunction with the laws of shock physics (Mie-Grüniesen shock-jump condition) and defined common CFRP properties to allow a full set of coarse material data to be determined from basic constituent properties. A review of applicable theories has been made, and in the case of multiple available techniques a selection has been

made based on a critical review. The derivation procedure has been applied to a space-grade CFRP laminate for which a full experimentally-characterised data set exists. A comparison between the experimentally- and theoretically- derived data sets showed good agreement. The two data sets were used to simulate a number of hypervelocity impact experiments and a comparison between the damage measurements and overall results showed no improvement in accuracy was provided by the experimentally-characterised material data set.

An extensive sensitivity study was performed to optimise the numerical set-up of the GAIA model. Good agreement was found in a comparison of experimentally- and numerically measured impact-induced transient waves in the facesheets of the GAIA CFRP/Al HC SP. The numerical model was used to enable characterisation of the induced disturbances across the four types of penetration cases previously defined.

In the numerical models a series of measurement points were used on the sandwich panel facesheets to enable characterisation of the impact-induced disturbance wave evolution. A polynomial-exponential decay function was used to simplify the disturbance signal, representing the physical phenomena expected at the impact location. The expression was empirically fit to the numerical measurements, and the empirical constants enabled extrapolation of the disturbance signal back to the impact site. The resulting waveform represented the elastic-equivalent excitation pulse. The excitation was found to occur over a finite area (rather than a point-source), defined on the front facesheet by the extent of permanent deformation (delamination) and on the rear sheet by the expansion of the fragment cloud within the honeycomb core. A series of numerical simulations were performed with different impact conditions (projectile diameter, impact velocity) which enabled the effect of impact momentum on the induced disturbance waveform to be characterised.

Local characterisation of the hypervelocity impact-induced disturbance is made to allow quantification of the disturbance magnitude at stability-critical locations on the spacecraft platform (i.e. measurement devices). The excitation function is expressed as force in terms of time for implementation in global satellite finite element models. Furthermore, the area and mass of the relevant facesheet subject to acceleration is defined to ensure consistency between the two numerical methods (hydrocode and FE package).

6.2 Recommendations

The work of Hiermaier et al. (1999) and Riedel et al. (2003) have provided significant advances in the reproduction of composite material behaviour under extreme loading rates such as hypervelocity impact. The new material modelling capability has shown clear improvements in terms of damage prediction in the impact locality, however problems still exist in formulation of the anisotropic equation of state which effects far-scale measurements (such as the propagation of impact-induced disturbances). The characterization and modelling of shock attenuation in anisotropic media is considered a critical area requiring further investigation.

The advanced orthotropic material model uses a polynomial formulation of the Mie-Grüneisen equation of state to describe the thermodynamic material behaviour. However, an important limitation of the Mie-Grüneisen EOS is that it is not capable of phase changes. Thus, for impact in the hypervelocity regime in which the projectile and target materials are subject to melting and vapourisation, a Mie-Grüneisen EOS describes only super-heated solids. For simulation of events involving phase changes, tabular expressions of the EOS (such as SESAME (Anon., 1983)) may be more accurate. An analytical alternative is the Tillotson EOS which was specifically derived for hypervelocity impact simulations and is valid from low to extremely high pressures (Tillotson, 1962).

Use of the polynomial Mie-Grüneisen EOS is made through application of Anderson et al.'s (1994) constitutive formulation for an anisotropic material which identifies that deviatoric strain produces contributions to hydrostatic pressure and volumetric deformation results in deviatoric stresses:

$$p = p^{EOS}\left(\varepsilon^{vol}\right) + p^{dev}\left(\varepsilon_{ij}^{dev}\right) \tag{128}$$

Experimental derivation of equation of state parameters also requires a more theoretically-sound methodology. In flyer plate impact tests a uniaxial state of strain is generated in the impact direction. The other directional stress components are considered equal to zero. Evaluation of the experimental results is made using existing Hugoniot theory, which means that the stress component normal to the shock wave is identified with Hugoniot pressure. In the case of isotropic materials this is correct; however for anisotropic materials (such as CFRP) this approximation fails

to take into account the directional dependency of shock wave velocity (and therefore Hugoniot stresses).

Experimental flyer plate measurements made on CFRP laminates at EMI show a clear deviation from a linear particle velocity-shock velocity relationship at low shock amplitudes (shown in Figure 6-1).

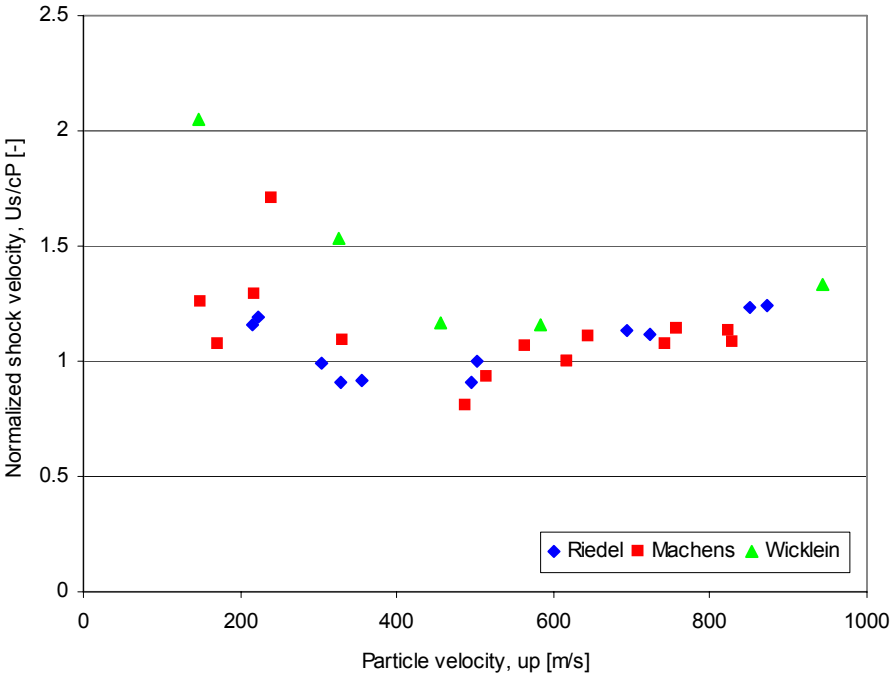

Figure 6-1 Normalized shock and particle velocity relationships for various CFRP composite structures.

Physically, a negative slope in the U_S-u_p diagram means the shock wave propagation velocity is decreasing with an increase in internal stress (or pressure). This can only be caused by phenomena (such as phase transition, porosity as discussed previously) which act as an energy sink, absorbing a part of the shock wave energy. This energy sink gives rise to dispersion of the shock front (instead of concentration), which can lead to a break up of the shock wave. Shock wave decay can generally be traced to geometrical spreading, porosity, large elastic waves, or phase transitions (Liu et al., 2002).

Similar shock velocity-particle velocity relationships have been shown for porous materials (e.g. Riedel, 2004), and GeO_2 glass (Liu et al., 2002). All CFRP materials tested at EMI (i.e. (IM7/8552, T800H/B413M15, UMS2526/Krempel BD)) were inspected for porosity via microscopy.

Figure 6-2 shows a comparison between a porous and non-porous CFRP material. It was found that all three CFRP/Epoxy materials under consideration had no visually-observable porosity.

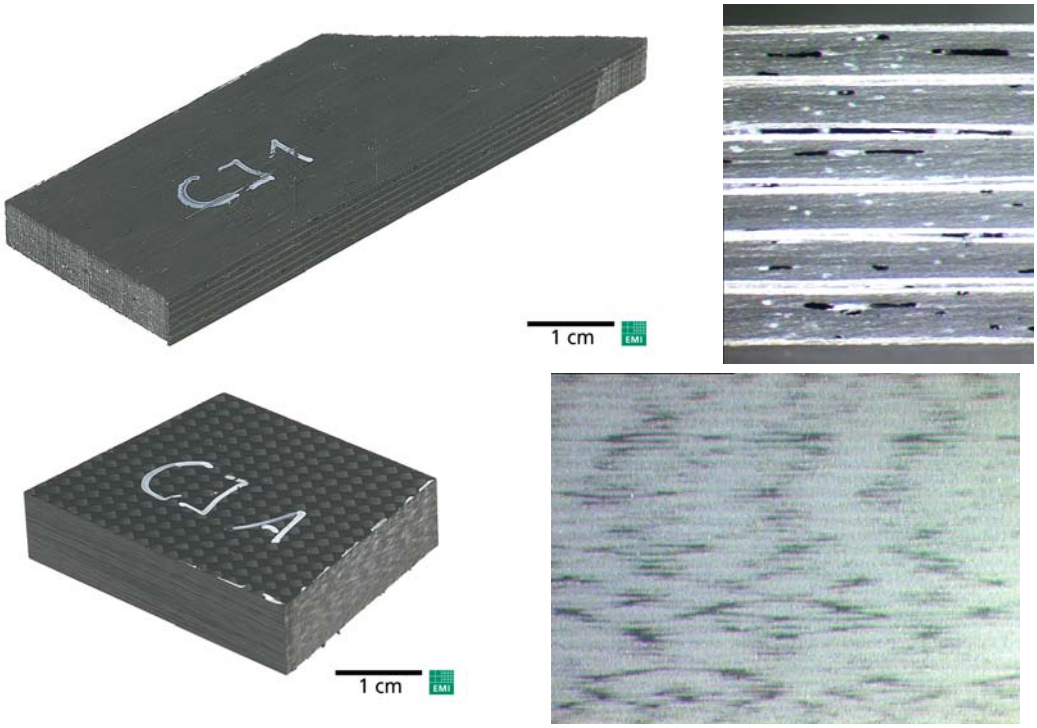

Figure 6-2 CFRP/epoxy composite materials showing porosity (upper) and no porosity (lower).

A phase transition of one composite constituent would also introduce a kind of pressure-dependent porosity in the composite laminate. Riedel et al. (2003) investigated the EOS of Kevlar/epoxy via planar plate impact tests. A selection of samples recovered from the tests is shown in Figure 6-3. It can be seen that for lower impact velocities, there is noticeable separation between the individual Kevlar layers; however the composite and the individual layers remain relatively intact. As the impact velocity increases (V2603), the recovered material is almost purely fabric, suggesting that the epoxy resin has been destroyed during transmission of the impact shock. Although a number of studies investigating the shock behaviour of epoxies (e.g. Barnes et al. (2001), Carter and Marsh (1995)) have found a linear U_s-u_p relationship up to particle velocities of ~2000 m/s, it is considered that the non-homogeneous structure of the fibre-reinforced composite results in a non-uniform pressure distribution within the composite, producing local pressures which may lead to destruction of the epoxy resin.

Figure 6-3 Kevlar/epoxy material recovered after planar plate impact tests. Upper left: original test sample; Upper right: V_{imp} = 117.9 m/s; Lower left: V_{imp} = 276 m/s; Lower right: V_{imp} = 660 m/s.

Chang et al. (2006) examined ultrasonic wave propagation through a unidirectional glass/polyester composite. The authors found that propagation of a shock wave through fibre reinforced composite materials is disturbed, leading to a dispersive (spreading) wave. It was observed that a section of the ultrasonic shockwave energy is reflected at the fibre/matrix interface. Additionally, due to the large differences in constituent moduli, the wave propagates significantly faster in the fibre than the matrix. These two effects combine to break the shock front and then disperse it as it passes through more fibre/matrix interfaces. This can be clearly observed in Figure 6-4. The reflection and dispersion of the shock wave at low shock amplitudes caused by the non-homogenous nature of the composite material structure is assumed to cause spreading of the wave front, producing an elastic precursor similar to that found in GeO_2 glass by Liu et al. (2002). As the shock amplitude increases above the material Hugoniot Elastic Limit, different physical phenomena are considered.

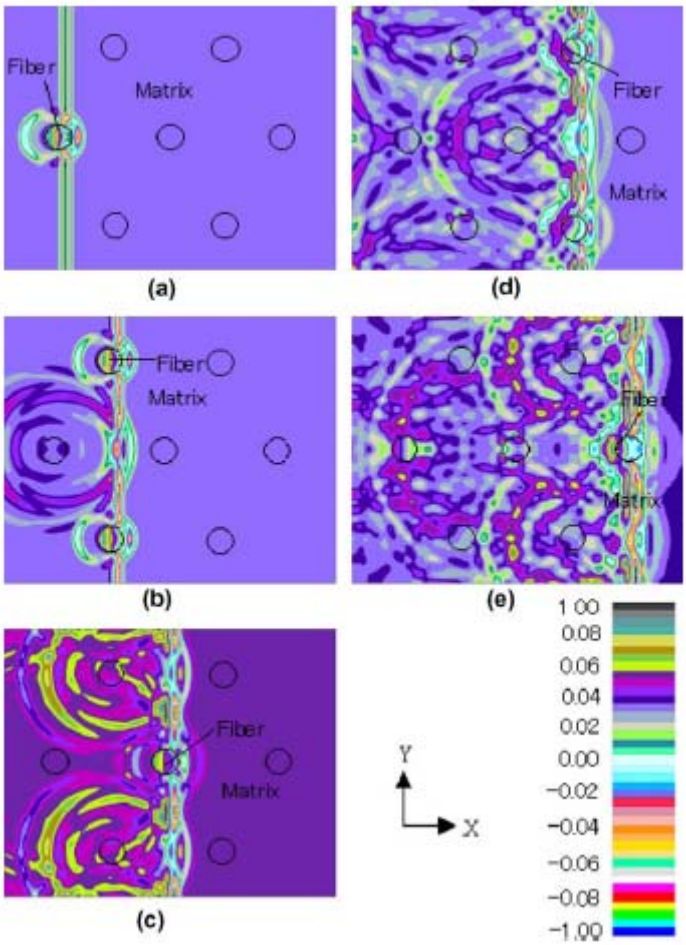

Figure 6-4 History of ultrasonic wave propagating in composite model for a fibre diameter of d=2λ. (Chang et al., 2006).

Similarly, Fowles and Williams (1970) suggests that the Rankine-Hugoniot jump conditions are not valid at pressure states one order of magnitude greater than the material Hugoniot elastic limit (HEL) or less. Rather than a shock wave, the authors state that at these pressure levels an isotropic stress wave should be considered with two wave velocities of constant material velocity and constant stress. This effect has been observed in concrete and mortar (Kawai et al., 2007), and may be relevant for fibre reinforced materials.

Finally, the use of an "average" bulk modulus for the linear expansion term of the Hugoniot series is required to ensure consistency at low pressures, however this "average" term can result in an over-prediction of pressure in directions of low rigidity (i.e. through-thickness).

Although much work has been done by Hiermaier et al. (1999) and Riedel et al. (2003) in development of composite material modelling capability in

hydrocodes, there remain a number of areas in which further improvements can be made, particularly for reproducing material behaviour away from the impact location. Many studies (e.g. Gilat et al., 2002) have shown the strain rate dependency of composite material mechanical properties. Tsai and Sun (2002) have developed a constitutive relationship for composites which uses a viscoplasticity model to describe the nonlinear rate dependent mechanical properties. A micro-mechanical non-linear strain rate dependent constitutive model has been developed by Tabiei et al. (2005) and implemented in the explicit finite element code LS-DYNA for simulation of material behaviour under quasi-static to impact loading rates. The inclusion of strain-rate dependencies may be beneficial in hydrocode composite material models for hypervelocity impact simulations which consider areas at which material strength is important (e.g. far-field, late times, etc.).

In current procedures for determining M/SD impact risk ballistic limit equations are required to define the limits of structural penetration. Of the multiple equations in existence, practically all are modifications of the original Cour-Palais Whipple shield equation for the non-optimum bumper condition. Although based on analytical cratering expressions, the original equations were empirically adjusted to fit experimental impact data. Since then, modifications to the equation have been made when additional impact data has become available. Although it includes a number of unique capabilities, the new ballistic limit equation is in essence an extension of the Whipple shield equation with different empirical factors. Further empirical adjustments of the equation do not appear feasible – indeed, it is considered that the adjustment of an equation originally derived for spaced Al-plates for application with composite sandwich panels is already not without issues. It can be noted by the inability of the new BLE to correctly predict every experimental result for all the structure panels considered that the empirical adjustment of the Whipple shield expression is effectively exhausted. Efforts have been made to derive analytical ballistic limit equations for application on both aluminium Whipple shields (Ding et al., 2006), and CFRP/Al HC sandwich panels (Banuelos, 2003) based on plate and structural mechanics theories. Although the approaches show promise, the applicability of these theories to hypervelocity impact problems remains questionable. Expressions which describe the physical behaviour and failure mechanisms present during hypervelocity impact event would be extremely valuable.

Appendix A
Calculation Parameters

Table A-1 Constants used in the micromechanics calculations.

Method	*Property*	*Constant*	*Units*	*Value*	*Reference*
Halpin-Tsai	E_{c22}	ξ	-	2	Jones (1999)
	G_{c12}	ξ	-	$1+40V_f^{10}$	Jones (1999)
	G_{c23}	ξ	-	$\frac{1+\nu_{c23}}{3-\nu_{c23}-4\nu_{c12}\nu_{c21}}$	Halpin & Kardos (1976)
Bridging model	[C]	α	-	0.35	Huang (2004)
	[C]	β	-	0.45	Huang (2004)
	strength	q	-	3	Huang (2004)

Table A-2 Parameter values used in Puck's action plane failure criteria analysis

Constant	*Symbol*	*Value*
Inclination parameter	$p_{12}^{(+)}$	0.35
Inclination parameter	$p_{12}^{(-)}$	0.3
Inclination parameter	$p_{22}^{(+/-)}$	0.3
Degradation constant	c	4
Degradation constant	ξ	2
Remaining stiffness	η_r	0.25

Appendix B
Material Data

Table B-1 Supplier data for the CFRP/Al HC sandwich panels tested in the Ballistic Limit experimental program: facesheet data

Face sheets	*Material*	*Density*	*Lamina type*	*Composition (by volume)*	*Lay-up*	*Stacking sequence*	*Thickness*
RAD1	FL01- HMF 196/34 T300-1k FL02- HYE K139-4349C	FL01- 1.80 g/cm^3 FL02- 1.80 g/cm^3 Total- 1.80 g/cm^3	FL01- Fabric FL02- u.d. ply	60% fibre, 40% resin (±3%)	Quasi-isotropic (0, ±45, 90)	9 plies [FL01 0, FL02 0,+45,90,-45,-45,90,+45,0]	FL01- 0.125mm (1 layer) FL02- 0.125mm (8 layers) Total- 1.13mm (9 layers)
RAD2	FL01- HMF 196/34 T300-1k FL02- HYE K139-4349C	FL01- 1.80 g/cm^3 FL02- 1.80 g/cm^3 Total- 1.80 g/cm^3	FL01- Fabric FL02- u.d. ply	60% fibre, 40% resin (± 3%)	Quasi-isotropic (0, ±45, 90)	10 plies [FL01 45, FL02 0,-45, +45, 90,90,+45,-45,0, FL01 +45]	FL01- 0.125mm (2 layer) FL02- 0.125mm (8 layers) Total- 1.25mm (10 layers)
RAD3	FL01- HMF 196/34 T300-1k FL02- HYE K139-4349C	FL01- 1.80 g/cm^3 FL02- 1.80 g/cm^3 Total- 1.80 g/cm^3	FL01- Fabric FL02- u.d. ply	60% fibre, 40% resin (± 3%)	Load-oriented (0, ±9)	10 plies [FL01 0,0, FL02 +9,-9, +9,-9,9,-9, FL01 0,0]	FL01- 0.125mm (4 layer) FL02- 0.125mm (6 layers) Total- 1.25mm (10 layers)
GOCE	VICOTEX M18/32%/M55J/145	1.65 g/cm^3	u.d. ply	60% fibre, 40% resin	Load-oriented (0, ±45)	16 plies [+45,0,0,-45,0,0, +45,0,0,-45,0,0, 45,0,0,-45]	2.0 mm
SAX	VICOTEX NCHM 14/34%137/6K/M40B	1.6 g/cm^3	u.d. ply	60% fibre, 40% resin	Load-oriented (0, ±60)	6 plies [0,+60,-60,-60,+60,0]	0.75 mm
H/P	M18/G801	1.7 g/cm^3	Fabric	48% fibre, 52% resin	Quasi-isotropic (0, ±45, 90)	4 plies (+45°,0°,90°,-45°)	0.4 mm

Table B-2 Supplier data for the CFRP/Al HC sandwich panels tested in the Ballistic Limit experimental program: honeycomb data

HC Core	*Adhesive*	*Designation*	*Material*	*Density*	*Cell size*	*Wall thickness*	*Foil treatment*	*Height*
RAD1	REDUX 112/312 L	3/16-5056-.001P	5056 Al alloy	0.0497 g/cm^3	4.7625 mm	0.0254 mm	None	50.8 mm
RAD2	REDUX 112/312 UL	3/16-5056-.001P	5056 Al alloy	0.0497 g/cm^3	4.7625 mm	0.0254 mm	None	25.4 mm
RAD3	REDUX 112/312 L	3/16-5056-.001P	5056 Al alloy	0.0497 g/cm^3	4.7625 mm	0.0254 mm	None	12.7 mm
GOCE	Unknown	3/16-5056-.001P	5056 Al alloy	0.0497 g/cm^3	4.7625 mm	0.0254 mm	None	11 mm
SAX	Unknown	3/16-5056-.001P	5056 Al alloy	0.0497 g/cm^3	4.7625 mm	0.0254 mm	None	31.5 mm
H/P	Unknown	3/16-5056-.0007	5056 Al alloy	0.0320 g/cm^3	4.7625 mm	0.0178 mm	None	20 mm

Table B-3 Structural configurations from literature used to further assess accuracy of the new BLE.

Mission	*Ref.*	*CFRP Facesheets*				*Honeycomb*	
		t (mm)	*Material*	*Density (g/cm^3)*	*stacking*	*Configuration*	*t (mm)*
Envisat	Lambert	1.1	M40/NCHM 914 fabric	1.579	(3x(0/±60))	3/16-.0015-5056P	45
Unknown	Taylor	1.62	HMF371/7714B fabric	1.825	$(0/90)_S$	5.2 ¼-.0025-3003	45
AXAF (A)*	Frost	0.254	M60J/954-2A u.d. ply	1.66$^+$	unknown	unknown	15.875
AXAF (B1)**	Frost	0.762	M60J/954-2A u.d. ply	1.66$^+$	unknown	unknown	15.875
AXAF (B2)**	Frost	0.762	P100/unknown u.d. ply	1.66$^+$	unknown	unknown	15.875
AXAF I*	Frost	0.508	M60J/954 u.d. ply	1.66$^+$	unknown	unknown	6.35
AXAF (D)*	Frost	1.016	M60J/954 u.d. ply	1.66$^+$	unknown	unknown	6.35
AXAF (E)*	Frost	1.524	M60J/954 u.d. ply	1.66$^+$	unknown	unknown	6.35
AXAF (F)***	Frost	0.406	M60J/954-3 u.d. ply	1.66$^+$	unknown	unknown	6.35

$^+$ Calculated from density of constituents assuming fibre volume content of 60%
* MLI blanket attached to outer side of front facesheet, see MLI type ABC in Frost & Rodriguez (1997). Estimated AD = 791 g/m²
** MLI blanket attached to outer side of front facesheet, see MLI type ST in Frost & Rodriguez (1997). Estimated AD = 791 g/m²
*** MLI blanket attached to outer side of front facesheet, see MLI type KF in Frost & Rodriguez (1997). Estimated AD = 516 g/m²

Table B-4 Mechanical properties of the GAIA CFRP constituents used for micromechanics.

Property	*Symbol*	*Units*	*Value*	*Source*
Fibre:				
Longitudinal tensile modulus	E_{f11}	GPa	540	Supplied
Transverse tensile modulus	E_{f22}	GPa	10.75	(b)
Major Poisson's ratio	ν_{f12}	-	0.2526	(a)
Transverse Poisson's ratio	ν_{f23}	-	0.33	(a)
In-plane shear modulus	G_{f12}	GPa	20.00	(b)
Transverse shear modulus	G_{f23}	GPa	4.04	(d)
Longitudinal tensile strength	X_{ft}	MPa	4000	Supplied
Longitudinal compression strength	X_{fc}	MPa	1551.72	(a)
Resin:				
Young's modulus	E_m	GPa	2.50[+]	Supplied
Poisson's ratio	ν_m	-	0.375	(a)
Shear modulus	G_m	GPa	0.9091	(d)
Tensile strength	X_{mt}	MPa	110	Supplied
Compression strength	X_{mc}	MPa	242.23	(c)
Shear strength	S_{mxy}	MPa	70.58	(a)
Fracture energy	G_{mf}	J/m^2	420	(e)
Composite:				
Fibre content by volume	V_f	%	58	Supplied
Density[**]	ρ	g/cm^3	1.52	(f)

[+] Flexural value
[**] Measured at EMI

(a) Common value based on review of u.d. tape properties
(b) Daniel and Ishai (1994)
(c) Hart-Smith (1992)
(d) From isotropy / transverse isotropy
(e) From similar material (Cech & Kretow, 1999)

Appendix C
Experimental Data

Table C-1 Ballistic limit test results of CFRP/Al HC sandwich panels with witness plate.

Panel	EMI no.	v (km/s)	α (°)	d_p (mm)	m_p (mg)	E_k (J)	Result		WP Damage (mm)			
							SP	WP	d_{WPh}	D_{WPh}	D_{DUST}	D_{WP99}
RAD1	S-4671	2.6	0	4.0	87.5	296	P	P	2.9	2.7x3.1	50x54	33x13
	S-4672	3.57	0	4.0	87.1	555	P	P	1.6	16.8x9.1	100x84	106x70
	S-4673	6.47	0	4.0	86.5	1810	P	P	1.75	5.8x4.8	150x190	28x27
	S-4616	6.99	0	4.0	87.2	2131	P	P	1.4	1.4x1.4	145x145	42x40
	S-4682	7.75	0	4.0	86.9	2610	P	NP		No hole	150x155	16x13
	S-4617	6.91	45	4.0	87.5	2089	P	NP		No hole	95x77	-
	S-4618	6.85	45	5.0	176	4129	P	NP		No hole	105x185	-
	S-4695	6.45	0	4.0	87.7	1824	P	P	2.2	1.8x2.6	150x130	56x54
	S-4694	6.53	0	4.0	86.8	1851	P	P	15.0	15.6x14.5	90x98	51x56
RAD3	S-4610	6.73	0	3.0	37.1	840	P	DSP		No hole	165x150	70x70
	S-4611	6.72	0	4.0	87.5	1976	P	P	2.5	10x17	230x235	81x99
GOCE	S-4693	4.13	0	4.0	87.3	745	P	NP		No hole	47x51	62x78
	S-4692	6.40	0	4.0	87.4	1790	P	DSP		No hole	140x117	72x50
SAX	S-4621	6.92	0	4.0	87.4	2093	P	P	3.35	11.0x11.4	205x190	85x80
	S-4622	6.64	45	4.0	86.7	1911	P	NP		No hole	160x190	-

Table C-2 Ballistic limit test results of CFRP/Al HC sandwich panels.

Panel	EMI no.	v (km/s)	α (°)	d_p (mm)	m_p (mg)	E_k (J)	Coarse result	Front FS (mm)		Rear FS (mm)	
								$d_{h,ave}$	d_{sp}	$d_{h,ave}$	d_{sp}
RAD1	B-107	2.02	0	1.25	2.9	2.9	NSP	2.3	5.0x4.7	No damage	
	B-106	2.36	0	1.0	1.3	1.8	DSP	2.2	4.2x5.8	-	1.5x0.7
	B-164	3.13	0	1.5	5.61	27	P	4.29	7.9x4.7	3.6	7.4x6.5
	B-119	6.24	0	1.0	1.2	20	P	4.3	8.3x8.9	3.1	5.9x7.7
	B-117	6.27	0	1.0	1.2	24	P	4.5	8.6x7.6	1.1	5.6x4.2
	S-4577	5.72	0	1.5	5.4	88	P	5.74	8.5x10	6.42	9.9x11.3
	S-4578	5.72	0	1.5	5.4	88	P	6.07	7.2x9.8	5.96	11.1x11.7
	B-108	6.27	0	1.5	5.6	110	P	6.19	9.4x9.8	6.16	8.5x9.6
	B-161	4.27	45	1.0	1.52	14	NSP	3.2	6.5x6.2	No damage	
	B-167	3.39	45	1.25	2.87	17	NSP	3.5	6.4x8.3	No damage	
	S-4579	5.87	45	1.5	5.3	91	NSP	5.96	8.3x10.0	No damage	
	S-4580	6.12	45	2.0	11.8	221	DSP	7.7	10.6x10.1	-	4.0x3.2
	S-4583	6.07	60	2.0	12	221	P	7.6	10.2x11.7	0.9	3.7x4.3
	S-4582	6.52	60	2.5	21	446	P	9.3	12.1x13.2	6.6	11.7x15.2
	S-4581	6.23	60	3.0	37.2	722	P	10.3	11.2x14.4	6.4	8.7x9.3
RAD 2	B-149	5.93	0	1.0	1.6	28	NSP	4.4	8.2x7.8	No damage	
	B-155	6.26	0	1.25	2.88	56	P	5.1	8.7x8.7	5.9	13.6x14.4
	S-4612	6.62	0	2.0	11.9	262	P	7.2	9.2x10.2	7.1	8.5x7.5
	B-150	5.96	45	1.0	1.56	28	NSP	4.5	7.0x8.1	No damage	
	S-4613	5.48	45	1.5	5.09	97	P	6.4	8.7 x 8	1.0	3x5

Table C-2 (cont.) Ballistic limit test results of CFRP/Al HC sandwich panels.

Panel	EMI no.	v (km/s)	α (°)	d_p (mm)	m_p (mg)	E_k (J)	Coarse result	Front FS (mm)		Rear FS (mm)	
								$d_{h,ave}$	d_{sp}	$d_{h,ave}$	d_{sp}
RAD3	B-105	2.82	0	1.0	1.3	2.5	P	2.3	3.0x3.0*	1.5	4.3x3.5
	B-139	3.36	0	1.0	1.51	8.5	P	2.3	3.7x2.5	1.0	1.9x4.1
	B-127	5.88	0	0.50	0.4	6.9	NSP	1.5	3.3x2.0	No damage	
	B-131	5.88	0	0.50	0.4	6.9	NSP	1.4	2.5x2.6+	No damage	
	B-132	6.05	0	0.70	0.45	8.2	NSP	2.2	4.2x4.1	No damage	
	B-154	5.94	0	0.80	0.31	16	DSP	2.6	4.4x2.9	-	0.5x0.5
	B-147	5.87	0	1.0	1.68	29	P	3.4	5.6x4.8	4.7	8.2x9.6
	B-162	3.42	45	1.0	1.51	8.8	NSP	2.6	3.4x4.2	No damage	
	B-140	3.33	45	1.25	2.92	16	DSP	3.4	5.2x4.7	-	2.2x1.8
	B-156	6.45	45	0.80	1.46	30	NSP	3.6	4.3x5.7	No damage	
	B-133	6.18	45	1.0	1.44	28	DSP	3.6	4.7x4.5	<0.5	3.5x2.7
	B-160	6.62	60	1.0	2.05	45	NSP	3.8	4.5x5.8	No damage	
	B-134	5.77	60	1.55	5.48	91	P	5.7	6.5x8.4	5.3	10.1x4.4
	B-138	2.96	0	0.076	0.55	2.4	NP	Not measured		No damage	
GOCE	B-146	5.98	0	1.0	1.57	28	NSP	3.7	30.1x39.0	No damage	
	B-152	6.26	0	1.5	5.85	115	P	6.5	29.0x28.7	5.5	57.9x61.8
	B-145	5.80	45	1.0	1.52	26	NSP	3.7	9.8x9.9	No damage	
SAX	B-153	5.94	0	0.80	0.91	16	NSP	3.1	3.6x8.3	No damage	
	B-148	5.96	0	1.0	1.52	27	P	3.4	4.4x8.8	4.3	13.6x46.5
H/P	B-176	5.93	0	1.0	1.73	30	P	2.6	3.2x4.0	5.5	6.1x8.8

+ Overlap of spall area from 2 tests. Average measurement taken
* Overlap from sabot part impact damage

References

Aboudi J. 1991. *Mechanics of Composite Materials. A Unified Micromechanical Approach*, Studies in Applied Mechanics, vol. 29, Elsevier, New York

Anderson Jr. C, Trucano T, Mullin S. 1990. *Debris Cloud Dynamics*, International Journal of Impact Engineering; 9(1): 89-113

Anderson Jr. C. 1987. *An Overview of the Theory of Hydrocodes*, International Journal of Impact Engineering; 5: 33-59

Anderson Jr. C., Cox P, Johnson G, Maudlin P. 1994. *A Constitutive Formulation for Anisotropic Materials Suitable for Wave Propagation Computer Programs – II*, Computational Mechanics; 15: 201-223

Anon. 1963. *Meteoroid Environment in Near Earth, Cislunar, and Near Lunar Space*, NASA MSC Engineering Criteria Bulletin EC-1

Anon. 1983. *SESAME*, Report on the Los Alamos Equation of State Library, Los Alamos National Laboraties, Los Alamos, LANL-83-4

Anon. 1995. *Guidelines for Assessment Procedures for Limiting Orbital Debris*, NASA Safety Standard, Office of Safety and Mission Assurance, Washington, NSS 1740.14

Anon. 1997. *Protecting the Space Station from Meteoroids and Orbital Debris*, Committee on International Space Station Meteoroid/Debris Risk Management, National Research Council, National Academy Press, Washington

Anon. 1999. *Pyroshock Test Criteria*, NASA Technical Standard, NASA STD-7003

Anon. 2002. *Magnamite IM6 Carbon Fiber – Product Data*, Hexcel Composites, www.hexcel.com

Anon. 2004. *Properties for Graphite/Epoxy (IM-6/3501-6), Fiber Volume = 63.5%*, University of California (San Diego), http://casl.ucsd.edu/oldindex.html, accessed: 2006-04-27

Anon. 2005. *AUTODYN Theory Manual*, Revision 4.3, Century Dynamics Inc., Concord

Anon. 2005b. *AUTODYN SPH User Manual and Tutorial*, Century Dynamics Inc., Concord, USA

Avans S, Horn J, Williamsen J. 1990. *Shielding Requirements for the Space Station Habitability Modules*, NASA and DoD Orbital Debris Conference: Technical Issues and Future Directions, Baltimore, April 16-19, AIAA Paper 1990-1333

Banuelos J. 2003. *Ballistic Limit Equation for Hypervelocity Impact on Composite-Orthotropic Materials*, PhD Thesis, Rice University, Houston

Barnes N, Bourne N, Millett J. 2001. *The Shock Hugoniot of an Epoxy Resin*, Shock Compression of Condensed Matter 2001, American Institute of Physics CP620, pp. 135-138

Cable A. 1970. *Hypervelocity Accelerators*, in: Kinslow (ed.), High-Velocity Impact Phenomena, Academic Press Inc., New York

Carlone, R. 1992. *Space Station: Delays in Dealing With Space Debris May Reduce Safety and Increase Costs*, Report to the Chairman, Subcommittee on Government Activities and Transportation, Committee on Government Operations, House of Representatives

Carter W, Marsh S. 1995. *Hugoniot Equation of State of Polymers*, Los Alamos National Laboratory, Los Alamos, Report LA-120006-MS

Cech J, Kretow B. 1999. *The Effectiveness of Toughening Technologies on Multifunctional Epoxy Resin Systems*, Surface Coatings Australia; 40(5): 19-23

Chai H, Knauss W, Babcock C. 1983. *Observation of Damage Growth in Compressively Loaded Laminates*, Exp. Mechanics; 23(3): 329-337

Chamis C. 1974. *Micromechanics Strength Theories*, in: L. Broutman (ed.), Composite Materials vol. 5: Fracture and Fatigue, Academic Press, New York

Chamis C. 1984. *Simplified Composite Micromechanics Equations for Hygral, Thermal, and Mechanical Properties*, SAMPE Quarterly; 15: 14-23

Chang J, Zheng C, Ni Q. 2006. *The Ultrasonic Wave Propagation in Composite Material and its Characteristic Evaluation*, Composite Structures; 75: 451-456

Chen J, Allahdadi F, Sun C. 1997. *A Quadratic Yield Function for Fiber-Reinforced Composites*, Journal of Composite Materials; 31(8): 788-811

Christensen R. 1990. *A Critical Evaluation for a Class of Micromechanics Models*, Journal of the Mechanics and Physics of Solids; 38(3): 379-404

Christiansen E, Nagy K, Lear D, Prior T. 2006. *Space Station MMOD Shielding*, 57th International Astronautical Congress, Valencia, Oct. 2-6

Christiansen E. 1987. *Evaluation of Space Station Meteoroid/Debris Shielding Materials*, NASA Johnson Space Center, Houston, CR-185627

Christiansen E. 1991. *Whipple Shield Sizing Equations*, NASA Johnson Space Center, NASA TM-105539

Christiansen E. 1993. *Design and Performance Equations for Advanced Meteoroid and Debris Shields.* Int. Journal of Impact Eng.; 14:145-156

Chung D. 1994. *Carbon Fiber Composites*, Butterworth-Heinemann, Newton

Clegg R, White D, Riedel W, Harwick W. 2006. *Hypervelocity Impact Damage Prediction in Composite. Part I – Material Model and Characterization*, Int. Journal of Impact Engineering; 33(1-2); 190-200

Cour-Palais B, Crews J. 1990. *A Multi-Shock Concept for Spacecraft Shielding*. International Journal of Impact Engineering; 10: 135-146

Cour-Palais B. 1985. *Hypervelocity Impact investigations and Meteoroid Shielding Experience Related to Apollo and Skylab*, Orbital Debris: 247-275

Cour-Palais B. 1987. *Hypervelocity Impact in Metals, Glass and Composites*, International Journal of Impact Engineering; 5: 221-237

Daniel I, Ishai O. 1994. *Engineering Mechanics of Composite Materials*, Oxford University Press, New York

Ding L, Zhang W, Pang B, Li C. 2006. *Analytical Ballistic Limit Equation for Dual Wall Structures*, 36th COSPAR Scientific Assembly, Beijing, July 16-23

Drolshagen G, Borge J. 1992. *Meteoroid/Debris Impact Analysis (ESABASE/DEBRIS): Technical Description*. ESA/ESTEC, Report No. ESABASE-GD-01/1, Noordwijk, The Netherlands

Dugdale J, MacDonald. 1953. *The Thermal Expansion of Solids*, Physical Review; 89(4): 832-834

Eshelby J. 1957. *The Determination of the Elastic Field of an Ellipsoidal Inclusion, and Related Problems*, Proceedings of the Royal Society of London, Series A; 241: 376-396

Evans M, Harlow F. 1957. *The Particle-In-cell Method for Hydrodynamic Calculations*, Los Alamos Scientific Laboratory, Los Alamos, LA-2139

Faraud M, Destefanis R, Palmieri D, Marchetti M. 1999. *SPH Simulations of Debris Using Two Different Computer Codes*, International Journal of Impact Engineering; 23: 249-260

Finlayson R, Freisel M, Carlos M, Cole P, Lenain J. 2001. *Health Monitoring of Aerospace Structures with Acoustic Emission and Acousto-Ultrasonics*, Insight; 43(3)

Frazier J, Karpov B, Holloway L. 1965. *The Behavior of Wax Targets Subjected to Hypervelocity Impacts*, 7th Hypervelocity Impact Symp., vol. 5

Frost C, Rodriguez P. 1997. *AXAF Hypervelocity Impact Test Results*, 2nd European Conference on Space Debris, Darmstadt, March 17-19

Frost V. 1970. *Meteoroid Damage Assessment*, Aerospace Corporation, Langley, NASA SP-8042

Gehrig J. 1970. *Theory of Impact on Thin Targets and Shields and Correlations with Experiment*, in: Kinslow (ed.), High Velocity Impact Phenomena, Academic Press, New York

Gilat A, Goldberg R, Roberts G. 2005. *Strain Rate Sensitivity of Epoxy Resin in Tensile and Shear Loading*, Ohio State University, Columbus, NASA TM-2005-213595

Gorman M. 1991. *Acoustic Emission for the 1990s*, Ultrasonics Symposium, Orlando, Dec. 8-11

Guyot M. 2005. *Spacecraft Disturbances from Hypervelocity Impact – General Test Objectives*, WP2500 of ESA Contract 18583/04/NL/CH, EADS Astrium, Toulouse, Report 2124.NT.MG.05.6585.ASTR

Guyot M. 2006. *Spacecraft Disturbances from Hypervelocity Impact – Target Detailed Design*, WP3400 of ESA Contract 18583/04/NL/CH, EADS Astrium, Toulouse, Report 2124.NT/MG.06.7 603.ASTR v1.1

Halpin J. 1969. *Effects of Environmental Factors on Composite Materials*, Wright-Patterson Air force Base, Dayton, AFML-TR-67-123

Halpin J, Kardos J. 1976. *The Halpin-Tsai Equations: A Review*, Polymer Engineering and Science; 16(5): 344-352

Hart-Smith L. 1992. *The Ten-Percent Rule for Preliminary Sizing of Fibrous Composite Structures*, Weight Engineering; 5(2): 29-45

Hayhurst C. Clegg R. 1997. *Cylindrically Symmetric SPH Simulations of Hypervelocity Impacts on Thin Plates*, International Journal of Impact Engineering; 20(1-5): 337-348

Hermans J. 1967. *The Elastic Properties of Fibre Reinforced Materials When the Fibres are Aligned*, Koninklijke Nederlandse Ackademie van Wetenschappen Amsterdam; B70(1): 1-9

Hiermaier S. 2003. *Numerik und Werkstoffdynamik der Crash- und Impaktvorgänge (German)*, Habilitation thesis, Faculty of Civil Engineering and Surveying, Universität der Bundeswehr, Munich

Hiermaier S, Riedel W, Hayhurst C, Clegg R, Wentzel C. 1999. *Advanced Material Model for Hypervelocity Impact Simulations*, FhG Ernst Mach Institute (EMI), Freiburg, ESA CR (P) 4305

Hinton M, Kaddour A, Soden P. 2002. *A Comparison of the Predictive Capabilities of Current Failure Theories for Composite Laminates, Judged Against Experimental Evidence*, Comp. Science & Tech.; 62: 1725-1797

Hinton M, Kaddour A, Soden P. 2004. *Failure Criteria in Fibre Reinforced Polymer Composites: The World Wide Failure Exercise*, Elsevier, Amsterdam

Hou J, Petrinic N, Ruiz C. 2000. *Prediction of impact damage in composite plates*, Composites Science and Technology; 60:273–281

Huang Z. 2004. *A Bridging Model Prediction of the Ultimate Strength of Composite Laminates Subjected to Biaxial Loads*, Composites Science and Technology; 64: 395-448

Hughes W, McNelis M. 2002. *Recent Advances in Vibroacoustics*, NASA Glenn Research Center, Cleveland, NASA TM-2002-211697

Jex D, Miller A, MacKay C. 1970 *The Characteristics of Penetration for a Double-Sheet Structure with Honeycomb,* NASA Marshall Space Flight Center, Huntsville, NASA TM X-53974

Johnson W, Anderson C. 1987. *History and Application of Hydrocodes in Hypervelocity Impact*, Int. Journal of Impact Engineering; 5: 423-439

Jones R. 1999. *An Introduction to Composite Materials*, Taylor & Francis Inc. Philadelphia

Kaiser C, Kuhnel E, Obst A. 2004. *Failure Criteria for Non-metallic Materials. Part I: Fibre Reinforced Plastics,* 11th European conference on composite materials, Rhodes, May 31-June 4

Klinkrad H. 2006. *Space Debris: Models and Risk Analysis*, Springer-Verlag, Berlin

Kwon Y, Berner J. 1995. *Micromechanics Model for Damage and Failure Analyses of Laminated Fibrous Composites*. Engineering Fracture Mechanics; 52(2): 231-242

Lambert M, Frey J, Rios J, Garaud X, Dubois J, Schneider E. 1991. *The Validation of Hydrocodes for Orbital Debris Impact Simulation*, International Conference on Spacecraft Structures and Mechanical Testing, Noordwijk, April 24-26

Lambert M, Schäfer F, Schneider E. 2001. *Impact Damage on Sandwich Panels and Multi-Layer Insulation*, Int. J. of Impact Eng.; 26: 369-380.

Lambert M. 1997. *Hypervelocity Impact and Damage Laws*, Advances in Space Research; 19(2): 369-378

Liou J (Ed.). 2007. *NASA Orbital Debris Quarterly News*, Vol. 11(2), NASA Johnson Space Center Orbital Debris Program Office, Houston

Liou J, Johnson N. 2006. *Instability of the Present LEO Satellite Populations*, 36th COSPAR Scientific Assembly, 16-23 July, Beijing, China Aboudi J. 1991. *Mechanics of Composite materials. A Unified Micromechanical Approach*, Studies in Applied Mechanics, vol. 29, Elsevier, New York

Liu C, Ahrens T, Brar N. 2002. *Effect of Phase Change on Shock Wave Attenuation in GeO_2*, Journal of Applied Physics; 91(11): 9136-9144

Machens M, Schäfer F, Riedel W, Rohr I. 2005. *Shock Properties of a Carbon Fibre Composite for Space Application.* CCN 1 & CCN 2 of ESA Contract 16483, FhG Ernst- Mach- Institut (EMI), Freiburg, EMI Report I-36/04

Maiden C, McMillan A, Sennett R, Gehrig J. 1965. *Experimental Investigations of Simulated Meteoroid Damage to Various Spacecraft Structures*, Summary Report, GM Defence Research Laboratories, Santa Barbara, NASA CR-65222

Maiden C. 1964. *Meteoroid Impact*, in: Space Exploration, McGraw Hill, New York, pp. 236-264

Mayes J, Hansen A. 2004. *A Composite Laminate Failure Analysis Using Multicontinuum Theory*, Comp. Science and Technology; 64: 379-394

Moening, C. 1985. *Pyrotechnic Shock Flight Failures*, Institute of Environmental Sciences Pyrotechnic Shock Tutorial Program, 31st Annual Technical Meeting

Nieder R. 1990. *Implication of Orbital Debris for Space Station Design*, NASA and DoD Orbital Debris Conference: Technical Issues and Future Directions, Baltimore, April 16-19, AIAA Paper 1990-1331

O'Brien T. 1997. *Composite Interlaminar Shear Fracture Toughness, G_{IIc}: Shear Measurement of Sheer Myth?*, NASA Langley Research Center, Hampton, NASA TM-110280

Oswald M, Wegener P, Stabroth S, Wiedemann C, Rosebrock J, Martin C, Klinkrad H, Vörsmann P. 2006. *The Master 2005 Model*, Final Report of ESA Contract 18014/03/D/HK(SC), Institute of Aerospace Systems, University of Braunschweig, Braunschweig

Pavarin D, Francesconi A, Debei S, Caporal G. 2002. *Preliminary Design of a Test Bed to Evaluate the Requirements of an Accelerometric Instrumentation to Study the Effects of Hypervelocity Impacts on Space Shields*, Mechanical Measurements Conference, Sept. 17-19

Pavarin D, Francesconi A, Destefanis R, Lambert M, Bettella A, Debei S, De Cecco M, Faraud M, Giacomuzzo C, Maruchhi-Chierro P, Parzianello G, Saggin B, Angrilli F. 2006. *Acceleration Fields Induced by Hypervelocity Impacts on Spacecraft Structures*, International Journal of Impact Engineering; 33: 580-591

Pavarin D, Lambert M, Francesconi A, Destefanis R, Bettella A, Debei S, De Cecco M, Faraud M, Giacomuzzo C, Maruchhi-Chierro P, Parzianello G, Saggin B, Angrilli F. 2005. *Analysis of GOCE's Disturbances Induced by Hypervelocity Impact*, 4th European Conference on Space Debris, Darmstadt, April 18-20

Pezzica G, Destefanis R, Faraud M. 1996. *Numerical Simulation of Orbital Debris Impact on Spacecraft*, Structures Under Shock and Impact Conference, Udine, July 3-5

Prosser W, Gorman M, Humes D. 1999. *Acoustic Emission Signals in This Plates Produced by Impact Damage*, Journal of Acoustic Emission; 17(1-2): 29-36

Prosser W. 1996. *Application of Advanced, Waveform Based AE Techniques for Testing Composite Materials*, SPIE Conference on Non-destructive Evaluation Techniques for Aging Infrastructure and Manufacturing: Materials and Composites, Scottsdale, Dec. 2-5

Puck A, Schürmann H. 2002. *Failure Analysis of FRP Laminates by Means of Physically Based Phenomenological Models*, Composites Science and Technology; 62: 1633-1662

Puck A, Schürmann H. 1998. *Failure Analysis of FRP Laminates by Means of Physically Based Phenomenological Models,* Composites Science and Technology; 58:1045-1068

Putzar R, Schäfer F, Romberg O, Stokes H, Heine A, Zimmermann J. 2006. *Vulnerability of Spacecraft Equipment to Space Debris and Meteoroid Impacts*, FhG Ernst- Mach- Institute (EMI), Freiburg, EMI Report I-15/06

Riedel W. 2004. *Beton Unter Dynamischen Lasten: Meso- und Makromechanische Modelle und Ihre Parameter (German)*, PhD thesis, Faculty of Civil Eng. and Surveying, Universität der Bundeswehr, Munich

Riedel W, Harwick W, White D, Clegg R. 2003. *Advanced Material Damage Models for Numerical Simulation*, FhG Ernst- Mach- Institute (EMI), ESA CR(P) 4397, Freiburg, Germany

Riedel W, Nahme H. 2001. *Shock Properties of a HEXCEL IM7/8552 – Experimental Investigations and Material Modelling*, FhG Ernst Mach Institute (EMI), Freiburg, EMI Report E-25/01

Riedel W, Nahme H, White D, Clegg R. 2006. *Hypervelocity Impact Damage Prediction in Composites: Part II – Experimental Investigations and Simulations*, Int. Journal of Impact Engineering; 33(1-2); 670-680

Riedel W, Thoma K, Hiermaier S, Schmolinske E. 1999. *Penetration of Reinforced Concrete by BETA-B-500: Numerical Analysis Using a New Macroscopic Concrete Model for Hydrocodes*, 9th International Symposium of Interaction of the Effects of Munitions with Structures, Academy for Communication and Information, Berlin, Germany

Rosen B, Hashin Z. 1987. *Analysis of Material Properties*, in: Dostal, C. (editor), Engineering Materials Handbook Vol. 1: Composites, ASM International

Schäfer F. 2006. *An Engineering Fragmentation Models for the Impact of Spherical Projectiles on Thin Metallic Plates*, International Journal of Impact Engineering; 33: 745-762

Schäfer F, Schneider E, Lambert M. 2004 *Review of Ballistic Limit Equations for CFRP Structure Walls of Satellites*. 5th International Symposium on Environmental Testing for Space Programmes, ESA SP-558, June 15-17, Noordwijk, The Netherlands

Schäfer F. 2001. *Hypervelocity Impact Testing. Impacts on Pressure Vessels.* Final Report of ESA Contract No. 10556, FhG Ernst- Mach-Institut (EMI), EMI Report No. I-27/01, Freiburg, Germany

Schäfer F, Ryan S, Destefanis R, Rott M, Mandeville J. 2005. *Composite Materials Impact Damage Analysis – Final Report*, FhG Ernst- Mach-Institute (EMI), Freiburg, EMI Report I-69/05

Schäfer F, Spencer G, Ryan S, Wicklein M, Guyot M, Lambert M. 2006. *Experimental and Analytical Study to Investigate Impact-Induced Wave Propagation in Spacecraft Structures*, 56th International Astronautical Congress, Valencia, Oct. 2-6

Schneider E, Schäfer F. 2001. *Hypervelocity Impact Research – Acceleration Technology and Applications*, Advances in Space Research; 28(9): 1417-1424

Schonberg W, Walker E. 1991. *Use of Composite Materials in Multi-Wall Structures to Prevent Perforation by Hypervelocity Particle Impact*, Composite Structures; 19: 15-40

Schonberg W, Walker E. 1994. *Hypervelocity Impact of Dual-Wall Space Structures with Graphite/Epoxy Inner Walls*, Composites Engineering; 4(10): 1045-1054

Schonberg W. 1990. *Hypervelocity Impact Response of Spaced Composite Material Structures*, Int. Journal of Impact Engineering; 10(1-4): 509-523

Soden P, Hinton M, Kaddour A. 1998. *Lamina properties, lay-up configurations and loading conditions for a range of fibre-reinforced composite laminates*. Comp. Science and Technology; 58: 1011-1022

Spencer G, Ryan S, Schäfer F. 2007. *Spacecraft Disturbances from Hypervelocity Impact - Test Set-Up Validation and Preparatory Tests*. WP3200 of ESA Contract 18583/04/NL/CH, FhG Ernst- Mach- Institut (EMI), EMI Report No. I-24/06, Freiburg, Germany

Summers J. 1959. *Investigation of High-Speed Impact: Regions of Impact and Impact at Oblique Angles*, NASA Ames Research Center, TN D-94

Swegle J. 1978. *TOODY-IV: A Computer Program for Two-Dimensional Wave Propagation*, Sandia National Lab., Albuquerque, SAND-78-0552

Taylor E, Herbert M, Kay L, Thomson R, Burchell M. 1997. *Hypervelocity Impact on Spacecraft Carbon Reinforced Plastic/Aluminium Honeycomb*, Journal of Aerospace Engineering; 211: 355-363

Taylor E, Herbert M, Vaughan B, McDonnell J. 1999. *Hypervelocity Impact on Carbon Fibre Reinforced Plastic / Aluminium Honeycomb: Comparison with Whipple Bumper Shields*, Int. J. of Impact Eng.; 23(1-2), 883-893

Taylor E. 1999. *Computational Study of Hypervelocity Impact onto Whipple Bumpers and Sandwich Plates with Honeycomb Core*. ESA/ESTEC, Report No. EWP-2029, Noordwijk, The Netherlands

Tennyson R, Manuelpillai G. 1994. *Prediction of Space Hypervelocity Impact Damage in Composite Materials*, 8th CASI Conference on Astronautics, Ottowa, Nov. 7-10

Tennyson R, Shortliffe G. 1997. *MOD Impact Damage on Composite Materials in Space*, 7th International Symposium on Materials in Space Environment, Toulouse, June 16-20

Terrillon F, Warren H, Yalle M. 1991. *Orbital Debris Shielding Design of the Radarsat Spacecraft*, 42nd International Astronautical Congress, Montreal, Oct. 7-11

Weeton J, Peters D, Thomas K (eds.). 1987. *Engineers' Guide to Composite Materials*, ASM International, Materials Park

White D. 2001. *Columbus Shielding Validation Using AUTODYN*, Century Dynamics Limited, Horsham, Report R192:03

Wicklein M, Ryan S, White D, Clegg R. 2007. *Hypervelocity Impact on CFRP: Testing, Material Modelling, and Numerical Simulation*, to be published in the International Journal of Impact Engineering

Wilkins M. 1964. *Calculation of Elastic-Plastic Flow*, Methods in Computational Physics; 3: 211-263

Williams J, Anderson M, Rhodes D, Starnes Jr. J, Stroud W. 1979. *Recent Developments in the Design, Testing, and Impact Damage Tolerance of Stiffened Composite Panels*, NASA Langley Research Center, NASA TM-80077

Yew C, Kendrick R. 1987. *A Study of Damage in Composite Plates Produced by Hypervelocity Impact*, International Journal of Impact Engineering; 5: 729-738

Index